Towards a more complete description of final-state interactions in electroweak single-pion production off atomic nuclei

Alexis Nikolakopoulos

Supervisor: prof. dr. N. Jachowicz
Dissertation submitted in fulfillment of the requirements for the degree of
Doctor (Ph.D.) in Science: Physics

Department of Physics and Astronomy
Faculty of Sciences
Ghent University
Academic year 2021-2022

GHENT
UNIVERSITY

Members of the examination committee

Voting members

prof. dr. Christophe Detavernier (Universiteit Gent, *Chair*)
dr. Jannes Nys (Universiteit Gent)
prof. dr. Jan Ryckebusch (Universiteit Gent)
prof. dr. Dirk Ryckbosch (Universiteit Gent)
prof. dr. Federico Sanchez-Nieto (University of Geneva)
prof. dr. José Manuel Udías (University Complutense Madrid)

Other members

prof. dr. Natalie Jachowicz (Universiteit Gent, *promotor*)
prof. dr. Wim Cosyn (Florida International University, Universiteit Gent, *promotor*)

Acknowledgement

I am grateful to my promotor Natalie, firstly for providing me with the opportunity to work in your group around 5 years ago. Your management style was to give me much freedom, which only works because you have the talent to steer me back into the right direction at just the right moments. I thank you for your trust and guidance, both in the scientific and practical aspects.

For most years I have shared an office with Nils, it was my pleasure to work with him on several projects and his explanations of the codes and physics have been invaluable to me.

Over the past years I have enjoyed a fruitful collaboration with Raúl and José-Manuel, and have enjoyed their hospitality during a stay at UCM. I am indebted to Raúl for a great amount of 'tricks', and wish to thank him especially for his eagerness to share his results and problems, and to think critically about mine. Many of the results in this dissertation rely on the 'numerology'[1] provided by José-Manuel, for which credit is due. More importantly, I have benefited greatly from José-Manuel's knowledge and insights, which were shared with me and others in discussions, and in many detailed emails.

Similarly I have had the pleasure to work closely with Kajetan and Jan Sobczyk, and have enjoyed their hospitality during a visit to Wrocław. Kajetan's contributions to our shared projects cannot be understated, and I greatly appreciate his visits to my office after 'working hours'[2] during which he asked me many questions to which I still don't have an answer.

1. The term numerology in this context has nothing to do with the irrational belief that numbers could influence or define personality traits. The term refers to the tricks of the trade used to build efficient (stable) programs for mathematical functions and numerical calculations.
2. Working hours tend to be a fluid concept for some of my colleagues and for me. This has worked to both my benefit and detriment.

I thank Federico, for his hospitality during my stay at the university of Geneva, and for taking time out of his busy schedule for numerous hour-long discussions. Your enthusiasm for physics is truly contagious.

A benefit of performing research comes from the possibility to talk to and work with a variety of people. I would like to thank W. Cosyn, H. Damien, S. Dolan, D. Douqa, M. Martini, G. D. Megias, J. G. Morfín J. Nys, V. Pandey, J. Ryckebusch, D. Ryckbosch, and T. Van Cuyck for providing me with code, insights, and opportunities which have helped me along the way.

Alexis Nikolakopoulos
Gent, December 12, 2021

Contents

Acknowledgement **v**

1 Introduction **1**

1.1 Neutrino oscillations and accelerator based experiments . 1

1.1.1 Neutrino oscillations 1

1.1.2 Accelerator-based neutrino experiments 5

1.2 Neutrino interactions 7

1.2.1 Neutrino-induced single pion production 8

1.2.2 Neutrino event generators 10

1.3 Outline 11

2 Lepton scattering off nucleons and nuclei **13**

2.1 Kinematics and cross section 13

2.2 The invariant matrix element 18

2.3 Rosenbluth decomposition 22

3 Single-pion production off the nucleon **25**

3.1 Isospin decomposition of the current and CVC 29

3.2 The axial current and PCAC 31

3.3 Modeling electroweak SPP 33

3.3.1 Spin 1/2 resonances 33

3.3.2 Spin 3/2 resonances 34

3.3.3 Resonance widths and coupling constants 35

3.3.4 Non-resonant background 38

3.3.5 Isospin coefficients and form factors 39
I. Vector current form factors 40
II. Axial form-factors 51
3.3.6 Partial unitarization in the Delta region 54
3.3.7 Reggeized background 57
I. Regge Poles 59
II. Reggeized Born-term model 67
III. Vector current 69
IV. Axial current 71
V. Hybrid model 73
3.4 Results for electromagnetic SPP and the vector current . 74
3.4.1 Photoproduction of pions 76
3.4.2 Electroproduction of pions 77
3.4.3 The Charge-changing vector current 79
3.5 Results for pion-nucleon scattering 86
3.6 Results for neutrino induced SPP 89
3.6.1 Total cross sections 92
3.6.2 Q^2- and W-dependence 92
3.7 Conclusions 99

4 Scattering off nuclei **101**
4.1 Kinematics 102
4.1.1 Missing energy distribution 103
4.2 Nuclear currents 104
4.3 Potentials for the final state nucleon 106
I. The RMF 107
II. The Relativistic Optical Potential (ROP) 107
III. The Real ROP (rROP) 108
IV. The Energy-Dependent RMF (ED-RMF) 109
V. Orthogonality of initial and final state, the Pauli-Blocked RPWIA (PB-RPWIA) 110

4.4 Orthogonality, Pauli-blocking and the ratio between ν_e and ν_μ cross sections 113

4.5 Consistent wavefunctions for initial and final state and CVC 120

4.6 Conclusions 122

5 RPWIA for single-pion production off the nucleus 123

5.1 Introduction 123

5.2 Results 125

5.2.1 The hybrid-RPWIA model 126

5.2.2 NuWro and Final State Interactions 129

5.3 Conclusions 134

6 RDWIA for single-pion production off the nucleus 135

6.1 Comparison of hadronic responses 137

6.2 Minerνa experiment 139

6.2.1 Charged pion production 140

6.2.2 Neutral pion production 148

6.3 T2K 154

6.4 Conclusions 158

7 Summary and Conclusions 161

8 Samenvatting 167

Appendices 177

A Notation and conventions 179

A.1 Four-vectors Lorentz transformations and Tensors 179

A.2 The free Dirac equation 182

B The Relativistic Mean Field 187

B.1 The Dirac equation 187

B.2 Relativistic mean field Lagrangian in the Hartree approximation 189

B.3 Bound states 190

B.4 Scattering states 191

C Multipole decomposition of the electroweak SPP amplitude 193

C.0.1 Charge-changing vector current 197

D Publications 199

Bibliography 203

Chapter 1

Introduction

1.1 Neutrino oscillations and accelerator based experiments

The research on neutrino oscillations is a rapidly moving field, with a large potential for fundamental discoveries in the near future. Refining measurements of the neutrino mixing angles, unraveling the neutrino mass hierarchy, possible confirmation of the existence of sterile neutrinos, and the determination of the CP-violating phase are only some of the current goals of the international neutrino community. In the following we give a short overview of the phenomenology of neutrino oscillations.

1.1.1 Neutrino oscillations

Neutrinos oscillate because the neutrino mass eigenstates are not the neutrino flavor eigenstates. We give a short overview of the general picture of neutrino oscillations without delving into proposed mechanisms for neutrino mass generation. The flavor eigenstate ν_α with $\alpha = e, \mu, \tau$ are orthogonal $\langle \nu_\alpha | \nu_\beta \rangle = \delta_{\alpha\beta}$ and can generally be described by a linear combination of any number of mass eigenstates ν_k

$$|\nu_\alpha\rangle = U_{\alpha k} |\nu_k\rangle \,. \tag{1.1}$$

$U_{\alpha k}$ is a general complex matrix describing the mixing of mass states into flavor eigenstates and summation over repeated indices is implied. For the following we assume that there are three mass eigenstates, the mixing matrix is a unitary 3-by-3 matrix such that

$$|\nu_k\rangle = \left(U^{-1}\right)_{k\alpha} |\nu_\alpha\rangle = U^*_{\alpha k} |\nu_\alpha\rangle . \tag{1.2}$$

To illustrate neutrino oscillations we assume a neutrino with flavor α and momentum p created in some weak interaction. If the neutrino travels over some distance L in vacuum the probability of observing a neutrino with weak flavor β is given by

$$\begin{aligned} &P(\alpha \to \beta)(L) = \\ &\delta_{\alpha\beta} - 2\mathcal{R}\left\{ \sum_{k>j} U_{\alpha j} U^*_{\alpha k} U^*_{\beta j} U_{\beta k} \left[1 - \exp\left(-i \frac{\Delta m^2_{jk}}{2E} L \right) \right] \right\} . \end{aligned} \tag{1.3}$$

Here $\Delta m^2_{jk} = m^2_j - m^2_k$ is the difference between the squared masses of the states $|\nu_j\rangle$ and $|\nu_k\rangle$. One thus sees that neutrino flavor states oscillate between mass states j and k over a length L with wave number determined by the fraction $\Delta m^2_{jk}/E$.

To derive this result, we consider a pure flavor state $|\nu_\alpha\rangle$ at time $t = 0$ with momentum $\boldsymbol{p}$. We can represent this state as a linear combination of mass eigenstates by using Eq. (1.1). It are the mass eigenstates, labeled by k, that will evolve as plane waves with energy $E_k = \sqrt{\boldsymbol{p}^2 + m^2_k}$. The evolution of the initially pure α state is thus given in terms of the mass states by

$$|\nu_\alpha(\boldsymbol{x}, t)\rangle = U_{\alpha k} e^{-i(E_k t - \boldsymbol{p} \cdot \boldsymbol{x})} |\nu_k\rangle . \tag{1.4}$$

Substituting in the flavor eigenstates we get the evolution of an α state to a superposition of β states at time t

$$|\nu_\alpha(\boldsymbol{x}, t)\rangle = U_{\alpha k} e^{-i(E_k t - \mathbf{p} \cdot \mathbf{x})} U^*_{\beta k} |\nu_\beta\rangle . \tag{1.5}$$

Squaring the amplitude $\langle\nu_\beta|\nu_\alpha(\boldsymbol{x}, t)\rangle$ results in

$$P(\alpha \to \beta)(t) = |\langle\nu_\beta|\nu_\alpha(\boldsymbol{x}, t)\rangle|^2 = U_{\alpha k} U^*_{\beta k} U^*_{\alpha i} U_{\beta i} e^{-i(E_k - E_i)t}, \tag{1.6}$$

Eq. (1.3) follows from this expression by assuming that the neutrino masses are small compared to their energy such that $E_k \approx E + m^2_k/2E$ with $E = |\boldsymbol{p}|$, and that $t \approx L$.

A common parametrization for the 3-by-3 unitary mixing matrix is the Pontecorvo-Maki-Nakagawa-Sakata (PMNS) matrix. The PMNS matrix is parametrized by 3 angles $(\theta_{12}, \theta_{23}, \theta_{13})$ and 1 complex phase $e^{i\delta_{CP}}$ as

$$U_{PMNS} = \begin{pmatrix} 1 & 0 & 0 \\ 0 & c_{23} & s_{23} \\ 0 & -s_{23} & c_{23} \end{pmatrix} \begin{pmatrix} c_{13} & 0 & s_{13}e^{-i\delta_{CP}} \\ 0 & 0 & 0 \\ -s_{13}e^{i\delta_{CP}} & 0 & s_{13} \end{pmatrix} \begin{pmatrix} c_{12} & s_{12} & 0 \\ -s_{12} & c_{12} & 0 \\ 0 & 0 & 0 \end{pmatrix}. \tag{1.7}$$

Here c_{ij} and s_{ij} are shorthand for $\cos(\theta_{ij})$ and $\sin(\theta_{ij})$ respectively.

The angle δ_{CP} is a source for CP violation. For antineutrinos, assuming CPT symmetry the oscillation probability is related to the neutrino oscillation probability by $P(\nu_\alpha \to \nu_\beta) = P(\overline{\nu}_\beta \to \overline{\nu}_\alpha)$. The oscillation probability for anti-neutrinos $P(\overline{\nu}_\alpha \to \overline{\nu}_\beta)$ can be obtained from $P(\nu_\alpha \to \nu_\beta)$ by considering the complex conjugate of U, i.e. by substituting U for U^* in Eq. (1.3). Clearly, if U is a real matrix, $P(\overline{\nu}_\alpha \to \overline{\nu}_\beta) = P(\nu_\alpha \to \nu_\alpha)$. For a general complex matrix however this is not the case and CP violation is implied unless δ_{CP} is either 0 or π or any of the mixing angles are trivial.

To see this explicitly we write Eq. (1.3) as

$$\begin{aligned} P(\nu_\alpha \to \nu_\beta) = \delta_{\alpha\beta} - 4\sum_{i>j} \mathcal{R}\left(U_{\alpha i}U^*_{\beta i}U^*_{\alpha j}U_{\beta j}\right) \sin^2\left(\frac{\Delta m^2_{ij}L}{4E}\right) \\ + 2\sum_{i>j} \mathcal{I}\left(U_{\alpha i}U^*_{\beta i}U^*_{\alpha j}U_{\beta j}\right) \sin\left(\frac{\Delta m^2_{ij}L}{2E}\right). \end{aligned} \tag{1.8}$$

Only the last term in this expression is affected when U is substituted for its complex conjugate such that the CP-violating asymmetry A^{CP} is given by

$$\begin{aligned} A^{CP}_{\alpha\beta} &= P(\nu_\alpha \to \nu_\beta) - P(\overline{\nu}_\alpha \to \overline{\nu}_\beta) \\ &= 4\sum_{i>j} \mathcal{I}\left(U_{\alpha i}U^*_{\beta i}U^*_{\alpha j}U_{\beta j}\right) \sin\left(\frac{\Delta m^2_{ij}L}{2E}\right). \end{aligned} \tag{1.9}$$

The four-tensor $J_{\alpha\beta,ij} \equiv \mathcal{I}\left(U_{\alpha i}U^*_{\beta i}U^*_{\alpha j}U_{\beta j}\right)$ which appears in these expressions is antisymmetric with respect to exchange of the two flavor indices and with respect to exchange of the mass indices. From the unitarity of U

$$U_{\alpha i}U^*_{\beta i} = \delta_{\alpha\beta}, \quad U_{\alpha i}U^*_{\alpha j} = \delta_{ij}, \tag{1.10}$$

it follows that the magnitude of all non-vanishing components of $J_{\alpha\beta,ij}$ is the same, they differ only by an overall sign. The magnitude of the non-zero components is called the Jarlskog invariant and denoted J. The CP-violating asymmetry is proportional to this one parameter, and is commonly written as

$$A_{\alpha\beta}^{CP} = 16J_{\alpha\beta}\sin\left(\frac{\Delta m_{21}^2 L}{4E}\right)\sin\left(\frac{\Delta m_{32}^2 L}{4E}\right)\sin\left(\frac{\Delta m_{31}^2 L}{4E}\right), \tag{1.11}$$

where $J_{\alpha\beta} = J_{\alpha\beta,12}$. The Jarlskog invariant can be expressed in terms of the elements of the PMNS matrix as

$$J_{\alpha\beta} = c_{12}s_{12}c_{23}s_{23}c_{13}^2 s_{13}\sin\left(\delta_{CP}\right)\sum_{\gamma}\epsilon_{\alpha\beta\gamma}, \tag{1.12}$$

with the antisymmetric accounting for the sign. From this expression one indeed sees that to allow CP-violation in neutrino oscillations J should be non zero, and hence all 3 mixing angles and δ_{CP} should be non-trivial.

As a last remark we discuss the parametrization of the PMNS matrix. An arbitrary unitary $N \times N$ matrix can be parametrized by

$$N^2 = 2N^2 - N(N-1) - N$$

real parameters. Here the first term simply counts the number of real numbers in a complex $N \times N$ matrix, the second term comes from the constraint that all columns should be mutually orthogonal, and the third term is obtained from the constraint that every column should have unit norm. In the case of a 3×3 unitary matrix one would therefore expect 9 parameters to be required instead of the 4 in the PMNS matrix. From Eq. (1.6) one sees that the elements of the mixing matrix for the mass states and the flavor states enter the oscillation probability in complex-conjugated pairs. The oscillation probability is thus invariant under redefinition of any of the mass or flavor states with an overall phase. This allows to remove $2N-1$ phases from the parameters that describe the mixing matrix, by fixing the relative phases between the different states, without affecting the phenomenology of neutrino oscillations.

With this absorption of phases, the PMNS matrix describes mixing for 3 lepton generations where 3 right handed neutrinos are introduced that are considered to be Dirac fermions. This global symmetry is lost in the case where one considers Majorana fermions, which are particular solutions of the Dirac equation for which the Majorana condition

$$\Psi = \pm C\overline{\Psi}^{\mathrm{T}} \equiv \Psi^c \tag{1.13}$$

holds. Here C is the charge-conjugation matrix ($C = i\gamma^2\gamma^0$ in the Dirac representation) and the right-hand side defines the charge-conjugate of

Ψ. Charge-conjugation transforms particle spinors into anti-particle spinors and vice versa, and for solutions that satisfy the Majorana condition particles and anti-particles are hence indistinguishable. For the charged leptons such solutions are ruled out because anti-particles have opposite charge with respect to particles. For the neutral neutrino however the Majorana condition can in principle be met. In this case the condition of Eq. (1.13) does not allow for the absorption of 5 phases and the mixing matrix U that can be considered as a more general version of the PMNS matrix, is parametrized as

$$U = U_{PMNS} \begin{pmatrix} e^{i\eta_1} & 0 & 0 \\ 0 & e^{i\eta_2} & 0 \\ 0 & 0 & 0 \end{pmatrix}, \tag{1.14}$$

including the Majorana phases η_1 and η_2. Given the discussion above, the Majorana phases do not affect neutrino oscillations in vacuum (or in matter [1]), as Eq. (1.6) is invariant with rephasing of rows or columns of the mixing matrix. A Majorana solution, which couples the particle to antiparticle solutions, would however allow for processes that violate total lepton number conservation. As such, the main prospect in determining the nature of neutrinos, be it Majorana or Dirac, is in the observation of neutrinoless double beta decay [2].

On the other hand, in this discussion we have considered mixing of 3 generations of neutrinos, corresponding to the 3 flavor states which enter in electroweak interactions. Some models consider the case of sterile neutrinos, in which mass mixing occurs between $3 + n$ neutrino states, of which the n sterile states do not interact. In this case the PMNS matrix can be considered as a sub-matrix of a larger matrix. As such the unitarity conditions of Eq. (1.10) do not apply when the sums are restricted only to the 3 interacting states. A possible consequence is that the CP-violating asymmetry of Eq. (1.11) differs in magnitude for different neutrino flavors. For more extensive discussions on neutrino mass terms, mass generating mechanisms, and their implications on neutrino oscillations we refer to Refs. [1, 3, 4].

1.1.2 Accelerator-based neutrino experiments

Neutrinos are produced in weak interactions, and there are several sources of neutrinos which can be detected on laboratories on earth. Extraterrestrial neutrinos are among others created in the nuclear reactions in the center of the sun, in the collisions of highly energetic cosmic rays with the atmosphere, and in supernovae. Terrestrial sources include neutrinos from nuclear reactors, from β-decay of nuclei, and neutrinos created with particle accelerators.

The intense neutrino beams created in accelerators provide great opportunities for experimental measurements of neutrino oscillation parameters. If the energy profile of the neutrino beam is known, detectors can be placed at optimized positions in the beamline in order to look for oscillation at specific values of L/E.

There are two main factors which complicate the setup of such a neutrino experiment. The first is that neutrinos only interact weakly, this means that their direct observation is impossible with traditional particle detectors. Instead, one measures the particles which are produced in interactions of the neutrino with the detector material. Due to the small cross sections of the weak interaction at the couple of GeV scale, neutrino detectors consist of a massive amount of target material to interact with. For this reason, in current and future experiments the active material in detectors consists mainly of atomic nuclei, and hence the neutrino-nucleus cross section has to be known.

The second complication stems from the fact that the neutrino beams from accelerators are not mono-energetic but span over an energy range of several GeV. To see how this leads to severe complications, one may consider as an example the inclusive interaction

$$\nu_l + {}^{12}\mathrm{C} \rightarrow l^- + X, \tag{1.15}$$

where only the outgoing charged lepton is measured. The measured amount of events in a bin with width Δ centered around a lepton scattering angle of the lepton θ_l' in a neutrino detector is then given by

$$N(\theta_l') = \int_{\theta_l'-\Delta/2}^{\theta_l'+\Delta/2} d\theta_l \int dE_l \epsilon(E_l, \theta_l) \int dE_\nu \Phi(E_\nu) \frac{d\sigma(E_\nu)}{d\theta_l\, dE_l}, \tag{1.16}$$

with $\Phi(E_\nu)$ the neutrino flux and $d\sigma(E_\nu)/\, d\theta_l\, dE_l$ the differential cross section for fixed E_ν, lepton angle and energy E_l. For completeness we added the factor ϵ to represent the detector efficiency which is a function of the lepton kinematics. Because the residual system X is not characterized, *all* possible interaction mechanisms which may occur at certain energy should in principle be taken into account to describe the event rate that is measured.

In the idealized case, where experimental uncertainty plays no role and Δ is negligible, the event rate of Eq. (1.16) is an integral transform

$$\frac{dN}{d\theta_l} = \int dE_\nu \Phi(E_\nu) K(\theta_l, E_\nu) \tag{1.17}$$

with kernel

$$K(\theta_l, E_\nu) = \int dE_l \epsilon(E_l, \theta_l) \frac{d\sigma(E_\nu)}{d\theta_l \, dE_l}. \tag{1.18}$$

Characterizing the (oscillated) neutrino flux $\Phi(E_\nu)$ from measured final state kinematics means solving the inverse transform. This problem is intractable even in the ideal case, and is further complicated by the fact that the description of the cross section requires challenging nuclear and hadron physics, such that the kernel is not exactly known. To characterize the flux in the analysis of neutrino experiments, simulations of the measured experimental signal are performed which are compared to the experimental data. Through these comparisons, parametrizations of the flux that are consistent with the experimental data are determined. Apart from (oscillation) parameters that determine the flux, simulations need to take into account the neutrino flux before oscillation, the response of the detector, the interaction cross section, and ideally the uncertainty on these quantities.

1.2 Neutrino interactions

Given the discussion in the previous sections it is clear that it is important to have good knowledge of the interaction cross sections for the processes which contribute to a neutrino experiment. On top of that, neutrino scattering experiments also provide a unique view of the axial response of hadrons and nuclei, which is not directly accessible in experiments with electromagnetic probes. Both these facts have spurred interest in, and have led to significant developments in the theoretical description of electroweak interactions with hadrons and nuclei [5, 6]. The first accelerator-based experiments, examples are MiniBooNE [7] and T2K [8], were mostly limited to measurements of the outgoing lepton in charged-current interactions. Therefore a lot of theoretical approaches have been applied to the calculation of inclusive neutrino-nucleus scattering. With the enhanced capabilities and better understanding of current and future detectors the need to describe semi-inclusive interactions in which some of the final-state hadrons are detected is growing [5, 9]. In this respect it it important to stress that the signal in current and future neutrino experiments is always necessarily semi-inclusive, rather than exclusive. In an exclusive signal, the kinematics of the final-state hadrons are fully determined, which is for example the case in studies of electron induced one proton knockout from nuclei. In these experiments one measures the final state proton (denoted p) and scattered electron (denoted e') in the interaction

$$e + A \rightarrow e' + p + B, \tag{1.19}$$

where the energy and momenta of the initial-state electron and nucleus, e and A respectively, are fully known. By energy-momentum conservation one can then fully characterize the kinematics of the unmeasured hadron system B. One can then restrict the experimental sample to those events for which the system B has a specific invariant mass, corresponding e.g. to a specific excited state of nucleus. In a typical neutrino experiment on the other hand, the incoming neutrino energy is not a fixed variable. This means that the kinematics of the final-state cannot be fully characterized on an event-to-event basis. This situation, in which part of the hadron final-state is measured, is referred to as semi-inclusive.

Pion production is an important reaction mechanism, both for the inclusive as the semi-inclusive case. The pion, being the lightest meson, is the most common reaction product in inelastic interactions with the nucleon for hadronic invariant masses of $W \approx 1.1 - 1.4$ GeV, and will contribute to the inclusive cross sections measured in experiments [10, 11]. On the other hand, in experiments that are sensitive to the content of the hadronic final state, single (and at higher energies multi-pion) pion production is a significant contribution to the measured signal.

1.2.1 Neutrino-induced single pion production

There are a number of models that aim to describe pion production in the kinematic phase space relevant to neutrino experiments [10, 12–25]. Many of these models focus on the kinematic region around the $\Delta(1232)$ resonance, although progress has been made in the description of the process at higher invariant masses [15, 24, 26–28]. We highlight in particular the approach of Hernandez et al. [14], which combines the direct resonance excitation of the $\Delta(1232)$ with the lowest order background diagrams required by ChPT. The model has been extended over the years with among others the addition of higher mass resonances, and partial unitarization in the delta region [29–33]. The main drawback comes from the fact that the tree-level background grows too quickly beyond the delta region, which yields unnaturally large cross sections. This unphysical behavior of the background is mitigated in the approach of Ref. [25], by introducing a phenomenological regularization factor for high-W. In the approach of Ref. [28], resonance contributions are instead added incoherently to a phenomenological background which grows only slowly with W.

The current state-of-the art model for electroweak pion production is the Dynamic Coupled Channels (DCC) model presented in Refs. [24, 34]. The dynamical model takes into account coupled-channels unitarity and is constrained by data of meson-baryon scattering and electromagnetic production of pions and other meson-baryon channels. The model is applicable from the pion-production threshold up to $W = 2$ GeV.

In general, the major uncertainty and issue in any of these approaches to electroweak SPP is the knowledge of the axial form factors of the resonances. While a reasonable guess of some of the couplings can be made by assuming PCAC and pion-pole dominance, this does not fix all possible axial couplings and does not predict the Q^2 dependence of the form factors [26].

Much of the work on electroweak SPP is applicable to the reaction on a free nucleon. In accelerator-based experiments, the target consists mainly of nuclei, and nuclear effects need to be taken into account. Some approaches for SPP off the nucleus have been presented with the explicit goal of describing neutrino scattering data [12, 18, 23, 35–39]. With the current and upcoming measurements of the hadronic final-state, it becomes important to describe the semi-inclusive process in which an outgoing pion is detected. In this respect the recent implementation of the DCC model amplitudes [24] in the effective spectral function model presented in Ref. [35, 40] is notable. This model should be able to describe the relevant kinematic degrees of freedom for the semi-inclusive process, although it has currently not yet been applied to flux-averaged neutrino pion production data.

Additional complications in neutrino-induced SPP off nuclei come in the form of final-state interactions (FSI). Because the incoming energy is unknown on an event-to-event basis it becomes impossible to make kinematic cuts on e.g. the missing energy. This means that it is impossible to restrict the experimental data to direct single pion production, and pions which rescatter in the nuclear medium are part of the signal. Because treating all the relevant FSI channels explicitly in a microscopic manner is an intractable problem, experimental analyses resort to classical intra-nuclear cascade models. The cascade models applied to neutrino-scattering data are mostly based on the model of Salcedo et al. [41], although the most recent models are developed in the context of neutrino event generators [42–46].

1.2.2 Neutrino event generators

Because of the large-scale problem posed by the need to describe all relevant neutrino-induced processes in addition to the FSI of hadrons the weapon of choice in analysis of experiments is the neutrino event generator. Commonly used generators include GENIE, NuWro, and NEUT [42–44]. In such programs a Monte Carlo simulation of neutrino-nucleus scattering events is performed, based on input of the interaction cross sections for different channels. Because there presently is no definite unified description of all interaction channels available, the interaction cross sections for different processes are obtained by stitching together different theoretical approaches, which might pose some risk of double counting. Moreover, for some interaction channels only limited kinematic degrees of freedom are available in the generator, e.g. the inclusive cross section. In such cases, the kinematics of the outgoing hadrons are often computed based on a different model, which may be inconsistent with the approach used to supply the inclusive cross section in the first place.

The treatment of FSI in these generators is done with cascade models, in which the initial neutrino interaction with the bound nucleon is detached from the final-state interactions (FSI) for the outgoing hadrons. Put differently, the cascade model affects only the kinematics of the particles in the final state, while it does not affect the magnitude of the cross section used as an input. An important exception to this rule is the GiBUU (Giessen Boltzmann-Uehling-Uhlenbeck) project [46, 47], which instead of a cascade model uses a transport approach to model the flow of particles through a nuclear mean-field potential.

In any case, the predictions of event generator rely on theoretical input for the cross sections. Neutrino event generators will generally use approximate treatments of nuclear effects and of processes with a large number of kinematic degrees of freedom. On the one hand this is because Monte Carlo simulations of all interactions are computationally intensive, and can rapidly become inefficient in a large multi-dimensional phase space. On the other hand the implementation of state-of-the-art models is labor intensive.

The results of event generators that are used in the analysis of neutrino experiments should ideally be informed by, or benchmarked against, the results of more complete treatments of the interaction in order to asses the relevant uncertainties.

1.3 Outline

In the present work we will address the description of the semi-inclusive cross section for neutrino SPP within a relativistic approach which incorporates fully the kinematic and modeling degrees of freedom of the process.

In Chapter 2, we present the general formulae for lepton scattering of nucleons and nuclei. In Chapter 3, the model for SPP off nucleons used in this work is discussed at length. This is the most recent version of the model presented in Ref. [31]. We perform an extensive benchmarking by comparison to established models for pion electroproduction, and pion-nucleon scattering data. Then, in Chapter 4 we describe the modeling of the nucleus in this work, and discuss the influence of the description of the nucleon wavefunction as a relativistic distorted wave. We present a comparison of results with the NuWro event generator and experimental data, originally published in Ref. [37], in Chapter 5.

The results obtained with the relativistic distorted wave treatment are compared to plane wave results and experimental data in Chapter 6, and finally conclusions are given in Chapter 7.

Chapter 2

Lepton scattering off nucleons and nuclei

In this chapter we present the kinematics and general formalism for the calculation of the lepton-nucleus scattering cross section. The presented formulae are general such that the formalism presented here is directly applicable for both electron and neutrino interactions. First we show the kinematics of the process and how the cross section for scattering off nucleons and nuclei is computed. Next, we take a closer look at the invariant matrix element that determines the probability of the interaction. By treating the lepton current in the plane wave Born approximation we can write the matrix element as a contraction of the lepton and hadron tensors. We give the explicit expressions for the lepton tensor, and show how by making use of rotational invariance the dependence on the angle between lepton and hadron planes can be written in terms of sines and cosines. The hadron current, which depends on the type of interaction and nuclear model, will be described in following chapters.

2.1 Kinematics and cross section

The kinematics for a lepton scattering off a nucleus are depicted in Fig. 2.1. The incoming lepton has four momentum $K^\mu = (E, \mathbf{k})$, and the outgoing lepton $K'^\mu = (E', \mathbf{k}')$. The four momentum transferred to the hadronic system is $Q^\mu = (\omega = E - E', \mathbf{q} = \mathbf{k} - \mathbf{k}')$. The vectors $\mathbf{k}$ and $\mathbf{k}'$ define the lepton scattering plane. We follow the conventions of Bjorken and Drell [48], as laid out in appendix A. will derive the

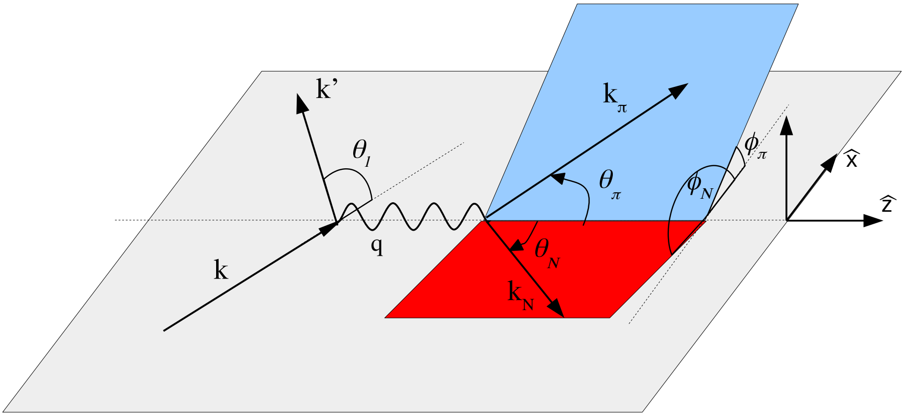

Figure 2.1: Kinematics for the pion-nucleon production off the nucleus.

expression for the cross section explicitly for the pion-production case, for other interaction mechanisms the expressions will be provided as they are derived with the same considerations.

The differential cross section is proportional to the density of final states per unit flux. For every on-shell fermion with mass m and momentum $\mathbf{p}$ in the final state the Lorentz-invariant phase space factor is given by

$$\frac{m\mathrm{d}\mathbf{p}}{E(2\pi)^3}, \tag{2.1}$$

while for a boson one has,

$$\frac{\mathrm{d}\mathbf{p}}{2E(2\pi)^3}, \tag{2.2}$$

with the energy given by the well-known dispersion relation $E = \sqrt{\mathbf{p}^2 + m^2}$. The normalization factors proportional to $1/E$ make these phase space volumes Lorentz-invariant. The factor m/E for fermions follows from the normalization of the spinors given in Eqs. (A.38-A.39), which yields a number density E/m . For bosons, the Klein-Gordon equation, Eq. A.18, when considered for either strictly positive or strictly negative energy solutions yields a number density of $2E$ [48], hence the normalization of Eq. (2.2). For the incoming lepton and hadronic target the kinematics are assumed to be fixed, such that the factor $\frac{\mathrm{d}\mathbf{p}}{(2\pi)^3}$ is not needed, i.e. the cross section is expressed per incoming lepton and per target. The flux is the relative colinear velocity of the incoming lepton and the hadron target, which is

$$|v_i - v_A| = |\frac{p_i}{E_i} - \frac{p_A}{E_A}| = |\frac{p_i}{E_i}| = 1, \tag{2.3}$$

in the laboratory system where the target is at rest and if the incoming lepton can be considered massless.

For single-pion production off nuclei, the final state consists of 4 particles, the lepton K'^μ, the pion $P_\pi^\mu = (E_\pi, \mathbf{p}_\pi)$, and the outgoing nucleon $P_N^\mu = (E_N, \mathbf{p_N})$ illustrated in Fig 2.1, and additionally the residual nucleus $P_B^\mu = (E_B, \mathbf{p_B})$. Their masses are denoted m', m_π, M_N, and M_B respectively, while the masses of the initial state lepton and nucleus are m and M_A. All final-state particles satisfy the free dispersion relation $E^2 = \mathbf{k}^2 + m^2$ after the scattering, the number of kinematic degrees of freedom for every particle is thus 3, these are included in the phase space factors of Eqs. (2.1-2.2). With the conventions explained above, this leads to the general expression of the cross section as

$$\begin{aligned} \mathrm{d}\sigma(E) = {} & \frac{m}{E}\,\frac{m'}{E'}\frac{\mathrm{d}\mathbf{k}'}{(2\pi)^3}\frac{m_N}{E_N}\frac{\mathrm{d}\mathbf{p_N}}{(2\pi)^3}\;\frac{1}{2E_\pi}\frac{\mathrm{d}\mathbf{p}_\pi}{(2\pi)^3}\frac{M_B}{E_B}\frac{\mathrm{d}\mathbf{p_B}}{(2\pi)^3} \\ & \times (2\pi)^4\delta^4(K^\mu + P_A^\mu - K'^\mu - P_N^\mu - P_\pi^\mu - P_B^\mu)|\mathcal{M}|^2, \end{aligned} \tag{2.4}$$

where the delta function accounts for four-momentum conservation. The squared invariant matrix element $|\mathcal{M}|^2$ contains the dynamics of the scattering process, including the spin degrees of freedom, and is discussed in the next section.

We can trivially integrate over the three-momentum of one of the particles by using the delta function. As we don't generally detect the outgoing nuclear system, we will integrate out its momentum, which then leads to

$$\mathrm{d}\sigma(E) = \frac{mm'M_NM_B}{2(2\pi)^8EE'E_NE_\pi E_B}\mathrm{d}\mathbf{k}'\mathrm{d}\mathbf{p_N}\mathrm{d}\mathbf{p}_\pi \tag{2.5}$$

$$\delta(E + M_A - E' - E_N - E_\pi - E_B)|\mathcal{M}|^2. \tag{2.6}$$

At this point the energy-conserving delta function can be used to eliminate one additional degree of freedom. We perform the integral over the magnitude of the outgoing nucleon's momentum $|\mathbf{p}_N|$ by using following property of the delta function

$$\int \mathrm{d}x\delta(a - f(x))g(x) = \left[\frac{g(x)}{|\frac{\partial f}{\partial x}|}\right]_{f(x)=a}. \tag{2.7}$$

In this case, we can rewrite the argument of the delta function as

$$E + M_A - E' - E_\pi - \sqrt{\mathbf{p}_N^2 + m_N^2} - \sqrt{(\mathbf{q} - \mathbf{p_N} - \mathbf{p}_\pi)^2 + (M_B^0 + E_B^*)^2}, \tag{2.8}$$

where the last term is the total energy E_B of the residual hadronic system with an invariant mass $M_B = M_B^0 + E_B^*$ that recoils with a momentum $\mathbf{q} - \mathbf{p_N} - \mathbf{p}_\pi$. We can thus identify $f(p_N)$ as

$$f(p_N) = \sqrt{p_N^2 + m_N^2} + \sqrt{(\mathbf{q} - \mathbf{p_N} - \mathbf{p}_\pi)^2 + (M_B^0 + E_B^*)^2}. \tag{2.9}$$

The derivative with respect to p_N is now easily computed and yields

$$|\frac{\partial f(p_N)}{\partial p_N}| = |\frac{p_N}{E_N} + \frac{p_N}{E_B}\left(1 + \frac{\mathbf{p}_N \cdot (\mathbf{p}_\pi - \mathbf{q})}{p_N^2}\right)|. \tag{2.10}$$

Further using the fact that $\mathrm{d}^3\mathbf{k} = \mathbf{k}^2\mathrm{d}k\mathrm{d}\Omega_k = E|\mathbf{k}|\mathrm{d}E\mathrm{d}\Omega_k$, the final result for the exclusive cross section as a function of energies and solid angles in the lab frame reads

$$\frac{\mathrm{d}^8\sigma(E)}{\mathrm{d}E'\mathrm{d}\Omega\mathrm{d}E_\pi\mathrm{d}\Omega_\pi\mathrm{d}\Omega_N} = \frac{m_i}{E}\frac{m'k'M_Nk_\pi k_N M_B}{2\,(2\pi)^8\,E_B f_{rec}}|\mathcal{M}|^2 \tag{2.11}$$

with

$$f_{rec} = \frac{E_N}{p_N}|\frac{\partial f(p_N)}{\partial p_N}| = |1 + \frac{E_N}{E_B}\left(1 + \frac{\mathbf{p}_N \cdot (\mathbf{p}_\pi - \mathbf{q})}{p_N^2}\right)| \tag{2.12}$$

the recoil factor that takes into account the phase space correction due to kinetic energy carried away by the residual nucleus. We here point out a commonly used approximation of neglecting the nuclear recoil energy. In this case we neglect the kinetic energy of the residual system, and its energy is simply $E_B = M_B^0 + E_B^*$, such that $f(p_N) = \sqrt{p_N^2 + M_N^2}$ and the recoil factor becomes 1. If part of the final state particles are not fully observed, this is a rather good approximation. This can be understood from the expression of the recoil factor in Eq. (2.12), which tends to 1 when $E_N << E_B$. Indeed, if the mass of the final nucleus is large it can carry a lot of momentum without gaining much kinetic energy, hence it does not change the energy balance by a significant amount.

Using exactly the same line of reasoning, just excluding the terms that account for the pion phase space, one obtains for the semi-inclusive one-nucleon knockout cross section

$$\frac{\mathrm{d}^5\sigma(E)}{\mathrm{d}E'\mathrm{d}\Omega'\mathrm{d}\Omega_N} = \frac{m_i}{E}\frac{m'k'M_Nk_N M_B}{(2\pi)^5\,f_{rec}E_B}|\mathcal{M}|^2, \tag{2.13}$$

where f_{rec} is obtained from Eq. (2.12) by setting the pion momentum to 0.

It is interesting to explicitly consider the kinematic degrees of freedom in scattering off nuclei, to illustrate the assumptions made to derive the expressions for the exclusive cross sections of Eqs. (2.11) and (2.13). All particles are on-shell before or after the scattering, as such their four-vectors are completely described by three parameters, the magnitude and direction of momentum,

$$K^\mu = \left(\sqrt{\mathbf{p}^2 + m^2}, \mathbf{p}\right), \tag{2.14}$$

if the invariant mass m is assumed to be known. In lepton-nucleus scattering in which $n \geq 1$ hadrons are created we will have $(2 + 1 + n + 1) \times 3$ kinematic degrees of freedom, where the first term counts the initial lepton and nucleus, the next term the scattered lepton, n the number of created hadrons, and the last term is the residual nucleus. The three momenta of the initial state particles are assumed to be known, which allows to eliminate 6 variables. We can always choose an arbitrary inertial frame for the calculation, e.g. the LAB frame in which $\mathbf{p}_A = 0$, to remove 3 of them. In this inertial frame we are free to choose the direction of the spatial axes, e.g. as in Fig. 2.1 the $x - z$ plane is defined as the leptonic plane, with $\mathbf{q}$ along the z-axis, obviously this choice is arbitrary. This leaves $(n + 2) \times 3$ independent variables, of which 4 can be eliminated by energy-momentum conservation, leaving $3n + 2$. A set of non-trivial variables in the system shown in Fig. 2.1 is the following: 3 variables to define the leptonic side of the interaction e.g. $(|\mathbf{k}|, |\mathbf{k}'|, \theta_l)$ or equivalently $(\omega, |\mathbf{q}|, E)$. Then $n - 1$ hadrons are described by 3 variables each, e.g. their three-momentum $(|\mathbf{p}|, \cos\theta, \phi)$. For the final hadron only the solid angle is needed, as the magnitude of the momentum of the n-th remaining hadron can be determined from energy conservation

$$\begin{aligned} &\omega + M_A = \\ &\sum_{i=1}^{n-1} \left(\sqrt{\mathbf{p}_i^2 + m_i^2}\right) + \sqrt{M_B^2 + \left(\mathbf{q} - \sum_{i=1}^{n-1}(\mathbf{p}_i) - \mathbf{p}_n\right)^2} + \sqrt{\mathbf{p}_n^2 + m_n^2}. \end{aligned} \tag{2.15}$$

One sees that the invariant mass of the residual system M_B is assumed to be known, and a fixed variable, this corresponds to an exclusive situation. In many situations, neutrino-nucleus scattering in particular, one deals with a semi-inclusive situation, in which the kinematics of all particles are not fully determined. In this case the invariant mass

M_B may take multiple values which are model dependent. We discuss the kinematics and modeling of the semi-inclusive lepton-nucleus cross section in Chapter 4.

Lastly, we give the expression for single pion production of a free nucleon in the lab frame. As there is no residual nucleus in this case, the integral over the recoiling nucleon's momentum can be performed directly in the same way as above. Energy conservation can be used to eliminate the magnitude of the pion momentum, the energy conserving delta function reads

$$\delta(E + M_N - E' - \sqrt{k_\pi^2 + M_\pi^2} - \sqrt{(\mathbf{q} - \mathbf{k}_\pi)^2 + M_N^2}) \tag{2.16}$$

which yields a recoil factor

$$f_{rec} = |1 + \frac{E_\pi}{E_N k_\pi^2} \mathbf{k}_\pi \cdot (\mathbf{k}_\pi - \mathbf{q})| \tag{2.17}$$

with the cross section

$$\frac{\mathrm{d}^5\sigma(E)}{\mathrm{d}E'\mathrm{d}\Omega'\mathrm{d}\Omega_\pi} = \frac{m_i}{E} \frac{m' k' m_N k_\pi}{(2\pi)^5 E_N f_{rec}} |\mathcal{M}|^2. \tag{2.18}$$

2.2 The invariant matrix element

In the previous section we simplified the kinematic prefactors in the cross section by energy and momentum conservation. The cross section is proportional to the squared invariant matrix element which may be a function of the remaining kinematic variables

$$|\mathcal{M}(P_1, P_2, \cdots, P_N)|^2 = \overline{\sum}_{i,f} |\mathcal{M}_{if}(P_1, P_2, \cdots, P_N)|^2 \tag{2.19}$$

where $\overline{\sum}_{i,f}$ implies the appropriate sum and average over unobserved degrees of freedom of the initial and final state systems, such as spins, and the P_i denote a set of independent kinematic variables. In this section we show how the squared matrix element decomposes into a lepton and hadronic tensor, and we give the expressions for the lepton tensor treating the leptons as plane waves. To simplify the notation we do not explicitly write any dependence on spin or kinematics unless needed.

The invariant amplitude for a semi-leptonic interaction, where all energy states are asymptotically stable is written in coordinate space as

$$M_{if} = \int \mathrm{d}\mathbf{x} \int \mathrm{d}\mathbf{y} j_l^\mu(\mathbf{x}) S_{\mu\nu}(\mathbf{x}, \mathbf{y}) j_H^\nu(\mathbf{y}) \tag{2.20}$$

Where j_l and j_H are the lepton and hadron currents respectively which are four-vectors, while S is the propagator that connects both vertices. In this work we will work exclusively in the plane wave born approximation for the lepton current, the propagator for the exchange of a single massive boson then has the form

$$S^{\mu\nu}(\mathbf{x},\mathbf{y}) = \int \mathrm{d}\mathbf{q} e^{-i\mathbf{q}\cdot(\mathbf{x}-\mathbf{y})} \frac{\Gamma^{\mu\nu}}{M_B^2 - Q^2}, \tag{2.21}$$

with M_B the mass of the boson, and Q^2 the squared four-momentum transfer. The vertex factor for the exchange of a massive boson, summed over the polarization is

$$\Gamma^{\mu\nu} = -g^{\mu\nu} + \frac{Q^\mu Q^\nu}{M_B^2} \approx -g^{\mu\nu} \tag{2.22}$$

where the second term arises from the longitudinal polarization of the exchanged boson, and thus does not enter for massless photon exchange. For the weak interaction the boson is either the W and Z that both have masses of around 90 GeV, such that for the region of Q^2 considered in this work this term can be dropped, thus yielding a vertex factor $g^{\mu\nu}$ for all electroweak interactions.

The lepton current for plane wave Dirac particles, using the definitions laid out in appendix A, is

$$j_l^\mu(\mathbf{x}) = e^{i(\mathbf{k}-\mathbf{k}')\cdot\mathbf{x}} \overline{u}(\mathbf{k}',s')\Gamma_l^\mu u(\mathbf{k},s), \tag{2.23}$$

with a vertex factor Γ_l^μ which we leave unspecified at this point. With this we can compute the integrals over $\mathbf{q}$ and $\mathbf{x}$ immediately, the integral over the exponential leads to momentum conservation in the leptonic vertex and the propagator. The resulting expression for the transition amplitude is

$$\mathcal{M}_{if} = \overline{u}(\mathbf{k}',s')\Gamma_\mu u(\mathbf{k},s) \frac{-1}{M_B^2 - Q^2} \int \mathrm{d}\mathbf{y} e^{-i\mathbf{q}\cdot\mathbf{y}} j_H^\mu(\mathbf{y}). \tag{2.24}$$

We now denote

$$\mathcal{J}^\mu(q) = \int \mathrm{d}\mathbf{y} e^{-i\mathbf{q}\cdot\mathbf{y}} i j_H^\mu(\mathbf{y}), \tag{2.25}$$

and define the hadron tensor $\mathcal{H}^{\mu\nu} = \mathcal{J}^\mu(q)(\mathcal{J}^\nu(q))^\dagger$. With this shorthand the squared matrix element is

$$|\mathcal{M}_{if}|^2 = \frac{1}{(M_B - Q^2)^2} l_{\mu\nu}\mathcal{H}^{\mu\nu}, \tag{2.26}$$

where $\mathcal{L}_{\mu\nu}(s,s')$ is then defined as $[\overline{u}(\mathbf{k}',s')\Gamma_{l,\mu}u(\mathbf{k},s)][\overline{u}(\mathbf{k}',s')\Gamma_{l,\nu}u(\mathbf{k},s)]^\dagger$ where the spin degrees of freedom for the initial and final state leptons are $s,\ s'$ respectively. We thus find that with single boson exchange, and with plane wave leptons, the lepton and hadron vertices can be treated separately. While the hadron part of the interaction is challenging to describe for most interaction mechanisms, the lepton vertex can be readily evaluated with the conventional Feynman rules. Derivations and expressions for the lepton tensor are readily found in e.g. Refs [49, 50], here we will only give a short overview consistent with the conventions used in this work.

The relevant electroweak vertex factors for the lepton current are

$$\Gamma^\mu_W = \frac{g}{\sqrt{2}}\gamma^\mu \frac{1}{2}\left(1 \pm \gamma^5\right), \tag{2.27}$$

$$\Gamma^\mu_Z = \frac{g}{\cos\theta_W 2}\gamma^\mu \frac{1}{2}\left(1 - \gamma^5\right), \tag{2.28}$$

and

$$\Gamma^\mu_\gamma = e\gamma^\mu, \tag{2.29}$$

for the coupling to the W and Z bosons, and photon (γ) respectively. The factor $\frac{1}{2}\left(1 \pm \gamma^5\right)$ is the projection operator with the $+$ sign for the right-handed neutrino and $-$ for the left-handed antineutrino. We now proceed by showing the result for the charged-current couplings to the $W^\pm$, i.e. for the interactions $\nu_l \to l^-$ and $\overline{\nu}_l \to l^+$ from which the other processes can be readily determined. We consider the sum over initial and final helicities explicitly to make use of the closure relation of the Dirac spinors, but the projection operators present in the current will select only the allowed spin states. With our convention of spinor normalization we then get,

$$l^{\mu\nu} = \sum_{s,s'} \mathcal{L}(s,s') = \frac{g^2}{8} Tr\left[\frac{(\not{k}+m)}{2m}\gamma^\mu\left(1 \pm \gamma^5\right)\frac{(\not{k}'+m')}{2m'}\gamma^\nu\left(1 \pm \gamma^5\right)\right]. \tag{2.30}$$

We will further neglect the initial lepton mass m in the numerator, valid for neutrinos and electrons in this work. One then finds that all terms that involve m' in the numerator are also zero as they involve 3 gamma matrices, and can write

$$l^{\mu\nu} = \frac{g^2}{16m'm} Tr\left[\gamma^\beta\gamma^\nu\gamma^\alpha\gamma^\mu\left(1 \pm \gamma^5\right)\right] k_\alpha k'_\beta. \tag{2.31}$$

The trace is easily evaluated with well-know theorems and is given explicitly by

$$l^{\mu\nu} = \frac{g^2}{4m'm}\left[k^\mu k'^\nu + k^\nu k'^\mu - g^{\mu\nu}k_\alpha k'^\alpha \pm i\epsilon^{\mu\nu\alpha\beta}k_\alpha k'_\beta\right]. \tag{2.32}$$

Here $g_{\mu\nu}$ is the metric tensor, $\epsilon_{\alpha\beta\gamma\delta}$ the Levi-Cevita tensor. We find a symmetric real part and an anti-symmetric imaginary term which depends on the neutrino's helicity.

For electron scattering we can make use of the same result when the electron mass is neglected by substituting the coupling constant $g^2/2 \rightarrow e^2$. Indeed, in the massless limit the projection operator $\frac{1}{2}\left(1 \pm \gamma^5\right)$ that enters in the neutrino interactions projects out the positive/negative helicity of the electron, such that the same tensor enters in polarized electron scattering. When the electron is not polarized, one averages over the two initial helicity states and the antisymmetric term disappears. Hence to treat electromagnetic and electroweak interactions on the same footing it is convenient to factor out the coupling constant and lepton masses and define

$$L^{\mu\nu} = k^\mu k'^\nu + k^\nu k'^\mu - g^{\mu\nu}k_\alpha k'^\alpha - ih\epsilon^{\mu\nu\alpha\beta}k_\alpha k'_\beta \tag{2.33}$$

with h the initial leptons helicity.

For this reason it is customary to also factor out a constant coupling from the hadron tensor. The coupling constants that arise in the three point vertex of a W, Z, and photon with point-like fermions (quarks) are

$$G_W = g\cos\theta_c 2\sqrt{2}, \tag{2.34}$$

$$G_Z = \frac{g}{2\cos\theta_W}, \tag{2.35}$$

and

$$G_\gamma = e, \tag{2.36}$$

respectively. Now, combining Eq. (2.26) with the result for the lepton tensor and factoring out the constants from the hadron current we have

$$|\mathcal{M}_W|^2 = \frac{1}{(M_W^2 - Q^2)^2}\frac{g^2}{4m'm}\frac{g^2\cos^2\theta_c}{8}L^{\mu\nu}H_{\mu\nu} \tag{2.37}$$

We can neglect Q^2 in the propagator and use $\frac{G_F}{\sqrt{2}} = \frac{g^2}{8M_W}$ to get

$$|\mathcal{M}_W|^2 = \frac{G_F^2\cos^2\theta_c}{m'm}L^{\mu\nu}H_{\mu\nu}. \tag{2.38}$$

For the coupling to the Z we have $M_W = M_Z \cos\theta_W$ and we obtain the same expression, but without the Cabibbo mixing angle

$$|\mathcal{M}_Z|^2 = \frac{G_F^2}{m'm} L^{\mu\nu} H_{\mu\nu}. \tag{2.39}$$

And finally the photon-mediated interaction gives

$$|\mathcal{M}_\gamma|^2 = \left(\frac{e^2}{Q^2}\right) \frac{1}{2m'm} L^{\mu\nu} H_{\mu\nu}. \tag{2.40}$$

2.3 Rosenbluth decomposition

In this section we show how the contraction of lepton and hadron current can be decomposed in physically meaningful terms, and moreover how the dependence on the azimuth angle between lepton and hadron planes can be made explicit in terms of cosines and sines.

The matrix element is invariant, as it is a Lorentz scalar defined by the contraction of the lepton and hadron current which are four-vectors. We are thus free to choose a specific reference system in which it is calculated, without affecting the results. Needless to say we will benefit from choosing a reference frame that is meaningful. A common choice is to use a spherical coordinate system with respect to the direction of the exchanged boson, we will however use a Cartesian coordinate system with the boson along the z-axis, the results are of course the same. The initial and final state leptons define a plane, and by choosing this plane to be the 1-3 (xz) plane, the symmetric and anti-symmetric parts of the lepton tensor are easily identified as k^μ and k'^μ are both zero for $\mu = 2$. For the off-diagonal elements of the lepton tensor $L^{\mu\nu}$ that contain an index 2 the symmetric term disappears and these terms are thus purely complex and anti-symmetric under exchange of the indices. On the other hand, for the terms that do not contain an index 2 the complex antisymmetric part disappears and these are thus real and symmetric.

With this the contraction of lepton and hadron tensor can be written as

With this the contraction of lepton and hadron tensor can be written with following 10 terms

$$\begin{aligned} L_{\mu\nu} H\mu\nu = {} & L_{00}H^{00} + L_{11}H^{11} + L_{22}H^{22} + L_{33}H^{33} && (2.41)\\ & + 2\left[L_{01}\Re H^{01} + L_{03}\Re\left(H^{03}\right) + L_{13}\Re\left(H^{13}\right)\right] && (2.42)\\ & + 2\left[L_{02}\Im H^{02} + L_{12}\Im\left(H^{12}\right) + L_{32}\Im\left(H^{32}\right)\right]. && (2.43) \end{aligned}$$

We have used that the real part of the hadron tensor is purely symmetric and the imaginary part purely antisymmetric by construction

$$\begin{aligned} H^{\mu\nu} &= \frac{1}{2}\left(H^{\mu\nu} + H^{\nu\mu}\right) + \frac{1}{2}\left(H^{\mu\nu} - H^{\nu\mu}\right) \\ &= \frac{1}{2}\left[\left((\mathcal{J}^{\mu})^{\dagger}\mathcal{J}^{\nu} + (\mathcal{J}^{\nu})^{\dagger}\mathcal{J}^{\mu}\right) + \left((\mathcal{J}^{\mu})^{\dagger}\mathcal{J}^{\nu} - (\mathcal{J}^{\nu})^{\dagger}\mathcal{J}^{\mu}\right)\right] \\ &= \frac{1}{2}\left[2\Re\left(H^{\mu\nu}\right) + 2\Im\left(H^{\mu\nu}\right)\right]. \end{aligned} \tag{2.44}$$

If we now orientate our axes such that the exchanged bosons momentum $\mathbf{q} = \mathbf{k} - \mathbf{k}'$ is aligned with the 3 (z) axis it is interesting to consider what happens when the hadronic system is rotated along this axis with respect to the lepton plane. As the hadron current is a four vector, any Lorentz transformation Λ^{μ}_{ν} of the hadronic system as a whole corresponds simply to the Lorentz transform of the hadron current. For a specific orientation of the hadron system, one can denote the value of the hadron tensor as $H_0^{\mu\nu}$. We can then write the hadron tensor elements of the same system after a rotation over an angle ϕ along the q-axis by using

$$H^{\mu\nu} = \left(R^{\mu}_{\alpha} J_0^{\alpha}\right)^{*}\left(R^{\nu}_{\beta} J_0^{\beta}\right) = R^{\mu}_{\alpha} R^{\mu}_{\beta} H_0^{\mu\nu}. \tag{2.45}$$

It is clear that the components of the hadron tensor that are composed only of time-like and elements parallel with q do not change, the result for the other relevant terms in Eq. (2.41) are the ones that mix up the time-like and the longitudinal components with the transverse components

$$\begin{aligned} H^{01} &= \cos\phi H_0^{01} - \sin\phi H_0^{02},\ H^{02} = \sin\phi H_0^{01} + \cos\phi H_0^{02}, \\ H^{31} &= \cos\phi H_0^{31} - \sin\phi H_0^{32},\ H^{32} = \sin\phi H_0^{31} + \cos\phi H_0^{32}. \end{aligned} \tag{2.46}$$

And the ones that mix up the transverse components by themselves

$$\begin{aligned} H^{11} &= \cos^2\phi H_0^{11} + \sin^2 H_0^{22} + \frac{1}{2}\sin 2\phi\left(H_0^{12} + H_0 21\right) \\ H^{22} &= \cos^2\phi H_0^{22} + \sin^2 H_0^{11} - \frac{1}{2}\sin 2\phi\left(H_0^{12} + H_0 21\right) \\ H^{12} &= \cos^2\phi H_0^{1}2 - \sin^2\phi H_0^{21} + \frac{1}{2}\sin 2\phi\left(H^{11} - H^{22}\right). \end{aligned} \tag{2.47}$$

In contrast to the previous ones, here we can find linear combinations that are invariant under a rotation, $H^{11} + H^{22} = H_0^{11} + H_0^{22}$, and the imaginary part of H^{12}

$$\Im(H^{12}) = \cos^2\phi\,\Im(H_0^{12}) - \sin^2\phi\,\Im(H_0^{21}) \tag{2.48}$$

$$= \frac{1}{2}\cos^2\phi(H_0^{12} - H_0^{21}) - \frac{1}{2}\sin^2\phi(H_0^{21} - H_0^{12}) \tag{2.49}$$

$$= \frac{1}{2}\left(H_0 12 - H_0^{21}\right) = \Im(H^{12}). \tag{2.50}$$

Substituting Eqs. (2.46) and (2.47) in Eq. (2.41) we then find

$$L_{\mu\nu}H^{\mu\nu} = L_{00}H_0^{00} + 2L_{03}\Re\left(H_0^{03}\right) + L_{33}H_0^{33}$$

$$+ \frac{L_{11}+L_{22}}{2}\left(H_0^{11}+H_0^{22}\right) + 2L_{12}\Im\left(H_0^{12}\right) \tag{2.51}$$

$$+ 2\left[L_{01}\Re\left(H_0^{01}\right) + L_{13}\Re(H_0^{13}) + L_{02}\Im(H_0^{02}) + L_{23}\Im(H_0^{23})\right]\cos\phi \tag{2.52}$$

$$+ \frac{L_{11}-L_{22}}{2}\left(H_0^{11}-H_0^{22}\right)\cos 2\phi \tag{2.53}$$

$$+ 2\left[-L_{01}\Re(H_0^{02}) + L_{02}\Im(H_0^{01}) - L_{13}\Re(H_0^{23}) + L_{23}\Im(H_0^{13})\right]\sin\phi \tag{2.54}$$

$$+ \left(L_{22}-L_{11}\right)\Re(H_0^{12})\sin 2\phi. \tag{2.55}$$

The power of this explicit separation of an azimuth angle ϕ is that it represents a physical degree of freedom in the scattering process. In the case of single-nucleon knockout or single-pion production on a free nucleon the ϕ angle represents the azimuth angle of the particle with respect to the H_0 reference system, which is usually taken with the outgoing hadron in the lepton plane. In the case of pion production on a nucleon, where an outgoing pion and nucleon are detected one can define for example the average azimuth angle $\phi = \frac{\phi_\pi+\phi_N}{2}$, and the difference $\Delta = \phi_\pi - \phi_N$, as independent variables, where the latter is then invariant under rotation of the system along $\mathbf{q}$. In experiments where the lepton is measured in coincidence with the outgoing hadron, this separation is used to probe distinct (combinations of) hadron tensor elements which are sensitive to certain parts of the current. Also, it should be pointed out that all possible ϕ dependencies disappear after integration over ϕ. This means that cross sections for which this angle is not observed, can be completely described with only the terms in Eq. 2.51.

Chapter 3

Single-pion production off the nucleon

We consider single-pion production (SPP) of nucleons, the process depicted in Fig. 3.1, a single gauge boson ($\gamma, Z, W^{\pm}$) is exchanged between lepton and hadron vertices and a single pion is produced. The kinematics are expressed in terms of the four-vectors

$$k^{\mu} + k_i^{\mu} = k'^{\mu} + k_{\pi}^{\mu} + k_N^{\mu}, \tag{3.1}$$

with k and k' for the initial and final lepton respectively. The four-vectors k_π and k_N denote respectively the final-state pion and nucleon, the initial nucleon is denoted k_i. The energy and momenta are denoted as $k_i^{\mu} = (E_i, \mathbf{k}_i)$ with the magnitude of the momentum denoted as $|\mathbf{k}_i| = k_i$ when it can be unambiguously distinguished from the four-vector. The four-momentum exchanged between lepton and hadron vertices is $Q^{\mu} = k^{\mu} - k'^{\mu}$ and as is customary we define the squared four-momentum transfer $Q^2 = -Q_{\mu}Q^{\mu}$ such that it is positive.

As discussed in Chapter 2 the cross section for this process is given by

$$\frac{\mathrm{d}^5\sigma}{\mathrm{d}E'\mathrm{d}\Omega'\mathrm{d}\Omega_\pi} = \frac{\mathcal{F}_X^2}{(2\pi)^5}\frac{k'}{E}\frac{m_N k_\pi}{E_N f_{rec}} L_{\mu\nu}H^{\mu\nu}, \tag{3.2}$$

where $X \equiv CC, WNC, EM$ with

$$\mathcal{F}_{CC}^2 = G_F^2\cos^2\theta_c,\ \mathcal{F}_{WNC}^2 = G_F^2,\ \mathcal{F}_{EM}^2 = \frac{1}{2}\left(\frac{4\pi\alpha}{Q^2}\right)^2, \tag{3.3}$$

for charged-current, weak neutral current, and electromagnetic interactions respectively.

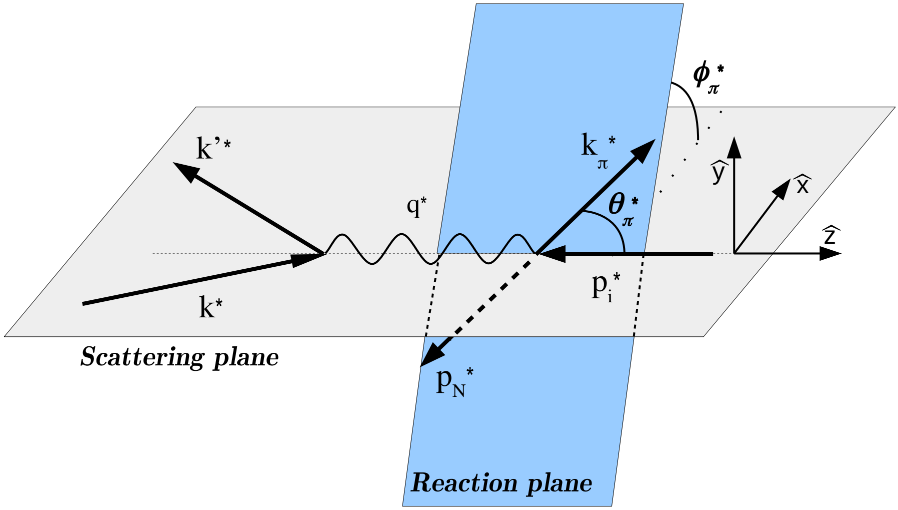

Figure 3.1: Lepton-induced single pion production off the nucleon in the CMS.

It is convenient to evaluate the cross section in the hadron center-of-momentum system (CMS) in which we denote the kinematic variables by a superscript *. In the CMS the final hadron system is at rest $\mathbf{k}_\pi^* = -\mathbf{k}_N^*$. We can then readily identify the Lorentz invariant

$$E_N^* f_{rec} = E_N^* |1 - (W - E_N^*)/E_N^*| = W, \tag{3.4}$$

where we introduced the hadronic invariant mass

$$W^2 = (k_\pi^\mu + k_N^\mu)^2 = (Q^\mu + k_i^\mu)^2 = s. \tag{3.5}$$

We thus have

$$\frac{\mathrm{d}^5\sigma}{\mathrm{d}E'\mathrm{d}\Omega'\mathrm{d}\Omega_\pi^*} = \frac{\mathcal{F}_X^2}{(2\pi)^5}\frac{k'}{E}\frac{m_N k_\pi^*}{W} L_{\mu\nu}H^{\mu\nu}, \tag{3.6}$$

or alternatively written in terms of invariants,

$$\frac{\mathrm{d}^5\sigma}{\mathrm{d}W\mathrm{d}Q^2\mathrm{d}\Omega_\pi^*} = \frac{\mathcal{F}_X^2}{2\,(2\pi)^4}\frac{k_\pi^*}{E^2} L_{\mu\nu}H^{\mu\nu}. \tag{3.7}$$

The hadron tensor contains all the non-trivial information on the process, we sum over the final and average over the initial nucleon spins to write

$$H^{\mu\nu} = \frac{1}{2}\sum_{s_i,s_f} J^{\mu,*}\left(k_\pi, k_N, Q, s_i, s_f\right) J^\nu\left(k_\pi, k_N, Q, s_i, s_f\right). \tag{3.8}$$

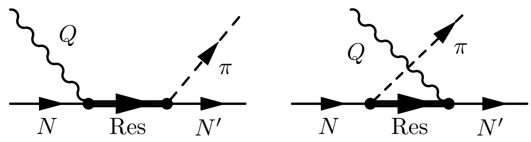

Figure 3.2: Feynman diagrams for the direct (left) and crossed (right) exchange of baryon resonances.

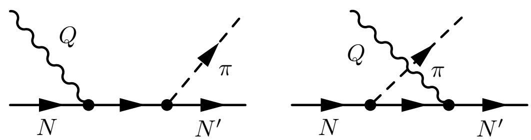

Figure 3.3: Feynman diagrams for the direct (left) and crossed (right) nucleon exchange.

Using the Dirac spinors to describe the initial and outgoing nucleon states the hadron current is

$$J^{\mu}\left(k_{\pi}, k_{N}, Q, s_{i}, s_{f}\right) = \overline{u}\left(k_{N}, s_{f}\right) \mathcal{O}^{\mu}\left(k_{\pi}, k_{N}, k\right) u\left(k_{i}, s_{i}\right). \tag{3.9}$$

Most of our understanding of leptonic single-pion production comes from detailed studies over the past half century of photon and electron induced pion production on nucleons. There has been an impressive amount of theoretical and experimental development in the field of electromagnetic scattering off nucleons and pion production reactions in particular [51]. In the kinematic region $W < 2$ GeV, $Q^2 \lesssim 3$ GeV^2 the pion production process proceeds predominantly through the direct excitation of baryon resonances which decay into a pion-nucleon pair, schematically depicted on the left in Fig 3.2. These resonances are characterized by their invariant mass M_R, width Γ, isospin I, spin J, parity P, and for SPP the branching ratio for decay into a pion and nucleon $\beta_{\pi N}$. Resonance properties have been studied in a multitude of hadronic and electroweak interactions [52] For electroweak interactions the main model-dependency lies in describing the excitation of a given resonance by a gauge boson for a certain Q^2 and W. The Q^2 dependence is usually parametrized by form-factors that are measured at $W = M_R$, while the W dependence is given by a (modified) Breit-Wigner form.

Next to the direct channel, in which resonance excitation results in a final state with specific $I(J^P)$ quantum numbers, baryon resonances can

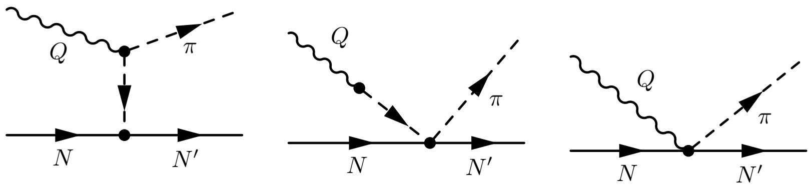

Figure 3.4: Feynman diagrams for the pion in-flight (left), pion-pole (middle) and contact-term (right).

contribute in the crossed channel, depicted on the right in Fig. 3.2. In this case the resonance contributes to multiple I, J final states. Crossing symmetry relates the form-factors for this crossed distribution directly to the ones in the direct channel within an isobar model.

Apart from the resonance exchanges in the s and u-channel, the description of SPP requires so-called 'background' contributions. These diagrams can be derived from an effective pion-nucleon Lagrangian. The background in this work is built from direct- and crossed nucleon exchanges shown in Fig. 3.3. And additionally the other contributions built from the 3-point and 4-point vertices shown in Fig. 3.4. In addition to these low-energy $\pi - N$ diagrams, the t-channel exchange of heavier virtual mesons, i.e. as depicted on the left in Fig 3.4 are found to be non-negligible beyond the delta region. The lightest mesons allowed in electroweak pion-production and included in most models of electromagnetic SPP are the ω and ρ vector mesons. We do not include these explicitly in this work.

We will discuss the contribution of these diagrams to the transition operator $\mathcal{O}^{\mu}$ in Section 3.3. First we discuss the isospin decomposition of the current, and give the relation between the electromagnetic and electroweak vector currents in Section 3.1. The assumption of PCAC may be used to constrain the axial couplings in the model and is discussed in Section 3.2. Finally in Sections 3.4-3.6, we show results for electromagnetic interactions, pion-nucleon scattering, and neutrino-induced interactions.

3.1 Isospin decomposition of the current and CVC

We first consider the isospin decomposition of SPP by the electromagnetic current, and show how the vector part of the weak current can be obtained from the electromagnetic current under the conserved vector current hypothesis (CVC).

While the electromagnetic interaction does not conserve strong isospin, we can still make use of the isospin formalism by considering that the electromagnetic current contains an isoscalar and isovector component

$$J^{\mu}_{EM} = V^{\mu}_{s} + \mathbf{V}^{\mu}. \tag{3.10}$$

The bold font indicates transformation as a vector in isospin space, while the letter V indicates that the four-vector current describing the coupling to the nucleon transforms as vector[1] under Lorentz transformations. Under isospin symmetry the different charged pions are identified as states in an isospin triplet,

$$\pi^{+} = |1,1\rangle\,,\ \pi^{0} = |1,0\rangle\,,\ \pi^{-} = |1,-1\rangle\,. \tag{3.11}$$

The proton and neutron are described by an isospin doublet

$$p = |\frac{1}{2},\frac{1}{2}\rangle\,,\ n = |\frac{1}{2},-\frac{1}{2}\rangle\,. \tag{3.12}$$

The physical final states are then coupled to states of total isospin 3/2 and 1/2 by the Clebsch-Gordan decomposition

$$|\pi N\rangle = |1, I^{\pi}_{3}\rangle \otimes |1/2, I^{N}_{3}\rangle \tag{3.13}$$

$$= \sum_{I=1/2}^{3/2} \sum_{I_3=-I}^{I} \big\langle 1\; 1/2\; I^{\pi}_{3}\; I^{N}_{3} \big|\, I\; I_3 \,\big\rangle\, |I, I_3\rangle\,. \tag{3.14}$$

The I_3 dependence of the matrix elements of the isovector current $\mathbf{V}^{\mu}$ is determined by the Wigner-Eckart theorem

$$\langle I, I_3 | V_q | I', I'_3 \rangle = \langle I\; I_3\; 1\; q |\, I'\; I'_3 \,\rangle\, \big\langle I \big|\big| V \big|\big| I' \big\rangle, \tag{3.15}$$

with $q = 0$ for the z component and ± 1 for the spherical components. For electromagnetic interactions, the charge is conserved and only the

1. Because of the presence of the pseudoscalar pion the current for SPP actually transform as an axial-vector, however it is customary to still refer to it as the vector current.

$q = 0$ component can contribute. With this we see that the amplitudes for the four physical electromagnetic interactions can be written as linear combinations of 3 distinct isospin amplitudes, the isoscalar, and two isovector amplitudes for the isospin 3/2 and 1/2 final states. We can define matrix elements for independent isospin components as e.g.

$$\begin{aligned} S^\mu &= \sqrt{\frac{1}{3}}\langle\frac{1}{2},\frac{1}{2}|V_s^\mu|\frac{1}{2}\frac{1}{2}\rangle \\ V_{1/2}^\mu &= \sqrt{\frac{1}{3}}\langle\frac{1}{2},\frac{1}{2}|V_0^\mu|\frac{1}{2},\frac{1}{2}\rangle \\ V_{3/2}^\mu &= \sqrt{\frac{1}{3}}\langle\frac{1}{2},\frac{1}{2}|V_0^\mu|\frac{3}{2},\frac{1}{2}\rangle. \end{aligned} \tag{3.16}$$

With these definitions and making use of Eq. (3.13) the physical amplitudes for electromagnetic interactions are written as

$$\langle\pi^+ n|J_{EM}^\mu|p\rangle = V_{3/2}^\mu - \sqrt{2}\left(V_{1/2}^\mu + S^\mu\right) \tag{3.17}$$

$$\langle\pi^- p|J_{EM}^\mu|n\rangle = V_{3/2}^\mu - \sqrt{2}\left(V_{1/2}^\mu - S^\mu\right) \tag{3.18}$$

$$\langle\pi^0 p|J_{EM}^\mu|p\rangle = \sqrt{2}V_{3/2}^\mu + \left(V_{1/2}^\mu + S^\mu\right) \tag{3.19}$$

$$\langle\pi^0 n|J_{EM}^\mu|n\rangle = \sqrt{2}V_{3/2}^\mu + \left(V_{1/2}^\mu - S^\mu\right). \tag{3.20}$$

The assumption of isospin symmetry and the structure of the current of Eqs.(3.10-3.12) thus introduces significant constraints, yielding relations between the four physical amplitudes by relating them to three isospin amplitudes. Separation of the isovector and isoscalar components are seen to require measurements off proton and neutron targets, however the different amplitudes are complex-valued such that the relation between the cross sections for different reactions are in general non-trivial.

For the weak charged-current interaction which proceeds through the exchange of a $W^\pm$ boson one has

$$J_{CC\pm}^\mu = \mathbf{V}^\mu - \mathbf{A}^\mu. \tag{3.21}$$

The charged current is completely isovector, and consists of currents which transform as a vector and axial-vector under Lorentz transformations. The CVC hypothesis now postulates that vector current $\mathbf{V}^\mu$ in the electromagnetic interaction and the weak interaction correspond to the same isovector current. Explicitly the vector part of the physical amplitudes for charged-current SPP, using the same definitions of

Eq. 3.16 are thus given by

$$\langle \pi^+ p | V_+^\mu | p \rangle = \langle \pi^- n | V_-^\mu | n \rangle = 3V_{3/2}^\mu, \tag{3.22}$$

$$\langle \pi^+ n | V_+^\mu | n \rangle = \langle \pi^- p | V_-^\mu | p \rangle = V_{3/2}^\mu + 2\sqrt{2}V_{1/2}^\mu, \tag{3.23}$$

$$\langle \pi^0 p | V_+^\mu | n \rangle = \langle \pi^0 n | V_-^\mu | p \rangle = -\sqrt{2}V_{3/2}^\mu + 2V_{1/2}^\mu. \tag{3.24}$$

The isospin amplitudes on the right-hand side are the same as in Eqs. (3.17-3.20), which hence can be obtained from knowledge of the electromagnetic interaction.

3.2 The axial current and PCAC

Chiral symmetry in QCD for the light quarks is a spontaneously broken symmetry, hence producing Goldstone bosons which are identified with the pseudoscalar mesons (the three pions when considering only up and down flavors). However, because the quarks have small and differing masses the symmetry is also explicitly broken such that the Goldstone bosons attain a mass. As such the axial current is not conserved, and its divergence is proportional to the pion mass, this is referred to as the Partially Conserved Axial Current (PCAC) hypothesis For practical purposes we may use

$$\partial_\mu J_A^{\mu,i}(x) = Q_\mu J_A^{\mu,i}(q) = f_\pi m_\pi^2 \hat{\pi}^i(Q) \tag{3.25}$$

where $J_A^{\mu,i}(q)$ is the axial current in momentum space with isospin index i, which takes values 0 or ± 1 for interactions that proceed through exchange of a Z or $W^\pm$ bosons respectively. The interpolating pion field $\hat{\pi}^i(Q)$ has corresponding isospin and four-momentum Q. This relates matrix elements due to the axial-current to the (off-shell) pion-nucleon interaction. In particular this yields the Goldberger-Treiman relation between the pion-nucleon coupling and the beta-decay of the neutron [53]. For an electroweak scattering amplitude with final state X on the nucleon due to the axial current, Eq. (3.25) implies that

$$\langle X | Q_\mu J_{A,i}^\mu | N \rangle = f_\pi \frac{m_\pi^2}{m_\pi^2 + Q^2} \langle X | \pi^i(Q) N \rangle , \tag{3.26}$$

where the amplitude on the right hand side is shorthand for the pion-nucleon interaction of off-shell pions with four-momentum Q. The pion-nucleon coupling is of course only determined for on-shell pions $Q^2 = -m_\pi^2$. When one assumes that the pion scattering amplitude varies slowly for small Q^2, e.g. $\langle X|\pi^i N\rangle|_{Q^2=0} \approx \langle X|\pi^i N\rangle|_{Q^2=-m_\pi^2}$ we have a relation between the physical amplitudes

$$\langle X|\, Q_\mu J_A^{\mu,i}(Q^2=0)\,|N\rangle \approx f_\pi \,\langle X|\pi_i(Q)N\rangle\,|_{Q^2=-m_\pi^2}. \tag{3.27}$$

With this assumption the part of the axial current that is not orthogonal to Q^μ at $Q^2=0$ may be determined from the pion-nucleon amplitudes.

This relation has been used to directly describe the inclusive cross section for meson production in neutrino interactions at $Q^2=0$ from the cross section of pion-nucleon (and nucleus) interactions [54–57]. Indeed in the limit of $Q^2=0$, i.e. for a forward scattered lepton with negligible mass, only the longitudinal part of the current enters and

$$L_{\mu\nu}H^{\mu\nu}|_{Q^2=0} = E'^2\left(H^{00} - 2H^{03} + H^{33}\right). \tag{3.28}$$

The cross section is seen to be proportional to $Q_\mu Q_\nu H^{\mu\nu}$, such that because of vector current conservation ($Q_\mu J_V^\mu = 0$) the vector current does not contribute, and that under the assumption of Eq. (3.27), it is completely determined by the pion nucleon scattering cross section.

The PCAC relation in Eq. (3.27) is used to constrain the axial couplings to the resonances in the model for electroweak SPP. The single pion production amplitude through an intermediate resonant state denoted simply by $|R\rangle$, by the axial current is schematically

$$\langle \pi N_f|\,\Gamma_{R\pi N}\,|R\rangle\,\langle R|\,\Gamma^\mu_{RQN,A}\,|N\rangle\,. \tag{3.29}$$

where $\Gamma^\mu_{RQN,A}$ describes the coupling at the resonance-nucleon-boson vertex, and $\Gamma_{R\pi N}$ describes the coupling of the resonance to the pion and nucleon. With the PCAC relation of Eq. (3.27) we thus have

$$\langle \pi N_f|\,\Gamma_{R\pi N}\,|R\rangle\,\langle R|\,Q_\mu\Gamma^\mu_{RQN,A}(Q^2=0)\,|N_i\rangle \tag{3.30}$$

$$\approx f_\pi\,\langle \pi N_f|\,\Gamma_{R\pi N}\,|R\rangle\,\langle R|\,\Gamma_{R\pi N}\,|\pi(Q)N_i\rangle\,. \tag{3.31}$$

Such that (part of) the axial coupling $\Gamma^\mu_{RQN,A}(Q^2=0)$ can be determined from the strong resonance decay vertex. Furthermore Eq. (3.25) implies that the divergence of the axial current should be zero in the limit of vanishing pion mass. This will be seen to not generally hold for the resonant axial currents because of the contribution of a pseudoscalar coupling, but may be imposed by assuming a pion-pole form for the pseudoscalar coupling.

While PCAC may be used to construct the axial couplings to different components in a model, this might not yield a total amplitude for which

Eq. (3.27) holds, i.e. one that reproduces the pion-nucleon scattering amplitude. This has been shown in Ref. [24], where the F_2 structure function for neutrino interactions at $Q^2 = 0$, which by Eq. (3.28) is proportional to $Q_\mu J_A^\mu$, obtained with the models of Refs. [26, 58] is compared to the structure function constructed from the pion-nucleon amplitudes of the DCC model of Refs. [57, 59]. Hence as an overall test of PCAC and consistency of the different components of the model, one may evaluate the elastic pion-nucleon amplitudes from a model for neutrino-induced SPP. We do this in Section 3.5 and perform a comparison to elastic pion-nucleon scattering data.

3.3 Modeling electroweak SPP

In the following we give the expressions used to model electroweak SPP. We first give general expressions for the currents corresponding to the resonance contributions and the background, parametrized by form-factors and isospin coefficients. The form-factors and isospin coefficients for specific SPP channels are then summarized in Section 3.3.5. We give the expressions for the matrices $\mathcal{O}_n^\mu$ such that

$$J^\mu = \sum_n \overline{u}\left(k_N, s_f\right) \mathcal{O}_n^\mu u\left(k_i, s_i\right), \tag{3.32}$$

with n the different contributions to the current.

3.3.1 Spin 1/2 resonances

The matrices for the diagram corresponding to s-channel spin 1/2 resonances are

$$\mathcal{O}_{R_{1/2}}^\mu = I_{iso,s}\Gamma_{R\pi N}(k_\pi)\ S_R\left(k_R\right)\ \Gamma_{QRN}^\mu(Q), \tag{3.33}$$

where $k_R = k_i + Q$. The crossed (u-) channel contribution is

$$\mathcal{O}_{CR_{1/2}}^\mu = I_{iso,u}\gamma^0 \left[\Gamma_{QRN}^\mu(-Q)\right]^\dagger \gamma^0\ S_R\left(k_R\right)\ \Gamma_{R\pi N}(k_\pi), \tag{3.34}$$

and $k_R = K_f - Q$ in this case. One can easily verify that

$$\gamma^0 \left[\Gamma_{QRN}^\mu(-Q)\right]^\dagger \gamma^0 = \Gamma_{QRN}(Q), \tag{3.35}$$

for the vertex function in Eqs. (3.37) and (3.38). The constants I_{iso} collect the factors arising from the coupling of the isospin at the weak and strong vertices, and are given for the different interactions in Section 3.3.5.

We split up the QRN vertex for spin 1/2 resonances of definite parity into the vector and axial part

$$\Gamma^{\mu}_{QRN} = \left(\Gamma_{QRN,V} - \Gamma_{QRN,A}\right)\tilde{\gamma}^5 \tag{3.36}$$

where $\tilde{\gamma}^5 = \gamma^5$ for negative parity and $\tilde{\gamma}^5 = 1$ for positive parity resonances. The vector part is

$$\Gamma^{\mu}_{QRN,V} = \frac{F_1}{\mu^2}\left(Q^{\mu}\not{Q} + Q^2\gamma^{\mu}\right) + i\frac{F_2}{\mu}\sigma^{\mu\alpha}Q_{\alpha}, \tag{3.37}$$

which is explicitly gauge-invariant as $Q_{\mu}\Gamma^{\mu}_{QRN,V} = 0$. The reduced mass $\mu = M_R + M_N$ is introduced to make the form-factors dimensionless.

The vertex for the axial current has an axial-vector and pseudoscalar term given by

$$\Gamma^{\mu}_{QRN,A} = G_A\gamma^{\mu}\gamma^5 + \frac{G_P}{M_N}Q^{\mu}\gamma^5. \tag{3.38}$$

The vector and axial form factors in these expressions depend on the interaction channel and are given in Section 3.3.5.

The propagator is

$$S_R(k_R) = \frac{\not{k}_R + M_R}{k_R^2 - M_R^2 + iM_R\Gamma(k_R^2)} \tag{3.39}$$

where $\Gamma(k_R^2)$ is the energy-dependent full width of the resonance which is discussed in Section 3.3.3. Finally, the decay vertex to pion-nucleon is given by

$$\Gamma_{R\pi N} = \sqrt{2}\frac{f_{\pi NR}}{m_{\pi}}\not{k}_{\pi}\gamma^5\tilde{\gamma}^5. \tag{3.40}$$

3.3.2 Spin 3/2 resonances

For spin 3/2 resonances, the spin-structure leads to a matrix element of the form

$$\mathcal{O}^{\mu}_{R_{3/2}} = I_{iso,s}\Gamma^{\alpha}_{R\pi N}\ S_{R,\alpha,\beta}\left(k_R\right)\ \Gamma^{\mu\beta}_{QRN}\left(K_i, Q\right), \tag{3.41}$$

for the s-channel contribution. While for the u-channel one has

$$\mathcal{O}^{\mu}_{CR_{3/2}} = I_{iso,u}\gamma^0\left[\Gamma^{\alpha\mu}_{QRN}\left(K_N, -Q\right)\right]^{\dagger}\gamma^0\ S_{R,\alpha,\beta}\left(k_R\right)\ \Gamma^{\beta}_{R\pi N}. \tag{3.42}$$

Again, the isospin coefficients I_{iso} are discussed in Section 3.3.5.

We again decompose the QRN vertex into vector and axial part as

$$\Gamma^{\beta\mu}_{QRN} = \left(\Gamma^{\beta\mu}_{QRN,V} + \Gamma^{\beta\mu}_{QRN,A}\right)\tilde{\gamma}^5. \tag{3.43}$$

In this case the vector current is generally described by four form-factors

$$\Gamma^{\beta\mu}_V = \left[\frac{C_3^V}{M}\left(g^{\beta\mu}\not{Q} - Q^\beta\gamma^\mu\right) + \frac{C_4^V}{M^2}\left(g^{\beta\mu}Q\cdot k_R - Q^\beta k_R^\mu\right)\right. \tag{3.44}$$

$$\left. + \frac{C_5^V}{M^2}\left(g^{\beta\mu}Q\cdot k_i - Q^\beta k_i^\mu\right) + C_6^V g^{\beta\mu}\right]\gamma^5, \tag{3.45}$$

but to explicitly impose vector current conservation $C_6^V = 0$ leaving 3 form-factors. For the axial current we have 4 form factors,

$$\Gamma^{\beta\mu}_A = \frac{C_3^A}{M}\left(g^{\beta\mu}\not{Q} - Q^\beta\gamma^\mu\right) + \frac{C_4^A}{M^2}\left(g^{\beta\mu}Q\cdot k_R - Q^\beta k_R^\mu\right) \tag{3.46}$$

$$+ C_5^A g^{\beta\mu} + \frac{C_6^A}{M^2}Q^\beta Q^\mu, \tag{3.47}$$

where one sees that the divergence of the axial current that is proportional to $Q_\mu\Gamma^{\beta\mu}$, is determined by C_5^A and the pseudoscalar form-factor C_6^A, such that these can be determined by the pion coupling under the assumption of PCAC. Again the explicit expressions for the form-factors are given in Section 3.3.5.

The propagator for spin 3/2 resonances is obtained from the Rarita-Schwinger theory and contains the spin 3/2 projection operator. It is given by

$$S_3^{\mu\nu} = \frac{\not{k}_R + M_R}{k_R^2 - M_R^2 + iM_R\Gamma(W)}\left[g^{\mu\nu} - \frac{1}{3}\gamma^\mu\gamma^\nu - \frac{2}{3}\frac{k_R^\mu k_R^\nu}{M_R^2} + \frac{k_R^\mu\gamma^\nu - k_R^\nu\gamma^\mu}{3M_R}\right]. \tag{3.48}$$

The $R\pi N$ vertex, finally is described as

$$\Gamma^\mu_{\pi NR} = \frac{\sqrt{2}f_{\pi NR}}{m_\pi}k_\pi^\mu\gamma^5\tilde{\gamma}^5. \tag{3.49}$$

3.3.3 Resonance widths and coupling constants

The coupling constants in the strong vertex of the resonance are related to the decay width to πN. The differential decay width is

$$d\Gamma = \frac{d\mathbf{k}_\pi}{2E_\pi\,(2\pi)^3}\frac{M_N\,d\mathbf{k}_N}{E_N\,(2\pi)^3}\,(2\pi)^4\,\delta^4\left(k_R - k_\pi - k_N\right)\overline{\sum}|\mathcal{M}|^2, \tag{3.50}$$

where the squared matrix element is summed and averaged over initial and final spins. We evaluate the total width in the CMS system where $\mathbf{k}_\pi^* = -\mathbf{k}_N^*$. Using the same method as outlined in Chapter 2 we make use of the δ-function to integrate over the nucleon momentum $\mathbf{k}_N^*$ and the magnitude of the pions momentum to obtain

$$\Gamma_{\pi N} = \frac{M_N k_\pi^*}{2\,(2\pi)^2\,W} \int \sum |\mathcal{M}|^2 \, d\Omega_\pi^* = \frac{M_N k_\pi^*}{2\pi W} \sum |\mathcal{M}|^2, \tag{3.51}$$

as in the CMS after summing over the spins of all particles the decay is isotropic. We can now compute the matrix elements from the vertices described above. For spin 1/2 resonances we have

$$\sum |\mathcal{M}|^2 = \frac{I_{iso}}{2} \frac{f_{\pi NR}^2}{m_\pi^2} \mathrm{Tr}\left[\frac{\not{k}_R + W}{2W} \gamma^0 \not{k}_\pi \tilde{\gamma}^5 \gamma^0 \frac{\not{k}_N + M_N}{2M_N} \not{k}_\pi \tilde{\gamma}^5 \right], \tag{3.52}$$

which together with Eq. (3.51) yields

$$\Gamma_{\pi N}^{1/2}(W) = \frac{I_{iso}}{4\pi} \frac{f_{\pi NR}^2}{m_\pi^2} k_\pi^* \frac{(W \pm M_N)^2}{W} \left(E_N^* \mp M_N \right). \tag{3.53}$$

While for the spin-3/2 resonances we have

$$\sum |\mathcal{M}|^2 = \frac{I_{iso}}{4} \frac{f_{\pi NR}^2}{m_\pi^2} \mathrm{Tr}\left[S_{3/2}^{\mu\nu}(W) k_{\pi,\mu} \gamma^0 \tilde{\gamma}^5 \gamma^0 \frac{\not{k}_N + M_N}{2M_N} k_{\pi,\nu} \tilde{\gamma}^5 \right] \tag{3.54}$$

where $S_3^{\mu\nu}$ is the Rarita-Schwinger propagator resulting in [60]

$$\Gamma_{\pi N}^{3/2}(W) = \frac{I_{iso}}{12\pi} \frac{f_{\pi NR}^2}{m_\pi^2} \frac{(k_\pi^*)^3}{W} \left(E_N^* \pm M_N \right). \tag{3.55}$$

In both cases $I_{iso} = 1(3)$ for isospin $3/2(1/2)$ resonances and the upper(lower) sign corresponds to positive(negative) parity resonances. With these formulae the strong couplings are fixed by requiring that the partial width at resonance mass is

$$\Gamma_{\pi N}(M_R) = \beta_{\pi N} \Gamma_{exp}, \tag{3.56}$$

where Γ_{exp} and $\beta_{\pi N}$ are the experimentally determined full width and branching ratio to pion-nucleon. Table 3.1 gives an overview of the values used for the included resonances.

In most models for SPP it is necessary to regularize the behavior of the resonance tree-level amplitudes for invariant masses far away from the resonances peak [61–66]. For this reason a cut-off form-factor is

Table 3.1: The couplings $f_\pi NR$ for each resonance are determined from the listed width and branching ratio $\beta_\pi N$

	M_R (MeV)	Γ_{exp} (MeV)	$\beta_{\pi N}$	$f_{\pi NR}$
P_{33}	1232	120	1	2.18
S_{11}	1535	150	0.45	0.16
P_{11}	1430	350	0.6	0.49
D_{13}	1515	115	0.6	1.62

introduced which multiplies both the s and u channel amplitudes and is symmetric under interchange of s and u [61–63]

$$F(s,u) = F(s) + F(u) - F(s)F(u). \tag{3.57}$$

The form-factor $F(x)$ is given by the combination of a Gaussian and dipole

$$F(x) = \exp\left(-\frac{\left(x - M_R^2\right)^2}{\lambda_R^4}\right)\frac{\lambda_R^4}{\left(x - M_R^2\right)^2 + \lambda_R^4} \tag{3.58}$$

where x is s or u. This function is inspired by the multi-dipole Gaussian form-factor proposed in Ref. [67], although the dependence on the resonance spin and width proposed in that work is not used here. Instead the dipole is included for both spin-1/2 and 3/2 and a cut-off $\lambda_R = 1200$ MeV is used for all resonances. With this we find the desired behavior of retaining the original resonance shape for $s \approx M_R^2$, while avoiding the unphysical behavior for higher s.

The width that enters the resonance propagator is the full width of the resonance, which consists of the partial width $\Gamma_{\pi N}$ for decay to pion-nucleon and the 'inelastic' width Γ_{in}. In Ref. [31] only the energy dependence of $\Gamma_{\pi N}$ was explicitly taken into account and the full width was parametrized as

$$\Gamma(W) = \Gamma_{\pi N}(W) + (1 - \beta_{\pi N})\Gamma_{exp}, \tag{3.59}$$

with Γ_{exp} the constant experimental full width. Other parametrizations of the full width, which include explicitly a W dependence of the inelastic width [33], or additionally a decrease of the width for high-W [63, 65] are found to not affect the cross section strongly because of the presence of the hadronic form factor of Eq. (3.58). Therefore, in the present work we keep the parametrization of Eq. (3.59), to be consistent with Ref. [31] although more elaborate parametrizations may be explored.

3.3.4 Non-resonant background

The nucleon and cross nucleon poles have the same structure as the spin 1/2 resonances discussed above, we have

$$\mathcal{O}_{NP} = \frac{-g_A}{\sqrt{2}f_\pi} \not{k}_\pi \gamma^5 \frac{\not{k}_s + M_N}{s - M_N^2} \Gamma^\mu_{QNN}, \tag{3.60}$$

for the nucleon pole in the s channel, and obtain the u-channel contribution by taking the Hermitian conjugate and replacing s by u

$$\mathcal{O}_{CNP} = \frac{-g_A}{\sqrt{2}f_\pi} \Gamma^\mu_{QNN} \frac{\not{k}_u + M_N}{u - M_N^2} \not{k}_\pi \gamma^5, \tag{3.61}$$

with $k_u^\mu = p^\mu - k_\pi^\mu$. The vertex function is here defined in the familiar form

$$\Gamma^\mu_{QNN} = \Gamma^\mu_{QNN,V} - \Gamma^\mu_{QNN,A}, \tag{3.62}$$

with

$$\Gamma^\mu_{QNN,V} = F_1(Q^2)\gamma^\mu + i\frac{F_2(Q^2)}{2M_N}\sigma^{\mu\alpha}Q_\alpha, \tag{3.63}$$

and

$$\Gamma^\mu_{QNN,A} = G_A(Q^2)\gamma^\mu\gamma^5 + \frac{G_P(Q^2)}{M_N^2}\not{Q}Q^\mu\gamma^5. \tag{3.64}$$

Note the difference in the coupling proportional to F_1 in comparison to the previously discussed spin 1/2 resonance case, in which the first term is constructed such that the spin-1/2 resonance current satisfies CVC as a matrix equation. We use the parametrization of Kelly [68] for the vector-current form factors $F_1^{p/n}$ and $F_2^{p/n}$ for protons and neutrons. The axial form factors are parametrized by dipoles under the assumption of pion-pole dominance of the pseudoscalar form factor G_P

$$G_A(Q^2) = \frac{g_A}{\left(1 + Q^2/M_A^2\right)^2}, \; G_P(Q^2) = \frac{G_A(Q^2)M_N^2}{m_\pi^2 + Q^2}, \tag{3.65}$$

with $M_A = 1.05$ GeV. The first order ChPT Lagrangian includes a four-point coupling that gives a vector and axial contribution $\mathcal{O}^\mu_{CT} = \mathcal{O}^\mu_{CT,V} + \mathcal{O}^\mu_{CT,A}$ with

$$\mathcal{O}^\mu_{CT,V} = F_{CT}(Q^2)\frac{-g_A}{\sqrt{2}f_\pi}\gamma^\mu\gamma^5, \tag{3.66}$$

$$\mathcal{O}^\mu_{CT,A} = F_\rho(t)\frac{1}{\sqrt{2}f_\pi}\gamma^\mu. \tag{3.67}$$

There is a purely axial pion-pole term

$$\mathcal{O}^{\mu}_{PP} = F_{\rho}(t)\frac{-1}{\sqrt{2}f_{\pi}}\frac{Q^{\mu}}{Q^2-m_{\pi}^2}\frac{(\not{Q}+\not{k}_{\pi})}{2}. \tag{3.68}$$

and the purely vector pion in flight term, i.e. the t-channel pion exchange

$$\mathcal{O}^{\mu}_{PF} = F_{PF}(Q^2)\frac{-g_A}{\sqrt{2}f_{\pi}}\frac{2k^{\mu}_{\pi}-Q^{\mu}}{t-m_{\pi}^2}\not{k}_t\gamma^5. \tag{3.69}$$

3.3.5 Isospin coefficients and form factors

The operators for the different components of the model where introduced in a general form applicable to electromagnetic and weak SPP. The difference between physical processes is contained in the isospin coefficients and form-factors. The different physical amplitudes are related by using the isospin decomposition of Section 3.1 which define the isospin coefficients once the couplings are fixed. In order to describe electroweak SPP one needs to define the couplings corresponding to the $V^{\mu}_{3/2}$, $V^{\mu}_{1/2}$, and S^{μ} amplitudes.

As resonances are isospin-eigenstates, the s-channel resonance diagrams only contribute to their respective isospin amplitude. For isospin 1/2 resonances we thus have a isovector and isoscalar amplitude each with their own coupling described by the appropriate form-factors. In the diagrammatic approach followed here, it is more natural to introduce the form-factors that correspond to the coupling of the exchanged boson at the hadron vertex. Proton and neutron currents for a nucleon resonance are defined as respectively the sum and difference of isovector and isoscalar currents defined in Section 3.1 e.g. for the contribution of the isospin-1/2 resonances

$$\langle\pi^0 p|J^{\mu}_{EM,I=1/2}|p\rangle = (V^{\mu}_{1/2}+S^{\mu}) = V^{\mu}_{p}, \tag{3.70}$$

$$\langle\pi^0 n|J^{\mu}_{EM,I=1/2}|n\rangle = (V^{\mu}_{1/2}-S^{\mu}) = -V^{\mu}_{n}. \tag{3.71}$$

As the amplitudes are proportional to the form-factors we may thus define isovector and isoscalar form factors as

$$F_V = F_p - F_n \tag{3.72}$$

$$F_S = F_p + F_n. \tag{3.73}$$

The isospin 3/2 resonances only contribute to the isovector current, thus the coupling to protons and neutrons is the same and described by the

Table 3.2: The form factors and isospin coefficients for the resonance contributions to the electromagnetic current

	$R_{3/2}$	$CR_{3/2}$	$R_{1/2}$	$CR_{1/2}$	other
$p \to \pi^0 p$	$\sqrt{1/3}\ C_V$	$\sqrt{1/3}\ C_V$	$\sqrt{1/2} F_p$	$\sqrt{1/2} F_p$	0
$p \to \pi^+ n$	$-\sqrt{1/6}\ C_V$	$\sqrt{1/6}\ C_V$	F_p	F_n	$-1F_1^V$
$n \to \pi^- p$	$\sqrt{1/6}\ C_V$	$-\sqrt{1/6}\ C_V$	F_n	F_p	$1F_1^V$
$n \to \pi^0 n$	$\sqrt{1/3}\ C_V$	$\sqrt{1/3}\ C_V$	$-\sqrt{1/2} F_n$	$-\sqrt{1/2} F_n$	0

Table 3.3: The isospin coefficients for the charged-current interactions.

	$R_{3/2}$	$CR_{3/2}$	$R_{1/2}$	$CR_{1/2}$	others
$p \to \pi^+ p$	$\sqrt{3/2}$	$\sqrt{1/6}$	0	1	1
$n \to \pi^0 p$	$-\sqrt{1/3}$	$\sqrt{1/3}$	$\sqrt{1/2}$	$-\sqrt{1/2}$	$-\sqrt{2}$
$n \to \pi^+ n$	$\sqrt{1/6}$	$\sqrt{3/2}$	1	0	-1

isovector form-factors C_V. With the coupling between the boson and initial nucleon to produce a resonance determined by form-factors, one can apply the same couplings in the crossed-channel resonance contributions. The resulting form-factors and isospin factors for the different channels accessible in the electromagnetic current are summarized in Table 3.2. The nucleon and crossed nucleon pole diagrams have the same structure as the $R_{1/2}$ and $CR_{1/2}$ columns. For the other background diagrams, only the pion-in-flight term and the vector part of the contact term contribute, and they are both purely isovector, corresponding to the last column in Table 3.2. To enforce vector-current conservation, the form-factors in these terms are set to the same vector form-factor in the nucleon-pole terms

$$F_{CT}\left(Q^2\right) = F_{PF}\left(Q^2\right) = F_1^V\left(Q^2\right) = F_1^p\left(Q^2\right) - F_1^n\left(Q^2\right). \tag{3.74}$$

The charged-current interaction is purely isovector hence the form-factors in every diagram correspond to the same $F_V = F_p - F_n$ and F_A. From the relations in Section 3.1 we obtain the isospin coefficients in Table 3.3.

I. Vector current form factors

The form-factors for the vector current can be inferred from electromagnetic pion production under the CVC hypothesis as detailed in Section. 3.1. For the isospin 1/2 resonances this requires measurements on both proton and neutron targets, in order to separate the isovector and isoscalar contribution. The extraction of 'bare' electromagnetic couplings to the resonances from scattering data is not model-independent but depends on the interplay between the different contributions to the current. In particular the interference between background and resonant diagrams has to be under control, and moreover the cross-channel diagrams for the resonances contribute to multiple spin-isospin final states, such that separating them from the direct-channel resonances is not possible. A wealth of data on electroproduction of pion on nucleons is available, and many different approaches give a good description of the data, however only a limited number of models have been used to describe electromagnetic and weak interactions in a consistent way.

In the tree-level approach followed here different strategies have been used to determine the vector coupling in CC scattering from the electromagnetic data. The form-factors used in Ref. [31] were determined by Lalakulich et al. [26] by fitting the experimental helicity amplitudes obtained at $W = M_R$ for the delta, D_{13}, S_{11}, and P_{11}.

The helicity amplitudes of the resonances are extracted from scattering data and are thus inherently model-dependent. However, in the analysis of experimental data many different models are used to obtain a practically model-independent measurement [51]. The resonant form-factors extracted in Ref. [26], and subsequently used to describe neutrino scattering in Refs. [14, 29–31, 37, 60] were fit in 2007. In this section, we compare the helicity amplitudes obtained with these form factors to the recent compilation of data from Ref. [69] and update the form factors if necessary in light of this more recent dataset.

The helicity amplitudes are defined as matrix elements for resonance production with definite spin projection by transverse and longitudinal photons, for details we refer to Refs. [51, 70].

The relation between the helicity amplitudes and the resonance form factors defined in previous sections are

$$A_{1/2} = \sqrt{\frac{N}{3}}\left[C_3\left(\frac{M_N^2 \pm M_N M_R + Q^2}{M_N M_R}\right) - C_4 Q\cdot k_R - C_5 Q\cdot k_N\right] \tag{3.75}$$

$$A_{3/2} = \sqrt{N}\left[C_3\left(M_N \pm M_R\right) + C_4 Q\cdot k_R + C_5 Q\cdot k_N\right] \tag{3.76}$$

$$S_{1/2} = \pm\sqrt{\frac{3N}{2}}\frac{q_z}{M_R}\left[C_3\frac{M_R}{M_N} + C_4\frac{M_R^2}{M_N^2} + C_5\left(\frac{M_R^2 + M_N^2 + Q^2}{2M_N^2}\right)\right] \tag{3.77}$$

for spin 3/2 resonances where $N = \frac{\pi\alpha}{M_N}\frac{(M_R \mp M_N)^2+Q^2}{M_R^2-M_N^2}$ and the upper(lower) sign corresponds to positive(negative) parity. For spin 1/2 resonances one has

$$A_{1/2} = \sqrt{2N}\left[\frac{F_1}{\mu^2}Q^2 + \frac{F_2}{\mu}(M_R \pm M_N)\right] \tag{3.78}$$

$$S_{1/2} = \pm\sqrt{N}q_z\left[\frac{F_1}{\mu^2}(M_R \pm M_N) - \frac{F_2}{\mu}\right]. \tag{3.79}$$

These relations agree with Refs. [51, 70, 71], keeping in mind that the definition of the resonance form-factors in Ref. [70] are different but related straightforwardly to our definitions, and that opposite parity transitions in Ref. [70] are defined by multiplication to the left of the Γ_{RQN} vertices by γ^5, while in our case they are defined by multiplication to the right.

Delta ($P_{33}(1232)$**:** We compare different parametrizations to the data for the Delta helicity amplitudes compiled in Ref. [69] in Fig. 3.5. The parametrizations due to Lalakulich [26] and Kabirnezhad [27] are obtained from the form factors they reported, where we use $M_R = 1232$ MeV in both cases. For the Lalakulich form factors we added an additional minus sign to the transverse amplitudes. We show the results of Kabirnezhad because this parametrization is used in a model which shares the parametrization of the background with the one presented here, and is currently in the process of being implemented in the GENIE and NEUT event generators [25]. We do not however take into account any possible deviations due to different values of the resonance width or mass in these results. The MAID07 results are obtained from the parametrization of the electromagnetic amplitudes that are reported in Ref. [66] which are trivially related to the helicity amplitudes. The MAID amplitudes where rescaled by a factor $\sqrt{115/130}$ to account for the difference in width of the delta used in MAID07 as explained in Ref. [66].

We see that the Lalakulich form factors provide a fair parametrization of the helicity amplitudes, although they tend to zero slower than the data. It is interesting to note that the $S_{1/2}$ amplitude would be slightly better described when it is multiplied by $\frac{q_{LAB}}{q_{CMS}} = M_\Delta/M_N$. The form factors implied by using a scaled value for $S_{1/2}$ can be obtained by inverting the relation between the helicity amplitudes, and we have checked that cross section results obtained with form factors defined by scaling $S_{1/2}$ with $\frac{M_\Delta}{M_M}S_{1/2}$ do not differ appreciably because the scalar amplitude is very small. Moreover the resulting form-factors are not

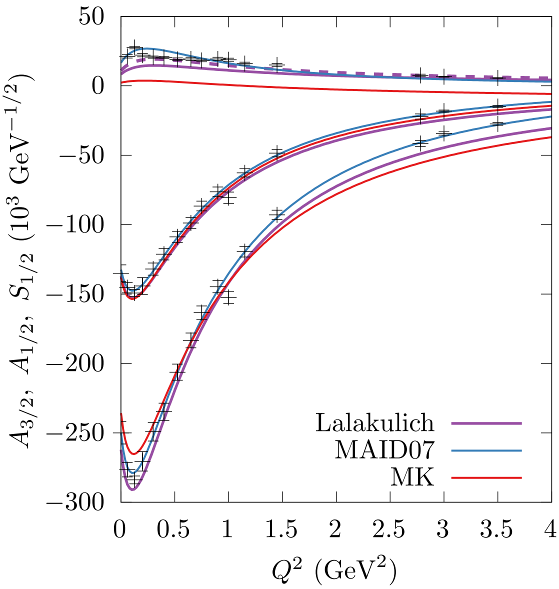

Figure 3.5: Helicity amplitudes $A_{3/2}$ (bottom), $A_{1/2}$ (middle) and $S_{1/2}$ (top), for the Delta resonance obtained with the form-factors of Lalakulich, Kabirnezhad (labeled MK) and the parametrization of MAID07. The dashed line shows the Lalakulich result for $S_{1/2}$ multiplied by $\frac{M_\Delta}{M_N}$.

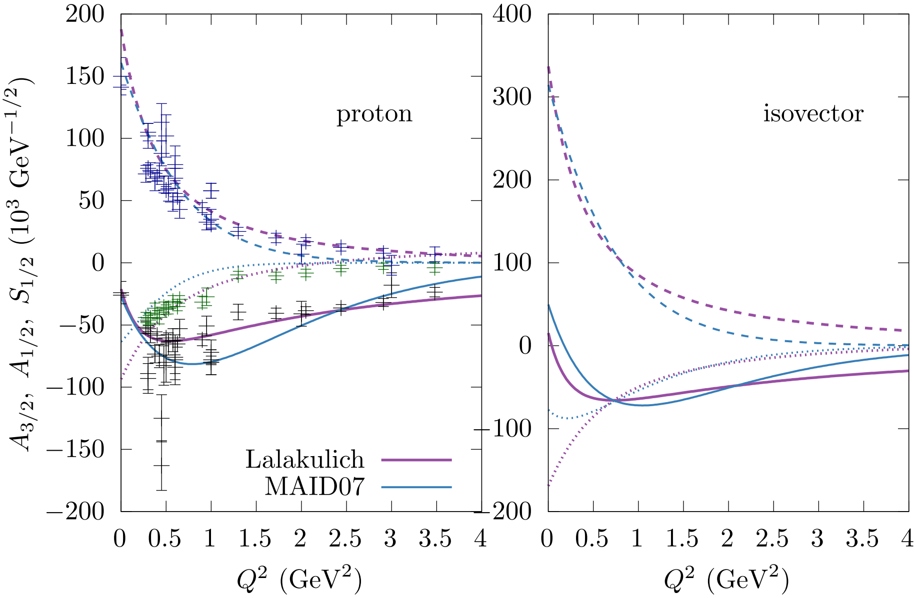

Figure 3.6: Helicity amplitudes $A_{3/2}$ (dashed lines, dark-blue data), $A_{1/2}$ (solid lines, dark-blue data) and $S_{1/2}$ (dotted lines, dark green data), for the D_{13} resonance obtained with the form-factors of Lalakulich [26], and the parametrization of MAID07 as reported in Ref. [66].

easily parametrized, in particular losing the proportionality between C_3 and C_4 which is enforced in the Lalakulich parametrization, informed by the result that when the Delta amplitude is purely magnetic $A_{1/2} = \sqrt{3}A_{3/2}$ and $S_{1/2} = 0$ and hence Eqs. (3.75-3.77) imply $C_4 = -\frac{M_N}{M_\Delta}C_3$. While different parametrizations could clearly be found, for simplicity and consistency with Refs. [14, 30, 31] we retain the form factors of Lalakulich in this work which are quoted here for completeness

$$C_3 = \frac{2.13/D_V(Q^2)}{1 + Q^2/4M_V^2} \tag{3.80}$$

$$C_4 = -1.51/2.13C_3 \tag{3.81}$$

$$C_5 = \frac{0.48/D_V(Q^2)}{1 + Q^2/0.776M_V^2}. \tag{3.82}$$

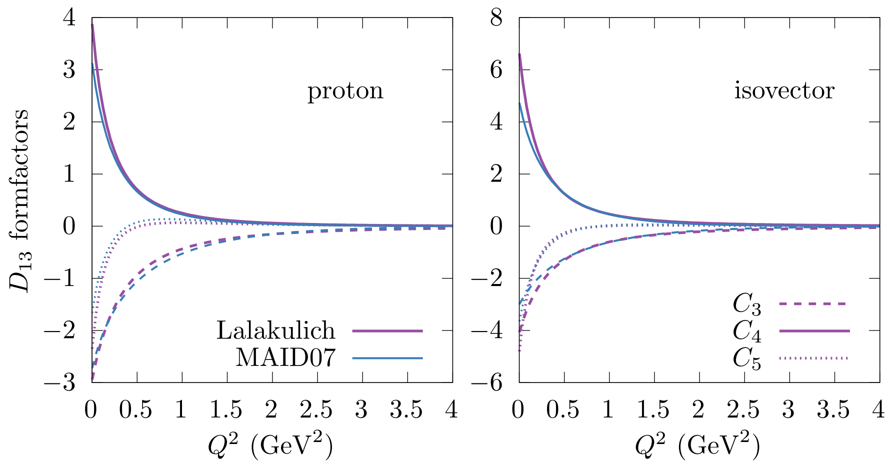

Figure 3.7: Form factors obtained by inverting the helicity amplitudes.

$D_{13}(1535)$: The helicity amplitudes for the D_{13} resonance computed from the form factors by Lalakulich, adding again a minus sign in the vector amplitudes and taking $M_R = 1535$ are compared to the data and the MAID07 parametrization. Lalakulich obtained results for both proton and neutron form-factors, here we compare the proton amplitudes to the data. Instead of a comparison of the neutron amplitudes, we compare the isovector amplitudes obtained with form-factors $C_V = C_p - C_n$ to the results of MAID07, as these are directly relevant to neutrino interactions.

We note that for the D_{13} we obtain good results for the transverse cross section in comparison to electron scattering only when using the Lalakulich form factors with opposite sign. Such a sign ambiguity was not relevant to the original work of Lalakulich as no interfering background was included.

We have inverted Eqs. (3.75-3.77) numerically to obtain the form factors shown in Fig. 3.7 from the helicity amplitudes, we use $M_R = 1535$ in all cases. One finds a very good agreement between the form factors from the different models, barring relatively large differences around $Q^2 = 0$. Given this agreement we choose to parametrize the form factors obtained from the MAID07 amplitudes, as we find a slightly better result for photoproduction with these, and moreover the values at $Q^2 = 0$ are closer to the values used in Ref. [33], which was included in the extraction of axial form factors of the delta in Ref. [30] which we will use as described in a further section.

With the values at $Q^2 = 0$ numerically defined, we use the combination of an exponential and a dipole to describe the form factors, but add a first order polynomial to the C_5 form factors. The result is

$$C_3^p = -2.72\ G_D\left(Q^2, 1.53\right) e^{-0.38Q^2}, \tag{3.83}$$

$$C_4^p = 3.13\ G_D\left(Q^2, 0.84\right) e^{-0.66Q^2}, \tag{3.84}$$

$$C_5^p = -1.66\ G_D\left(Q^2, 0.80\right) e^{-0.96Q^2}\left(1 - 2.513Q^2\right), \tag{3.85}$$

$$C_3^V = -3\ G_D\left(Q^2, 2.00\right) e^{-0.54Q^2}, \tag{3.86}$$

$$C_4^p = 4.73\ G_D\left(Q^2, 1.13\right) e^{-0.73Q^2}, \tag{3.87}$$

$$C_5^p = -3.65\ G_D\left(Q^2, 0.99\right) e^{-0.97Q^2}\left(1 - 1.150Q^2\right), \tag{3.88}$$

$$\tag{3.89}$$

where Q^2 enters with unit GeV^2 and $G_D(Q^2, x) = \left(1 + Q^2/(xM_V^2)\right)^{-2}$ a modified dipole with $M_V = 0.84$ GeV. A more meaningful parametrization might be found, but the aim is simply to have a convenient description of the form-factors implied by the MAID amplitudes. Note that the parametrization is not perfect, and as the shape of the amplitudes, especially for high Q^2, is quite sensitive to small differences in the form factors these functions do not exactly reproduce the original amplitudes at high Q^2.

$S_{11}(1520)$**:** For the spin 1/2 resonances only the proton form factors were obtained in Ref. [26]. To estimate the coupling to the neutron the isoscalar amplitude was assumed to be negligible such that $F_n = -F_p$. Through comparison of the electromagnetic cross sections around $W =$ 1.5 GeV with the results of MAID07 and the ANL-Osaka DCC model of Ref. [34], we find that this approach might not be satisfactory for the S_{11}.

In Fig. 3.8 the proton and isovector helicity amplitudes of the $S_{11}(1520)$ are shown using the form factors of Lalakulich under the assumption that $F_n = -F_p$. The results are compared to the data compiled in Ref. [69] and the results of the MAID07 analysis. We note that the $S_{1/2}$ amplitude obtained from the Lalakulich form-factors has been multiplied by a factor M_R/M_N in order to obtain agreement with the original results reported in Ref. [26]. The proton helicity amplitudes of the S_{11} resonance decrease slowly with Q^2, hence there is a pronounced contribution to the cross section up to large values of Q^2. In contrast, the helicity amplitudes for the neutron decrease much faster than the proton ones in the results of the MAID07 analysis. One sees however

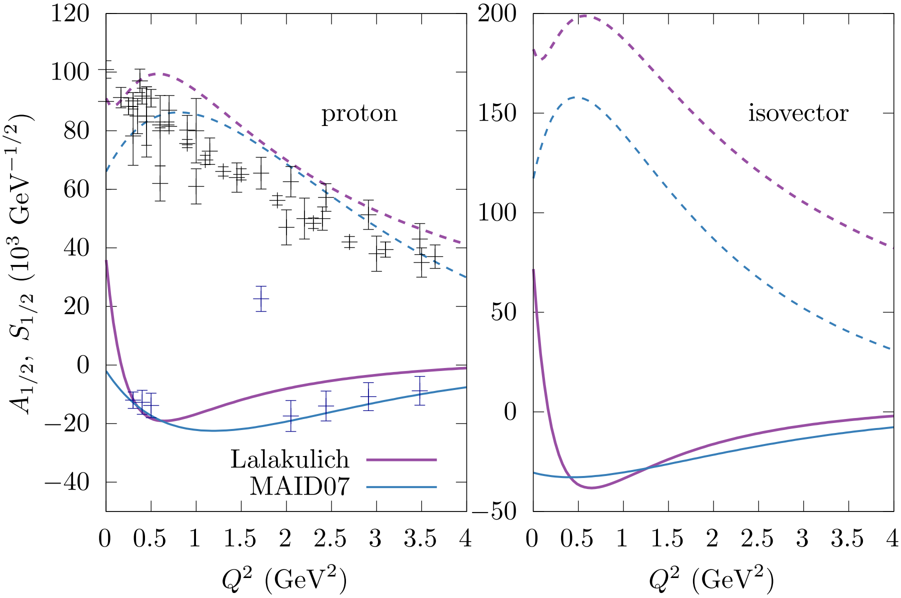

Figure 3.8: Helicity amplitudes $A_{1/2}$ (dashed lines, black data) and $S_{1/2}$ (solid lines, dark-blue data), obtained with the form-factors of Lalakulich and from the MAID07 analysis. Note that the $S_{1/2}$ amplitude obtained with the Lalakulich form factors has been multiplied by a factor $\frac{M_R}{M_N}$ as discussed in the text. The isovector amplitudes shown in the right panel are defined as $A_p - A_n$.

that the $A_{1/2}$ amplitude obtained from the Lalakulich for-factors in general overshoots the data, while the $S_{1/2}$ is slightly too large for $Q^2 > 2$ GeV. Comparing the data shown in Ref. [26] that was originally used to constrain these form-factors with the recent compilation shown in Fig. 3.8, one sees that this set of data, which includes electromagnetic η production, is simply lower in magnitude than those originally used in the fit. In general however, while improvements are certainly possible, the Q^2 dependence and the magnitude of the amplitudes for the proton is quite reasonable, and when combined with the other components of the model gives adequate results for the angle-integrated electromagnetic SPP cross sections on protons.

Under the assumption that $F_n = -F_p$, this is found to not be the case for SPP on neutron targets, in comparison to the ANL-Osaka DCC model and the MAID07 results of Refs. [34, 66], and one overshoots the cross section around $W = 1500$ MeV. This is consistent with the comparison to the isovector amplitudes shown in the right panel of Fig. 3.8 one sees in the MAID07 results that at low Q^2 indeed $A_{1/2,n} \approx -A_{1/2,p}$ but that at high Q^2 $A_{1/2,V} \approx A_{1/2,p}$, i.e. the neutron amplitude is found to drop off much faster than the one for the proton with increasing Q^2. The isovector scalar amplitude seems to be similar in MAID07 and using the Lalakulich form-factors with $F_n = -F_p$, except at low Q^2. In MAID07 the neutron amplitude is large compared to the proton one at low Q^2, and drops of fast such that beyond $Q^2 \approx 1$ GeV the isovector amplitude is practically the same as the proton one. In the Lalakulich approach on the other hand $S_{1/2,V}$ is doubled compared to the proton result making it closer to the proton amplitude in MAID07. Based on these results and the resulting comparisons presented in Section 3.4, we choose to retain the parametrization of Lalakulich for the proton form-factors, albeit with an overall minus sign as already pointed out in Ref. [31]

$$
\begin{aligned}
F_1^p &= -2\frac{G_D(Q^2,1)}{1+Q^2/\left(1.2M_V^2\right)}\left[1+7.2\ln\left(1+Q^2/(\mathrm{GeV}^2)\right]\right. ,\\
F_2^p &= -0.84G_D(Q^2,1)\left[1+0.11\ln\left(1+Q^2/\left(\mathrm{GeV}^2\right)\right)\right].
\end{aligned}
$$

We use a simple prescription to obtain a behavior of the isovector form factor that is similar as the MAID07 result, namely that we define $F^n_{1,2}(Q^2) = -\frac{1}{2}F^p_{1,2}(Q^2)$. This is simply based on the fact that with this $F_V(Q^2) = \frac{3}{2}F_p(Q^2)$, which agrees better with the MAID07 result shown in Fig. 3.8 than than the Lalakulich result $F_V(Q^2) = 2F_p(Q^2)$ shown in the same figure.

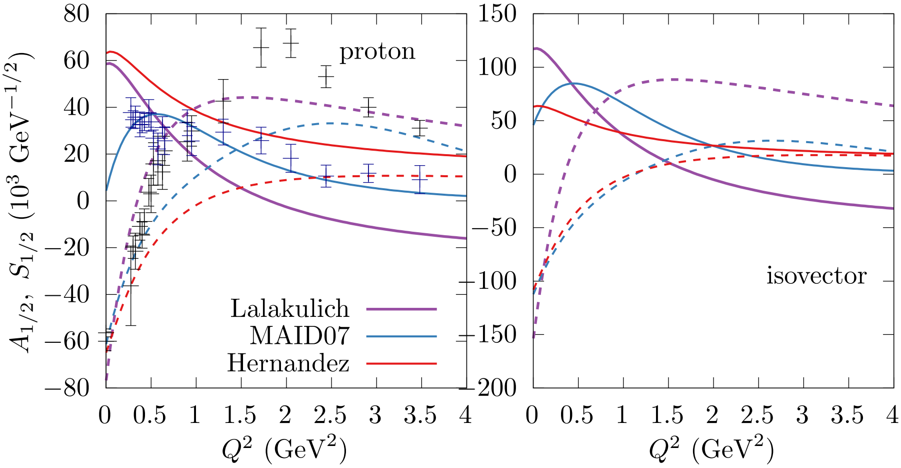

Figure 3.9: Helicity amplitudes $A_{1/2}$ (dashed lines, black data) and $S_{1/2}$ (solid lines, dark-blue data), obtained with the form-factors of Lalakulich, from the MAID07 analysis and from Hernandez. Note that the $S_{1/2}$ amplitude obtained with the Lalakulich form factors has been multiplied by a factor $\frac{M_R}{M_N}$ as discussed in the text. The isovector amplitudes shown in the right panel are defined as $A_p - A_n$.

$P_{11}(1440)$: For the Roper ($P_{11}(1440)$) we also include here the results obtained with the form-factors of by Hernandez et al. [71] that are obtained from a fit of proton helicity amplitudes, and which were used to describe the vector coupling in describing neutrino-induced two pion production. The amplitude $A_{1/2}$ shows the same behavior in all three descriptions, rising sharply from negative to positive values. The Hernandez and MAID07 results satisfy the data at $Q^2 = 0$ while the Lalakulich result underestimates only slightly, for higher Q^2 however the result by Lalakulich seems to provide a more satisfying description. For the scalar amplitude we find that the Hernandez and Lalakulich results are similar for small Q^2. Here is should be noted that these results were fitted to data in 2007, and that the current data differ to some extent for the scalar amplitude. It is noteworthy that the scalar amplitude obtained by Lalakulich drops sharply and changes sign around $Q^2 = 1.5$. This behavior is indeed supported by the data used in the original fit [26], however the same data were included with a positive sign in later publications [51, 69].

For the neutron amplitude, Lalakulich again assumes that the isoscalar current is small such that $F_n = -F_p$, the corresponding isovector amplitudes $A_p - A_n$ are shown in the right panel of Fig 3.9. Hernandez et al. assume instead that $A_n = -2/3A_p$ and $S_n = 0$, following the predictions of quark models [71]. We see that this prescription provides similar results as the MAID07 analysis especially for the isovector $A_{1/2}$, although a larger disagreement is found for the proton amplitude to begin with.

In Fig. 3.10 we show the form-factors implied by these helicity amplitudes. In obtaining the form-factors from the MAID07 helicity amplitudes we include a minus sign in the scalar amplitude consistent with Ref. [71]. We see that the different F_2 form factors agree too a large extent for both the proton and isovector types. The main differences arise in F_1, here Hernandez and MAID07 agree in sign while the Lalakulich result is opposite. This sign discrepancy has been noted and corrected for by a number of authors [39, 71]. The MAID07 form factors have a bending point at low Q^2 which follows from the quick rise in the scalar amplitude, which makes them cumbersome to parametrize in a meaningful way.

In view of these results, because the isovector amplitudes are similar with respect to those in MAID07, we choose to use the Hernandez parametrization for simplicity. In view of the comparison to data in Fig. 3.9 it is clear that a better description of the amplitudes would

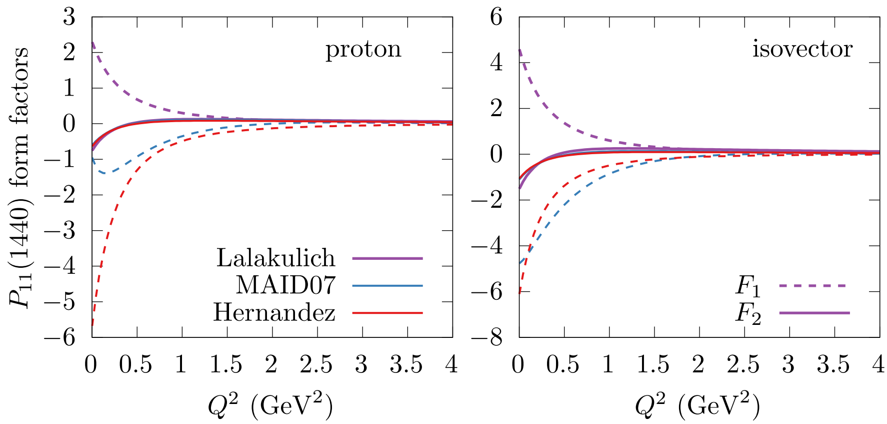

Figure 3.10: Form-factors F_1 (dashed lines) and F_2 (solid lines) from Lalakulich [26], Hernandez [71] and from the Helicity amplitudes of the MAID07 analysis. In extracting the form-factors from the MAID amplitudes the scalar amplitude is multiplied by a minus sign consistent with Hernandez [71].

however be attainable. For completeness we quote the form-factors here

$$F_1^p(Q^2) = \frac{-5.7/G_D(Q^2)}{1 + Q^2/1.4M_V^2}, \tag{3.90}$$

$$F_2^p(Q^2) = \frac{-0.64}{G_D(Q^2)}\left(1 - 2.47\ln\left(1 + \frac{Q^2}{\mathrm{GeV}^2}\right)\right) \tag{3.91}$$

where $G_D(Q^2) = \left(1 + Q^2/M_V^2\right)^{-2}$ a dipole with cut-off mass $M_V = 0.84$ GeV. The assumption that $A_n = -2/3A_p$ and $S_n = 0$ then results in following formula for the isovector form factors evaluated at $W = M_R$

$$F_1^V = \frac{F_1^p\left((M_N + M_R)^2 + 5Q^2/3\right) + 2/3F_2^p\,(M_N + M_R)\,\mu}{(M_N + M_R)^2 + Q^2}, \tag{3.92}$$

$$F_2^V = \frac{F_2^p\left(5(M_N + M_R)^2 - 3Q^2\right)\mu - 2F_1^p Q^2\,(M_N + M_R)}{3\mu\left((M_N + M_R)^2 + Q^2\right)}. \tag{3.93}$$

II. Axial form-factors

While the vector form-factors can in principle be determined from the available electron scattering data, for the axial current no extensive

Table 3.4: The axial couplings $C_A^5(0)/F_A(0)$ from PCAC for the different resonances.

$P_{33}(1232)$	$D_{13}(1535)$	$S_{11}(1520)$	$P_{11}(1440)$
1.2	2.1	0.21	0.51

dataset is available. One can make use of PCAC and the assumption of pion pole dominance to fix the values of some of the form-factors at $Q^2 = 0$ by relating them to the pion-nucleon couplings as explained in Section 3.2. The PCAC relation at $Q^2 = 0$ applied to the weak and hadronic vertices of the spin 1/2 resonance is then

$$Q_\mu \Gamma^\mu_{RQN,A}(Q^2 = 0) = F_A(0) \not{Q} \gamma^5 \tilde{\gamma}^5 \tag{3.94}$$

$$= f_\pi \Gamma_{\pi NR}(k_\pi = Q) = f_\pi \frac{\sqrt{2} f_{\pi NR}}{m_\pi} \not{Q} \gamma^5 \tilde{\gamma}^\mu. \tag{3.95}$$

which is satisfied when

$$F_A(0) = f_\pi \frac{\sqrt{2} f_{\pi NR}}{m_\pi}. \tag{3.96}$$

The divergence of the axial current is proportional to

$$u(k_R) \left(F_A(Q^2) \not{Q} - \frac{G_P}{2M} Q^2 \right) \gamma^5 \tilde{\gamma}^5 u(k_i) \tag{3.97}$$

$$= u(k_R) \left(F_A(Q^2)(M_R \pm M_N) - \frac{G_P}{2M} Q^2 \right) \gamma^5 \tilde{\gamma}^5 u(k_i) \tag{3.98}$$

where the Dirac equation was used to write $\not{Q}$ in terms of the constant masses. It is seen that the divergence does not generally disappear in the limit of zero pion mass, however if one assumes that the pseudoscalar form-factor is dominated by a pion pole then with

$$G_P = 2M_N (M_R \pm M_N) \frac{F_A(Q^2)}{Q^2 + m_\pi^2}, \tag{3.99}$$

the divergence goes to zero when $m_\pi^2 = 0$. The assumption of pion-pole dominance and PCAC thus gives a prediction for the axial current at $Q^2 = 0$ and relates the Q^2 dependence of the pseudoscalar form-factor to the axial one.

For the spin-3/2 resonances one sees that the terms proportional to C_A^3 and C_A^4 disappear when the current is contracted with Q^μ, and hence PCAC offers no prediction for these form-factors. Under the assumption that the pseudoscalar term, proportional to C_A^6, is again of the pion-pole form we find by similar reasoning as above

$$C_A^5(0) = f_\pi I_{iso} \frac{\sqrt{2} f_{\pi NR}}{m_\pi \sqrt{3}} \tag{3.100}$$

$$C_A^6(Q^2) = -M_N^2 \frac{C_A^5(Q^2)}{Q^2 + m_\pi}. \tag{3.101}$$

with $I_{iso} = 1(\sqrt{2})$ for isospin $3/2(1/2)$ resonances. The values for $F_A(0)$ and $C_A^5(0)$ for the resonances obtained in this way are given in Table 3.4. These values are the same as those given in Ref [26] and we adopt them for the non-delta resonances in this work. For the delta we use a slightly different value $C_5^A(0) = 1.12$, obtained from Ref. [30] as explained in section 3.3.6. We take the sign convention consistent with Lalakulich, such that the vector-axial interference term is positive and the ν_μ induced cross section is hence larger than the corresponding $\overline{\nu}_\mu$ cross section.

For the Q^2 dependence of the form-factors no clear guiding principle exists, and the most straightforward approach would be to fit to electroweak SPP data. The neutrino-induced single pion production cross section has been measured for different channels by numerous experiments, however most experiments utilize nuclear targets. In that case the pure SPP signal is obscured by initial and final state nuclear interactions. This fact combined with the broad neutrino fluxes and incomplete measurement of the hadrons in the final state makes it almost impossible to reconstruct the relevant kinematic variables (i.e Q^2, W, and ideally $\cos\theta^*$) in these experiments. A number of experiments have measured neutrino induced SPP on deuterium which can be used for a fit, notably the ANL [72] and BNL [73] bubble chambers. In these experiments the relevant kinematic variables can be reconstructed more accurately because of the absence of mayor nuclear effects. However, tensions between the different experimental data exists, in particular between the magnitude of the cross sections in the ANL and BNL experiments. This tension seems to be resolved by applying a renormalization of the flux in the BNL data [74, 75]. Moreover in Ref [76], it is suggested that final-state deuterium effects have not been fully taken into account in the analysis of these data.

For these reasons only the form factors of the dominant delta-resonance can generally be constrained by the experimental data. As in Ref. [14] we use the model of Adler for the delta, namely that

$$C_A^4(Q^2) = -\frac{C_A^5(Q^2)}{4}, \quad C_A^3(Q^2) = 0, \tag{3.102}$$

leaving only the Q^2 dependence of C_A^5 to be determined. In a number of works, the Q^2 dependence of C_A^5 within the framework of the model presented here (delta and crossed delta plus background) was fit to the π^+ production ANL data for $W < 1.4$ GeV. In these fits the form-factor was parametrized by a dipole and $C_A^5(0)$ was treated as a free parameter next to a single cut-off mass $M_{A,\Delta}$ for the dipole. In Ref. [14] a value of $C_5^A(0) = 0.86$ was found, significantly smaller than the PCAC value relation. With the addition of the Olsson phases in the direct delta contribution in Ref. [30], a value in closer accordance with the PCAC prediction was found. We will use this result for the delta form factors as described in Section 3.3.6.

Within the dynamic coupled-channels model of Refs. [24], the PCAC restrictions at $Q^2 = 0$ are satisfied exactly in the sense that they are directly constructed from the πN amplitudes in the same framework which reproduce pion-nucleon scattering amplitudes with high degree of precision. Moreover the interference between the resonances and background are under control as unitarity is satisfied in the coupled-channels approach. Within this model, with the axial form-factors described by dipoles, the agreement with the BNL data was found to be excellent, but to describe the ANL data the axial coupling to the delta had to be reduced by ≈ 0.8. Recently the DCC model was compared to the HNV model [77], in this comparison the axial coupling to the delta in the DCC model was reduced by a factor 0.9 compared to the PCAC value, in which case the models agree quite well for $W < 1.4$ GeV for the $p\pi^+$ and $n\pi^0$ production channels.

For the resonances other than the delta we follow Ref. [26] and use a form-factor which drops slightly faster than a dipole at high-Q^2

$$G_A(Q^2) = G_A(0)\left(1 + \frac{Q^2}{M_A^2}\right)^{-2}\left(1 + \frac{Q^2}{3M_A^2}\right)^{-1} \tag{3.103}$$

with $M_A = 1.05$ GeV and $G_A = F_A$ or $G_A = C_5^A$ for the spin 1/2 and 3/2 resonances respectively.

3.3.6 Partial unitarization in the Delta region

A necessity when constructing electroweak single-pion production amplitudes is controlling the relative phase between the different interfering components of the model. The background constructed from tree-level diagrams yields a real amplitude, and the only relative imaginary part in the currents stems from the inclusion of the phenomenological widths in the resonance propagators. Following the parametrization of Section 3.3.3 the widths in the crossed resonance poles are zero, and their contribution is real. Unitarity however demands that both the resonant and non-resonant contributions have complex phases. The constraint of unitarity together with the assumptions that only pion-nucleon states are considered and that the electromagnetic interaction is negligible can be shown to lead to Watson's theorem [78]

$$A^{\alpha}_{SPP} = |A^{\alpha}_{SPP}| e^{i(\delta^{\alpha}_{\pi N} + n\pi)}. \tag{3.104}$$

Where A^{α}_{SPP} on the LHS is a multipole amplitude for electroweak single pion production in a channel defined by quantum numbers $\alpha = l, J, I, \epsilon$ i.e. relative pion nucleon angular momentum and spin, isospin and boson polarization. $\delta^{\alpha}_{\pi N}$ then is the phase shift of elastic pion nucleon scattering in the same channel α. This relation holds below the 2 pion production threshold, or generally as long as the contribution of final-states beyond πN are negligible in the specific partial wave channel.

In building a model for electroweak pion production based on a multipole decomposition one could assume the most practical approach and add to every multipole a phase $\delta^{\alpha}(W, Q)$ such that Watson's theorem is satisfied [63].

Splitting the amplitude up in a resonant and background piece, one can see that far away from resonance the background should satisfy Watson's theorem by itself such that it is necessarily complex. In unitary isobar models [51, 66], this constraint is implemented by applying to the background the phase implied by the background in pion-nucleon scattering. Then, as every resonance only contributes to the partial wave channel with its quantum numbers, the resonance contributions are multiplied by a W-dependent phase such that Watson's theorem is satisfied. In a (coupled-channels) dynamical model on the other hand the phases are under control by explicitly treating the pion-nucleon rescattering [24, 34].

In Ref. [30] Alvarez-Ruso et al. partially unitarized the HNV model presented above in the delta region by determining phases that multiply the vector and axial currents for the direct delta excitation such that Watson's theorem is satisfied for the most important vector and axial partial waves. A derivation of Watson's theorem and the definition of the multipole amplitudes in the helicity basis is presented and discussed in Ref. [30], we just sketch the main idea here. The amplitude of the HNV model in a multipole channel where the only allowed direct resonance contribution is the delta can be schematically written as

$$A(W, Q^2) = B(W, Q^2) + R_{\Delta}(W, Q^2) e^{i\phi_{\mathrm{r}}} \tag{3.105}$$

i.e. as a real background contribution B and the resonant delta contribution for which the phase $\phi_\Gamma(W) = \tan^{-1}\frac{M_R\Gamma(W)}{s^2-M^2}$ is completely determined by the propagator. One can then multiply the delta contribution by an additional phase $\Psi(Q^2,W)$, thus fixing its relative phase with respect to the background such that the amplitude satisfies Watson's theorem

$$\Im(Ae^{-i\delta_\pi}) = -B(Q^2,W)\sin(\delta_\pi) + R(Q^2,W)\sin\left(\phi_\Gamma(W) + \Psi(Q^2,W) - \delta_\pi\right) = 0 \tag{3.106}$$

hence

$$\Psi(Q^2,W) + \phi_\Gamma(W) = \delta_\pi + \sin^{-1}\left(\frac{B(Q^2,W)}{R(Q^2,W)}\sin\delta_\pi\right). \tag{3.107}$$

This procedure is referred to as *partial* unitarization because the background is still treated as real, and the relative phases are only determined in a single partial wave and isospin channel.

Separate Olsson phases for the vector and axial current where determined taking into account the contributions of the background described in Section 3.3.4, the direct- and crossed channel delta, and the crossed D_{13}. The vector current in both cases was parametrized by the Lalakulich form-factors [26] for the delta and the ones of Ref. [23] for the D_{13}, identical or similar to the ones used in this work. A parametrization of the vector and axial phases is given in appendix D of Ref. [30] and we apply them to the delta resonance in this work. With the determination of the phases, the fit of the axial coupling of the delta was performed within Adler's model for the axial form-factors, yielding a coupling consistent with the Goldberger-Treiman relation

$$C_5^A(0) = 1.12 \pm 0.11, \quad M_A = 953.7 \pm 62.6 \text{ MeV}. \tag{3.108}$$

where M_A is the cut-off in the dipole form-factor. We will use this result for the delta coupling in this work, which is possible because the model in the region $W < 1.4$ GeV is practically identical to what is used in the fit [14, 23].

Eq. (3.107) implies that if we want to modify a part of the model which contributes to the π^+p channel, the Olsson phases $\Psi(Q^2,W)$ have to be determined again. If the relative contribution of background and delta contribution remains approximately the same, and e.g. only the phase of the delta contributions is significantly affected by a modification, the Olsson phases can be retained by simply subtracting from $\Psi(Q^2,W)$ the modification of the phases.

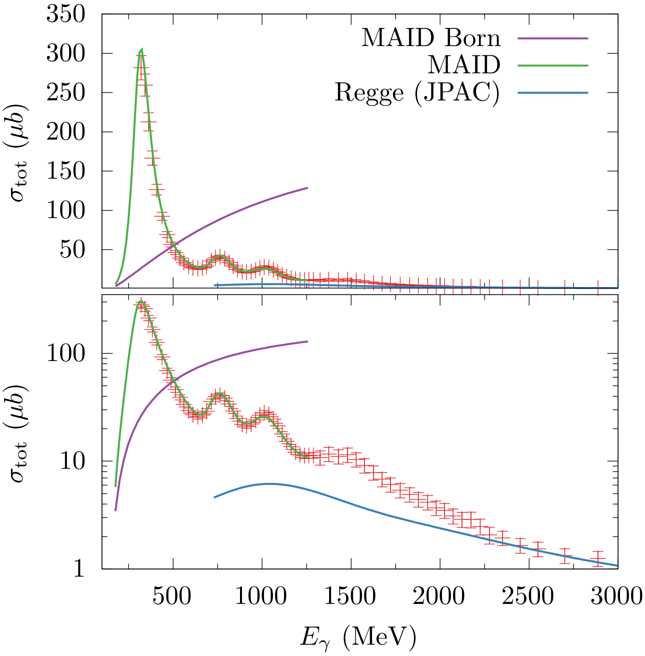

Figure 3.11: The MAID07 SPP solution [66] is shown alongside the cross section when only the born terms are considered. We compare it to the JPAC Regge model of Ref. [79] and a compilation of neutral pion photoproduction data on the proton. The bottom panel shows the same on a logarithmic scale.

3.3.7 Reggeized background

The background contribution stemming from diagrams of Section 3.3.4 are constructed from a non-linear sigma model Lagrangian truncated at tree-level [14]. In principle ChPT provides the recipe to improve the description of the background from this Lagrangian order-by-order, however direct calculation of higher-order diagrams is cumbersome and a multitude of unknown constants would need to be constrained by data. It should be understood that the introduction of form-factors at the vertices (and in the case of resonances the effective width in the propagator) effectively includes corrections beyond tree-level. The cross section due to the background however still grows rapidly at high invariant mass, even after the introduction of the form-factors. This increase of the background at high W is kept under control in phenomenological modeling by the interference with the resonant contributions, and in some cases by introducing W-dependent cut-offs. At high energies however it is not natural to describe SPP with tree-level exchanges even with effective form-factors, and Regge theory proves to be a more robust approach. As an example, in Fig 3.11 we show the cross section of the full MAID07 model [66] and the result when only the Born terms are taken into account. There is an excellent agreement with the data in the resonance region, it is seen that the background contribution grows quickly with energy and that the interference with the resonant contributions leads to large cancellations. On the other hand, the JPAC[2] Regge model [79], which is constrained for photon energies of 6 GeV and larger, should lead to a natural description of the cross section at high energy. One sees that the Regge model seems to account for practically all the strength for $E_\gamma = 2.5$ GeV and above. In this respect it is also important to note that the Regge model only gives a description of the low-$|t|$ (small $\cos\theta^*$) cross section, and that a backward peak in the cross section is not described, hence an underprediction of the cross section would be expected, but as the forward peak largely dominates the cross section at high energy it accounts for practically all of the strength.

The result in Fig. 3.11 illustrates that beyond a certain point in energy one could construct a background contribution which incorporates a Regge description rather than one build from tree-level diagrams. In this way a whole class of diagrams beyond the nucleon born terms and t-channel exchanges of the lightest mesons is taken into account. Such an approach was applied to the analysis of photon and electroproduction data by Aznauryan and collaborators in Refs. [81, 82], where it was found that indeed an isobar model with a (unitarized) background that incorporates Regge poles is able to describe the data up to $W \approx 2$ GeV without the introduction of additional W-dependent phases in the resonant contributions [51]. Similarly, background contributions based on the extrapolation of Regge amplitudes constrained by high-energy scattering data to lower W have been used successfully in conjunction with resonant contributions in the so-called Regge-plus-resonance approach for e.g. Kaon electroproduction [83, 84].

In Ref. [31] a Regge model constructed from the background contributions of Section 3.3.4 was presented. By smoothly transitioning from the tree-level ChPT background to a Regge model, the unphysical behavior of the background at high-W is mitigated and one is able to extend the

2. The result of the JPAC model correspond to an independent implementation within our framework, we have checked that the same total cross section is obtained with the results available via the JPAC website [80].

description of electroweak SPP to higher invariant mass in a natural way. We present and discuss this model in the following.

I. Regge Poles

We briefly describe the assumptions underlying Regge theory, and give the necessary expressions needed to appreciate the scattering amplitude resulting from the contribution of a Regge pole. For some excellent reviews and more in-depth discussions we refer the reader to Refs. [85–88]. Per illustration we consider the scattering, $1 + 2 \to 3 + 4$ of equal mass particles of spin-0. The extension to non-zero spins is in principle straightforward, but comes with complications which do not add to the aim of the present discussion, see e.g. Refs. [85, 86, 89].

We introduce the partial wave expansion of the scattering amplitude in the s-channel, which for spinless particles can be written as

$$\langle 3, 4|\mathcal{M}|1, 2\rangle \equiv A(s, t) = \sum_{l=0}^{\infty} A_l(s) P_l(z_s), \tag{3.109}$$

where $z_s(s, t) \equiv \cos\theta_s$ the s-channel CMS scattering angle. The partial wave amplitudes $A_l(s)$ are defined by the projection

$$A_l(s) = \frac{1}{2}\int_{-1}^{1} dz_s P_l(z_s) A(s, t(z_s, s)), \tag{3.110}$$

for positive integer values $0 \leq l$. A partial wave amplitude in this expansion represents the exchange of angular momenta l in the s-channel, and yields a natural description of the small and intermediate s-region. For low s the higher order partial waves are kinematically suppressed, and a truncation of the sum is feasible, thus the cross section is largely understood by the exchange of resonances with small angular momenta. For values beyond the resonance region ($\sqrt{s} \gtrsim 2.5$ GeV) a truncation of the partial wave sum becomes unfeasible, and an inclusion of higher order partial waves becomes necessary. Such an approach quickly becomes intractable, and it is natural to reconsider the relevant degrees of freedom. For describing forward scattering at high invariant mass, one sees that $-t > 0$ is small compared to s, and that the probed values of t are closer to the masses of particle exchanges in the t-channel than s is to the typical mass of particles exchanged in the s-channel. For hadron reactions at high s, it is observed that relatively large scattering cross sections are often dominated by a large forward peak in $\cos\theta_s$ (small $-t$), while processes with relatively small cross sections lack this peak.

One finds that the interactions which allow for the exchange of particles in the t-channel exhibit such a forward peak, while the interactions for which no t-channel exchanges are allowed lack it [87].

As such one may just as well consider the t-channel partial wave expansion of the amplitude

$$A(s,t) = \sum_{l=0}^{\infty} A_l(t) P_l(z_t) \tag{3.111}$$

where now $z_t(s,t) \equiv \cos\theta_t$, the t-channel CMS scattering angle. In the same way as before the partial-wave amplitudes are

$$A_l(t) = \frac{1}{2}\int_{-1}^{1} dz_t P_l(z_t) A(t, s(z_t,t)). \tag{3.112}$$

This series is a natural description in the physical region of the t-channel, i.e. for positive $t > (2m)^2$ and $s < 0$ with $|z_t| \leq 1$. It is however of no direct use in the physical s-channel where z_t grows indefinitely. Indeed z_t becomes proportional to s, in particular in the considered equal mass case one has

$$z_t = 1 + \frac{2s}{t - 4m^2} \tag{3.113}$$

such that $P_l(z_t) \sim s^l$ for large s and the partial wave series cannot be truncated.

In order to make use of the t-channel degrees of freedom in the s-channel region we assume that we can analytically continue the partial wave amplitude to complex values of l to yield a function $A(l,t)$ such that $A(l,t) = A_l(t)$ for positive integer values of l on the real axis. In this case we can recast the series of Eq. (3.111) as a contour integral by using the Sommerfeld-Watson theorem

$$A(s,t) = \sum_{l=0}^{\infty} A_l(t) P_l(z_t) = \frac{-1}{2i}\oint_C A(l,t)\frac{P_l(-z_t)}{\sin(l\pi)}\, dl, \tag{3.114}$$

where the contour C shown in Fig. 3.12 contains all the poles generated by the factor $1/\sin(l\pi)$ in the right-hand l-plane.

Clearly the function $A(l,t)$ seems to be completely arbitrary, as one may interpolate between the values $A_l(t)$ in an infinite number of ways. We will discuss the details of the analytic continuation shortly, but to illustrate the Regge pole model we will for now assume what is called 'maximal analyticity of the second kind', namely that $A(l,t)$ has only isolated singularities in l [90]. This is the fundamental assumption of

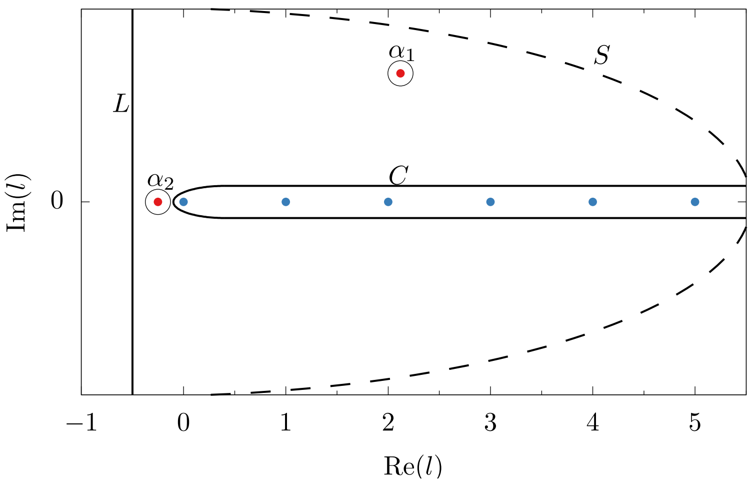

Figure 3.12: Integration contours in the complex angular momentum plane, the original contour C which includes all the poles on the real axis is deformed to a semi-circle at infinity S and a line integral L at $\mathcal{R}(l) = -1/2$. In doing so we pick up the residue of the isolated poles at positions α, α_1 shows a typical pole in the upper-half complex plane characteristic of Regge's original work while α_2 shows a pole on the real axis at small negative α which one would encounter in the physical s-channel in the scattering of spin-zero particles.

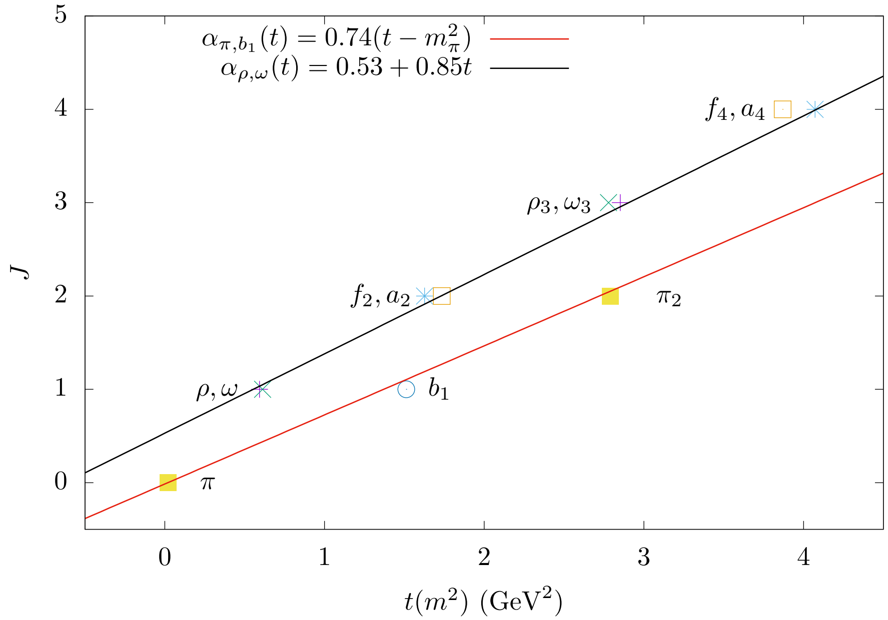

Figure 3.13: Meson spin as function of their squared mass. Mesons with the same quantum numbers are found to lie on linear Regge trajectories. The vector mesons of ω, ρ, f_2, a_2 lie on a degenerate linear trajectory. The pion and b_1 share a different linear trajectory.

Regge theory, Regge showed that this condition holds for certain non-relativistic potential scattering models [91]. This should not hold in a general particle physics context however, as we expect to encounter singularities other than simple poles, but in certain conditions the amplitude can be expected to be dominated by the contributions of these isolated Regge poles.

We can now use Cauchy's theorem to deform the contour C to the contour $L+S$ which consists of a line-integral and a semi-circle in the right-half plane as shown in Fig. 3.12. When doing this, as we assumed no other singularities are present, we may pass only isolated singularities in the complex plane. The position of the singularities will depend on t and is written $\alpha(t)$, while the residue of the singularity is denoted as $\beta(t)$, e.g. for a simple pole we have

$$A(l,t) \rightarrow \frac{\beta(t)}{l-\alpha(t)} \text{ for } l \rightarrow \alpha(t). \tag{3.115}$$

When deforming the contour over n poles we pick up their residues in the amplitude

$$\begin{aligned} A(s,t) = \frac{-1}{2i} \oint_{L+S} A(l,t) \frac{P_l(-z_t)}{\sin l\pi}\, dl \\ - \sum_{i=0}^{n} \pi \frac{\beta_i(t) P_{\alpha_i(t)}(-z_t)}{\sin(\pi\alpha_i(t))}. \end{aligned} \tag{3.116}$$

The s-dependence of the amplitude is fully described by the Legendre functions, which for large s behave as $P_l(z_t) \sim z_t^l \sim s^l$. As such one sees that the rightmost pole in l will dominate the amplitude at large values of s. The integral over the semi-circle in the right hand plane gives a zero contribution as the amplitude is presumed to disappear for large l. The remaining integral over the line L is referred to as the background integral which, with the contour shown in Fig. 3.12, lies at $\mathcal{R}(l) = -1/2$. This is the value of l such that for large z_t the Legendre function still behaves as $P_{1/2}(z_t) \sim z_t^{-1/2}$, hence for sufficiently large $s \sim z_t$ the contribution of the background integral can be neglected with respect to the poles for which it is implied that $\mathcal{R}(\alpha(t)) > -1/2$. With the Regge pole dominance of the amplitude, we extrapolate to the physical s-channel, where then for large s and small $-t > 0$ the amplitude is predicted to behave quite generally as

$$A(s,t) \sim -\frac{\beta(t)}{\sin \pi\alpha(t)} \left(\frac{s}{s_0}\right)^{\alpha(t)}, \tag{3.117}$$

with $\alpha(t)$ the position of the rightmost pole in the l-plane, for which unitarity demands that $\mathcal{R}(\alpha(t)) \leq 1$.

The interpretation of the Regge pole amplitude is as follows, one sees that the factor $1/\sin\pi\alpha(t)$ will generate poles when $l = \alpha(t)$ takes an integer value. Because the amplitude $A(l,t)$ should match the partial wave amplitudes $A_l(t)$ in the physical t-channel at integer values of l, the amplitude should reduce to the one for an exchange of a particle with definite spin l and mass for which $\alpha(m^2) = l$. The trajectory $\alpha(t)$ should hence describe the spin-mass relation of the particles that are exchanged in the t-channel. In Fig. 3.13 we show a so called Chew-Frautschi plot depicting the spin-mass relation of a number of mesons with the same quantum numbers [90]. The Regge-trajectories $\alpha(t)$ can hence be experimentally determined, and are found to be linear in the physical t-channel. By extrapolation of this amplitude to large s and small $-t > 0$, the exchange of a Regge-pole trajectory hence takes into account the t-channel exchange of a whole class of particles with the same quantum numbers and increasing angular momentum.

This Regge-pole dominance hinges on a number of non-trivial assumptions such that one could have some doubts about the applicability to describe scattering in particle physics. Before providing some context for the made assumptions, it is important to remember that there is a large amount of experimental evidence for the Regge behaviour of high energy cross sections [86, 87], and because of this one might simply consider modelling amplitudes in terms of Regge poles inherently useful.

The main assumption that we made was of maximal analyticity of the second kind. This is however not crucial to the Regge-pole dominance of forward scattering cross sections and many of the assumptions underlying this maximal analyticity may be softened somewhat without hampering the applicability of the result. One of the critical assumptions is that it is possible to analytically continue the partial wave amplitude in the right-hand l plane down to a certain value of $\mathcal{R}(l) \leq 1$ in such a way that the integral over the semi-circle at infinity can be neglected. One sees that a definition such as the one in Eq. (3.112) is not suitable for this purpose because the Legendre functions diverge for large l off the real axis in the complex plane. There is a way in which the amplitude can be analytically continued such that it dissapears fast enough at large $|l|$ in the righthand plane, and moreover it can be shown that in this case the continuation is uniquely defined by the values of $A_l(t)$ for integer l.

The uniqueness is guaranteed by Carlson's theorem which, loosely stated for our purposes, asserts that an analytic function which is zero for a set $n \in \{N, N+1, N+2, ...\}$ of non-negative integers on the real axis is either zero everywhere or diverges too fast at large $|l|$. Thus, given an amplitude $A(l,t)$ which matches the partial waves amplitudes $A_l(t)$ at all l and disappears for large l in the righthand plane, any alternative amplitude which would satisfy these constraints can generally be written as

$$A^*(l,t) = A(l,t) + F(l,t), \tag{3.118}$$

with a function $F(l,t)$ that is zero for integer values of l. By Carlson's theorem then, either $A^*(l,t)$ does not disappear fast enough at the semi-circle or $F(l,t)$ is identically zero everywhere, such that $A(l,t)$ is the unique amplitude with the required large l behaviour defined by the $A_l(t)$.

This amplitude is provided by the Froissart-Gribov projection, we will only state the final results in order to introduce and discuss the concept of signature in Regge theory, for details we refer the reader to Refs. [85, 86]. The construction requires the assumption of analyticity and unitarity of the amplitude such that the amplitude $A(s,t)$ can be represented by a fixed-t dispersion relation. If one then substitutes this form of the amplitude in the definition of the t-channel partial wave amplitude of Eq. (3.112), we can exchange the order of integration and obtain for positive integer values of l

$$A_l(t) = \frac{1}{\pi}\int_{z_t(s_0,t)}^{\infty} dz_t \left[D_s(s,t) + (-1)^l D_u(s,t)\right] Q_l(z_t), \tag{3.119}$$

where $D_{u/s}$ are the so called u and s-channel discontinuities [85], s_0 is the s-channel threshold, and $Q_l(z)$ are the Legendre functions of the second kind. We will tacitly assume that the dispersion relation is valid and that this integral converges for all l with $\mathcal{R}(l) \geq -1/2$. In general, if $N(t)$ subtractions are made one will encounter singularities other than Regge poles in the complex plane for $\mathcal{R}(l) \leq N(t) \leq 1$, where the upper bound for $N(t)$ in the s-channel physical region follows from the Froissart bound [92]. This is not problematic however, these singularities will also yield contributions to the amplitude, which in the many cases (for small $-t$) can be considered to be less important than the leading Regge-pole [85].

The whole l dependence is now provided by the $Q_l(z)$ and the phase $(-1)^l$ which permit analytic continuation. The $Q_l(z)$ are well behaved for large $|l|$ and provide convergent behaviour over the semi-circle at infinity as long as $\mathcal{R}(l) > -1/2$ as we require [3]. The factor $(-1)^l$ however would be analytically continued to $e^{-i\pi l}$ which diverges for large $\mathcal{I}(l)$. This issue is circumvented by considering separately the even and odd partial waves such that we get two amplitudes

$$A^{\pm}(l,t) = \frac{1}{\pi}\int_{z_t(s,t)}^{\infty} \left[D_s(s,t) \pm D_u(s,t)\right] Q_l(z_t)\, dz_t \tag{3.120}$$

where $A^+(l,t) = A(l,t)$ for even l and $A^-(l,t) = A(l,t)$ for odd l. These amplitudes are referred to as having positive and negative signature $\tau = (-1)^l$, and both separately behave as required for the manipulation of the Sommerfeld-Watson transform. The Legendre functions $P_l(z_t)$ that enter in Eq. (3.114) are symmetric with respect to z for even l and antisymmetric for odd l such that the physical amplitude is recovered from the ones with definite signature as

$$\begin{aligned} A(s,t) = \frac{1}{2}\big[&A^+(s,z_t(s,t)) + A^+(s,-z_t(s,t)) \\ &+A^-(s,z_t(s,t)) - A^-(s,-z_t(s,t))\big]\,. \end{aligned} \tag{3.121}$$

Thus if we find a Regge pole with positive or negative signature in one the separate amplitudes its contribution to the physical amplitude is

$$A(s,t) = -\frac{\pi}{2}\frac{\beta(t)}{\sin\pi\alpha(t)}\left(P_\alpha(-z_t) \pm P_\alpha(z_t)\right). \tag{3.122}$$

For large real values of z_t we have $P_\alpha(-z_t) \sim e^{-i\pi\alpha}P_\alpha(z_t)$, such that in the physical s channel for large values of s we finally obtain

$$A(s,t) = -\beta(t)\frac{\tau + e^{-i\pi\alpha(t)}}{\sin\pi\alpha(t)}\left(\frac{s}{s_0}\right)^{\alpha(t)} \tag{3.123}$$

as the contribution of a Regge pole with signature $\tau = (-1)^l$, which differs from Eq. (3.117) only through the appearance of the signature factor $\tau + e^{-i\pi\alpha}$.

3. The background integral is placed along the line $\mathcal{R}(l) = -1/2$ because this provides the most convergent behaviour of the Legendre functions for large z_t, $P_{-1/2}(z_t) \sim z_t^{-1/2}$, such that the physics it contains can be neglected with respect to the pole contributions for large s. As such one might think that the Regge-pole model is only applicable when $\mathcal{R}(\alpha(t)) \geq -1/2$. While this is indeed the region in which the Regge pole dominance works the best, this is not a fundamental lower bound. It is possible, using a technique originally presented by Mandelstam [93], to push the background integral to arbitrarily small values of $\mathcal{R}(l)$. The price one has to pay is tha additional singularities will show up which at some point (larger $-t > 0$) will become more important than the Regge poles [85, 87].

With the concept of signature in hand it is instructive to revisit the Chew-Frautschi plot in Fig. 3.13. One sees that the signature factor cancels the pole corresponding to a meson with the wrong signature, e.g. the π and b_1 have positive and negative signature respectively and hence lie on independent trajectories. It is experimentally found however that $\alpha_\pi(t) \approx \alpha_{b_1}(t)$, and the same is found for e.g. the ρ and f_2. The property that Regge trajectories overlap, is known as weak exchange degeneracy, while the property that the residues $\beta(t)$ of different trajectories are the same is called strong exchange degeneracy. When combining Regge pole contributions of trajectories with opposite signature which exhibit both weak and strong exchange degeneracy one gets

$$A(s,t) = \beta(t) \frac{\phi(t)}{\sin \pi\alpha(t)} \left(\frac{s}{s_0}\right)^{\alpha(t)}, \tag{3.124}$$

with $\phi(t) = 1$ or $\phi(t) = e^{-i\pi\alpha(t)}$ when the trajectories are subtracted or added respectively.

II. Reggeized Born-term model

As we have seen, Regge theory provides the s-dependence of scattering amplitudes at high invariant masses in terms of Regge trajectories which in this case can be interpreted as the t-channel exchange of a whole family of mesons with increasing angular momentum. Given an allowed exchange, the trajectory $\alpha(t)$ is known, but Regge theory does not directly describe the t(i.e. $\cos\theta^*$) or Q^2 dependence of the residue. For this a model is needed. The most general strategy is to identify the dominant allowed Regge trajectories, i.e. the allowed t-channel exchanges, and parametrize the t-dependence in a general way using a number of free parameters which can be fit to data. The success of such an approach clearly depends on the availability of detailed scattering data, which is problematic, in particular for modeling neutrino-induced interactions.

To overcome this, a procedure of 'Reggeized' tree-level diagrams for t-channel meson exchanges can be used instead. The idea of the Reggeized t-channel exchange model is to use the same parameters as in a tree-level diagram that are applicable at low energies in the parametrization of the Regge amplitudes. This is motivated by the fact that in the region of applicability, i.e. for small negative t, one is not far removed from the physical t-channel pole. A heuristic argument for this approach can be found by considering the behavior of a Regge amplitude when one approaches the physical t-channel pole. For a pion exchange, omitting a possible Q^2 dependence and phase, one may write

$$A_{\pi,\text{Regge}}(s,t) = \beta(t)\alpha'_\pi \Gamma\left[-\alpha_\pi(t)\right]\left(\alpha'_\pi s\right)^{\alpha_\pi(t)} \tag{3.125}$$

where the pion trajectory is $\alpha_\pi(t) = \alpha'_\pi\left(t - m_\pi^2\right)$ with typically $\alpha'_\pi \approx 0.7\ \text{GeV}^2$. The function $\beta(t)$ represents the unknown, but presumably smooth and slowly varying, t-dependence of the amplitude. The gamma function includes the pole generating factor $1/\sin\pi\alpha$ as

$$\Gamma\left[-\alpha(t)\right] = -\pi\left(\sin\left[\pi\alpha_\pi(t)\right]\Gamma\left[\alpha_\pi(t)+1\right]\right)^{-1}, \tag{3.126}$$

such that when one extrapolates $t \to m_\pi^2$ the amplitude approaches

$$\frac{\beta(t)\pi\alpha'}{\sin\left[\pi\alpha_\pi(t)\right]} \to \frac{\beta(t)}{t-m_\pi^2}, \tag{3.127}$$

i.e. the t-channel pion pole. When considering small positive values of $-t$ it thus is reasonable to assume that $\beta(t)$ can be described by the tree-level pion exchange, which is referred to as the 'reggeizing' of t-channel exchanges. Such arguments are of course not formal, and the reggeizing procedure should be considered at best a reasonable guess for the parametrization of the amplitude. Nonetheless this procedure leads to remarkably good results, especially when one considers that practically no parameters are fit to high-energy data. In particular this technique has been successfully used to describe photoproduction of pions [79, 94], and has been extended to finite Q^2 to model electroproduction [95–100].

The procedure is then as follows: given an allowed t-channel meson exchange in the low-energy sector one replaces the tree-level propagator $\frac{1}{t-m^2}$ by a Regge propagator $\mathcal{P}$ which is parametrized as

$$\mathcal{P}(t,s) = \alpha'\phi(t)\Gamma\left[-\alpha(t)\right]\left(\alpha' s\right)^{\alpha(t)} \tag{3.128}$$

where $\alpha(t)$ is the Regge trajectory which is taken to be a linear function $\alpha(t) = \alpha' t + \alpha_0$. The appearance of the slope of the trajectory multiplying s in the propagator is rather arbitrary, one merely needs to set a scale for s, but we follow Ref. [99] and use this convention. An additional t-dependent phase is added through the factor $\phi(t)$. Comparing this expression with Eq. (3.124), one sees that this corresponds to the addition of degenerate poles of opposite signature. Indeed, for the SPP reactions under study here, there is no reason to explicitly exclude a degenerate trajectory of opposite signature. The assumption is hence made that for these trajectories there is also strong exchange degeneracy, such that the residue associated with the exchange of degenerate trajectories may be described by the lightest meson that lies on it.

We will use the model developed in Ref. [99], based on reggeizing of the background amplitudes presented in Section 3.3.4. This approach has the benefit of being consistent with the background, at least in certain kinematic limits. The drawback is that the background model does not include explicitly any t-channel meson exchanges beyond the pion. Therefore this Regge model is not complete, as not all allowed or even dominant Regge trajectories are included in the model.

III. Vector current

For the vector-current we use the approach of Guidal, Laget and Vanderhaeghen (GLV) which was originally applied to charged pion photoproduction in Ref. [94]. For charged pion photoproduction the pion and rho are the dominant trajectories, at small $-t$ the data exhibits a sharp peak which cannot be reproduced with the pure reggeized pion and rho exchange however. To reproduce this forward peak in the approach of GLV one reggeizes instead an extended set of low-energy Born diagrams in addition to the pure pion exchange. The justification for doing so given in Ref. [94] comes from the fact that the pure t-channel pion exchange is not gauge invariant by itself, but requires the addition of the nucleon s and u-channel exchanges in pseudoscalar coupling. In our case, as we use pseudovector coupling, additionally the vector part of the contact-term has to be included as described in section 3.3.4. If we adopt an electric coupling, in which the photon only couples to protons, the gauge-invariant vector-current background contributions are

$$\mathcal{O}^{\mu}_{BG} = \mathcal{O}^{\mu}_{PF} + \mathcal{O}^{\mu}_{CT,V} + \mathcal{O}^{\mu}_{NP,V} + \mathcal{O}^{\mu}_{CNP,V}, \tag{3.129}$$

where the operators correspond to those in Eqs. (3.69), (3.66), (3.60), and (3.61) respectively. The assumption of electric coupling implies that one should set $F_1^n = F_2^{p,n} = 0$. With this, the minimal amount of terms are kept which need to be added to the pion-in-flight term to have a gauge-invariant operator.

In order to reggeize the pure pion exchange one would replace the tree-level pion propagator by the Regge propagator, however no pion propagator is present in the CT, NP, and CNP terms. To reggeize the whole operator of Eq. (3.129), we multiply by a factor $(t - m^2)\mathcal{P}(s,t)$ instead. This procedure has the required effect of replacing the classical by the Regge propagator in the PF term, while giving the other diagrams the suitable high-energy behavior. The pion Regge trajectory can be extracted from the pion spectrum and we use $\alpha_{\pi,a_1}(t) = \alpha'_{\pi,a_1}\left(t - m_\pi^2\right)$ with $\alpha'_{\pi,a_1} = 0.74$ GeV^{-2} as shown in Fig. 3.13. For photoproduction of pions off on-shell nucleons, by construction, this model is the same as the original GLV model presented in Ref. [94], although we do not include the far smaller contribution of the ρ exchange in the vector current as it is not present in the low-energy background to begin with.

When this model is extended to electroproduction $Q^2 > 0$, in principle only the Q^2 dependence of the $F_1(Q^2)$ form factor should be added, then to retain CVC it should be added to the PF and CT terms as discussed before. It is found however that in this case the transverse cross section is not well described for high s. In Ref. [96] Kaskulov and Mosel proposed an s-dependent form factor $F_1(Q^2, s)$ which aims to take into account that the possibly highly off-shell intermediate nucleon oscillates into higher mass resonances explicitly. A more practical parametrization of such an effective form factor was introduced by Vrancx and Ryckebusch in Ref. [98],

$$F_1^p(Q^2, s) = \left(1 + \frac{Q^2}{(\Lambda^*(s))^2}\right)^2 \tag{3.130}$$

with

$$\Lambda^*(s) = \Lambda_0 + (\Lambda_\infty - \Lambda_0)\left(1 - \frac{M^2}{s}\right) \tag{3.131}$$

which reduces to the on-shell dipole form factor with cutoff $\Lambda_0 = M_V = 0.84$ GeV when $s = M_N^2$. For the crossed nucleon pole, the functional form of Eq. (3.130) stays the same with substitution of s by u and

$$\Lambda^*(u) = \Lambda_0 + (\Lambda_\infty - \Lambda_0)\left(1 - \frac{M^2}{2M^2 - u}\right) \tag{3.132}$$

The (only) free parameter Λ_∞ was fitted to experimental data in Ref. [98], and we use the same value $\Lambda_\infty = 2.194$ GeV. Other effects and corrections to this model where discussed in Ref. [98], for simplicity however we do not include any of them here, we find that the description of the photo and electroproduction data with this minimal model is already quite satisfactory [99].

The main ingredients that are lacking in this model for the vector current are additional Regge trajectories, notably the ω and ρ meson trajectories, which are not explicitly included in the low-energy background. The lack of the ω exchange means that the Regge model does not provide any background for neutral-current neutral pion production, which would be dominated by ω exchange. This is also the case of course for the low-energy model to begin with, the only contribution to the background for electromagnetic π^0 production comes from the nucleon and cross nucleon poles, while rest does not contribute.

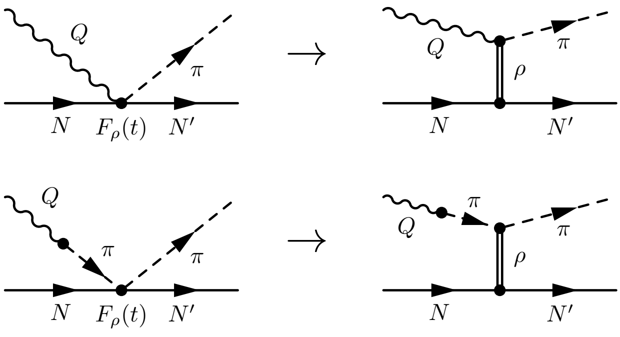

Figure 3.14: The axial contact term (top) and pion-pole (bottom) are interpreted as effective ρ-meson exchanges, figure from [31].

IV. Axial current

For the axial current one faces the problem that there are no explicit t-channel exchanges in the axial current in the model presented here. To Reggeize the axial current, the axial part of the contact term, and pion-pole are identified as effective ρ-meson exchanges as shown schematically in Fig. 3.14, we motivate this in the following.

The axial current for an explicit ρ exchange corresponds to the operator [101]

$$\mathcal{O}^\mu_\rho = \frac{g_{\rho NN} g_{W\rho\pi}}{t - m_\rho^2} F_A(Q^2) \{ g^{\mu\alpha} + \frac{Q^\mu Q^\alpha}{Q^2 + m_\pi^2} \} \left(\gamma_\alpha + i \frac{k_\rho}{2M_N} \sigma_{\alpha\nu} K^\nu_\rho \right), \tag{3.133}$$

where the second term between braces corresponds to a pion-pole term, and a transition form factor is added for which $F_A(Q^2 = 0) = 1$. PCAC [101] implies that

$$g_{\rho NN} g_{W\rho\pi} = m_\rho^2 / f_\pi, \tag{3.134}$$

such that for $Q^2 = 0$ and $k_\rho = 0$ the non-pole and pion-pole terms give the same amplitude as the axial part of the contact term and the pion-pole terms of Eqs. (3.67) and (3.68) respectively[4]. To construct a Regge model from the low-energy background, we thus set $k_\rho = 0$ and reggeize the axial part of the contact term and the pion-pole term using

4. For on-shell Dirac spinors energy-momentum conservation implies that $\overline{u}(k_f) \not{Q} u(k_i) = \overline{u}(k_f) \left(2M_N + \not{K}_\pi \right) u(k_i) = \overline{u}(k_f) \frac{(\not{Q} + \not{K}_\pi)}{2} u(k_i)$.

a ρ trajectory in the same way as before. For the spin-1 ρ the Regge propagator may be written as

$$\mathcal{P}_\rho(s,t) = -\alpha'_\rho \phi_\rho(t) \Gamma\left[1-\alpha_\rho(t)\right] \left(\alpha'_\rho s\right)^{\alpha_\rho(t)-1}, \tag{3.135}$$

where $\alpha_\rho(t) = 0.53 + \alpha'_\rho t$ with $\alpha'_\rho = 0.85$ GeV^{-2} as shown in Fig. 3.13. One sees that $\alpha_\rho(t) \approx 1$ when $t = m_\rho^2$ such that again the Regge propagator resembles a simple t-channel pole close to the ρ mass.

At this point, no additional low-energy diagrams in the axial current resembling an exchange in the t-channel are available, hence the Regge model based on the background is in principle complete. From pion-nucleon scattering data one knows that the ρ-exchange is dominant in the charge-exchange process [102–104] which by PCAC is related to the charged-current neutral pion production channels. For the elastic scattering, related to the charged-current charged pion production channels, the pomeron trajectory is instead dominant [104]. The pomeron has $\alpha_0 \approx 1$ and corresponds to the exchange of no quantum numbers except for angular momentum in the t-channel.

In Ref. [31] it was proposed to reggeize also the axial contribution of the nucleon and crossed nucleon pole in conjunction with the CT, A and PP terms. Unlike in the vector case, where the argument is made that the (electric) nucleon Born-terms are required in conjunction with the pion-in-flight term to satisfy CVC, in the axial current the CT and PP terms together already satisfy PCAC, as do the axial parts of the nucleon terms by themselves. Hence there is no good reason to include these terms beyond the analogy with the vector-current, and based on the idea that the Regge model should resemble the full low-energy background when $-t$ is small. We then have for the reggeized axial current

$$\mathcal{O}^\mu_{A,Regge} = \left[\mathcal{O}^\mu_{CT,A} + \mathcal{O}^\mu_{PP} + \mathcal{O}^\mu_{NP,A} + \mathcal{O}^\mu_{CNP,A}\right]\left(t - m_\rho^2\right)\mathcal{P}_\rho(s,t) \tag{3.136}$$

where the operators are defined in Eqs. (3.67), (3.68), (3.60), (3.61). In addition, the axial transition form factor $F_{A,\rho}$ is added to the CT and PF terms for which we use

$$F_{A\rho\pi}(Q^2) = \left(1 + Q^2/\Lambda_\rho^2\right)^{-2}, \tag{3.137}$$

with $\Lambda_\rho = m_{a_1} = 1260$ MeV inspired by a meson-dominance framework [105]. As the CT and PF terms already satisfy PCAC by themselves there is no reason to apply this form factor in the nucleon terms.

In analogy with the vector case, we may define an off-shell axial form-factor of the same form as before

$$G_A\left(Q^2, s\,[u]\right) = g_A\left(1+\frac{Q^2}{(\Lambda_A^*(s\,[u]))^2}\right)^{-2}, \qquad (3.138)$$

with again

$$\Lambda_A^*(s) = M_A + \left(\Lambda_\infty^A - M_A\right)\left(1-\frac{M^2}{s}\right), \qquad (3.139)$$

and

$$\Lambda_A^*(u) = M_A + \left(\Lambda_\infty^A - M_A\right)\left(1-\frac{M^2}{2M^2-u}\right), \qquad (3.140)$$

for the direct and crossed-channel respectively. The parameter Λ_∞^A is again the only free parameter introduced in the axial sector which was fitted to data in Ref. [99]. It was found that a large value of $\Lambda_\infty^A = 7.2$ GeV was required to reproduce the magnitude of the (rather limited) total cross section data for $W > 2$ GeV. This seems to indicate indeed that other trajectories are required in the axial current, which with the choice of reggeizing also the axial nucleon and cross nucleon poles are compensated in some way.

V. Hybrid model

So far the choice of the phase $\phi(t)$ in the reggeized pion and rho exchanges has not been discussed. In view of building a model valid at energies beyond the resonance region, the phases that are added in the propagator in the vector and axial sector can only affect the vector-axial interference terms in the cross section. It is known that at high-energies and for forward scattered leptons, i.e. where the Regge model is most reliable, the vector-axial contribution to the inclusive cross section becomes small, and hence the relative phase between the vector and axial contribution has only a small effect on the total cross section. In view of extrapolating the reggeized background to lower values of s, and combining it with resonant contributions, the phases do indeed represent a more important degree of freedom which may be informed by data. For simplicity however we take $\phi(t) = 1$ for both the vector and axial sectors, in this case the relative phases are completely determined by the low-energy model.

We combine the high-energy model with the low-energy one in a 'hybrid' model by a smooth W-dependent transition as

$$\mathcal{O}^\mu_{hybrid,BG} = \cos^2\left[\phi(W)\right]\mathcal{O}^\mu_{LEM} + \sin^2\left[\phi(W)\right]\mathcal{O}^\mu_{Regge} \qquad (3.141)$$

with

$$\phi(W) = \frac{\pi}{2}\left(1 - \frac{1}{1+\exp\left[\frac{W-W_0}{L}\right]}\right). \tag{3.142}$$

The width and the center of the transition are $L = 200$ MeV and $W_0 = 1600$ MeV respectively. This means that below $W = 1400$ MeV the model is practically identical to the low-energy one, while above $W = 1800$ MeV the background is completely determined by the Regge model. We note that we consider the crossed resonance contributions as part of the LEM background in this work. Indeed they lack the resonant phases of the direct-channel resonances, and moreover compared to he direct channel exchanges lack the suppression of the amplitude from the propagator at high s. This makes the crossed-channel resonances more background-like than resonant, and indeed in many models they are not even explicitly included.

Finally, it is clear that building a Regge model from the available low-energy background has some advantages, the main one being that only a limited number of free parameters is introduced ($\Lambda_\infty^{(A,V)}$ in this case), because most parameters are already determined by the low-energy model or can be estimated in a reasonable way. The low-energy Lagrangian proves too restrictive however, and additional exchanges should be included. Most importantly the ω is necessary to describe neutral-current neutral pion production, and the pomeron should be included in the axial section to better describe charged-current charged pion production. It would be beneficial to do away with the restraint of sticking to the content of the low-energy Lagrangian and instead build a more complete Regge model, either fully or only partly based on reggeized born terms, which includes the constraints of high-energy strong and electromagnetic scattering data in a more satisfying way. Work in this direction is in progress, a comparison of a more complete reggeized Born-term model to electromagnetic, pion-nucleon scattering, and the available neutrino scattering data was presented in Ref. [100] with promising results.

3.4 Results for electromagnetic SPP and the vector current

In electron induced single-pion production it is customary to write the differential cross section as

$$\frac{d\sigma}{dE'\,d\Omega'\,d\Omega_\pi^*} = \Gamma_{em}\frac{d\sigma}{d\Omega_\pi^*}, \tag{3.143}$$

where

$$\Gamma_{em} = \frac{\alpha}{2\pi^2}\frac{E'}{E}\frac{1}{Q^2}\frac{1}{1-\epsilon}k_\gamma. \tag{3.144}$$

here $k_\gamma = \frac{W^2-M_N^2}{2M_N}$ is the lab-frame energy of an on-shell photon that would yield the same invariant mass W, and the longitudinal polarization is

$$\epsilon = \left[1 + 2\frac{|\mathbf{q}|^2}{Q^2}\tan^2\theta_l/2\right]^{-1}, \tag{3.145}$$

where $\mathbf{q}$ and the electron scattering angle θ_l are taken in the lab frame. The differential cross section for SPP induced by a (virtual) photon is

$$\frac{d\sigma}{d\Omega^*_\pi} = \frac{d\sigma_T}{d\cos\theta^*_\pi} + \epsilon\frac{d\sigma_L}{d\cos\theta^*_\pi} + \sqrt{\epsilon\,(1+\epsilon)}\frac{d\sigma_{LT}}{d\cos\theta^*_\pi}\cos\phi^* \tag{3.146}$$

$$+\,\epsilon\frac{d\sigma_{TT}}{d\cos\theta^*_\pi}\cos 2\phi^* + h\sqrt{\epsilon\,(1+\epsilon)}\frac{d\sigma'_{LT}}{d\cos\theta^*_\pi}\sin\phi^*. \tag{3.147}$$

The different terms in this expression can be identified in terms of the elements of the hadron tensor as

$$\frac{d\sigma_T}{d\cos\theta^*_\pi} = \sigma_0\frac{H^{11}+H^{22}}{2}, \tag{3.148}$$

$$\begin{aligned}\frac{d\sigma_L}{d\cos\theta^*_\pi} &= \sigma_0\frac{1}{Q^2}\left[q^{*2}H^{00} - 2\omega^* q^* H^{03} + \omega^{*2}H^{33}\right]\\ &= \sigma_0\frac{Q^2}{\omega^{*2}}H^{33} = \frac{Q^2}{q^{*2}}H^{00},\end{aligned} \tag{3.149}$$

$$\frac{d\sigma_{LT}}{d\cos\theta^*_\pi} = \sigma_0\sqrt{\frac{Q^2}{\omega^*}}\mathrm{Re}H^{13}, \tag{3.150}$$

$$\frac{d\sigma_{TT}}{d\cos\theta^*_\pi} = \sigma_0\frac{H^{11}-H^{22}}{2}, \tag{3.151}$$

$$\frac{d\sigma_{LT'}}{d\cos\theta^*_\pi} = \sigma_0\sqrt{\frac{Q^2}{\omega^*}}\mathrm{Im}H^{13}, \tag{3.152}$$

with $\sigma_0 = \frac{\alpha M_N |k^*_\pi|}{4\pi W k_\gamma}$, and where in Eq. (3.149) the conservation of vector current has been used explicitly. The hadron tensor elements are computed for $\phi^*_\pi = 0$ and the partial cross sections $d\sigma_i/\,d\cos\theta^*_\pi$ thus do not depend on the pion azimuth angle. For real photons ($\epsilon = 0$) only σ_T contributes, and the term proportional to $\sin\phi^*$ is only accessible in polarized electron scattering. The angle integrated cross section only gets contributions from the σ_T and σ_L terms and is given by

$$\frac{d\sigma}{dE\,d\Omega'} = \Gamma_{em}\int d\Omega^*_\pi\frac{d\sigma}{d\Omega^*_\pi} = \Gamma_{em}\left(\sigma_T + \epsilon\sigma_L\right), \tag{3.153}$$

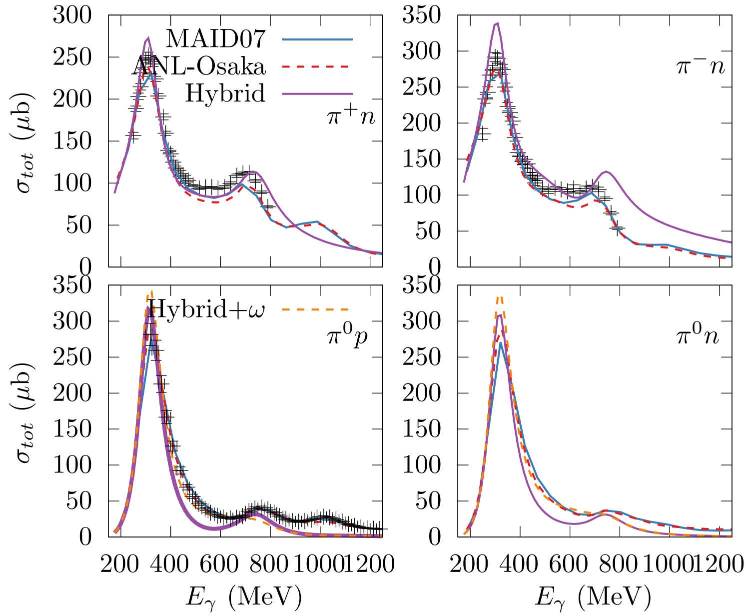

Figure 3.15: Total cross sections for single pion photoproduction

with

$$\sigma_i = 2\pi \int d\cos\theta_\pi^* \; \sigma_i \left(Q^2, W, \cos\theta_\pi^*\right) \tag{3.154}$$

used as shorthand for the angle-integrated partial cross sections.

3.4.1 Photoproduction of pions

We first compute the cross section for SPP by real photons. While the vector current does not contribute to the weak process at $Q^2 = 0$ and is suppressed at low values of Q^2, the photoproduction cross section gives insight in the W dependence of the cross section and the contribution of different ingredients. We compare the photoproduction cross section obtained within the hybrid model with experimental data in Fig. 3.15. In the comparison we also include the results of the ANL-Osaka DCC model [34] and the MAID07 analysis [66] obtained from the published multipole amplitudes as described in appendix C.

We find a good agreement in the threshold region, dominated by the delta and born terms, and for the charged pion production channels a satisfying agreement is found up to the second resonance region in particular for the positive pion production channel. Although heavier resonances are lacking the behavior of the high-E_γ cross section is quite well described for this channel, certainly much better than were we to use the low-energy model.

In the neutral pion production channels the lack of background contributions in the high-energy model becomes obvious. As discussed previously the high-energy Regge model currently do not include the ω-exchange such that the cross section goes to zero beyond the resonance region. It is also seen that the cross section is underestimated between the first and second resonance regions. Purely for illustrative reasons, we include the t-channel ω-exchange in the low-energy background of the hybrid model. We use the operator

$$\mathcal{O}^\mu_\omega = \frac{g_{\omega\pi\gamma} g_{\omega NN}}{t - m_\omega^2} \epsilon^{\nu\mu\rho\alpha} Q_\nu K_{t,\rho} g_{\alpha\beta} \gamma^\beta \tag{3.155}$$

where $K_t = Q - K_\pi$ the t-channel four momentum, with standard parameters $g_{\omega\pi\gamma} = \frac{0.314}{m_\pi}$ and $g_{\omega NN} = 15$ taken from Ref. [94]. The result in Fig. 3.15 show that indeed the ω exchange gives the correct magnitude in this region needed to fill the dip, however we will neglect its contribution further on.

3.4.2 Electroproduction of pions

Instead of comparing the model directly to data we will compare the results to the MAID07 [66] and ANL-Osaka Dynamic Coupled-Channels (DCC) [34] analyses. The MAID07 and DCC results are computed from the multipole amplitudes available at Ref. [106] and Ref. [107] respectively as detailed in appendix C. As such we compare directly the inclusive longitudinal and transverse responses of the hybrid model to what is obtained in state-of-the-art analyses of electron scattering data. This gives a more direct view of the Q^2 and W dependence of the integrated cross sections than by comparing to angular distributions.

In Fig. 3.16, we compare the W dependence of σ_T and σ_L for several values of Q^2 for proton targets. We see that the Q^2 dependence of the delta is well described, as well as the resonances around $W = 1.5$ GeV. In the region between both peaks the MAID07 and DCC model give different results as Q^2 increases, and the hybrid model is seen to undershoot both models. We tend to value the result of the ANL-Osaka DCC model more here, on the one hand because it is more recent and hence uses a more comprehensive dataset. Additionally the DCC model is more complete, it is able to describe consistently hadronic and electromagnetic

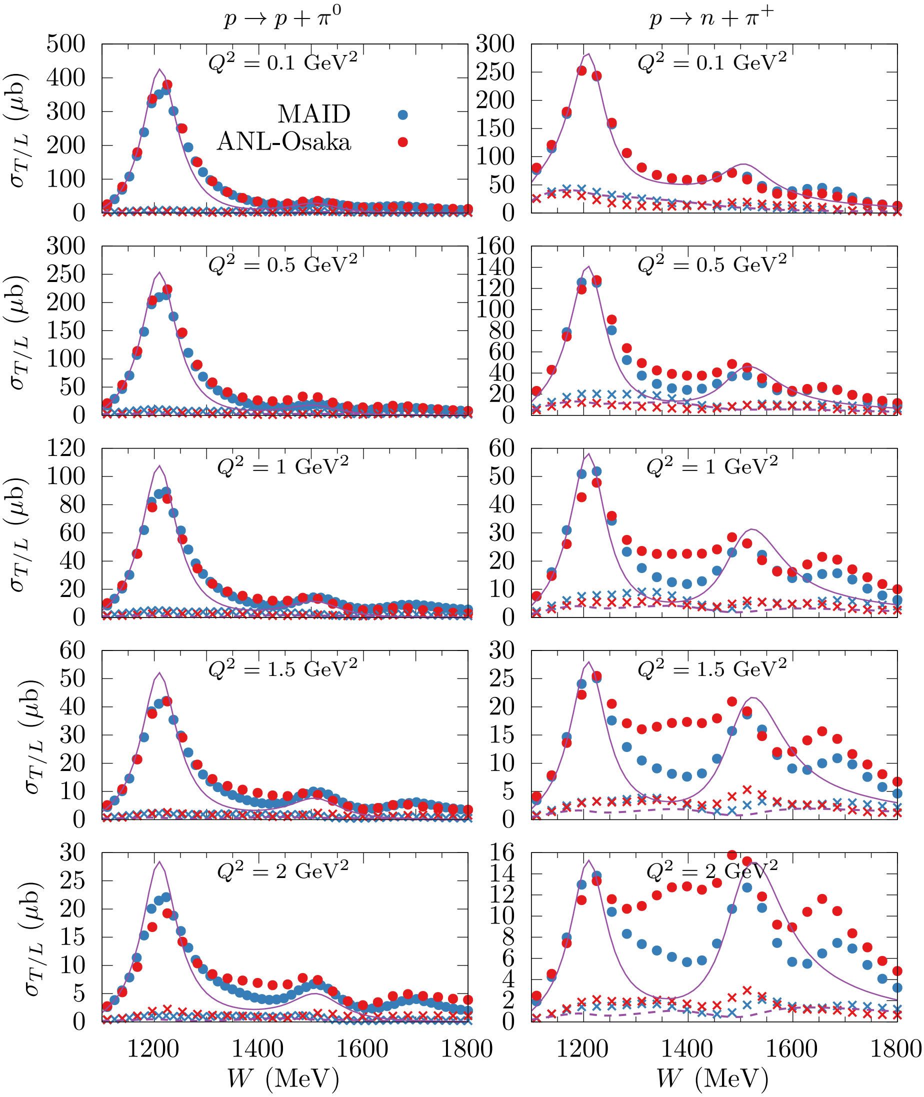

Figure 3.16: Angle integrated cross sections for electroproduction of pions on the proton as functions of W for different values of Q^2. The transverse(longitudinal) cross sections obtained with the hybrid model are shown by solid(dashed) lines. For the ANL-Osaka and MAID07 models the transverse(longitudinal) cross sections are depicted by circles(crosses). The left(right) column shows neutral(charged) pion production

interactions, and is able to describe the inclusive electron scattering cross section while MAID07 takes only SPP into account.

In Fig. 3.17, the same comparison is made but in this case for neutron targets. The hybrid model is found to agree with the MAID07 result in the dip, but then when the Regge background takes over tends to give similar results to the DCC.

The Q^2 dependence of the cross section is again described reasonably well, but it becomes more obvious that the height of the delta peak becomes larger in the hybrid than in the other models at high Q^2. This is however partly due to the interpolation in W which is performed in the multipole amplitudes, such that the delta peak is not fully resolved. To show this in more detail, we compare the Q^2 dependence at a number of fixed values of the invariant mass, corresponding to the regions of the delta peak ($W = 1232$ MeV), the second peak at $W = 1520$ MeV, and the dip between both ($W = 1350$ MeV). The results for the delta are shown in Fig. 3.18, and excellent agreement is found for all interaction channels, including for the small longitudinal response for the charged channels.

The results for $W = 1350$ MeV and $W = 1520$ MeV are shown in Figs. 3.19 and 3.20 respectively. In the dip we clearly find a severe underestimation of the neutral pion production channels at low-Q^2 which is again consistent with the lack of e.g. the ω exchange as noted in the description of photoproduction.

For $W = 1520$ the DCC and MAID07 models give similar results for the charged pion production channels, in agreement with the hybrid model when Q^2 is larger than about 0.5 GeV^2. For neutral pion production it is interesting to note that the DCC model shows a distinctive bump for $Q^2 < 1$ GeV. The hybrid model gives a similar shape and magnitude as the MAID07 model.

3.4.3 The Charge-changing vector current

The previous comparisons of cross sections were all done for electromagnetic interactions, for which both the isovector and isoscalar amplitudes contribute. The charged-current neutrino induced interaction however only has contributions from the isovector current. As explained previously, a separation of isoscalar and isovector contributions requires measurements on both proton and neutron targets, and is not necessarily unambiguous if only a limited number of neutron target data exist. Given that there exist differences between the models in the description

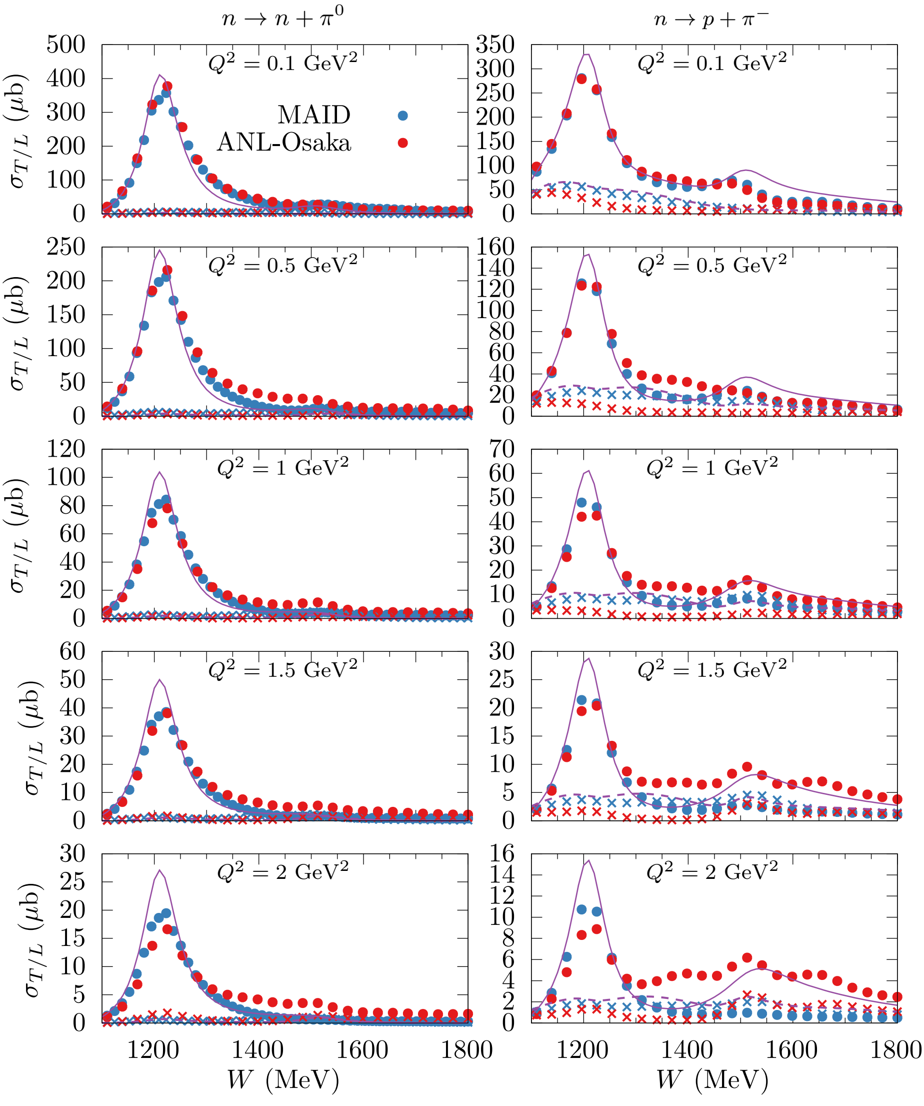

Figure 3.17: Angle integrated cross sections for electroproduction of pions on the neutron as a function of W for different values of Q^2. The lines are the same as in Fig. 3.16. The left(right) column shows neutral(charged) pion production.

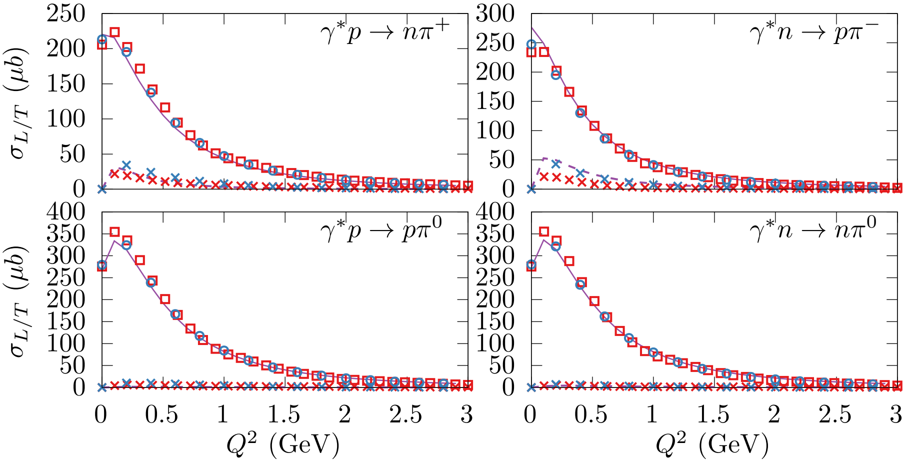

Figure 3.18: Q^2 dependence of the angle integrated cross sections for electroproduction of pions Q^2 at a fixed invariant mass $W = 1232$ MeV. The transverse cross section in the MAID07 and DCC models are represented by blue circles and red squares respectively, the longitudinal cross section is shown by crosses.

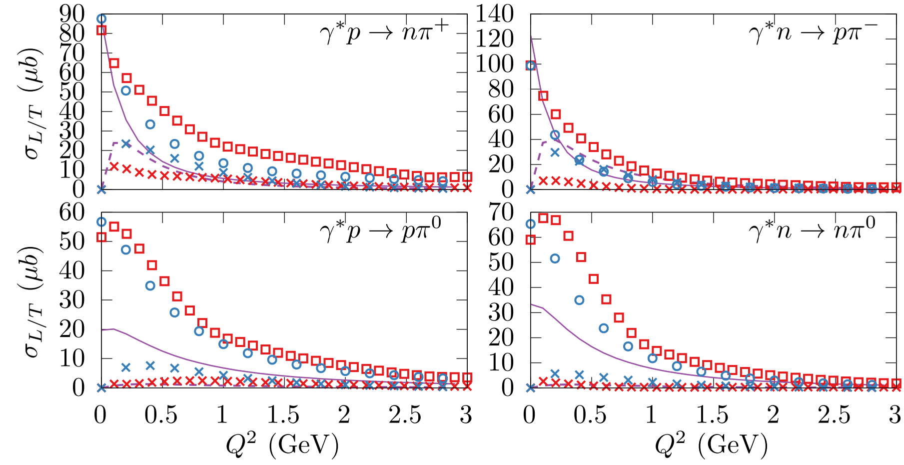

Figure 3.19: Q^2 dependence of the angle integrated cross sections for electroproduction of pions Q^2 at a fixed invariant mass $W = 1350$ MeV. Legend as in Fig. 3.18.

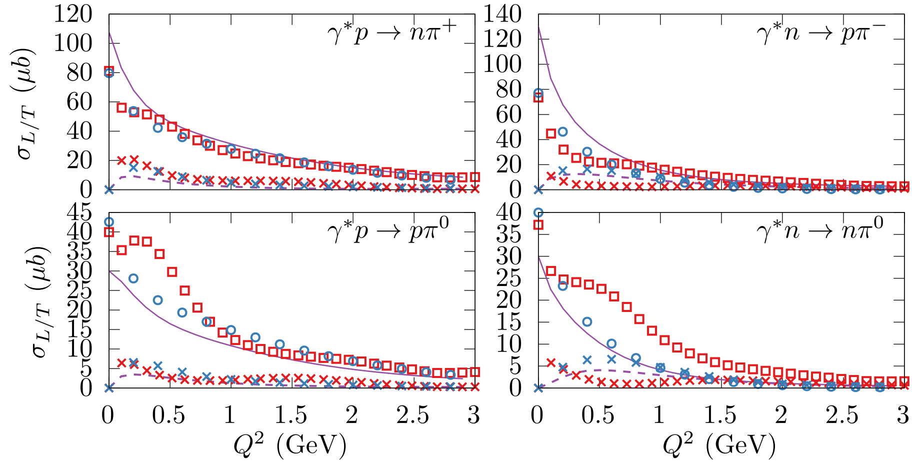

Figure 3.20: Q^2 dependence of the angle integrated cross sections for electroproduction of pions Q^2 at a fixed invariant mass $W = 1520$ MeV. Legend as in Fig. 3.18.

of the electromagnetic processes as shown in the previous section it is of importance to ask how well the vector current is determined by the analysis of electron scattering data.

To see how well the isovector current is constrained by the state-of-the art models for electromagnetic interactions and to see how the hybrid model fares, in Fig. 3.21 we show again the results of the hybrid model, MAID07, and the DCC model, this time for the vector current contribution to the cross section for the different charged-current neutrino-induced SPP processes. We obtain the isovector contribution in MAID07 and the DCC from the partial-wave amplitudes as described in appendix C.0.1.

The absence of the photon propagator $(Q^2)^{-2}$ means that the Q^2 dependence of the resulting cross section will be different in the neutrino case than for electrons. We show the Q^2 dependence at fixed values of W in Fig. 3.21. In order to retain all kinematic factors we show simply the contribution of the vector-vector current to the double differential cross section at a fixed incoming energy of 3 GeV. We find that the discrepancies between the different models found in the electromagnetic case disappear to a large extent for the weak charge-changing isovector current. Only for charged pion production the hybrid model clearly undershoots the MAID07 and DCC analyses when W grows. It should

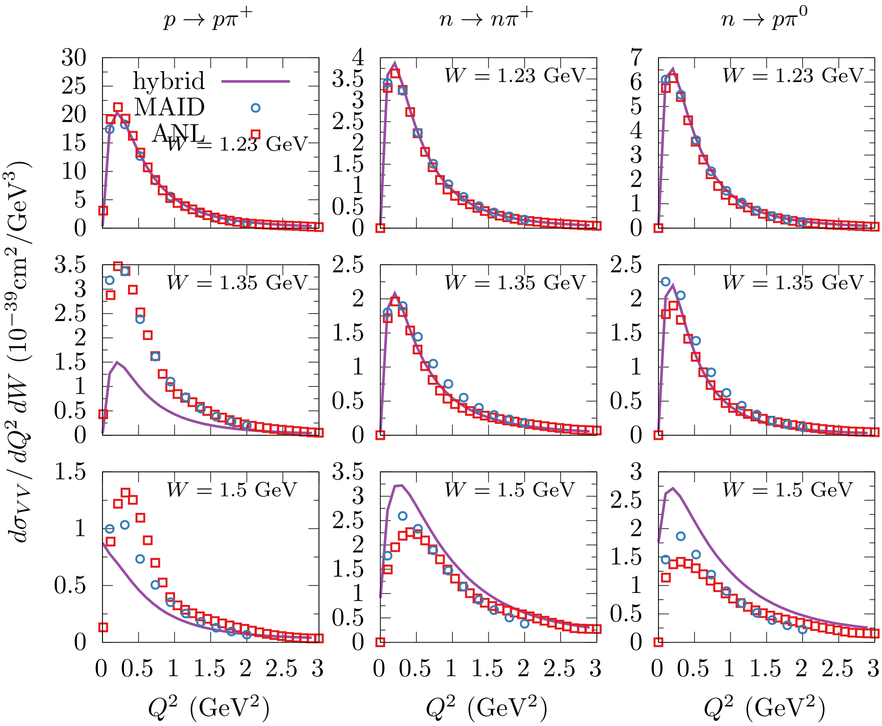

Figure 3.21: Q^2 dependence of the angle integrated weak cross section for the charge-changing vector current. Results obtained at different fixed values of invariant mass.

be noted that this channel is dominated by the delta peak and that the cross section drops quickly beyond the delta region, the cross section at $W = 1.5$ GeV is less than 5 percent of the one around the delta.

We may again compare the models in an energy-independent way by comparing longitudinal and transverse contributions, but we will first define responses which contain most of the kinematic dependence on Q^2 and W. Following Eq. (3.7), the inclusive cross section is

$$\frac{\mathrm{d}^2\sigma}{\mathrm{d}W\mathrm{d}Q^2} = \frac{G_F^2 \cos\theta_c}{2\,(2\pi)^4}\frac{k_\pi^*}{E^2}\int d\Omega_\pi^* L_{\mu\nu}H^{\mu\nu}. \tag{3.156}$$

From the Rosenbluth separation in Eqs. (2.51-2.55), and because the vector current yields a symmetric hadron tensor we then have

$$\frac{\mathrm{d}^2\sigma}{\mathrm{d}W\mathrm{d}Q^2} = \frac{G_F^2 \cos\theta_c}{2\,(2\pi)^3}\frac{k_\pi^*}{E^2}\times \left[\left(L_{00} - 2\frac{\omega^*}{q^*}L_{03} + \left(\frac{\omega^*}{q^*}\right)^2 L_{33}\right)H_0^{00} + \frac{L_{11}+L_{22}}{2}\left(H_0^{11}+H_0^{22}\right)\right], \tag{3.157}$$

after integration over the pion angles. If the outgoing lepton mass can be neglected the lepton current is also conserved such that

$$\frac{\mathrm{d}^2\sigma}{\mathrm{d}W\mathrm{d}Q^2} = \frac{G_F^2 \cos\theta_c}{2\,(2\pi)^3}\frac{k_\pi^*}{E^2}\left[\left(\frac{Q^2}{q^{*2}}\right)^2 L_{00}H_0^{00} + \frac{L_{11}+L_{22}}{2}\left(H_0^{11}+H_0^{22}\right)\right]. \tag{3.158}$$

The relevant lepton tensor elements in the zero mass limit can be written [77],

$$L^{00} = q^{*2}\frac{\epsilon}{1-\epsilon}, \qquad \frac{L^{11}+L^{22}}{2} = \frac{Q^2}{2}\frac{1}{1-\epsilon}. \tag{3.159}$$

With this we have

$$\frac{\mathrm{d}^2\sigma}{\mathrm{d}W\mathrm{d}Q^2} = \frac{G_F^2 \cos\theta_c}{2E^2\,(2\pi)^3}\frac{k_W}{1-\epsilon}\left(R_T + \epsilon R_L\ \right), \tag{3.160}$$

where $k_W = k_\gamma = (W^2 - M_N^2)/(2M_N)$. This expression is similar as the one in Eqs. (3.143-3.144) for electron scattering but with a factor Q^2 absorbed in the responses

$$R_T = \frac{k_\pi^*}{k_W}Q^2\frac{\left(H_0^{11}+H_0^{22}\right)}{2}, \qquad \frac{k_\pi^*}{k_W}Q^2\frac{Q^2}{q^{*2}}H_0^{00}. \tag{3.161}$$

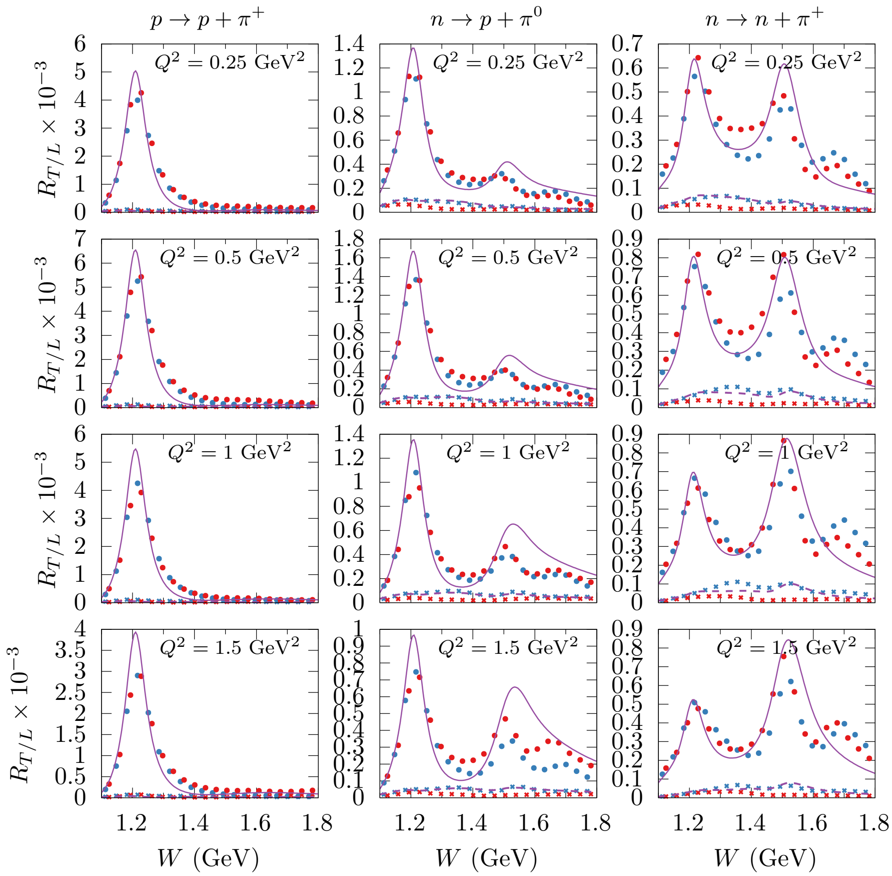

Figure 3.22: W-dependence of the functions R_L(crosses) and R_T(circles) of Eqs. (3.160) and (3.161) obtained in the MAID07, ANL-Osaka DCC, and hybrid model. Legend as in Fig. 3.16. Only the isovector current is included.

We will present the functions $R_{L/T}$ instead of the partial cross sections relevant to electroproduction as the former include more of the kinematic dependence of the electroweak cross section.

The results are shown in Fig. 3.22, with these definitions one sees that the responses vary only weakly with Q^2, it is mainly the relative magnitude of resonances which changes instead of the overall cross section. The hybrid model performs better for the charged-current than for the electromagnetic case. It is interesting to see that where in the electromagnetic case the DCC and MAID07 models differed mainly for large Q^2, here the opposite tends to happen for π^+ production off the neutron. In general we find that the models tend to agree to a larger extent for all channels for the weak charge-changing vector current than what seemed to be the case in the electromagnetic charged-pion production channels. It is also clear that the second resonance region is expected to play a rather significant role in neutrino interactions, due to the slow drop with Q^2 of the $S_{11}(1520)$ combined with the absence of the factor $(Q^2)^{-2}$. We will revisit the vector-current contribution in flux-folded signals when comparing to neutrino data in Section 3.6.

3.5 Results for pion-nucleon scattering

The axial current at $Q^2 = 0$ for the hybrid model was constructed by using PCAC and pion-pole dominance both for the background and different resonant contributions. For the resonances in particular the axial form-factors that contribute to $Q_\mu J^\mu$ at $Q^2 = 0$ were set consistently with the pion-resonance couplings for on-shell pions, while the background in the non-linear sigma-omega model exhibits PCAC by construction [14]. We point out again that extrapolation to the on-shell pion couplings by the Goldberger-Treiman relation is an approximation in itself, and that the axial couplings for $Q^2 = 0$ should be expected to deviate from these values [53]. Nonetheless, by using the on-shell couplings, the model can be applied to compute the elastic pion-nucleon scattering cross sections. Following Ref. [104] we may write the cross section for $\pi + N \to \pi' + N$ as

$$\frac{d\sigma_{\pi N}}{dt} = \frac{\pi}{q_{CMS}^2}\frac{1}{8\pi W}\left(|T_{++}|^2 + |T_{+-}|^2\right). \tag{3.162}$$

The pion nucleon scattering T-matrices are then seen to be obtained from the currents in the hybrid model as [57]

$$T_{+\pm} = \left(\frac{M}{2f_\pi}\right)^2 \langle p_N, s_N = \pm | Q_\mu J^\mu_{(A)} | p_i, s_i = +\rangle \tag{3.163}$$

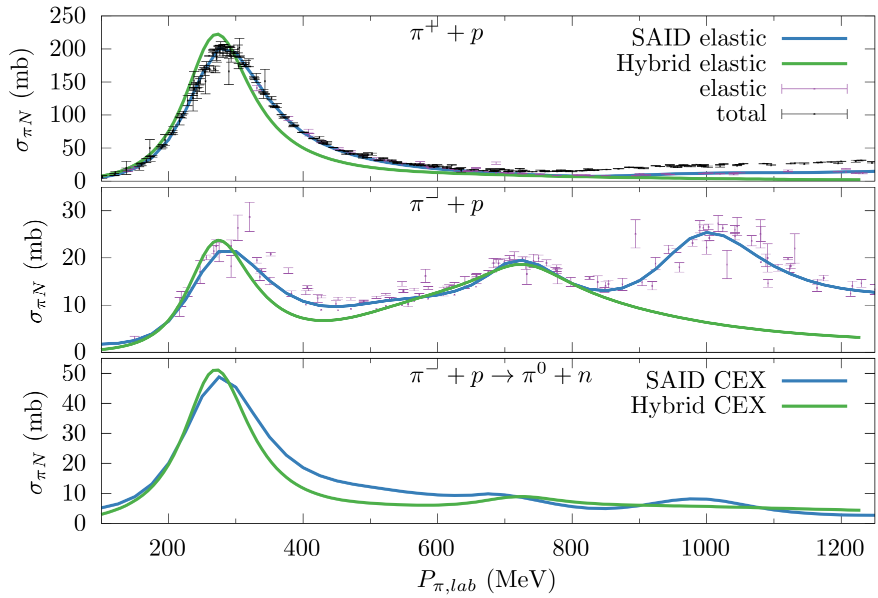

Figure 3.23: Elastic and charge exchange pion nucleon scattering cross sections obtained from the axial current in the hybrid model.

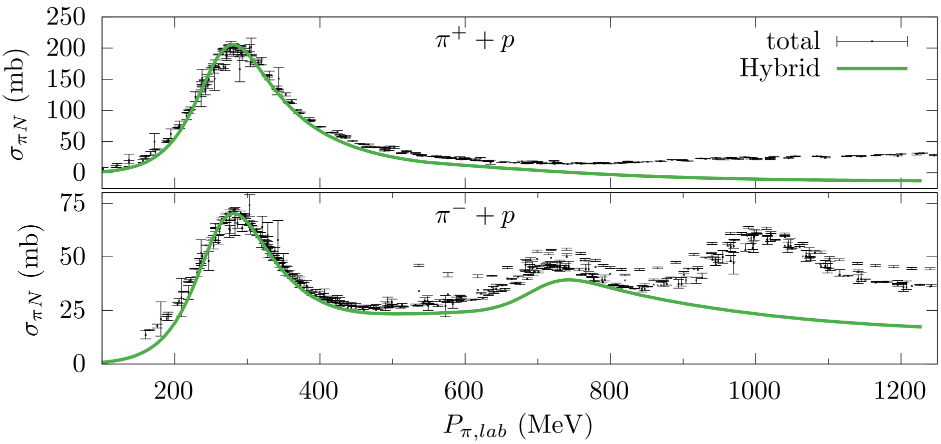

Figure 3.24: Total positive and negative pion nucleon scattering cross sections obtained from the axial current in the hybrid model using the optical theorem.

where the subscript A referring to the axial part of the current can in principle be dropped as for the vector current $Q_\mu J^\mu_V = 0$.

In this section, we compare the cross section computed from the hybrid model to elastic and charge-exchange pion-nucleon scattering data and the results of the SAID analysis [108, 109]. This provides a further consistency check of the different components of the model, as the PCAC relation should apply for the *total* amplitude while we apply it to the different components, in the ideal case this construction should yield the pion-nucleon scattering amplitudes when the different components of the model are combined.

In Fig. 3.23, the results for the different angle-integrated elastic and charge-exchange (CEX) cross sections are shown. We find a rather good description of the cross section, although some trends are clearly visible. For each of the channels the delta peak is seemingly shifted slightly towards lower energies while the region beyond the delta is slightly underpredicted. This is due to the background contributions which interfere constructively with the delta for low P_π and as such give a correct description of the threshold region but then when the sign of the imaginary part of the delta changes result in a decrease of the cross section. On the other hand, when we include only the resonance contributions and no crossed-resonances or background, the delta peak is better reproduced, but the threshold region is underpredicted.

Both the elastic channels are underpredicted at high values of W, most obviously for π^- scattering. This is of course partly due to the lack of higher mass resonances. The magnitude of the charge-exchange cross section on the other hand is quite well reproduced for high P_π, in particular at high energies the Regge background from ρ-exchange is seen to give a good reproduction of the magnitude.

In Fig. 3.24, we compute the total pion-nucleon scattering cross section from the model by making use of the optical theorem

$$\sigma_{tot} = \frac{1}{2q_{CMS}W}\Im\left(T_{++} + T_{+-}\right)|_{t=0}. \tag{3.164}$$

This comparison is sensitive to the imaginary part of the amplitude, and not to the absolute value. In the hybrid model the only imaginary contributions arise from the propagators in the direct resonance contributions, and in the case of the delta also from the Olsson phase which is multiplied with the axial current [30]. With the addition of the Olsson phase the total cross section can be reproduced in the delta region and for the π^- scattering the agreement is reasonable up to and including the second resonance region. For the positive pion channel one sees that in the high-energy region the imaginary part of the amplitude becomes negative however.

Finally, in Fig. 3.25, we show the comparison with the data and the SAID results as function of the CMS pion angle for different values of W in the delta region. As with the comparison of the integrated cross sections the agreement is satisfactory for all channels.

3.6 Results for neutrino induced SPP

For electromagnetic SPP a vast amount of qualitative data exists, which allows models to be constrained and extract resonance couplings in a reliable manner [51]. For the electroweak process however, no such extensive dataset exists, and the available data is of limited quality. We will compare the results of the hybrid model with the ANL [72], BNL [73] and BEBC [110] bubble chamber data. Apart from limited statistics, a complicating factor in these data is that the incoming neutrino energy is not fixed, but is instead given by a broad distribution. While in semi-inclusive neutrino-nucleon (or deuteron) measurements, it is in principle possible to extract total cross sections as function of the energy, and it is possible to reconstruct relevant kinematic variables, the uncertainty on the normalization and shape of the flux can severely complicate this

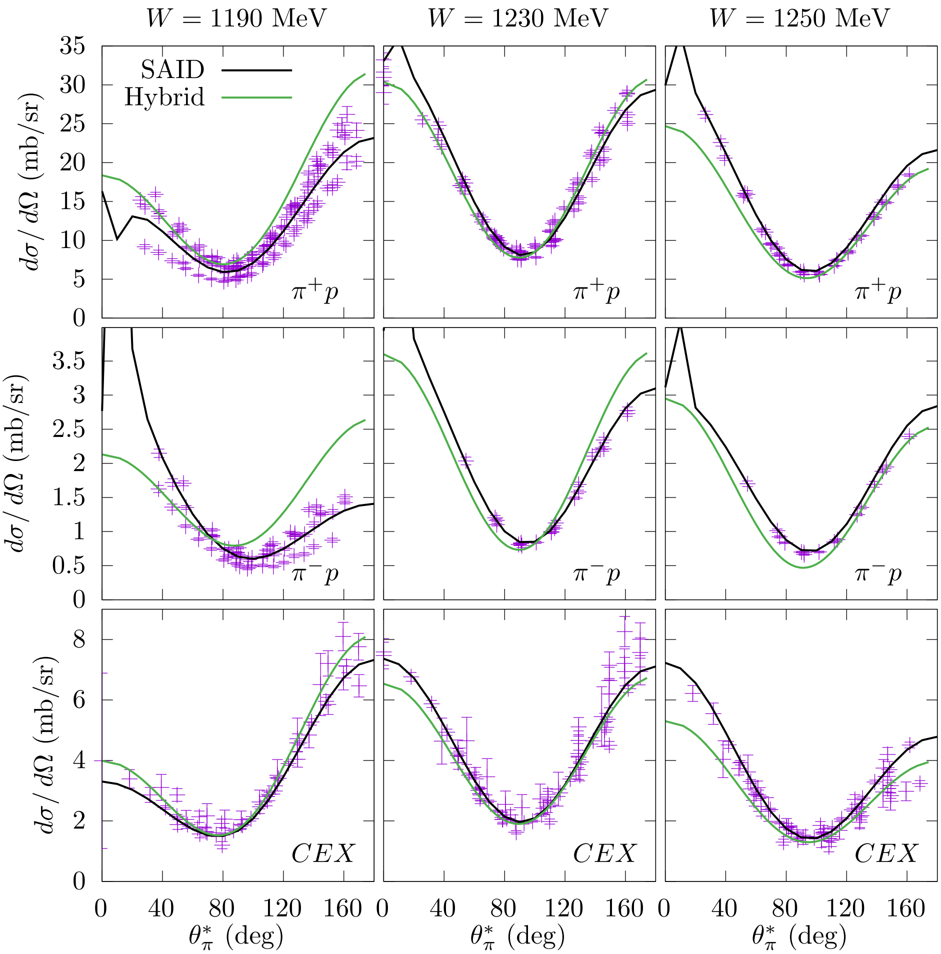

Figure 3.25: Cross section in terms of center-of-mass scattering angle for elastic and charge-exchange pion nucleon scattering obtained from the axial current in the hybrid model near to the delta region.

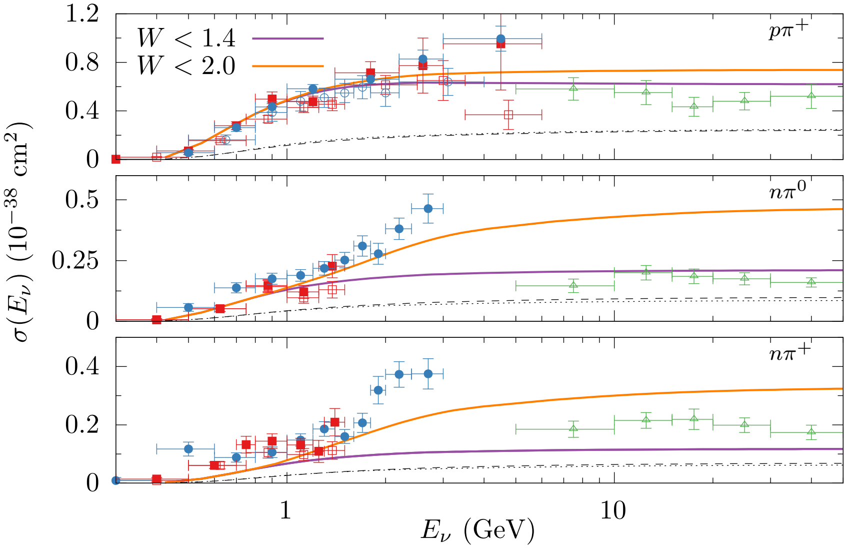

Figure 3.26: Total cross sections for the three neutrino-induced SPP channels. We show the reanalyzed ANL (red squared) and BNL (blue circles) along with the BEBC (green triangles) data. The filled data correspond to a cut $W < 2$ GeV while the empty ones are for $W < 1.4$ GeV. The thin black lines show the vector-vector contribution in the hybrid (dashed) and ANL-Osaka DCC (dotted) models for $W < 1.4$ GeV.

task. This leads to disagreement in magnitude between the originally published ANL and BNL total cross section data, which has been pointed out and seemingly resolved in Refs. [74, 75, 111]. Nonetheless tensions between model-data comparisons still persist, and in particular it turns out to be difficult to consistently describe the bubble chamber data and the more recent Minerνa data taken on nuclear targets [112].

Comparisons of the hybrid model results with neutrino-nucleon scattering data have been presented in Refs. [113, 114], here we include some additional comparisons with different data and observables, and we compare the vector-vector contribution to what is obtained with the DCC model of Ref. [34] when relevant.

3.6.1 Total cross sections

In Fig. 3.26, we compare the total cross sections obtained within the hybrid model with experimental data. For the ANL and BNL data we show the results of the reanalysis of Ref. [75]. The experimental data is tainted by large errorbars and, especially for SPP on the neutron, by some discrepancies between different experiments. Being optimistic, in general the experimental cross sections tend to allow at least a 20% margin. Nonetheless, clear trends arise from this comparison. We find a rather satisfying agreement with the data for π^+ production of the proton, which is largely dominated by the delta especially in the lower energy region. For the π^0 channel the agreement tends to be good, in the high energy region the model converges close to the BEBC data. For lower energies the BNL data is systematically underpredicted, while the model provides a better agreement with the ANL data. The description of π^+ on the neutron is problematic however, we see that the BEBC data for which a cut $W < 1.4$ GeV is applied tends to be underestimated by a factor 2. A similar discrepancy is found for the high-W data at $E_\nu \approx$ 2 GeV. Per illustration we have included in Fig. 3.26 the contribution of the vector-vector current obtained with the ANL-Osaka DCC model [34] and we find that it provides a similar magnitude as the vector-vector contribution in the Hybrid model. In the high-energy region spanned by the BEBC data the vector-axial contribution becomes completely negligible, and hence the total cross section comes purely from the sum of the non-interfering axial-axial and vector-vector contributions. It is fair to assume that the ANL-Osaka DCC model takes into account the electron scattering data in constructing the vector current as good as possible, certainly much better than the hybrid model, and as we have seen in the previous section for $W < 1.4$ GeV gives results very similar to the MAID07 analysis. The agreement of the vector-vector contribution in both models then clearly implies that the discrepancies in describing the neutrino data should be sought in the description of the axial form-factors.

3.6.2 Q^2- and W-dependence

In Fig. 3.27 the BEBC flux-averaged cross section in terms of Q^2 is shown and compared to the data. The experimental errors are again quite large which makes that the data does not provide a clear constraint on the model. As was he case for the total cross section, the worst agreement comes from π^+ production off the neutron, where the factor 2 discrepancy with experimental data is visible for low-Q^2 when $W <$

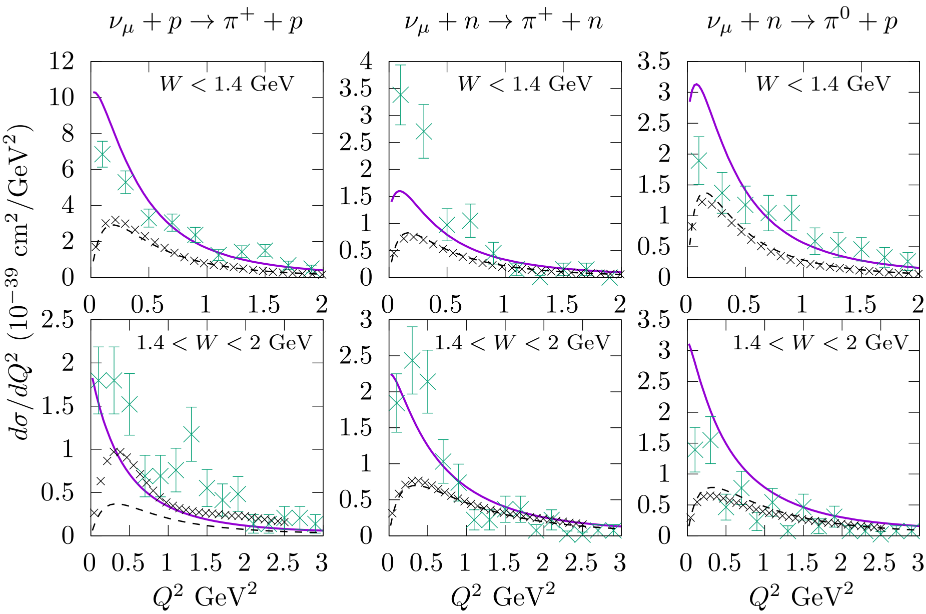

Figure 3.27: Q^2-dependence of the BEBC-flux averaged cross section in the hybrid model (purple lines) is compared to the data (green crosses). The black dashed line shows the vector-vector contribution in the hybrid model while the black crosses show the one obtained in the DCC model of Ref. [34]. In the top row a cut $W < 1.4$ GeV is applied in both the model and the data, while in the bottom row 1.4 GeV $< W <$ 2 GeV.

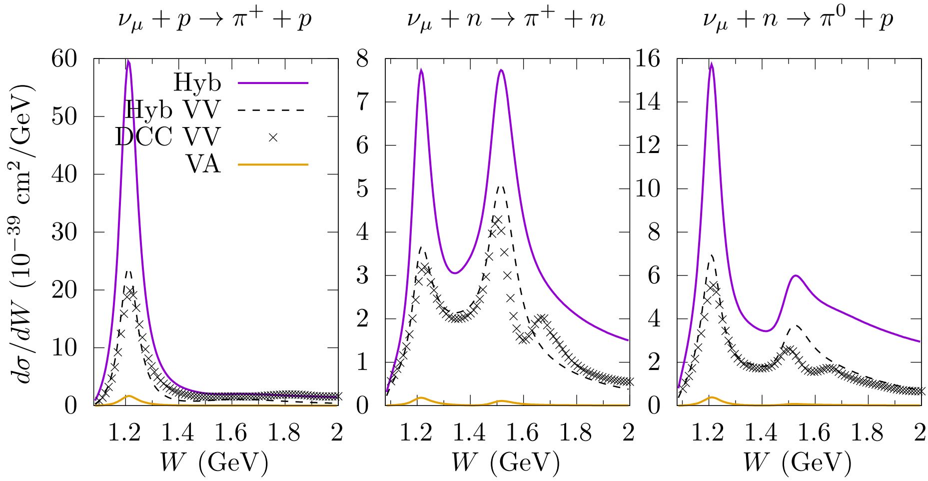

Figure 3.28: W-dependence of the flux-averaged cross section for the BEBC experiment. The thin black line shows the vector-vector contribution in the hybrid model while the black crosses show the one obtained in the DCC model of Ref. [34] where Q^2 up to 2.5 GeV^2 are included. The vector-axial contribution (VA, yellow lines) is computed in the hybrid model.

1.4 GeV, while on the contrary the higher-W data for this process is described much better. For both π^+ production off the proton and π^0 production at small W we see that the BEBC data is overpredicted at low-Q^2 with reasonable agreement with the higher-Q^2 data.

In all comparisons we show again the vector-vector contribution separately and compare it to the one obtained from the DCC model. As the vector-axial contribution is completely negligible this again means that the discrepancies should be due purely due to the description of the axial current. As a matter of fact, to show just how well the vector current tends to be described within the hybrid model for a flux-averaged signal we show in Fig. 3.28 the cross sections in terms of W. While discrepancies are clearly present in the vector current as seen in the previous section, we find that the overall shape of the cross section is very similar in both approaches. In particular the high-W behavior of the DCC model is very similar to the one of the hybrid model which uses a Regge-pole description. The largest discrepancy in the high-W region is found for π^+ production off the proton, where the DCC is

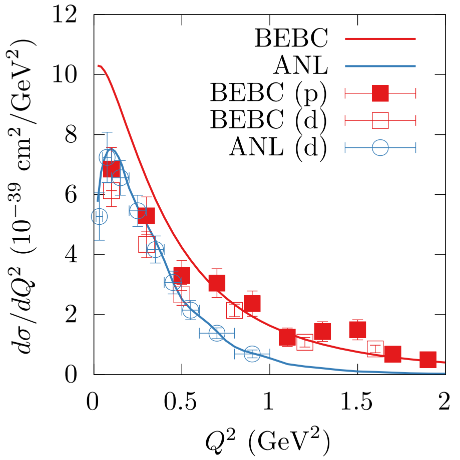

Figure 3.29: Q^2-dependence of the flux-averaged cross section for π^+ production off the proton in ANL and BEBC. We show data for the ANL and BEBC experiments obtained with a deuteron target (empty circles and squares respectively) and for the BEBC with a proton target (solid squares). A cut $W < 1.4$ GeV is applied to the model and the data.

larger than the hybrid model, which explains the discrepancy in the Q^2 distribution for these kinematics shown in Fig. 3.27. As the cross-section is far smaller here than in the low-W region we do not consider this problematic for the time being, although it indicates that a small contribution of higher-mass isospin-3/2 resonances could be needed for a more detailed description of this channel when only higher W are considered.

Given the overprediction of the low-Q^2 BEBC data for π^+ production off the proton, it is interesting to compare these results to what we obtain for the ANL data which was used to determine the axial form-factor of the delta in Ref. [30]. The comparison is shown in Fig. 3.29, the difference between the BEBC and ANL results is due to the difference in flux, with the BEBC operating at much larger energies, a cut $W < 1.4$ GeV is applied for both experiments. A clear discrepancy of the data-model comparison is found when comparing the two datasets. The agreement with the ANL data is of course expected as it was used to fit the axial form-factor of the delta. The BEBC data is described quite well for large Q^2 as found previously, but tends to values similar to the ANL

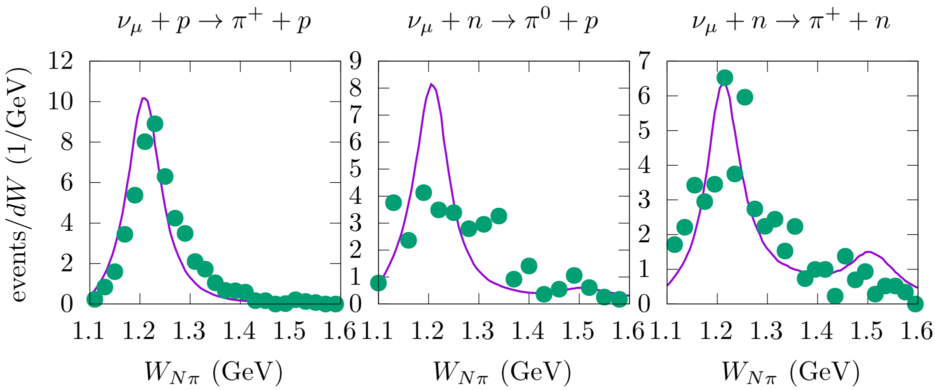

Figure 3.30: W-dependence of the ANL data (green dots), the hybrid model results (purple lines) have been normalized to the same are as the data in the shown region of W.

data for low Q^2 while the model predicts a cross section that is some 20 percent larger. Thus, either the experimental data is inconsistent, or the axial form factor of the delta is not well constrained by only the low-energy ANL data for which the vector-axial contribution is a complicating factor compared to the high-energy data.

We note that the ANL data is obtained from a predominantly deuteron target and that we make no effort here to include nuclear corrections in this comparison. It is unclear which, if any, corrections due to deuteron effects have been made in the experimental data reported by ANL. For the BEBC data we show the results obtained with a proton fill of the detector and a deuteron-fill. A quite significant decrease is found for small Q^2, although the large uncertainties dominate this effect.

In the fit of the axial coupling to the delta [30] which we use in this work, deuteron corrections where implemented following the approach of Ref. [32]. In said approach the momentum distribution implied by the initial-state deuteron wavefunction is taken into account, with the neutron acting as a spectator. Practically speaking, the off-shell inclusive cross section is folded with the deuteron momentum distribution, i.e. the plane-wave impulse approximation. The resulting smearing of the cross section, because of the fast drop in the deuteron momentum distribution, is reported to lead to at most a 7-percent reduction of the cross section compared to the free proton result [30]. In recent work [76, 115] the effects of FSI on the neutrino-deuteron SPP cross

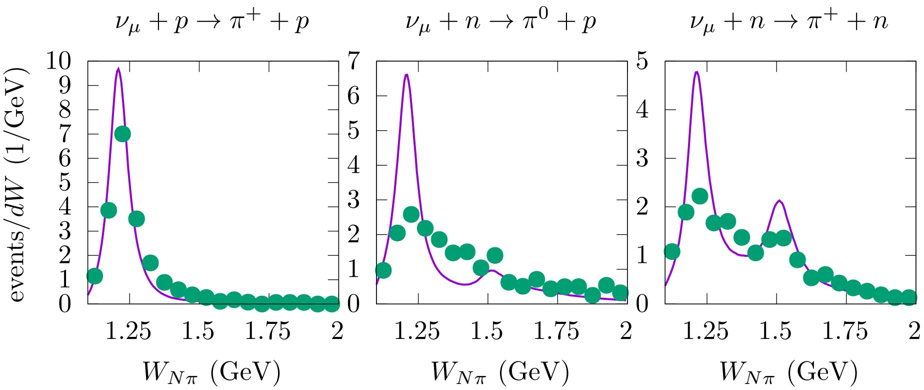

Figure 3.31: W-dependence of the BNL data (green dots), the hybrid model results (purple lines) have been normalized to the same are as the data in the shown region of W.

sections where taken into account explicitly, the results show that in interactions on the deuteron where the final-state is $p + n$, FSI effects are sizable while with a $p + p$ final state the spectator approach suffices to describe the interaction. In Ref. [76], the authors apply corrections to the ANL and BNL total cross sections due to deuteron effects indicating an increase up to 10 percent for the charged pion production channels. This model has to our knowledge not yet been applied to the Q^2 or W distributions, but one might expect that effects would be largest at small Q^2 as hinted to by the BEBC data.

Deuteron corrections and flux uncertainties aside, the large underestimation of the total π^+ production cross section off the neutron is of course indicative of different problems in this channel. The crossed delta contributes strongly to this reaction, and large cancellations between the crossed delta and the background are present. This observation spurred the authors of Ref. [29] to introduce an additional contact term derived from the difference between the Rarita-Schwinger spin-projector and the pure spin-3/2 projector. The strength of the contact term was fitted to data and a better description of this channel was obtained, while retaining a reasonable description of the other interaction channels, with the only cost seemingly being that the experimental ϕ^*_π distributions seem to be mirrored as can be seen in Ref. [77]. We do not include this contact term here, in view of these results however it seems interesting to assess the effect of consistent higher spin interactions, in particular in the crossed channel.

Another possibility for resolving the discrepancy might be found in the axial form-factors of the other components of the model. The W-dependence shown in Fig. 3.28 shows that the second resonance region (here the S_{11} and D_{13}) play a large role in this channel. While the delta contribution is determined by a fit to the data (in the $p\pi^+$ channel), for these resonances we make use of PCAC and a simple ansatz for the Q^2-dependence of the form factors. Moreover for the D_{13} the form-factors that cannot be determined by PCAC are simply set to zero. In Ref. [26] Lalakulich showed, by setting the undetermined form-factors (C_4^A and C_3^A) to one, that the contribution of the other terms can be of a similar size if not larger than the C_5 terms. Given the rather complex behavior of the form-factors in the case of the vector current, where notably the S_{11} helicity amplitudes drop slowly with Q^2, it would be optimistic to assume that the Q^2-dependence of the axial form factors for resonances beyond the delta is well determined. This is evidenced by the comparisons in Fig. 3.27, but also more clearly by duality studies [116, 117]. There, one finds that for the total inelastic electromagnetic structure functions a resonance description oscillates around, and converges smoothly to the structure functions obtained from DIS, this property is referred to as quark-hadron duality. This is at variance with what is obtained in the case for neutrino interactions in many models, one finds that the resonant contributions undershoot the DIS structure function and drop off too quickly [116, 117]. In Ref. [118], for purely illustrative purposes, Sato showed that when the Q^2 dependence of the axial helicity amplitudes (or form-factors) was taken to be the same as those for the vector current, duality was found also for neutrino interactions.

The discrepancy is however already visible in comparison to data where $W < 1.4$ GeV, such that in the absence of significant W-smearing higher-mass resonances are mostly rejected. A shape-only comparison to the W distribution found in the ANL and BNL experiments is shown in Figs. 3.30 and 3.31 respectively. In these comparisons both the model and the data are normalized to one. We find a good agreement for the delta-dominated charged pion production off the proton for both experiments, but for the other interaction channels (especially for the higher-energy BNL data) the relative contribution of the delta peak tends to be overestimated. Surprisingly, we do tend to find a good agreement with the shape of the high-W cross section. Given the comparison to these W-distributions, and knowing that we underpredict the $n\pi^+$ cross section, if we assume that the delta contribution is well constrained it seems that the data imply that the high-W region is instead underpredicted and that the intermediate W region is more significantly filled. Due to the large scatter on the data however it is impossible to draw any definite conclusions from this comparison, and the broadening along the delta may just as likely be due to experimental precision. Based on invariant mass, a candidate for inducing an increase in the dip between the delta and D_{13}/S_{11} region could be the Roper resonance ($P_{11}(1440)$). The problem is that its branching ratio to pion-nucleon is small and its width is large such that it only provides a small contribution, as such even when we increase the axial coupling to the Roper to twice its PCAC value, the effect on the total cross section is far too small to affect the model-data comparison significantly.

3.7 Conclusions

We have presented the model of Ref. [113] for electroweak single pion production off the nucleon and discussed minor modifications made in this work. We have benchmarked the vector-current of the model by comparison to the ANL-Osaka DCC and MAID07 analyses of electroproduction [34, 66]. We find reasonable agreement for electromagnetic interactions, and have pointed out where the model is lacking. We find moreover that the DCC and MAID07 models can disagree up to a factor 2 for charged pion production reactions at large values of Q^2. We have extracted the charge-changing vector current from the MAID07 and DCC analyses and performed a comparison to the hybrid model presented in this work. Contrary to the electromagnetic case, we find that the DCC and MAID07 results agree much better for the isovector current, and that the hybrid model gives a good reproduction of these results especially when considering the relative simplicity of the model. The axial couplings in the hybrid model are estimated from the pion-nucleon couplings through the PCAC hypothesis. We have as an additional benchmark used the axial current to compute pion-nucleon scattering observables with good results. Finally we showed results for flux-averaged neutrino-induced pion production and compared them to the ANL, BNL and BEBC datasets [72, 73, 75, 110]. We find a reasonable description of neutrino induced positive pion production off the proton and neutral pion production, but underestimate the positive pion production of the neutron by almost a factor two for high energies. We argue, by comparing the vector-vector contribution of the hybrid model to the one of the ANL-Osaka DCC for flux-averaged results, that the discrepancies in describing neutrino data should be due to the description of the axial current.

Chapter 4

Scattering off nuclei

In this chapter we explain our approach for the description of single pion production of nuclei. We treat the process described schematically by the conservation of four-momenta

$$k^\mu + P_A^\mu = k'^\mu + k_\pi^\mu + k_N^\mu + P_B^\mu, \tag{4.1}$$

where $k^\mu = (E, \mathbf{k})$ and $k'^\mu = (E', \mathbf{k}')$ describe the initial and final-state lepton respectively. The initial state nucleus $P_A^\mu = (M_A, \mathbf{k}_A = \mathbf{0})$ is at rest in the lab-frame, and the final-state nucleus $P_B = (E_B = M_B^0 + E_B^* + T_B, \mathbf{p}_B)$ is left in a state with invariant mass $M_B = M_B^0 + E_B^*$ and excitation energy E_B^*.

Following the definitions in Chapter 2 the cross section is given by

$$\frac{\mathrm{d}^8\sigma(E)}{\mathrm{d}E'\mathrm{d}\Omega\mathrm{d}E_\pi\mathrm{d}\Omega_\pi\mathrm{d}\Omega_N} = \mathcal{F}_X^2 \frac{k'}{E} \frac{M_N k_\pi k_N M_B}{2\,(2\pi)^8\, E_B f_{rec}} L_{\mu\nu} H_X^{\mu\nu} \tag{4.2}$$

with the recoil factor

$$f_{rec} = |1 + \frac{E_N}{E_B}\left(1 + \frac{\mathbf{k}_N \cdot (\mathbf{k}_\pi - \mathbf{q})}{|\mathbf{k}_N|^2}\right)|. \tag{4.3}$$

where $\mathbf{q} = \mathbf{k} - \mathbf{k}'$. The couplings are

$$\mathcal{F}_{CC}^2 = G_F^2 \cos\theta_c^2,\ \mathcal{F}_{WNC}^2 = G_F^2,\ \mathcal{F}_{EM}^2 = \frac{1}{2}\left(\frac{4\pi\alpha}{Q^2}\right)^2, \tag{4.4}$$

for charged-current, weak neutral-current and electromagnetic interactions respectively.

4.1 Kinematics

The $2 \to 4$ scattering process, where one of the final state particles is left in an arbitrary excited state requires 9 non-trivial independent kinematic variables. For single-pion production these can be chosen as $(E, E', \cos\theta_l, E_\pi, \Omega_\pi, \Omega_N, M_B)$. From these variables, given that the direction the incoming beam is known and the initial nucleus is at rest in the lab frame, the four-vectors of all particles can be determined. Energy and momentum conservation, with $\omega = E - E'$, give

$$\omega + M_A = E_B + E_N + E_\pi, \tag{4.5}$$

$$\mathbf{p}_B = -\mathbf{p}_m = \mathbf{q} - \mathbf{k}_N - \mathbf{k}_\pi. \tag{4.6}$$

We can define the missing mass

$$M_m = M_B + M - M_A = M_B^0 + E_B^* + M - M_A \tag{4.7}$$

such that

$$\omega = M_m + T_B + T_N + E_\pi, \tag{4.8}$$

and the missing energy is $E_m = M_m + T_B$. The kinetic energy of the final-state nuclear system with invariant mass $M_B = M_B^0 + E_B^*$ is given by

$$T_B = \sqrt{M_B^2 + (\mathbf{q} - \mathbf{k}_\pi - \mathbf{k}_N)^2} - M_B, \tag{4.9}$$

One can solve Eqs. (4.8 - 4.9) for the nucleon momentum, the solution is given in Ref. [119].

We will however simplify this by neglecting the small kinetic energy of the recoiling nuclear system. The recoil energy is small as the residual nucleus is heavy and hence can gain quite some momentum with a relatively small gain in kinetic energy. The momentum with which the residual system recoils comes from the knockout of a bound nucleon with a momentum of the order of the Fermi momentum. The kinetic energy is then

$$T_B = \sqrt{M_B^2 + \mathbf{p}_m^2} - M_B \approx \frac{\mathbf{p}_m^2}{2M_B} + \mathcal{O}(\frac{p_m^4}{M_B^2}). \tag{4.10}$$

If we assume values suitable for a carbon nucleus, $M_B \approx 11 M_N$ and $|\mathbf{p}_m| \lesssim k_F \approx 220$ MeV, we obtain $T_B \lesssim 2.5$ MeV, and clearly this decreases with larger nuclear masses. If we neglect the recoil energy, the missing energy is $E_m = M_m = M_B + M - M_A$, and the nucleon energy is simply given by $T_N = \omega - E_\pi - E_m$.

4.1.1 Missing energy distribution

We will model the nucleus with the relativistic mean field (RMF) framework. The RMF model and structure of the wavefunctions are described in more detail in Appendix B.

In the central RMF potential one finds that nucleons occupy discrete orbitals that are labeled by the relativistic angular momentum quantum numbers κ m_j, with fixed energy-eigenvalues for every κ, the states are degenerate in m_j. The residual nucleus can then be left in an excited state corresponding to knockout of a nucleon from these orbitals. The semi-inclusive cross section is then

$$\begin{aligned}&\frac{\mathrm{d}^8\sigma}{\mathrm{d}E'\mathrm{d}\Omega'\mathrm{d}E_\pi\mathrm{d}\Omega_\pi\mathrm{d}\Omega_N} = \\ &\int \mathrm{d}E_m \delta\left(\omega - E_m - T_N - E_\pi\right) \mathcal{F}_X^2 \frac{k'}{E} \frac{M_N k_\pi k_N M_B}{2\left(2\pi\right)^8 E_B} L_{\mu\nu} H^{\mu\nu} \\ &= \mathcal{F}_X^2 \frac{k'}{E} \frac{k_\pi}{2\left(2\pi\right)^8} L_{\mu\nu} \sum_\kappa \left(\frac{M_N k_N M_B}{f_{rec} E_B} H_\kappa^{\mu\nu} \right), \end{aligned} \tag{4.11}$$

e.g. it is the sum of exclusive cross sections, each for a different fixed missing energy $E_m = -E_\kappa$ corresponding to the shells. We discuss the hadron tensor and its dependence on the kinematics in the next section.

Such a pure shell model treatment is known to be an approximation to more realistic missing-energy profiles that are obtained in experimental one-nucleon knockout studies. Electron scattering data shows that the discrete states obtain a width, and are partly de-occupied with some of the strength appearing at large missing energies beyond the shell-model region. This spreading and de-occupation is understood to be due to correlations not included in the mean-field (both long- and short-range) and the effect of FSI [120]. These more complex missing energy and momentum profiles have been taken into account in neutrino interactions in particular in the factorized plane wave impulse approximation (PWIA). In such an approach the off-shell single-nucleon cross section is weighted by an effective spectral function [40, 121–123]. A similar missing-energy profile, that takes into account also a background due to short-range correlations, based on the spectral function of Ref. [121, 124], was added to the same RDWIA approach described in the next section in Ref. [125] to describe one nucleon knockout in neutrino experiments.

4.2 Nuclear currents

The hadron tensor for the interaction with a shell labeled by the angular momentum κ is

$$H_{\kappa}^{\mu\nu} = \frac{N_{\kappa}}{2J+1} \sum_{m_j, s_N} \left[J^{\mu}\left(m_j, s_N, Q^{\mu}, k_N^{\mu}, k_{\pi}^{\mu}\right)\right]^{\dagger} J^{\nu}\left(m_j, s_N, Q^{\mu}, k_N^{\mu}, k_{\pi}^{\mu}\right) \tag{4.12}$$

where s_N and m_j are the projections of the spin of the final-state nucleon and the angular momentum of the bound state, and we average over the $2J+1$ possible states for m_j. The occupation of the state is N_{κ}, which in the pure shell model will also simply be $2J+1$ per shell.

To make approximations to the hadron current clear, it is instructive to first consider the current in momentum space

$$\begin{aligned} J^{\nu} = & \frac{1}{(2\pi)^{3/2}} \int d\mathbf{p}'_N \int d\mathbf{p}'_{\pi} \overline{\psi}^{s_N}\left(\mathbf{p}'_N, \mathbf{k}_N\right) \phi^{*}\left(\mathbf{p}'_{\pi}, \mathbf{k}_{\pi}\right) \\ & \mathcal{O}^{\nu}\left(Q^{\mu}, k'_N, k'_{\pi}, p'_m\right) \psi_{\kappa}^{m_j}\left(\mathbf{p}'_m = \mathbf{p}'_N + \mathbf{p}'_{\pi} - \mathbf{q}\right). \end{aligned} \tag{4.13}$$

Here $\psi^{s_N}\left(\mathbf{p}', \mathbf{p}_N\right)$ and $\phi^{*}\left(\mathbf{p}', \mathbf{k}_{\pi}\right)$ are the outgoing nucleon and pion wavefunctions which are functions of the primed momenta and have asymptotic momenta $\mathbf{k}_N$ and $\mathbf{k}_{\pi}$. The bound state wavefunction is ψ_{κ}, and the projections of spin and angular momentum of the bound state are denoted by superscripts s_N and m_j respectively.

In our spherical-symmetric nucleus the outgoing nucleon and pion are described by energy eigenstates, the energies are defined by the on-shell dispersion relation $E^2 = \mathbf{k}^2 + M^2$ with $\mathbf{k}$ the asymptotic momentum. In the nuclear interior however the wavefunctions are not states with fixed momentum, the momentum operator acting on the wavefunctions yields the primed momenta. As such the transition operator should be determined as function of the primed four-momenta, e.g. $k'_N = (E_N, \mathbf{p}'_N)$, which are related by energy momentum conservation $Q^{\mu} + p_m^{\mu} = p_{\pi}^{\prime\mu} + p_N^{\prime\mu}$. This implies a non-trivial computational problem, as for every single value of the asymptotic momenta and for every single-particle orbital, a six-dimensional integral has to be performed where. Moreover a complicated transition operator has to be computed for every point of the integral. We will discuss the approximations that are made to make the computation of the hadron current feasible over the broad phase space spanned by neutrino experiments.

We will in this work always treat the pion as a plane wave. A plane wave function in momentum space gives simply a delta-function $(2\pi)^{3/2}\delta(\mathbf{p}' -$

p) such that one of the integrals can be performed immediately and we get

$$J^{\nu} = \int d\mathbf{p}'_N \, \overline{\psi}^{s_N} \left(\mathbf{p}'_N, \mathbf{k}_N\right) \mathcal{O}^{\nu} \left(Q, p'_m, k^{\mu}_{\pi}, k'^{\mu}_N\right) \psi^{m_j}_{\kappa} \left(\mathbf{p}'_m\right). \qquad (4.14)$$

We can introduce the approximation in which the operator is evaluated for the asymptotic four-momenta

$$\mathcal{O}^{\mu} \left(Q, p'_m, p'_N, p'_{\pi}\right) \to \mathcal{O}^{\mu} \left(Q, p_m, k_N, p_{\pi}\right) \qquad (4.15)$$

instead of for every primed momentum in the integral. With this additionally, the operator is independent of $\mathbf{p}'_N$ and we can rewrite the hadron current by writing the momentum space wavefunctions as the Fourier transform of the coordinate space wavefunctions

$$\begin{aligned} J^{\mu} &= \frac{1}{(2\pi)^3} \int d\mathbf{p}'_N \int d\mathbf{r} \; e^{i\mathbf{p'_N}\cdot\mathbf{r}} \overline{\psi}^{s_N}(\mathbf{r}, \mathbf{k}_N) \mathcal{O}^{\mu}(Q, p_m, k_{\pi}, k_N) \\ &\times \int d\mathbf{r}' e^{-i(\mathbf{p}'_N + \mathbf{k}_{\pi} - \mathbf{q})\cdot\mathbf{r}'} \psi^{m_j}_{\kappa}(\mathbf{r}') \\ &= \int d\mathbf{r} e^{i(\mathbf{q}-\mathbf{k}_{\pi})\cdot\mathbf{r}} \psi^{s_N}\left(\mathbf{r}, \mathbf{k}_N\right) \mathcal{O}^{\mu}\left(Q, p_m, k_{\pi}, k_N\right) \psi^{m_j}_{\kappa}\left(\mathbf{r}\right). \qquad (4.16) \end{aligned}$$

This reduction of the hadron current to a 3-dimensional integral in coordinate space does not rely on the plane-wave approximation of the pion, but only on the fact that the operator is evaluated for asymptotic momenta. Starting from the full expression in Eq. (4.13), under the assumption of Eq. 4.15, the 6 dimensional momentum space integral can be written as a 3d integral in coordinate space. One obtains the same result with substitution of the factor $e^{-i\mathbf{k}_{\pi}\cdot\mathbf{r}}$ by the distorted pion wave $\phi^*(\mathbf{r}, \mathbf{k}_{\pi})$.

This expression is reminiscent of the one used in quasielastic scattering [125, 126], of course with a different operator and without the pion plane wave $\mathbf{k}_{\pi} = \mathbf{0}$. In the case of quasielastic scattering the operator can be written as function of only Q^{μ} by using energy momentum conservation and the Gordon identity. For completeness, and as we will use results for quasielastic scattering to motivate our choice of potential the transition operator is

$$\mathcal{O}^{\mu}_{QE} = F_1(Q^2)\gamma^{\mu} + \frac{F_2(Q^2)}{2M_N}\sigma^{\mu\nu}Q_{\nu} - G_A(Q^2)\gamma^{\mu}\gamma^5 - \frac{G_P(Q^2)}{2M_N}Q^{\mu}\gamma^5. \qquad (4.17)$$

Where the form factors are the same as in Eqs. (3.63-3.64). In the case of SPP the operator is more complicated, and it is not possible to remove all explicit momentum dependence. Calculations of photo- and electroproduction of single pions without assuming the asymptotic approximation were performed in Ref. [127] in a non-relativistic mean field model with distorted pion and nucleon waves obtained in optical potentials. It is found that the cross section (obtained for fixed energy and angle of both the pion and the nucleon) tends to be more smeared out, but does not seem to differ much in total magnitude.

We will also consider the relativistic plane-wave impulse approximation (RPWIA) where the final state nucleon is also described by a plane wave and final-state interactions are thus neglected completely. In this case $\mathbf{p}'_N = \mathbf{k}_N$, and the asymptotic evaluation of the operator, Eq. (4.15), is imposed automatically. With the plane-wave $\overline{u}(\mathbf{k}_N, s_N)e^{-i\mathbf{k}_N \cdot r}$ as final state nucleon, the integral over $\mathbf{r}$ can be performed immediately and one has

$$J^\mu = (2\pi)^{3/2}\,\overline{u}\,(\mathbf{k}_N, s_N)\,\mathcal{O}^\mu(Q, p_m, k_\pi, k_N)\psi_\kappa^{m_j}(\mathbf{p}_m = \mathbf{k}_\pi + \mathbf{p}_N - \mathbf{q}). \tag{4.18}$$

We point out that this is not the same as the PWIA, in which a off-shell single-nucleon cross section is weighted with a momentum distribution. The relativistic bound state contains negative energy components which prevents such a factorization [128–130]. Comparisons of the RPWIA with the factorized PWIA calculation using the same momentum distributions show however that the differences are small for flux-averaged neutrino cross sections [125]. One sees that within the RPWIA the initial state is probed at a fixed value $\mathbf{p}_m$, and that the nuclear degrees of freedom separate to some extent. This contrasts with the RDWIA, where the outgoing wavefunction is not a fixed momentum eigenstate, and the initial state is probed in a broader region in momentum space.

4.3 Potentials for the final state nucleon

We describe the outgoing nucleon as a scattering state of the Dirac equation with central scalar and vector potentials as described in Appendix B. There are several choices for the potential with which to describe the final-state, the optimal choice of potential in our framework will depend on which observables are described, in particular on whether or not the outgoing nucleon is detected. We discuss the drawbacks and applicability of several choices below.

I. The RMF

An obvious choice is to use the same RMF potential that is used to describe the initial state to also describe the outgoing nucleon wavefunctions. This is an attractive choice especially because of its consistency. In this case the initial and final state wavefunctions are orthogonal and consistent, because they are solutions of the same Dirac equation. The importance of orthogonality and consistency is discussed in the following sections. It seems natural that, at least for small energies and momenta comparable to those of the bound nucleons, the outgoing nucleon would experience a similar effect from the nuclear system. RDWIA calculations with an RMF potential are able to describe inclusive electron scattering data at moderate momentum transfers, it is especially successful in the quasielastic region for ω values before the quasielastic peak [131]. When the nucleon energy becomes larger, comparisons to (e, e') data show that RMF potential is too strong, it predicts a large reduction of the quasielastic peak, with a large cross section in the high-ω tail.

II. The Relativistic Optical Potential (ROP)

A real potential, such as the RMF, can only describe the elastic propagation of a nucleon in the medium, the phase shifts of scattering states are all real. Inelastic interactions, in which the nucleon may exchange significant energy with the medium however are not included. The strength of inelastic interactions increases with the energy of the nucleon as both the phase space and number of interaction channels will increase. This is a coupled-channels problem, as the flux of nucleons has to be distributed over the different interaction channels. When the inelastic channels are dense and smoothly distributed in the energy, in contrast to a process dominated by a sharp peak at specific energy, the flux lost to them can be described by adding an imaginary part to the potential. The resulting complex, i.e. optical, potential describes elastic scattering observables with all inelastic processes lumped together in the imaginary part which removes flux from the elastic channel. Such relativistic optical potentials (ROP) can be obtained for example by phenomenological fits of elastic proton-nucleus $(p - A)$ scattering cross sections [132–134]. The total $p - A$ cross section can be split up $\sigma_{tot} = \sigma_{el} + \sigma_{reac}$ in elastic an inelastic (reaction) cross sections. The ROP describes explicitly σ_{el}, such that using the optical theorem the total cross section (and hence the total reaction cross section) are obtained. With the increase in energy comes a larger reaction cross section, and the real part of the potential should decrease accordingly. These ideas are most clear in what is called the

Dispersive Optical Model (DOM) [135–138]. The DOM aims to link the description of scattering observables and nuclear structure with a smoothly evolving energy-dependent optical potential which described bound states and scattering states. The idea is to determine the real part of the potential from its imaginary part, which is constrained by scattering data, by a subtracted dispersion relation. By assuming a static real mean field potential as the residual potential not given by the dispersion relation, one links the description of bound and scattering states. Such approaches are successful in their prediction of properties of bound nucleons.

III. The Real ROP (rROP)

When one uses a ROP for the description of the final state nucleon in Eq. (4.16) one only describes the cross section for nucleons that undergo elastic FSI, as the imaginary part absorbs the flux that goes into inelastic channels. As such the ROP approach has been applied to exclusive $(e, e'p)$ cross sections, where the probed missing energy is restricted to a narrow region corresponding to a specific single-particle state [139–142]. Because inelastic interactions would lead to the nucleon exchanging significant energy with the medium, the strength lost to inelastic FSI will not contribute to the exclusive cross section and should be removed. In interactions where the final-state nucleon is not detected however, the flux lost to inelastic channels should be kept. This is possible for example in the Relativistic Green's Function (RGF) approach, which consistently redistributes the flux in all final-state channels, and conserves the total flux in the sum over these channels [49, 143–147].

Another approach, which lacks the consistency of the RGF but is much simpler, is to describe inclusive scattering by retaining only the real part of the ROP obtained from $p - A$ scattering, which we denote as the rROP. In this way the total flux is conserved, and the energy-dependent real part becomes weaker in a way which is empirically found to describe the inclusive quasielastic cross section [148–150]. The approach has some drawbacks, the ROP parameters are only constrained in the energy region in which it is fit, and it is not necessarily clear how to extrapolate to energies beyond this region. As ROP are available for kinetic energies up to 1 GeV, this does not pose a very significant issue for describing neutrino interactions in the few-GeV region, as at sufficiently high energies the RPWIA should give comparable results. A different issue is the extrapolation to small nucleon energies, the optical model is mostly applicably when the inelastic channels are dense and smoothly distributed in the energy. For small energies however this assumption breaks down, as the excitation of narrow resonances in the nucleus may provide a sharply peaked inelastic channel. Optical potentials are generally fit to elastic $n-A$ scattering down to incoming kinetic energies of around 20 MeV.

IV. The Energy-Dependent RMF (ED-RMF)

At smaller nucleon energies, even within the range in which the ROP is constrained, one still has to deal with the fact that the rROP potential will produce wavefunctions which are inconsistent and not orthogonal with respect to the initial state which in any case is described by the RMF. In order to cure these ailments of the rROP, in Ref. [131] an empirical energy-dependent potential for the description of inclusive scattering was proposed. The simple approach consists of scaling the static vector and scalar RMF potentials as function of the outgoing nucleon energy. Instead of relying on the energy dependence of ROPs fit to $n-A$ scattering, the parametrization of the ED-RMF is inspired by the SuSAv2 analysis of inclusive (e, e') data [151–153]. In the SuSAv2 model for the quasielastic peak, use is made of the scaling functions for inclusive nuclear responses obtained from the RDWIA with a RMF potential and RPWIA models. These scaling functions are combined with relative weights as function of momentum transfer q, where at small q the RMF is mostly used, while at large q the resulting cross section becomes closer to the RPWIA. This weights are used to determine the scaling factor for the RMF potential as function of the nucleon energy as described in Ref. [131].

The potential cures the inconsistency of potentials at low energy as it is constructed to yield the same RMF potential used to describe the initial state in that case. Hence while not fully consistent over the full energy-range, it is consistent at small energies where the effect of orthogonality matters most. Additionally the simple parametrization may be extended to arbitrarily large nucleon energies. A comparison between several rROP, ED-RMF, and the SuSAv2 model for QE scattering was presented in Ref. [148], where it is found that all approaches tend to give similar results from $q = 300$ MeV and larger.

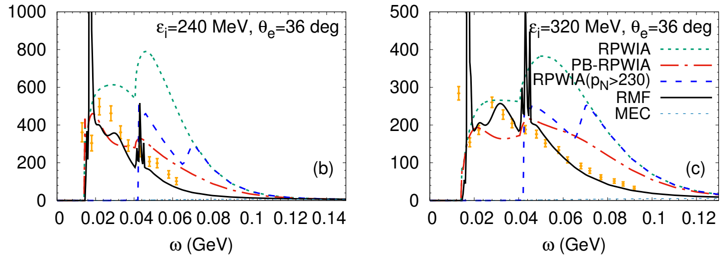

Figure 4.1: Comparison of the (e, e') cross sections for scattering off ^{12}C at small energy and momentum transfer obtained with different models for the outgoing nucleon wavefunction. Figure is from Ref. [131].

V. Orthogonality of initial and final state, the Pauli-Blocked RPWIA (PB-RPWIA)

In order to isolate the effect of orthogonal wavefunctions we can orthogonalize the outgoing wave with respect to the bound-state wavefunctions of the nucleus. An orthogonalized plane wave can be written as

$$|\Psi(\mathbf{p}_N, s_N)\rangle = |\psi_{pw}(\mathbf{p}_N)\rangle - \sum_i \langle\psi_{pw}(\mathbf{p}_N)|\psi_i\rangle\, |\psi_i\rangle \tag{4.19}$$

where the sum extends over a set of bound states ψ_i. When this set of states are all mutually orthogonal it is easy to see that indeed $\langle\Psi(\mathbf{p}_N, s_N)|\psi_i\rangle = 0$ for all the included bound states. Explicit values for the projection coefficients $\langle\psi_{pw}(\mathbf{p}_N)|\psi_i\rangle$ for relativistic bound states, and the proof that the wavefunction defined by Eq. (4.19) is properly normalized can be found in Ref. [131].

There are several lines of reasoning to determine the set of wavefunctions which should enter in the orthogonalization. One could argue for minimal-orthogonalization, including only the single-particle bound state for which a transition matrix element is evaluated. There is a caveat to this argument however, which is particularly important to consider in the case of charged current interactions. The proton and neutron bound states are not the same in the RMF model of the nucleus, specifically the potential used to compute proton and neutron states differs by the inclusion of the Coulomb potential in the former. For a neutral-current interaction this poses no issue, but when a neutron is transformed into a proton or vice versa this minimal approach gives no clear recipe, nor argument, for what bound-state to orthogonalize to.

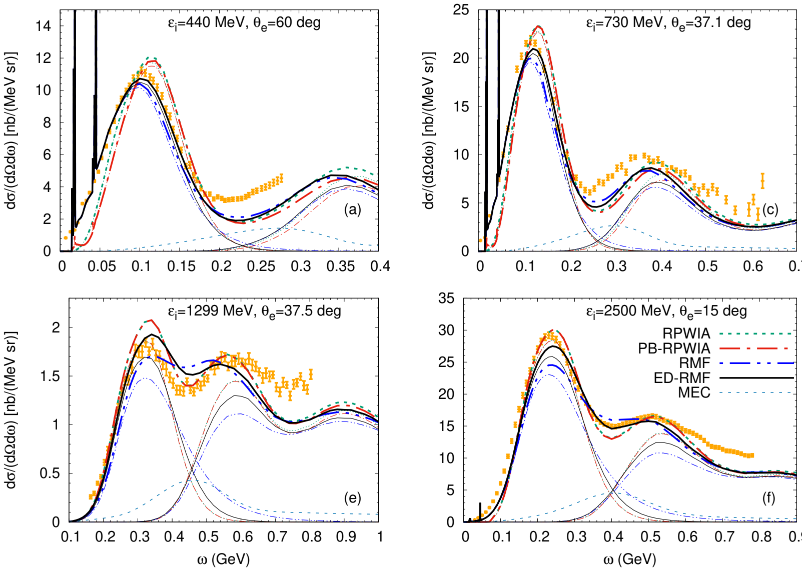

Figure 4.2: Comparison of the (e, e') cross sections for scattering off ^{12}C at intermediate energy and momentum transfer obtained with different models for the outgoing nucleon wavefunction. Figure is from Ref. [131].

This problem is solved when one orthogonalizes the outgoing wavefunction for protons or neutrons with respect to all occupied states of the same particle type. One sees that this approach introduces the Pauli-exclusion principle for the momentum states of the outgoing nucleon explicitly. Consider a simple RFG model: both the initial and final state are described as plane waves, with the initial state consisting of plane waves with momenta up to a fixed Fermi momentum. One sees that Eq. (4.19) implies that the outgoing wavefunction, and hence the cross section, is zero when its momentum is below the Fermi momentum.

We can however take the orthogonalization one step further by orthogonalizing the outgoing wavefunction with all bound states of the same particle type whether or not they are occupied. The rationale for this procedure comes from the idea that both the scattering states and bound states should be described by a single Hamiltonian, in which case all the wavefunctions obtained from this Hamiltonian are orthogonal. It was additionally found, that one obtains cross sections closer to the full RMF result at low energies by including in the orthogonalization procedure only those bound states which are accessible in the scattering, these are bound states for which $\omega > E_m$. This last treatment was used in

Refs. [131, 154], we further note that effect of orthogonality in nucleon knockout reactions with electromagnetic probes has been studied in Refs. [155–157].

To illustrate and summarize the discussion of different treatments of the final-state wavefunctions we include a number of comparisons to data for (e, e') scattering off ^{12}C, these were originally published[1] in Ref. [131]. In Fig. 4.1, we show the comparison of the RMF, RPWIA and PB-RPWIA approaches at small values of energy and momentum transfer. The RMF is indeed seen to give a good description of the cross section, while the RPWIA overpredicts the cross section significantly. If one implements Pauli-blocking in the RPWIA in a way that resembles a RFG, i.e. by setting the cross section to zero for outgoing energies below some cut-off, one sees that the correct strength of the cross section is found, but the cross section is shifted to high ω compared to the RMF. The PB-RPWIA on the other hand, with the orthogonalization only to bound states for which $\omega > E_m$, yields a similar magnitude as the RMF for small ω, although still overpredicting the higher-ω region slightly.

In the results of Fig. 4.2 we move to higher energy and momentum transfer, for the top panels a clear quasielastic peak is visible and dominates the cross section, while for the bottom panels the importance of meson-exchange currents (MEC) and the Delta peak become comparable to the QE peak. The MEC contribution is from Refs. [158, 159]. The resonance region is computed with the hybrid model introduced in the previous chapter, these calculations include only the single-pion production channel. The effect of orthogonality is negligible for these kinematics and the PB-RPWIA and RPWIA give practically the same result. For the kinematics of the top panels the ED-RMF and RMF give similar results by construction. It is seen that compared to the RPWIA the QE peak is shifted toward smaller ω in these approaches, which gives an excellent reproduction of the data notably in the low-ω part of the peak. For the higher energy cross sections in the lower panels the ED-RMF and RMF give different results, in the RMF the peak strength is shifted toward high-ω, which tends to overpredict the dip-region, the ED-RMF cures this ailment to some extent and behaves more like the RPWIA results.

In the following section we show the effect of orthogonal wavefunctions on the relative cross section of muon- and electron-neutrino induced interactions at the same incoming energy and scattering angle. This

1. The contribution of A. Nikolakopoulos as author to published manuscripts of which results are included in this thesis can be found in Appendix D.

section was originally published[2] in Ref. [154], and for completeness it is included fully.

4.4 Orthogonality, Pauli-blocking and the ratio between ν_e and ν_μ cross sections

In recent years, the quest to elucidate issues concerning neutrino oscillation parameters, the existence of sterile neutrinos, and CP violation has resulted in a worldwide boom in neutrino experiments and collaborations [5, 6]. Accelerator-based oscillation experiments such as MiniBooNE, T2K, MicroBooNE, and the upcoming DUNE and T2HK facilities [8, 160–164] rely on neutrino scattering off atomic nuclei in order to detect them in their near and far detectors. A reliable determination of the neutrino-nucleus cross section is hence pivotal for energy reconstruction and oscillation analyses. Theoretical analyses are equally important for dedicated neutrino-nucleus experiments such as e.g. MINERνA [165]. In view of the determination of oscillation parameters, and in particular the CP-violating phase, an accurate knowledge of ν_e, ν_μ and $\overline{\nu}_e$, $\overline{\nu}_\mu$ cross sections over a large kinematic region is indispensable. The differences between ν_e and ν_μ induced cross sections have been puzzling the community for the last couple of years [166–169], as it is crucial for the interpretation of the low-energy ν_e excess [160] and for investigations of the neutrino mass hierarchy and the CP-violating phase δ_{CP} [5, 161].

In Ref. [167] we have shown that the calculated ratio $\sigma_{\nu_e}/\sigma_{\nu_\mu}$ shows important model dependencies. While models agree that electron neutrinos induce larger total cross sections than muon neutrinos [166, 168], the picture can be radically different for specific kinematics. Evaluating cross sections in a mean-field based Hartree-Fock continuum random phase approximation (HF-CRPA) model, we found that for reactions at forward lepton scattering angles, surprisingly charged current muon neutrino-induced interactions show larger cross sections than their electron neutrino counterparts [167]. In Ref. [166] it was argued that a ν_μ dominance could be an artifact of an incomplete treatment of the phase space available to the interaction. This could e.g affect processes studied with a Fermi gas model, as commonly done in experimental analyses. Meanwhile, the question of which cross section is the larger one at specific kinematics remained unanswered.

2. The contribution of A. Nikolakopoulos as author to published manuscripts included in this thesis can be found in Appendix D.

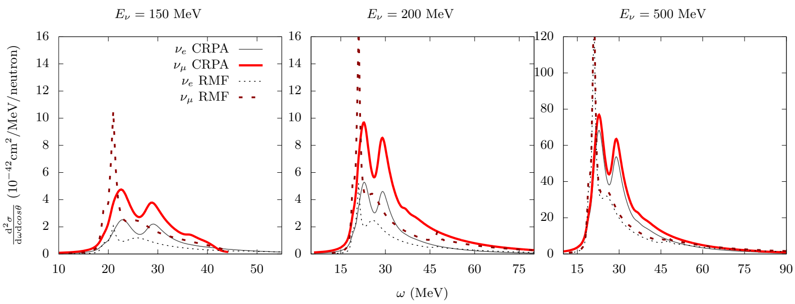

Figure 4.3: CRPA (full lines) and RMF (dashed) cross sections for different incoming neutrino energies for a lepton scattering angle of $\theta_l = 5°$ for muon (thick lines) and electron neutrino (thin lines) induced interactions with ^{12}C.

In this Letter, we examine the effect of final-state distortion in the modeling of the cross section on this problem and show that a proper treatment of the distortion of the outgoing nucleon's wave function resolves the issue. Using two different models and independent codes we demonstrate that describing the reaction with a cross section model that includes nucleon wave functions calculated in a nuclear potential instead of unbound plane waves reveals that ν_μ induced cross sections can indeed be larger than their ν_e counterparts at forward lepton kinematics. Approximating the outgoing nucleon's wave function by a plane wave description, which introduces inaccuracies related to Pauli blocking and orthogonality issues, results in a considerable overestimation of the responses at low energies and forward lepton scattering angles [170]. This kinematic region is especially relevant for the T2K experiment where the oscillated ν_μ signal peaks around 300 MeV [161] and the low-energy excess of electron-like events found predominantly for forward scattering angles in the MiniBooNE experiment [160].

This Letter is organized as follows: first we show that in mean-field approaches which include distortion of the final nucleon, the ν_μ induced cross section is indeed larger than its ν_e counterpart in certain kinematic regions. Then the influence of the kinematics of the process on these cross sections is reviewed, and finally we show that a proper description of Pauli blocking plays an essential role in this effect.

The first approach used in this work, the HF-CRPA model, is based on a mean-field ansatz where the bound-state wave functions are obtained through a Hartree-Fock calculation with a Skyrme interaction [171, 172]. The final-state nucleon is described with a continuum wave function obtained using the same potential to describe the interaction with the residual system. Long-range correlations are taken into account through a random-phase approximation approach using the same Skyrme parametrization as residual interaction [172–174]. The width of the nucleon states is taken into account in an effective way, folding responses with a Lorentzian [175]. In this formalism, the nuclear dynamics are treated in a non-relativistic way, and relativized using the effective procedure proposed in Ref. [176]. The HF-CRPA approach has been successfully applied to the description of various electroweak scattering processes [172, 173, 175, 177–179]. Short-range correlation effects are very small at the kinematics of interest [166, 180].

The second model is the relativistic mean field (RMF) model for quasielastic one-nucleon knock-out, where the initial and final state nucleon single-particle wave functions are obtained as solutions of the Dirac equation with a mean field potential. The potential is obtained by a self-consistent calculation with a nucleon-nucleon interaction described by a Lagrangian which includes meson fields to parameterize the coupling [181, 182]. It has been shown that the RMF model describes well inclusive electron scattering off nuclei [183–186].

In both approaches, the outgoing wave function is computed in the same nuclear potential as the one used for the bound nucleon states, thereby including the essential feature of orthogonality of initial and final state. In this respect, our models contrast with other approaches that ignore secondary interactions of the outgoing nucleon.

The RMF and HF-CRPA charged current quasi-elastic (CCQE) cross sections for a selected set of kinematic conditions with small energy and momentum transfers are shown in Fig. 4.3. Although giant resonances cannot be reproduced with the RMF model, its basic features agree well with the HF-CRPA results, in particular confirming the ν_μ/ν_e ratios found in [167], with larger cross sections for the reactions producing the heavier lepton in the final state.

The fact that cross sections producing a relatively heavy muon in the final state can be larger than the ones with a light outgoing electron at the same incoming energy, scattering angle and energy transfer, may seem counter-intuitive, but should in fact not be so surprising. Looking into the kinematics of the reaction, it becomes clear that for forward lepton scattering angles, at a given energy transfer ω, the corresponding momentum transfer q is larger for muon neutrinos than for electron neutrinos *exactly* because the former reaction generates a charged lepton with a larger mass. Indeed, for forward scattering kinematics

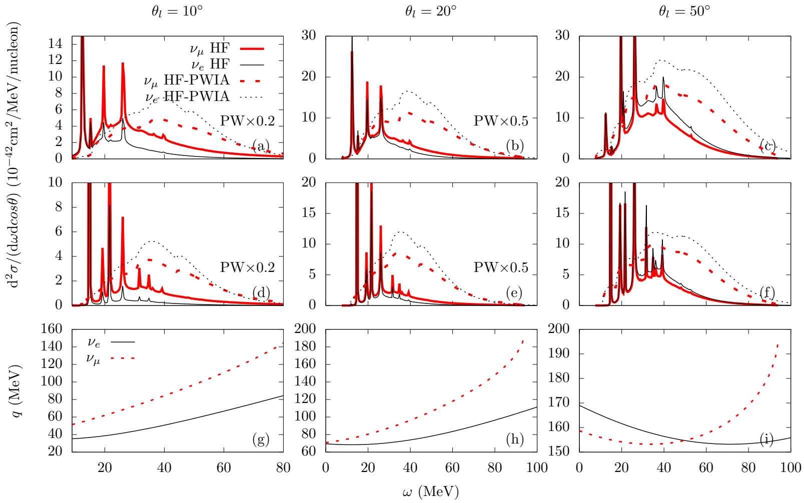

Figure 4.4: HF (full line) and HF-PWIA (dashed) cross section for scattering off ^{40}Ar for different lepton scattering angles at a fixed neutrino energy of 200 MeV, for neutrinos in panels (a)-(c) and antineutrinos in panels (d)-(f). The momentum transferred to the nucleus as a function of the energy transfer for both muon and electron neutrinos at the same kinematics is shown in panels (g)-(i). To better represent the cross section at the most forward angles the HF-PWIA cross sections have been scaled down in some panels.

($\cos\theta_l \approx 1$), the momentum transferred to the nucleus by a neutrino with incoming energy E_ν that in the charged-current process transforms into a lepton with mass m_l and momentum P_l, is for fixed energy transfer ω given by

$$q = \sqrt{E_\nu^2 + P_l^2 - 2\cos\theta_l E_\nu P_l} \approx E_\nu - \sqrt{(E_\nu - \omega)^2 - m_l^2}, \tag{4.20}$$

and hence increases with growing lepton mass. The struck nucleon receives a smaller momentum q from the electron neutrino than in a muon neutrino-induced interaction. This brings along larger nuclear responses $R(q,\omega)$ for muon neutrinos. The lepton kinematic factors that are combined with the responses [175, 187, 188] to construct the cross section generally tend to favor smaller lepton masses in the forward scattering region, but this effect is not large enough to neutralize the dominance of the ν_μ responses [186, 189]. This leads to higher cross sections for reactions induced by muon neutrinos, the larger lepton mass in the final state notwithstanding. Due to their geometry, near detectors tend to be sensitive mostly to forward lepton scattering events. The effect observed here is therefore not marginal but could strongly influence total rates if the angular dependence of the cross section ratio is not fully taken into account. In this kinematic region the cross section is extremely sensitive to subtle nuclear effects that require careful modeling to be fully understood. The importance of a meticulous analysis, judging the impact of the different mechanisms at play in the interaction and the nuclear medium, is illustrated in the following paragraphs.

In Fig. 4.4, we demonstrate the link between momentum transfer and cross section, showing the double differential cross section for both electron and muon (anti)neutrino scattering off argon for a fixed incoming energy, and various scattering angles of the charged lepton together with the momentum transfer in the interaction. For small momentum transfers the ratio $\sigma_{\nu_\mu}/\sigma_{\nu_e}$ can be straightforwardly understood by the difference of momentum transfers depicted in the panels (g) to (i) of the figure. The cross sections are shown for a Hartree-Fock as well as for a HF plane wave impulse approximation (HF-PWIA) calculation. As described above, in the former one the outgoing nucleon wave is distorted by the presence of the nuclear potential, in the latter one, the wave function is replaced by a plane wave. Comparing the full HF results to the HF-PWIA ones, it is obvious that modeling the distortion induced by the nuclear medium is essential. For small momentum transfers, a plane-wave treatment of the nucleon completely passes by the strong influence of the nuclear potential on the slow final nucleon and yields far too high responses.

In the following, we will compare RMF with relativistic plane wave impulse approximation (RPWIA) results and look into the role of Pauli blocking. In an RPWIA approach, the outgoing nucleon is modeled by a relativistic plane wave with fixed momentum. On the other hand, in the RMF approach presented above, the outgoing nucleon has a well-defined energy, but its momentum is only asymptotically defined. Indeed, only far enough from the nuclear potential, the wave function behaves as an on-shell nucleon with well-defined momentum. The outgoing wave function in the RPWIA hence has a large component which is non-orthogonal to the bound states of the nucleus. To illustrate the effect of this on cross sections, we introduce the Pauli-blocked RPWIA (PB-RPWIA). In this approach the outgoing nucleon wave function is described by a relativistic plane wave which is orthogonalized with respect to the bound states. This is done by projecting out the overlap with the bound states [186, 190–192].

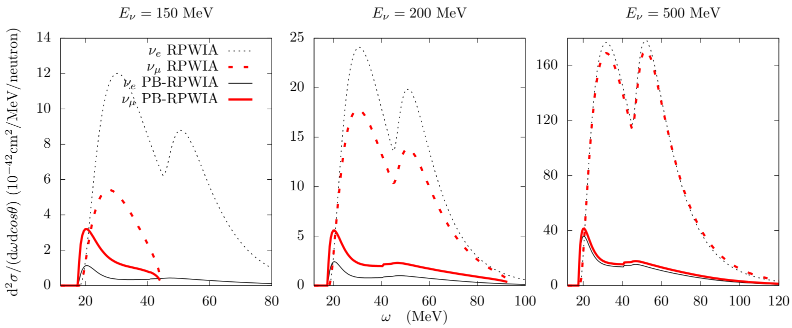

Figure 4.5: Comparison of the ν_e (thin lines) and ν_μ (thick lines) cross sections on carbon for RPWIA (dashed) and PB-RPWIA (solid), in which the non-orthogonal contributions of the plane wave have been projected out. The lepton scattering angle is $\theta_l = 5°$.

In Fig. 4.5 the RPWIA approach is compared with the PB-RPWIA results for both ν_μ and ν_e induced interactions. In the RPWIA results the different shells are clearly visible, and the results greatly overestimate the PB-RPWIA cross sections, which reproduce the magnitude of the RMF and CRPA cross sections of Fig 4.3. It is worth noting that the RPWIA results probe the same kinematic range as the PB-RPWIA, RMF and HF-CRPA approaches. In the calculations, no cuts are made in the phase space, the momentum distribution of the initial- and final-state nucleons are completely determined by the wave functions. As seen in the HF-PWIA results above, in the RPWIA the ν_e cross sections always have a larger magnitude than the ν_μ ones. However, once the spurious non-orthogonal contributions are removed from the plane wave the situation is reversed for forward kinematics. In the RMF and HF-CRPA approaches this effect is naturally implemented because the final-state nucleon is constructed from continuum states, with well-defined quantum numbers, in the same potential as the initial state. In this way Pauli-blocking is implemented in a straightforward quantum mechanical way. This consistency between initial and final states is also present in the Pauli blocked relativistic Fermi gas model, however the treatment of the nuclear initial and final state as plane waves is unrealistic in this kinematic region. In the presented approaches nucleons with small momenta can still be emitted from the nucleus, contrary to in a Fermi gas, but the treatment of the final-state wave function naturally leads to a strong reduction of the cross section for slow nucleons.

Figure 4.6 summarizes our findings. The left panel shows the ratio of ν_e

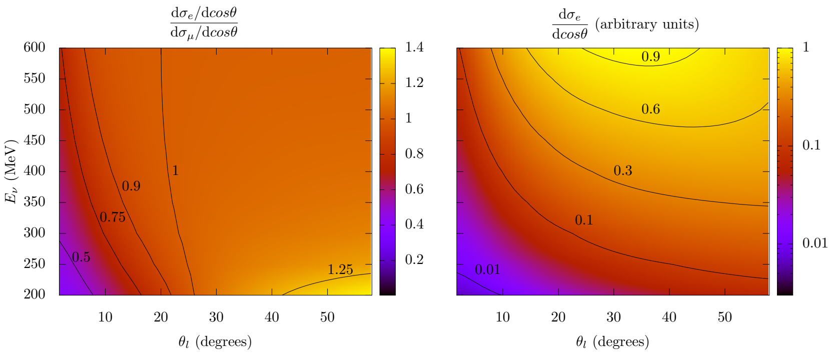

Figure 4.6: Ratio of ^{12}C cross sections as a function of incoming energy and lepton scattering angle, combined with relative strength of the cross section at the same kinematics (normalized such that the maximum in this kinematic region is 1). Results shown here were obtained within the CRPA approach, RMF ratios are very similar [186].

to ν_μ CRPA cross sections to be smaller than 1 over a large part of the forward scattering region for a broad range of incoming energies. The right panel testifies that this region represents a considerable part of the scattering strength.

In conclusion, using different models and independently developed codes, we have shown that taking into account the distortion of the final-state nucleon in the description of charged-current quasi-elastic neutrino scattering off atomic nuclei, muon neutrino-induced CCQE cross sections are larger than the equivalent reaction caused by an electron neutrino for reactions at small energy and momentum transfer. Indeed, in this kinematic regime the nuclear response is extremely sensitive to subtle differences in energy and momentum transfer, resulting in sizable differences in cross sections. This result sheds light on existing uncertainties in ratios that are essential in the analysis of neutrino oscillation and CP violation searches.
As shown, the effect is robust and cannot be seen as an artifact of one model. It is present for neutrinos as well as antineutrinos and manifests itself throughout the nuclear mass table. It is related to the kinematic peculiarities of the interaction in this regime. An incomplete treatment of the distortion of the final nucleon's wave function and of Pauli-blocking effects might however obscure the dominance of muon neutrino induced processes over electron neutrino induced ones. These findings point to the importance of an appropriate description of nuclear effects

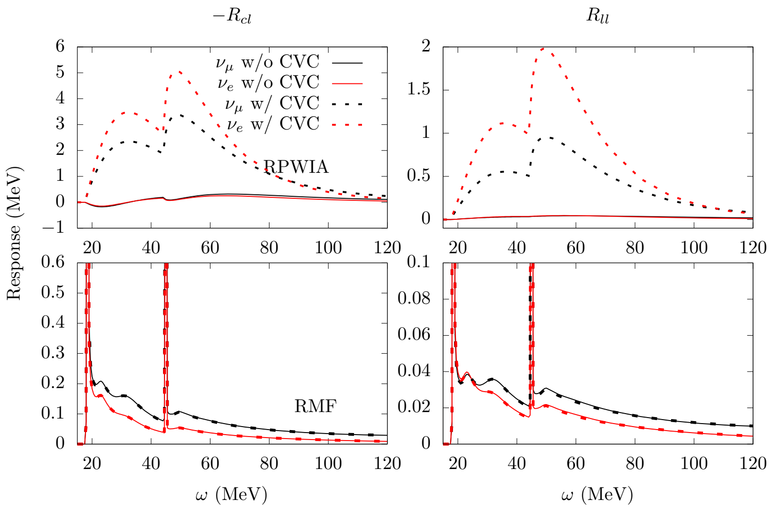

Figure 4.7: Comparison of the responses probed in ν_μ and ν_e charged-current scattering at an incoming energy of 250 MeV and lepton scattering angle of 10 degrees. In the dashed lines CVC is explicitly imposed by setting $J^3 \equiv \frac{\omega}{q}J^0$. Figure from Ref. [193]

on neutrino-induced cross sections, especially for forward scattering, and the need for a careful evaluation of the relevance of various influences of the nuclear medium on the interaction.

4.5 Consistent wavefunctions for initial and final state and CVC

A common issue with applying a single-nucleon current derived for free nucleons to nuclear matrix elements is that there is no prescription to apply said operators to a general off-shell nucleon. Notably this often leads to violation of current conservation, expressed as the relation

$$Q_\mu J^\mu = \omega J^0 - qJ^3 = 0, \tag{4.21}$$

where $\boldsymbol{q}$ is along the z-axis and J^μ is some conserved current such as the Dirac current associated with the operator γ^μ. When this relation is not satisfied it may be explicitly imposed by *defining* $J^3 \equiv \frac{\omega}{q}J^0$. The opposite approach, where J^0 is defined in terms of J^3, is also possible but usually not employed as the 0 component is related to the conserved charge and is assumed to be more accurately described. In the RMF approach, the initial and final nucleon states are solutions of the Dirac equation with central potentials

$$i\partial\!\!\!/_{\mu}\psi(r) = \left[M - S(r) + \gamma^0 V(r)\right]\psi(r). \tag{4.22}$$

By making use of $i\partial_\mu\psi(r) = k_\mu(r)\psi(r)$ we can see that the Dirac current, corresponding to the vector operator γ^μ, evaluated between initial and final state spinors ψ and ϕ respectively with $Q^\mu = k_f^\mu - k_i^\mu$

$$Q_\mu J^\mu = \int d\mathbf{r} e^{i\mathbf{q}\cdot\mathbf{r}}(k_f(r) - k_i(r))_\mu \overline{\psi}\gamma^\mu\phi \tag{4.23}$$

$$= \int d\mathbf{r} e^{i\mathbf{q}\cdot\mathbf{r}}(i\partial_\mu\overline{\psi})\gamma^\mu\phi + \overline{\psi}\gamma^\mu(i\partial_\mu\phi) \tag{4.24}$$

$$= \int d\mathbf{r} e^{i\mathbf{q}\cdot\mathbf{r}}\overline{\psi}\left[M - S_f + \gamma^0 V_f\right]\phi - \overline{\psi}\left[M - S_i + \gamma^0 V_i\right]\phi. \tag{4.25}$$

Hence, the vector current is conserved if the initial and final-state are computed within the same potential. While this is not the case for the energy-dependent potentials introduced earlier, we point out that this is not a fundamental flaw of the energy-dependent potential but rather comes from the limitation we imposed ourselves of using stationary solutions $\psi(r,t) = \psi(r)e^{-iEt}$ of fixed energy, meaning a trivial integral over the time coordinate was already performed in arriving to our expression of the current. In any case, some deviation from current conservation should be expected in neutrino interactions, as e.g. in charged-current interactions on a neutron the final state is a proton an vice-versa. The Coulomb potential which we include for protons should violate current conservation, as isospin is not a symmetry of the electromagnetic interaction.

The previous discussion implies that the problem with violation of CVC does not necessarily arise from the off-shellness of the initial state, but instead from the fact that initial and final state are not treated consistently. We show this explicitly in Fig. 4.7. We compare responses for single nucleon knockout at low energies obtained within the RPWIA and EDRMF. In both cases we compare the result obtained with the full transition current, and when CVC is explicitly imposed by setting $J^3 \equiv \frac{\omega}{q}J^0$. If both descriptions differ, the conservation of the current is violated. We see that in the RMF approach indeed both approaches give the same result, while in the RPWIA differences arise between both approaches, where the results in which CVC is not explicitly imposed are significantly smaller.

4.6 Conclusions

We have provided the expressions for the cross section and nuclear currents within the relativistic distorted wave impulse approximation (RDWIA). We have discussed the applicability of different approaches for the potential in which the outgoing nucleon wavefunction may be treated. We pay special attention to the effects of consistency and orthogonality of initial and final-state wavefunctions and show how these lead to Pauli-blocking and current conservation. We put forward that the Energy Dependent RMF (ED-RMF) approach retains the good low-energy behavior of the RMF approach, while curing its problems at high nucleon energies. We conclude that the ED-RMF should be a suitable potential for the description of the outgoing nucleon wavefunction in situations where the outgoing nucleon remains undetected.

Chapter 5

RPWIA for single-pion production off the nucleus

In this chapter the comparison of RPWIA results to π^+ production data on a water target reported by the T2K experiment is presented. The contents of this chapter were published[1] originally in Ref. [37].

5.1 Introduction

Neutrino energies from beams in accelerator-based experiments, such as MiniBooNE [194, 195], T2K [196, 197], MINERvA [198, 199] and NOvA [200], are spread over a broad range with contributions from increasingly more energetic neutrinos (as is the case in e.g. DUNE [162]). As the energy of the incoming neutrino in an interaction is not precisely known, all measurements are averaged over the incoming neutrino flux. This means that the interaction of the neutrino with nuclear targets should be known and reliably described over a large energy range in order to be able to extract neutrino mixing parameters [5]. Single pion production (SPP) provides a significant contribution to the signal in current and future oscillation experiments. In addition to this, neutrino-induced pion production is important in unraveling the axial structure of the nucleon.

In this paper we compare the predictions of the hybrid relativistic plane wave impulse approximation (hybrid-RPWIA) model for SPP with the charged-current single charged pion ($CC1\pi^+$) cross section on water

1. The contribution of A. Nikolakopoulos as author to published manuscripts of which results are included in this thesis can be found in Appendix D.

reported by the T2K experiment [197]. The T2K ν_μ-flux has a peak for neutrino energies of approximately 600 MeV. The CC1π^+ signal in this energy region mostly consists of elementary single-pion production through the decay of the delta resonance. The delta region is the main focus of most models describing SPP [10, 12, 13, 15–23, 201]. Most models that aim at describing the low energy resonance region tend to exhibit problematic behavior when they are extended to large values of invariant mass ($W \gtrsim 1.4$ GeV) because only first-order diagrams are taken into account [31]. As an exception we mention the coupled channel model of Nakamura et al. [22], which can be extended to larger values of invariant mass ($W \lesssim 2$ GeV) through unitarization of the amplitudes. The T2K data has a larger contribution from interactions with $W > 1.4$ GeV compared to the MiniBooNE [194] and MINERvA [198] data. It is in this respect an interesting dataset, the contributions of the high-W and Delta dominated regions are combined in the cross section, clearly showing the need of a model that can be extended over a broad kinematic range.

The hybrid model for SPP on the nucleon is described in Ref. [31]. The aim is to describe the elementary reaction over a large range of the invariant mass. The hybrid model combines a low energy model (LEM), with a high energy description based on a Regge formalism. The LEM is based on the combination of the first order background diagrams obtained from the Chiral Perturbation Theory (ChPT) Lagrangian density for the πN-system [202], with the contributions of the delta and more massive isospin-1/2 resonances [$P_{11}(1440)$, $S_{11}(1535)$, and $D_{13}(1520)$] [23, 201, 203]. For the resonances, the s- and u-channel diagrams are included. The resonant amplitudes are regularized by a Gaussian-dipole form factor [204, 205] in order to retain the correct amplitude when $s(u) \approx M^2_{res}$, meanwhile eliminating the unphysical contributions far away from the resonance peak. For high values of the invariant mass, the non-resonant amplitudes present pathologies due to the fact that only the lowest order diagrams are considered [31]. Taking into account higher order diagrams quickly becomes unfeasible. Alternatively, the high-energy region can be readily described by a Regge approach, which provides the correct s-dependence of the amplitude at high W. Our approach is based on the procedure for "reggeizing" the non-resonant background as proposed in Refs. [206, 207] for the vector current contributions, which was extended to the axial current in Ref. [31]. The low- and high-energy models for the non-resonant contributions are combined by a smooth W-dependent transition function centered at $W = 1.7$ GeV, with a narrow width such that the models are combined in the region

$1.5 \text{ GeV} \lesssim W \lesssim 1.9 \text{ GeV}$.

The hybrid model is embedded in the nucleus using the relativistic plane wave impulse approximation (RPWIA). The hybrid-RPWIA model is described in Ref. [36], and was compared to pion production data presented by MINERvA [198, 199] and MiniBooNE [194, 195]. The impulse approximation (IA) is adopted in the sense that we treat the hadronic current as the incoherent sum of single nucleon interactions. The bound nucleons are modeled by relativistic mean field (RMF) [181, 182] wavefunctions occupying discrete shells with well-defined angular momentum and binding energy. The hadronic current in the RPWIA is then obtained by describing the final-state pion and nucleon by plane waves with well-defined momentum.

The hybrid-RPWIA model is fully relativistic in both the operators and the wavefunctions. However it does not contain any final state interactions (FSI). The elastic distortion of the outgoing nucleon and pion is ignored as they are described by plane waves. This can be treated consistently in our relativistic quantum mechanical framework by distortion of the outgoing wavefunctions, which will be the next step in this project. Inelastic FSI, which should be taken into account to fully describe π^+ production on the nucleus include pion-absorption, charge-exchange reactions, and secondary pion production. These processes are usually treated in Monte Carlo generators using intra-nuclear cascade models [43, 208, 209], or kinetic transport theory [47], to propagate the particles originating from an elementary vertex through the nucleus. As mentioned, the use of reliable microscopic models is essential to gauge the understanding of the fundamental process. In this work, the effect of FSI is judged by comparing the results to the predictions of the NuWro Monte Carlo event generator, with and without FSI [209].

The structure of this paper is as follows. In Sec. 5.2, we compare the results of the model to experimental data. In the first subsection 5.2.1 the effects of higher mass resonances, medium modification of the delta, and the especially interesting high-W behavior of the LEM and hybrid-RPWIA model are explored. In subsection 5.2.2 we compare our results with those of the NuWro generator. The conclusions are presented in Sec. 5.3.

5.2 Results

These data were obtained with the ND280 detector in the T2K experiment. The phase space is restricted to $P_\mu > 200$ MeV, $P_\pi > 200$ MeV,

$\cos\theta_\pi > 0.3$, and $\cos\theta_\mu > 0.3$ [197]. The signal is defined as a single π^+ and muon in the final state with no other mesons. We compute the cross section on the water target by adding the contributions of two free protons and the nucleons in ^{16}O described within the RMF model.

5.2.1 The hybrid-RPWIA model

The hybrid-RPWIA model is confronted with the T2K CC1π^+ data in Fig. 5.1. Most information on the underlying pion-production mechanism is obtained from the P_π distribution, Fig. 5.1(a). The low momentum region around the peak is dominated by delta-mediated pion production, the higher mass resonances are seen to contribute up to around 1 GeV, and the Regge approach mainly affects the high momentum tail.

The dominance of the delta resonance in charged pion production is clear from comparison with the calculation where only the delta, ChPT, and Regge contributions are taken into account, omitting the higher mass resonances. This is labeled as "Delta+BG" in Fig. 5.1, and is computed without medium modification of the delta width. We see that the higher mass resonances contribute up to 20% of the cross section for P_π between 0.5 GeV and 1 GeV. The other resonances have isospin 1/2; therefore, they can only contribute in the u-channel to π^+ production on the proton. Indeed, the $p(I_3 = 1/2) + \pi^+(I_3 = 1)$ final state can only couple to $I_3 = +3/2$, allowing no $I = 1/2$ resonances in the direct channel. For a full list of isospin coefficients for the different reaction channels in the hybrid-RPWIA model see for instance table I in Ref. [31]. The influence of the isospin 1/2 resonances is thus mainly important for interactions with the neutron, where they contribute in the s-channel.

Because of the importance of the delta resonance, the medium modification of its decay width leads to a significant suppression of the cross section. The width of the delta resonance is modified by the complex part of the delta self-energy in the nuclear medium. We compute this effect within the Oset and Salcedo medium modification (OSMM) formalism [10, 23, 210]. The hybrid-RPWIA model with medium modification of the delta is plotted with the solid red line in Fig. 5.1. The uncertainties and inconsistencies pertaining to the use of this procedure for the medium modification of the delta in the framework of our model were discussed in [36]. In particular the $\Delta N \to \pi NN$ process is included in the modification of the width, a process that contributes to the experimental signal. The contribution of this channel has previously been modeled by multiplying the delta amplitude by a weighting factor, which is then added incoherently to the cross section [23, 36]. We do not

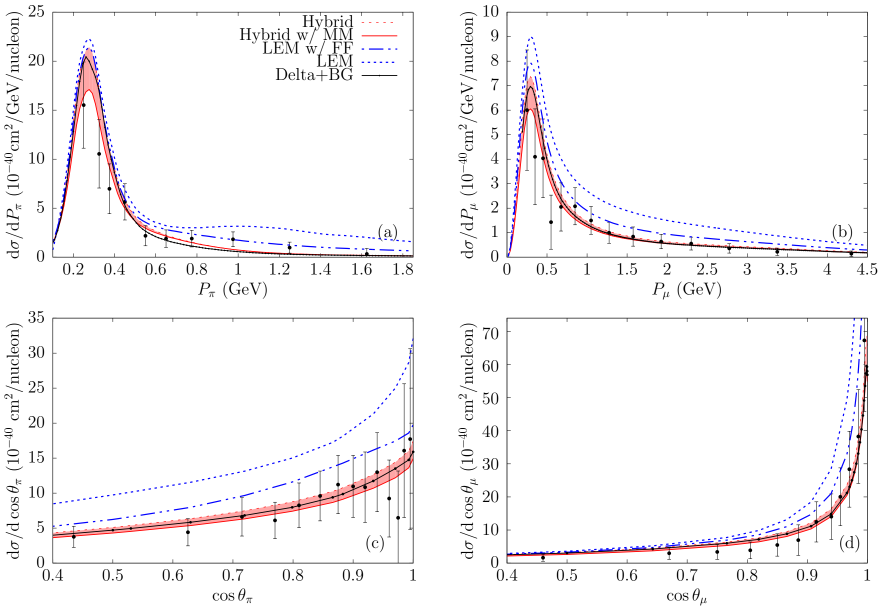

Figure 5.1: Single differential cross sections for the T2K CC1π^+ data sample [197]. We show the hybrid-RPWIA prediction with and without OSMM of the delta width (dashed and solid red lines respectively), compared to the low energy model (LEM), which consists of the resonant and ChPT background diagrams extended to arbitrarily large values of invariant mass W (blue dotted lines). The LEM with cutoff form factors for the resonances is depicted with the blue dash-dotted line. To show the contribution of higher mass resonances the hybrid model calculation including only the background, delta resonance, and Regge-based model is also shown (Delta+BG), it is computed without medium modification of the delta width.

include this reaction here, hence we consider the results with (without) OSMM of the delta as a lower (upper) limit, so that the hybrid-RPWIA model is illustrated by the red band. In principle, the decay width of the other resonances is also modified in the nuclear medium. Including this effect is in the best of cases not free of ambiguities, because the other resonances are not as well known as the delta. Anyhow, their contribution to the overall cross section is small, and approximately limited to the region 0.5 GeV $< P_\pi <$ 1 GeV. Therefore, the medium modification of the higher lying resonances is not taken into account, and can be considered as a (relatively) small uncertainty in our predictions.

The LEM (with or without form factors) and the hybrid-RPWIA were practically identical in there comparison to MiniBooNE and MINERvA $CC1\pi^+$ data as presented in Ref. [36]. In the MINERvA data, which probes significantly more energetic neutrinos, a cut is made restricting the phase space to $W <$ 1.4 GeV, thereby ensuring that the dominant reaction mechanism is delta-mediated pion production. For the kinematics presented here however, we see important deviations between the different curves in Fig. 5.1, showing that regions of higher W contribute significantly to the T2K signal. Indeed, due to the smooth transition between the LEM and the Regge approach, the hybrid-RPWIA model is identical to the LEM with form factors for $W \lesssim$ 1.5 GeV. The point at which these models start diverging can thus serve as a mark for the onset of the region where interactions with higher W contribute.

The $W >$ 1.5 GeV cross section is restricted to the high pion momentum region, where comparison of the hybrid-RPWIA with the LEM is most interesting. The cross section in the LEM for T2K kinematics is illustrated with the dash-dotted blue line in Fig. 5.1(a). The LEM with inclusion of Gaussian-dipole form factors for the resonances is also shown, labeled as "LEM w/ FF". Both results are computed without OSMM. There are large deviations between these different model variations. Both the hybrid-RPWIA and the LEM with form factors seem to compare favorably with the high P_π datapoints. It should be clear however that the LEM is unsuitable to describe the high W interactions, it exhibits unphysical behavior because only the lowest order background diagrams are taken into account [31, 201]. The cutoff form factors cure some of the pathological behavior due to the resonant diagrams, but a significant difference between the LEM with form factors and hybrid-RPWIA model still exists, and is clearly exemplified by the results with $P_\pi >$ 0.5 GeV.

In Figs. 5.1(b) and 5.1(c) where the cross section is presented in terms of P_μ and $\cos\theta_\pi$ respectively, the hybrid-RPWIA approach predicts a

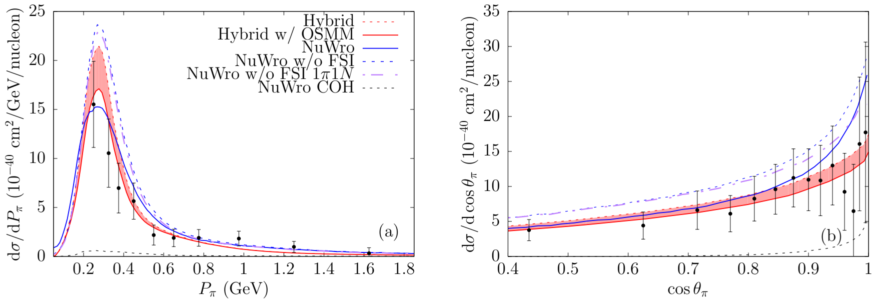

Figure 5.2: Single differential cross sections in terms of pion momentum (a) and scattering angle (b) compared to the CC1π^+ data reported by the T2K experiment [197]. The hybrid-RPWIA model is shown with a red band, where the lower and upper limits correspond to calculations with and without medium modification of the delta width respectively. The NuWro cross section corresponding to the $1\pi 1N$ final state, and the full NuWro calculation before and after FSI, both corresponding to the definition of the CC1π^+ signal, are shown. We also show separately the contribution of coherent scattering in NuWro.

notably smaller cross section over the whole kinematic range compared to the LEM. For these variables the delta contribution and higher W components are not clearly separated. When comparing the models in terms of $\cos\theta_\mu$ in Fig. 5.1(d), we see that the main differences are found at forward muon scattering angles. This forward scattering region has large contributions from neutrinos of higher energies, events with high W and P_π are mainly found here. Muons at larger angles mostly stem from lower energy neutrinos, the kinematic region in which the delta dominates. The differences seen in the forward lepton scattering cross section are thus consistent with the variations of the models in the high P_π tail.

5.2.2 NuWro and Final State Interactions

The hybrid-RPWIA model compares favorably to the T2K CC1π^+ data sample. The total cross section reported by T2K is $\sigma_{\text{tot}} = 4.25 \pm 0.48(\text{stat}) \pm 1.56(\text{syst}) \times 10^{-40}\text{cm}^2/\text{nucleon}$ [197], compatible with $\sigma_{\text{tot}} = 4.82 \times 10^{-40}\text{cm}^2/\text{nucleon}$ obtained with the hybrid-RPWIA model. This result is the average of the predictions with and without OSMM, the uncertainty (as illustrated by the red band in Fig. 5.2) due to medium modification of the delta width is around 9 %. However, these results do not include any FSI, which are expected to reduce the cross section due to absorption and charge-exchange of the produced pion. Indeed, the NuWro Monte Carlo generator predicts a total cross section of $6.97 \times 10^{-40}\text{cm}^2/\text{nucleon}$ before FSI, and $5.44 \times 10^{-40}\text{cm}^2/\text{nucleon}$ after taking into account FSI. In this section, we judge the impact of FSI on the single differential cross sections in terms of muon and pion kinematics by comparing our results to NuWro calculations. One should however be careful in estimating the effect of FSI by directly comparing both models because there are significant differences between them.

We use NuWro version 17.09, with default values for all parameters [211]. The elementary SPP mechanism in NuWro, i.e. before FSI, consists of the delta resonance treated in the Adler-Rarita-Schwinger model [212], parametrized by dipole form factors fitted to SPP data [74]. A phenomenological non-resonant background is obtained from deep inelastic scattering (DIS), it is added incoherently to the resonant cross section [213]. For $W > 1.6$ GeV a model based on DIS [213, 214] and Pythia hadronization routines is used [215]. A smooth transition from the resonance region to DIS is implemented for W between 1.4 and 1.6 GeV [216].

In NuWro, events originating from quasi-elastic scattering (QE), meson-exchange currents (MEC), and coherent scattering are generated, in addition to the elementary SPP process. The final-state particles from these interactions, excluding those from coherent pion production, are propagated through the nuclear medium where they can undergo secondary interactions [209].

We compare the hybrid-RPWIA model to three results corresponding to different selection cuts in the NuWro simulation. First, we present the result where only a π^+ and a single nucleon are found in the hadronic final state, before taking into account FSI. This result, labeled as "NuWro w/o FSI $1\pi 1N$" and depicted with the dash-dotted blue lines in Fig. 5.2, corresponds to the elementary SPP cross section described above, which should be comparable to the hybrid-RPWIA model. The second result is labeled as "NuWro w/o FSI" and corresponds to the full calculation before FSI, where the hadronic final state is defined as a single π^+ and any number of nucleons (dashed blue lines in Fig. 5.2). In practice, the main difference between the "NuWro w/o FSI", and the "NuWro w/o FSI $1\pi 1N$" cross sections stems from the contribution of coherent scattering, which makes up around three percent of the former, and does not contribute to the latter. We show the contribution of coherent scattering in NuWro separately, it is depicted with the dotted line and

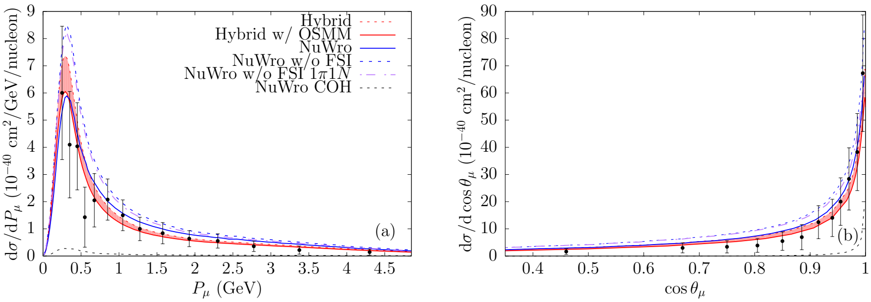

Figure 5.3: Single differential cross sections in terms of P_μ (a), and $\cos\theta_\mu$ (b), compared to T2K CC1π^+ data [197]. The labels are the same as in Fig. 5.2.

labeled as "NuWro COH". Finally, the cross sections corresponding to the experimental signal after FSI are also shown. The contributions of QE and MEC to the cross section are negligible, and the most important effect of FSI is a decrease of the cross section. This final NuWro result corresponds to the solid blue line in Figs. 5.2 and 5.3.

The influence of FSI on the P_π distribution mainly consists of a strong reduction of the amount of pions with low momenta, this is shown in Fig. 5.2(a). The characteristic shape of the T_π cross section as shown in Refs. [10, 23, 36], with a pronounced peak at low pion energies, is largely missing in this dataset. This can be ascribed to the T2K phase space being restricted to more forward pion scattering angles. The cuts on muon variables only lead to an overall reduction of the P_π cross section leaving its shape unaffected. The restriction $\cos\theta_\pi > 0.3$ however results in a very strong reduction of pions with small momenta, thereby quenching this peak. This can be seen in Fig. 5.4, where the NuWro cross section with and without FSI is plotted for different kinematic cuts as used in the T2K analysis.

The NuWro $1\pi 1N$ cross section is basically the same as the full cross section without FSI, the latter is slightly larger mainly due to the inclusion of coherent scattering. In any case, the NuWro $1\pi 1N$ cross-section is larger than the hybrid-RPWIA over the whole kinematic range. This is consistent with our comparison to NuWro $1\pi^+$ calculations at MiniBooNE and MINERvA kinematics [36]. The difference could be attributed to the form factors used to describe the couplings. It was shown in Ref. [31], where both models are compared to SPP neutrino-deuterium data [217], that NuWro systematically obtains a larger total cross section.

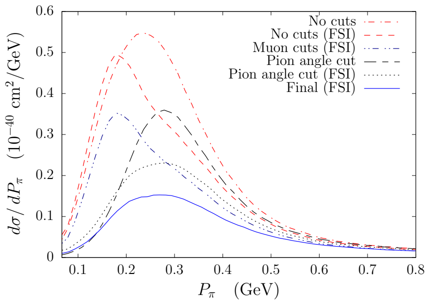

Figure 5.4: Single differential cross sections in terms of P_π without any cuts, and for different kinematic cuts used in the T2K data. The restriction to forward pion scattering angles, necessary in this T2K analysis, masks the migration to low pion momenta due to FSI.

The hybrid-RPWIA model tends to overestimate the number of pions at the lowest momenta, leaving room for FSI. However, a reduction of the low momentum peaks, as estimated by comparing to NuWro, would lead to the hybrid-RPWIA underpredicting the lowest momentum bins for both the P_π, and P_μ cross sections shown in Figs. 5.2(a) and 5.3(a). This is also found in the GiBUU prediction of Ref. [218], where it is argued that coherent pion production could provide additional strength in this region.

In the comparison of the hybrid-RPWIA model with MiniBooNE and MINERvA $1\pi^+$ data, pion momenta up to approximately 500 MeV were studied, but predictions for higher momentum were provided [36]. Here the comparison is extended to larger pion momenta and we again see that NuWro cross section in the high-P_π region, which is dominated by DIS, is larger than the Regge description in the hybrid-RPWIA model. The small cross section in the higher P_π regions, relative to the T2K data, may point to a lack of higher mass resonances [219], or of high energy mechanisms that may contribute to the signal after FSI. The problem is tied to the description of the transition region. Adding additional higher mass resonances would require unitarization of the amplitude in the LEM, thereby extending the validity of the LEM such that the transition region can be moved to larger values of W.

We show the comparison with the $\cos\theta_\pi$ distribution in Fig. 5.2(b). The cross section in the hybrid-RPWIA model does not show the sharp rise at forward scattering angles present in the NuWro calculations. It is in this kinematic region that contributions from coherent scattering and

DIS are most important. The effect of FSI is a constant reduction over the whole range of $\cos\theta_\pi$, except for the most forward angles where the reduction is not as strong as for the rest of the angular range. This can be partly attributed to the fact that the coherent scattering events are not subject to FSI through the cascade in NuWro.

In Fig. 5.3 the comparison with the data in terms of muon kinematics is shown. Again, a difference in the overall strength in the cross section compared to NuWro is evident. The high-P_μ tail is described well by the hybrid-RPWIA model, as is the low momentum peak. One could expect a slight underestimation of the low-P_μ peak if FSI, as predicted by NuWro, would be included. The same holds for the forward scattering cross section, in agreement with the findings of Ref. [218]. We see that these are exactly the kinematic regions where the NuWro coherent scattering cross section provides additional strength. For $\cos\theta_\mu < 0.9$ the model would be in agreement with the data even after a reduction of the cross section from FSI as estimated from the NuWro result. The coherent scattering cross section is negligible for larger muon angles, therefore, the lower $\cos\theta_\mu$ cross section would remain unaffected.

It is interesting to compare the T2K-flux [220] with the neutrino fluxes in MiniBooNE and MINERvA, and confront the datasets with each other via comparison to the hybrid-RPWIA model predictions. The T2K flux has a peak for neutrino energies around 600 MeV, comparable to the energy regime spanned by MiniBooNE [221]. However, the T2K-flux has a more significant high-energy tail. This, along with the restrictions on lepton and pion kinematics in the T2K data, leads to the T2K data having a larger contribution from high energy neutrinos than the MiniBooNE data [194]. The MINERvA experiment spans a far larger energy range, the flux peaks around 3 GeV, and extends to about 20 GeV [222]. But, contrary to the MINERvA samples [198, 199], there is no restriction on (reconstructed) quantities such as W in the T2K data. Both the hybrid-RPWIA, and NuWro calculations compare favorably to the T2K and previously presented MINERvA [36] $CC1\pi^+$ datasets. Both models however underpredict the MiniBooNE data. The comparison of the MiniBooNE and T2K data in the delta-dominated region is the most direct as the neutrino energy range of both experiments is similar. In that sense there seems to be no obvious reason that explains why the hybrid-RPWIA model underestimates the MiniBooNE data for low values of T_π (see Fig. 5 in Ref. [36]), while overpredicting T2K data in the same kinematic region, Fig. 5.2(a). Note that a large systematic error of the measured cross sections originates from uncertainties in the flux, this could play an important role in bridging the apparent disagreement between the data.

5.3 Conclusions

We compared the hybrid-RPWIA to the low energy model (LEM) and the T2K CC1π^+ data. It is shown that a high energy model is necessary at T2K kinematics. The contributions from the high energy tail of the flux are significant, and using the LEM leads to a sizeable overestimation of the cross section. Introducing Gaussian-dipole form factors to regularize the resonant amplitudes cures some of the pathological behavior due to the resonant amplitudes far away from $s(u) \approx M_{res}^2$. Still, the LEM with form factors overestimates the cross section for high pion momenta when compared to the hybrid-RPWIA model. These pion momenta were inaccessible in the MiniBooNE and MINERvA CC1π^+ kinematics presented in Ref. [36], due to the cut on W in MINERvA, and the smaller high energy contributions in MiniBooNE.

The shape of the single differential cross sections obtained within the hybrid-RPWIA model presented here are similar to the NuWro results, with the main exception being the forward pion scattering region. It is in this region that the coherent and DIS contributions in NuWro predict a sharp rise. The shape of the cross section in terms of pion momentum after FSI is seen to be affected by the restriction on the pion scattering angle.

When considering the size, we see that the hybrid-RPWIA model systematically predicts a lower cross section than the NuWro Monte Carlo generator. These results are consistent with the previous comparisons shown in Refs. [31, 36]. Both the MINERvA and T2K $CC1\pi^+$ compare consistently to the NuWro and hybrid-RPWIA models, the comparison to these datasets and to the results reported by MiniBooNE seems to suggest an unresolved disagreement between the former and latter data.

The general comparison of the hybrid-RPWIA model to the T2K data is favorable, the model reproduces the shape and strength of the data well, meanwhile leaving room for FSI at low pion and lepton momenta. The coherent scattering cross section obtained in the NuWro calculation provides additional strength in the kinematic regions where the hybrid-RPWIA might underestimate the data after FSI, specifically along the delta region, and for forward muon angles.

Chapter 6

RDWIA for single-pion production off the nucleus

We perform RDWIA calculations for electroweak single-pion production (SPP) off nuclei and compare the results to experimental data. In this chapter we present results for charged-current interactions off 12C, we compute cross sections integrated over the outgoing hadron angles. As the neutrino flux for accelerator experiments is broad, it is computationally non-trivial to do flux-folded calculations for SPP off nuclei. Following the definitions described in Chapter 4, we can write the semi-inclusive cross section as a sum of exclusive cross sections from different single-particle levels in the nucleus. The flux-weighted cross section for scattering off a single-particle level is

$$\frac{\mathrm{d}^8\sigma}{\mathrm{d}E_\nu \mathrm{d}E' \mathrm{d}\cos\theta_l \mathrm{d}E_\pi \mathrm{d}\Omega_\pi \mathrm{d}\Omega_N} = \Phi(E_\nu)\frac{G_F^2\cos^2\theta_c}{2}\frac{k'}{E}\frac{M_N k_\pi k_N}{2\,(2\pi)^7\, f_{rec}} L_{\mu\nu} H_\kappa^{\mu\nu} \tag{6.1}$$

where a trivial integral over ϕ_l was performed yielding a factor 2π. The experimental data are for the most part reported as single-differential cross sections. This means that 7-dimensional integrals have to be performed over the kinematic variables to compare the results to cross sections reported by experiments.

To make calculations over the broad phase space covered by experiments possible we make use of the Rosenbluth separation as detailed in Section 2.3. The hadron tensor depends only on the hadronic degrees of freedom. We compute it in the reference system where $\mathbf{q} = \mathbf{k}_\nu - \mathbf{k}_l$ is along the z-axis as function of the variables $\omega, Q^2, T_\pi, \Omega_\pi, \Omega_N$ such that we don't need to compute the hadron tensor separately for every E_ν.

The rotation of the whole hadronic system along the direction of $\mathbf{q}$ leaves the difference of azimuth angles $\phi_\pi - \phi_N$ invariant while the average azimuth angle $\frac{\phi_\pi+\phi_N}{2}$ is rotated. Hence, we set $\phi_N = -\phi_\pi$, fixing the average angle to zero. The dependence on the average angle is then described by the Rosenbluth decomposition of Eqs. (2.51-2.55), such that after integration over the average angle we retain only the angle-independent hadron tensor elements of Eq. (2.51). With this we may define angle-integrated hadronic tensor elements as

$$\tilde{H}^{\mu\nu}(\omega, Q^2, T_\pi) = 2\pi \int d\Omega_\pi \, d\cos\theta_N \frac{M_N k_\pi k_N}{2(2\pi)^8 f_{rec}} \\ H^{\mu\nu}\left(\omega, Q^2, T_\pi, \Omega_\pi, \cos\theta_N, \phi_N = -\phi_\pi\right), \tag{6.2}$$

such that the cross section integrated over hadron angles is given by

$$\frac{\mathrm{d}^4\sigma}{\mathrm{d}E_\nu \mathrm{d}E' \mathrm{d}\cos\theta_l \mathrm{d}T_\pi} = \Phi(E_\nu) G_F^2 \cos^2\theta_c \frac{2\pi k'}{E} \\ \times \left[L_{00}\tilde{H}^{00} + 2L_{03}\tilde{H}^{03} + L_{33}\tilde{H}^{33} + \frac{L_{11}+L_{22}}{2}\left(\tilde{H}^{11} + \tilde{H}^{22}\right) + 2iL_{12}\tilde{H}^{12}\right]. \tag{6.3}$$

It are these angle-integrated hadron tensor elements which we compute as function of ω, Q^2, and T_π, these are then stored in tables which may be used to compute the cross section for any experimental flux using Eq. (6.3). For the carbon nucleus we compute 2 such tables, corresponding to the $s1/2$ and $p3/2$-shells, for every reaction channel.

The main advantage of precomputing these angle-integrated hadronic tensor elements as function of ω, Q^2 and T_π is that we can make use of efficient integration routines to perform the angular integrals in the $\mathbf{q}$ along z-system. The downside is that we can only compare to data which cover the whole angular phase space for the pion, as angular cuts in neutrino experiments are expressed as function of angles with respect to the beam direction, while we compute angles with respect to $\mathbf{q}$.

In addition, in the RDWIA we perform the 3-dimensional r-integral for the hadron current of Eq. (4.16) numerically. In order to asses the numerical precision of this procedure, we have computed it also numerically for RPWIA, by setting the potential for the final state to zero. These results have been compared to RPWIA calculations in which the hadron current is computed analytically using Eq. (4.18), and they are found to agree to within less than half a percent.

In the neutrino-nucleus scattering data to which we will compare, the experimental signal is defined by (at least) a single pion and associated

$\mu^{\pm}$. No explicit restrictions are placed on the type of the other hadrons that are present in the final-state.

Here, the pion state is treated as a plane wave, this is an approximation as clearly the outgoing pion will experience FSI in the nuclear medium. The treatment of the pion FSI is non-trivial as not all inelastic FSI processes remove the pion from phase space which determines the experimental signal. For example a pion which rescatters without charge-exchange and knocks out an additional nucleon would still count towards the experimental signal, while an optical-potential model would remove the strength associated with these interactions. In contrast, in an electron scattering experiment in which the incoming energy is known, this would show up as an event with a larger missing energy/momentum and can be rejected based on kinematics. The complications due to microscopic modeling of pion FSI fall beyond the scope of the current work, and we treat the pion as a plane wave in order to keep the full strength of the interactions. In Chapter 5 we have directly compared to the NuWro results with and without FSI to explicitly look at the effect of pion FSI. Here we will contextualize the possible effect of pion FSI on the data-model comparison by referring to cascade model predictions which are presented together with the data releases when available.

We treat the outgoing nucleon wavefunction in the Energy-Dependent Relativistic Mean Field (EDRMF) potential which was discussed in Section 4.3. The reasoning is that, as the outgoing nucleon remains undetected, the real potential makes sure that all strength is retained. The outgoing nucleon may rescatter, be absorbed, knock out additional nucleons, and undergo any type of FSI in general, but any of these cases should still contribute to the cross section. From comparisons to inclusive electron data, especially in the quasielastic regime, the EDRMF is found to give a good description in exactly this case [131, 148].

6.1 Comparison of hadronic responses

Before comparing cross sections to neutrino scattering data which are averaged over the experimental fluxes, we first take a look at the hadron tensor elements which enter in the current in order to give an energy-independent comparison of the RPWIA and RDWIA calculations. After integration of Eq. (6.3) over T_π, the cross section differential in lepton

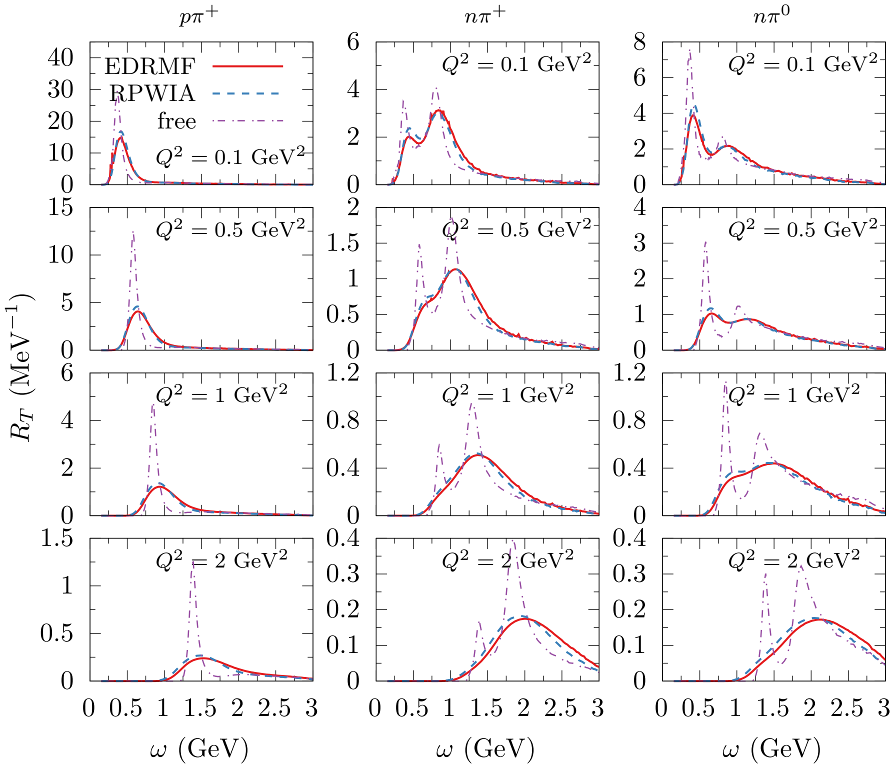

Figure 6.1: Transverse response as defined in Eq. 6.4 as function of ω for fixed values of Q^2. The solid red lines and blue dashed lines correspond to EDRMF and RPWIA results for ν-induced SPP off the carbon nucleus, normalized per target nucleon. The left column corresponds to π^+ production off the protons, while the middle and right columns are for positive and neutral pion production off the neutrons respectively. These results are compared to the corresponding cross section obtained for a free nucleon target.

kinematics at a fixed incoming energy is

$$\frac{\mathrm{d}^2\sigma}{\mathrm{d}E'\mathrm{d}\cos\theta_l} = G_F^2 \cos^2\theta_c \frac{2\pi k'}{E} \times \left[L_{00}R_{CC} + 2L_{03}R_{CL} + L_{33}R_{LL} + \frac{L_{11}+L_{22}}{2}R_T + 2iL_{12}R_{T'} \right], \tag{6.4}$$

where the responses R, which only depend on ω and Q^2, are obtained by integration of the corresponding terms in Eq. (6.3) over the pion energy. In Fig. 6.1 we show the ω dependence of R_T at different fixed values of Q^2. We compare results obtained in EDRMF and RPWIA for carbon normalized per nucleon, and for free nucleons for the three charged-current interaction channels. A clear smearing of the resonance peaks is found for the cross section on carbon compared to the free nucleon case, this smearing becomes more pronounced as Q^2 increases. We see that for $Q^2 \gtrsim 1$ GeV^2, the different resonance peaks which are clearly present in the free responses, become indistinguishable in the nuclear response. Beyond the resonance region, we find that the high-ω tail in all models are comparable in shape and magnitude.

The difference between the EDRMF and RPWIA responses are rather modest, one finds that the EDRMF results are slightly shifted to higher ω compared to the RPWIA, this becomes most obvious for large value of Q^2. For the smaller values in the reactions on neutron targets, it seems that some of the strength that is shifted to higher ω from the delta peak ends up filling up the second resonance region, this makes the EDRMF and RPWIA results comparable in this region.

6.2 Minerνa experiment

The MINERνA (Main Injector Neutrino ExpeRiment to study ν-A interactions) is located at FNAL and is specifically designed to measure neutrino-nucleus cross sections for a variety of interaction mechanisms. The experiment is exposed to the NuMI (Neutrinos at the Main Injector) beam [222, 223]. The pion-production measurements in MINERνA were performed with the NuMI beam in low-energy mode, which spans an energy region between 1 and 20 GeV with a peak around 3 GeV. Several measurements have been reported for neutrino and antineutrino-induced charged and neutral pion production on a CH target [224–230].

Apart from the directly measurable kinematic variables, the angles and energies of the detected particles, the MINERνA experiment has also reported a number of cross sections in terms of reconstructed variables, most notably Q^2 and W^{free}. These are denoted reconstructed variables because they depend on the neutrino energy E_ν, which is not known on an event-to-event basis

$$Q^2 = 2E_\nu \left(E_\mu - p_\mu \cos\theta_\mu\right) - m_\mu^2, \tag{6.5}$$

$$W^{free} = \sqrt{M_N^2 + 2M_N(E_\nu - E_\mu) - Q^2}. \tag{6.6}$$

Here W^{free} corresponds to the invariant mass when scattering off a free nucleon that is at rest in the lab-frame resulting in the same lepton kinematics. In all but one of the datasets the experiment makes use of calorimetric reconstruction of the neutrino energy. The exception is the recent measurement of antineutrino π^- production of Ref. [230]. In this case the reconstructed energy is defined as the incoming energy which would yield the same pion and lepton energies and scattering angles in the case that the scattering occurred on a nucleon which is at rest in the lab-frame, corrected for binding energy. In any case, these energy estimators are used in the definition of Q^2_{rec} and W^{free}_{rec}, such that these do not to true values. A comparison of a model to these reconstructed variables, while their definition is clear and unambiguous, is cumbersome. This is especially true for the reconstructed energy defined from calorimetry as one in principle needs to model or estimate all visible energy deposits in the detector. In the following we will compare these reconstructed variables to true variables, computed with the real incoming energy.

6.2.1 Charged pion production

Measurements of neutrino and antineutrino induced charged-pion production on carbon where reported in Refs. [224, 226, 229, 230]. The interactions are obtained on a predominantly hydrocarbon target which we model as a carbon nucleus and a free proton (CH). In view of isospin symmetry between the neutrino and anti-neutrino interaction we discuss these measurements jointly. Charged pion production may occur due to the interactions on the protons and neutrons in the carbon nucleus. Isospin symmetry implies that for free nucleons the interactions

$$W^+ + p \to p + \pi^+, \tag{6.7}$$

and

$$W^- + n \to n + \pi^-, \tag{6.8}$$

share the same amplitude, which is purely isospin 3/2 and is dominated by the direct excitation of the delta. The interactions

$$W^+ + n \to n + \pi^+, \tag{6.9}$$

$$W^- + p \to p + \pi^-, \tag{6.10}$$

also have the same amplitude on the nucleon level, which gets a relatively large contribution from the isospin 1/2 resonances and for which the coupling to the direct delta is a factor 3 smaller than for the reaction channels of Eqs. (6.7-6.8).

Under the assumption of perfect isospin symmetry for the carbon nucleus, both the neutrino and antineutrino process can hence be described by the same responses where only the vector-axial interference term enters with an opposite sign in both reactions. In the nuclear medium small isospin breaking effects are present even for an even-even nucleus however. In our mean field framework, the wavefunctions for protons and neutrons in shells with the same quantum numbers are practically identical, but the binding energies for equivalent shells are around 3 MeV smaller for the protons than for the neutrons in ^{12}C due to the Coulomb potential. Additionally, in the RDWIA, the outgoing protons are subject to the Coulomb potential of the nucleus while the neutrons are not. These effects have been studied e.g. in Ref. [231] for single-nucleon knockout at kinematics relevant to T2K. For a light nucleus as carbon these effects are small, especially compared to other uncertainties, and can be neglected for describing SPP in MINERνA. We will hence use the same responses to describe the neutrino and anti-neutrino reactions with carbon, specifically the responses were computed for the neutrino-induced interactions. We add also the interaction with the free proton in CH when appropriate.

Cross sections for neutrino-induced single π^+ production in MINERνA were first reported in Ref. [224]. Two different kinematic cuts were employed, one for $W_{rec}^{free} < 1.4$ GeV to emphasize delta-mediated single pion production, and one with $W_{rec}^{free} < 1.8$ GeV where the signal is defined as at-least one positive pion. A later publication supersedes these original data [226]. We will not compare to the datasets in which the signal allows explicitly for multiple charged pions, but will only consider the data for which multiple pions are rejected. For the $1\pi^+$ production, an updated dataset has been released which includes lepton kinematics and reconstructed quantities [232]. Compared to the originally published data [224] the cross section in these updated data seems to be only

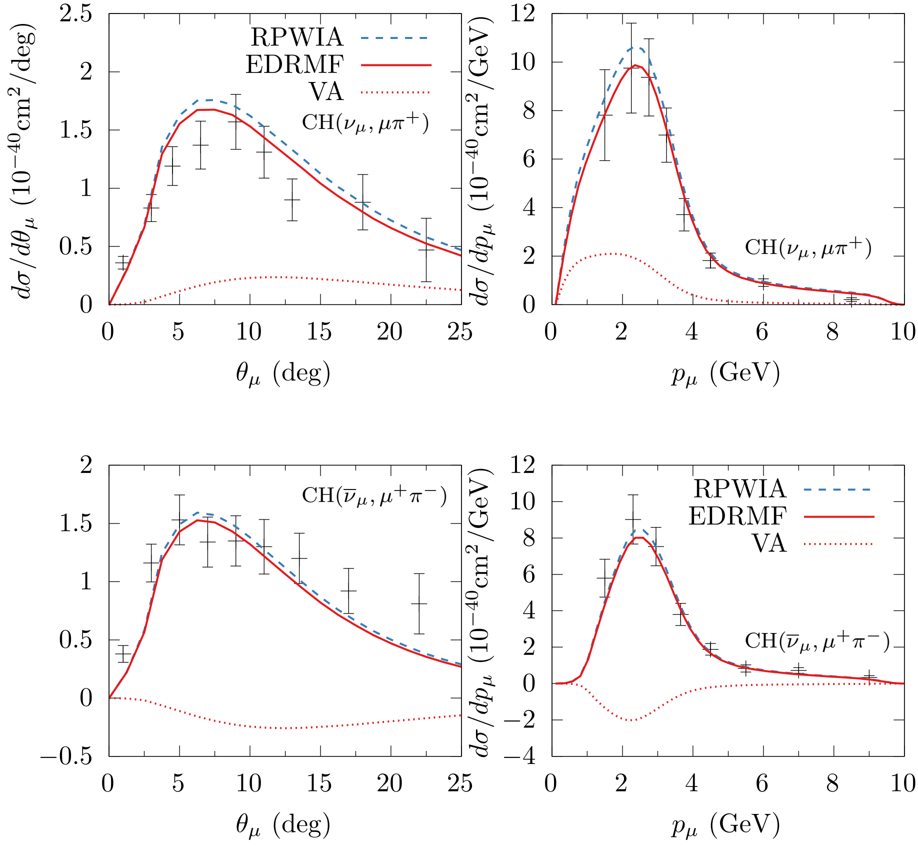

Figure 6.2: Cross sections differential in lepton kinematics for the MINERνA CC1π^+ signal (top panels) and the CC1π^- (bottom panels), normalized per nucleon.

slightly larger. While no specific publication describing the updated data exists, we will compare to them assuming that the experimental constraints are the same as in the original publication. Specifically this means that the data are obtained for $E_{\nu,rec} < 10$ GeV and $W_{rec}^{free} <$ 1.4 GeV which we apply to the true values of E_ν and W^{free}. For the anti-neutrino data $W_{rec}^{free} < 1.8$ GeV, and additionally $\theta_\mu < 25$ deg. Due to the different kinematic cuts in these datasets, one should be careful when directly comparing cross sections between both signals.

We show the comparison to the cross section in terms of lepton kinematics in Fig. 6.2. In both cases we find a excellent description of the cross section in terms of muon momentum, which indicates an overall

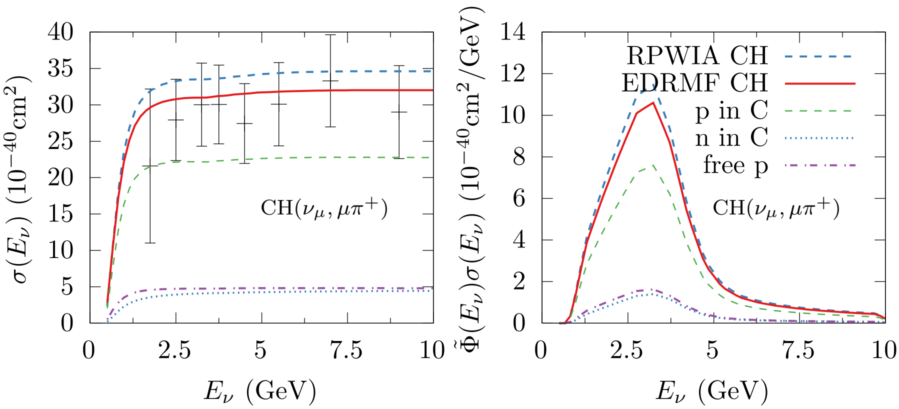

Figure 6.3: Total cross section as function of energy for the MINERνA CC1π^+ signal, normalized per nucleon. The right panel shows the cross section weighted with the normalized neutrino flux.

magnitude in line with the data. Unlike the scattering angle data, the muon momentum data should cover the whole phase space in both cases. For the anti-neutrino comparison a cut $\theta_\mu < 25$ deg is applied to the data and the model, while for the neutrino data all lepton angles are included. The cross section in terms of lepton angle is overpredicted at small angles and in agreement for larger angles in the neutrino case, while for the antineutrino data the cross section is underpredicted at the largest angles, and in line with the data for the smaller angles.

The total cross section is shown in Fig. 6.3. From the plateau in the total cross section the overall reduction observed in the RDWIA compared to the RPWIA is approximately 10 percent. This contrasts with the total cross sections obtained for the antineutrino induced interaction shown in Fig. 6.4, where the relative difference between the RPWIA and EDRMF result is smaller.

The reason for this seems to be that in the CC1π^+ signal a cut $W^{free} <$ 1.4 GeV is imposed while in the anti-neutrino calculation W^{free} values up to 1.8 GeV are included. In Fig. 6.5 we compare the cross sections in terms of W^{free} and the energy transfer ω for both the π^+ and π^- production channels. It is seen that the EDRMF implies a reduction of the cross section for intermediate W^{free}, while at large values the RPWIA and EDRMF give more similar results. The effect of distortion does not tend to vary much with ω. Apart from a minor shift, the shape

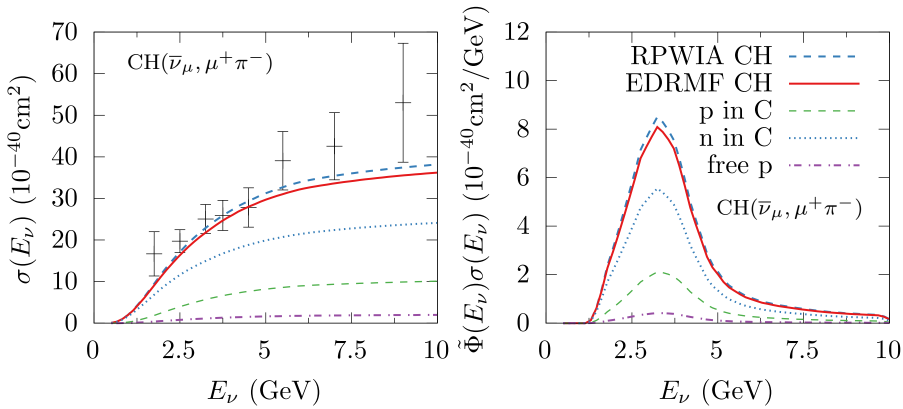

Figure 6.4: Total cross section as function of energy for the MINERνA CC1π^+ signal, normalized per nucleon. The right panel shows the cross section weighted with the normalized neutrino flux.

of the cross sections in terms of ω are almost identical in RPWIA and EDRMF for π^+ production. In π^- production a slight dependence of the shape on ω is present, which follows the scaling with W^{free} as larger values only become accessible for large ω. Hence, the larger proportion of small W^{free} due to the cut at 1.4 GeV explains why the relative reduction in EDRMF compared to RPWIA is larger for the neutrino-induced interaction in this case.

The effect of the final-state potential is most appreciable in the cross section as function of nucleon energy shown in Fig. 6.6. In this figure we show the cross section for scattering off carbon only, the free proton contribution is not included. One sees the main effect at low T_N, the nucleon energy in EDRMF is shifted towards lower values. This results in a reduction along the peak, which is counteracted by an increase at the smallest values of T_N. In the data to which we compare, the outgoing nucleon remains undetected. This final-state nucleon is also subject to inelastic final-state interactions, which may result in the knockout of additional nucleons or production of other particles. The energy T_N in this case can hence be interpreted as a proxy for the total energy which is redistributed over the undetected hadronic system.

The cross section as function of pion kinetic energy is shown in Fig. 6.7. The data in this case densely covers a rather limited region of phase space. The comparison to the π^+ data is satisfactory if one takes into

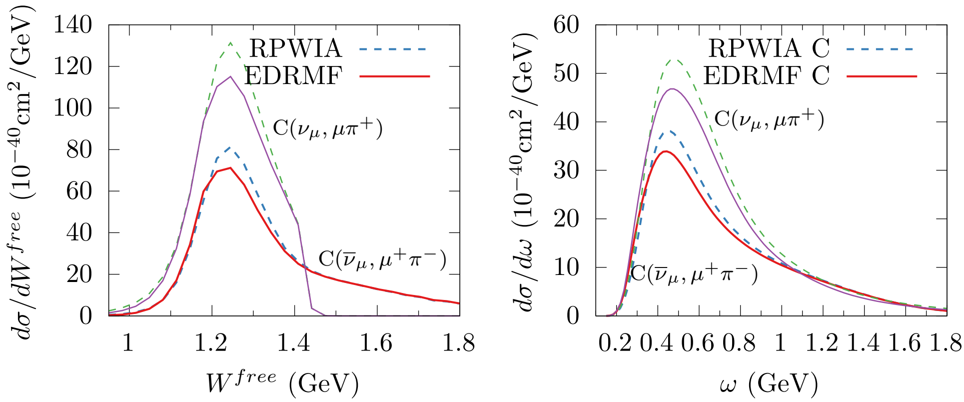

Figure 6.5: Comparison of RDWIA (solid) and RPWIA (dashed) cross sections for π^+ production (green and purple lines) and π^- production (blue and red lines) in MINERνA

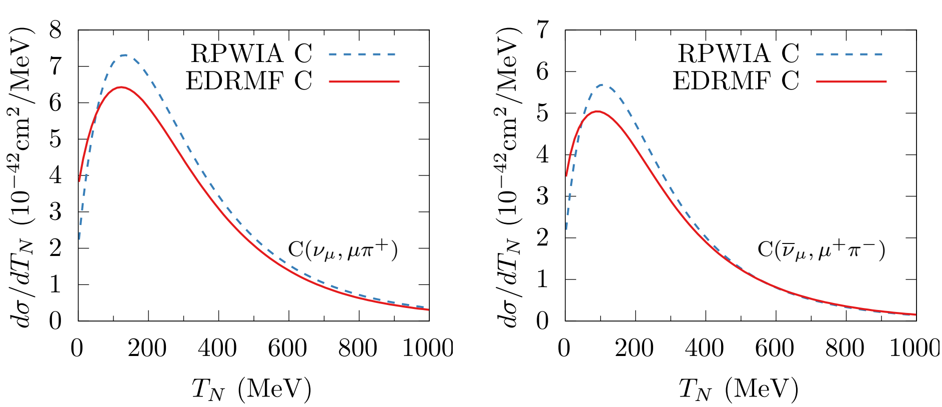

Figure 6.6: Comparison of RDWIA (solid) and RPWIA (dashed) cross sections for π^+ production (green and purple lines) and π^- production (blue and red lines) in MINERνA

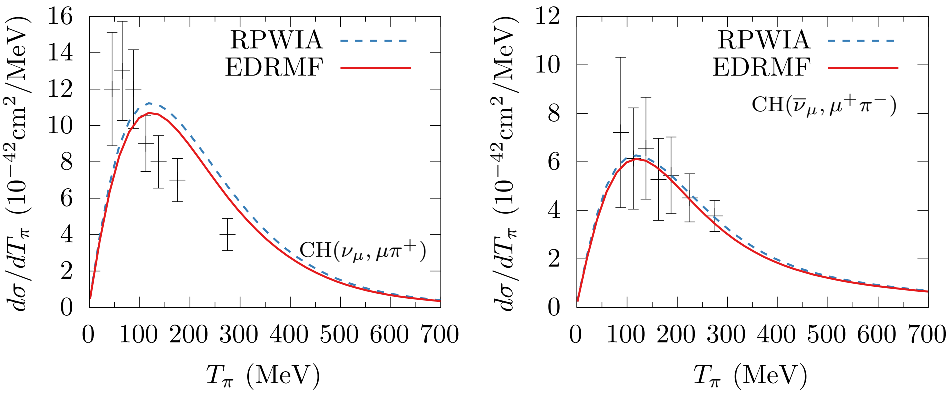

Figure 6.7: Cross section as function of pion kinetic energy for the MINERνA CC1π^+ signal on the left and for CC1π^- on the right.

account the predictions of cascade models for pion FSI. These models predict a reduction of the number of pions at energies above 150 MeV with an increase at smaller energies due to pions losing energy in FSI. A similar effect of FSI is predicted for the π^- cross section, but in this case the model leaves less room for a reduction due to FSI. It should be remembered that the π^- data extends up to $W^{free} = 1.8$ GeV while the π^+ data only goes up to 1.4 GeV, meaning that the π^- data receives more sizable contributions from the higher-mass resonances through interactions with the protons in the target. This interaction mechanism has been found to be underpredicted in the comparison to data obtained on free nucleons.

The cross section as a function of (reconstructed) Q^2 is shown in Fig. 6.8. As mentioned before, the calculations are performed for true values of Q^2 while the data correspond to reconstructed Q^2. The results in Ref. [233] show that MC simulations imply that, when integrated over all other kinematic variables, there is an average symmetric spread of about 0.02 GeV^2 of the reconstructed Q^2 around the true one. The π^- data is rather well reproduced by the model, although one would expect a reduction due to pion FSI not included here, in which case the data would be slightly underpredicted. The comparison to the π^+ data shows an overprediction at small values of Q^2, the discrepancy might be reduced with pion FSI, but would likely not disappear even in that case. This trend of overpredicting the low-Q^2 cross section is present in almost all neutrino event generators that are compared to this data,

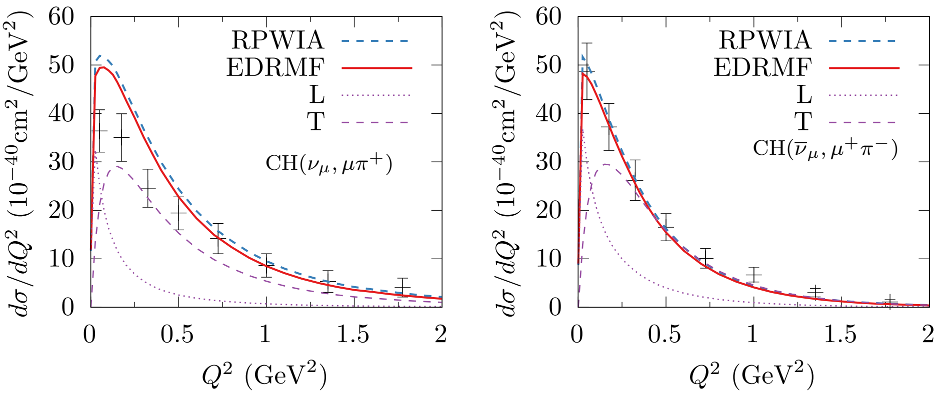

Figure 6.8: Cross section as function of Q^2 for the MINERνA CC1π^+ signal on the left and the CC1π^- on the right. Note that the calculations correspond to true Q^2.

and is moreover found also in the comparison to measurements of the inclusive cross section in the NOνA experiment [234]. In Refs. [112, 234] the reason for this reduction is speculated to be caused by a lack of nuclear effects beyond the RFG model. In particular Pauli-blocking is cited as a possible explanation in Ref. [233]. In the NOνA analysis as well as in the analysis of MINERνA data of Ref. [112] use is made of a phenomenological suppression factor as function of Q^2 which is inspired by the effect of RPA-like corrections to one-nucleon knockout in a local Fermi gas as computed in Ref. [235]. Here, the EDRMF calculation explicitly includes Pauli-blocking, while the RPWIA does not. Moreover there is indication that such RPA-like corrections to a non-interacting local Fermi gas tend to already be included at mean-field level in consistent distorted-wave calculations [167]. We hence find that such effects are unlikely to resolve this data-model discrepancy. It is notable that a similar overprediction of the low-Q^2 cross section is already present in our comparison to the BEBC data off free nucleons, as we showed in Fig. 3.29. It seems just as reasonable to speculate that the axial couplings on the nucleon level are to blame for this overprediction, rather than an unaccounted for nuclear effect.

To facilitate a more in-depth comparison, we show in Fig. 6.9 the cross section separated by the type of target nucleon.

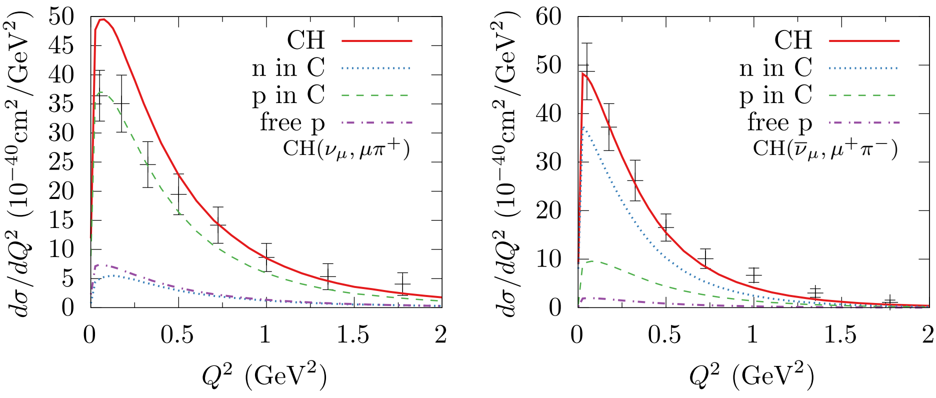

Figure 6.9: Cross section as function of Q^2 for the MINERνA CC1π^+ signal on the left and the CC1π^- on the right broken down per target nucleon type.

6.2.2 Neutral pion production

MINERνA has done measurements for π^0 production induced by neutrinos [228] and antineutrinos [229]. Both datasets include W_{rec}^{free} up to 1.8 GeV where calorimetry is used for the reconstruction of the neutrino energy. As we did for the charged pion case, we discuss the neutrino and antineutrino data jointly as they are connected by isospin symmetry. We use the same response tables, computed for the neutrino induced process, for both processes. One should again be careful in directly comparing the neutrino and antineutrino interactions. Firstly the free-proton contribution enters in the antineutrino process while it does not contribute to the neutrino-induced signal. And secondly, in the neutrino data a cut $\theta_\mu < 25$ deg is included while there is no such restriction for the anti-neutrino data. Because of this angular cut, the model predicts a similar magnitude for the cross sections for neutrino and antineutrino-induced interactions as can be seen in Figs. 6.10 and 6.11. Comparing these figures, one sees that the magnitude of the antineutrino induced process is reproduced well, especially in the region where the flux peaks. On the contrary the neutrino-induced process is severely underpredicted.

The data in terms of lepton kinematics is compared to the models in Fig. 6.12. As, apart from the slight differences in the shape of the neutrino flux, the only difference in the kinematics covered in both measurements lies in the restriction on scattering angle in the neutrino

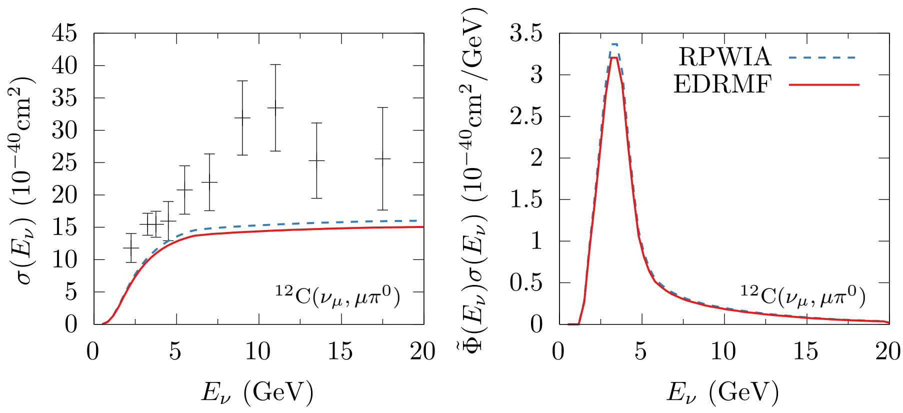

Figure 6.10: Total cross section as function of energy for the MINERνA νCC1π^0 signal, normalized per nucleon. The right panel shows the cross section weighted with the normalized neutrino flux.

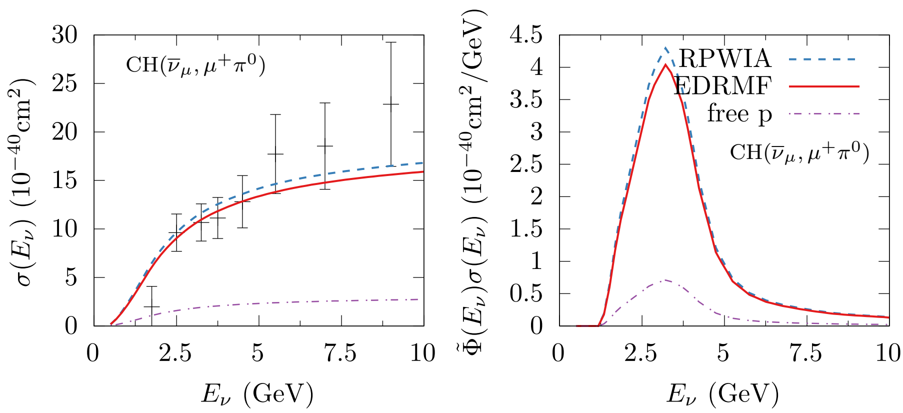

Figure 6.11: Total cross section as function of energy for the MINERνA $\overline{\nu}$CC1π^0 signal, normalized per nucleon. The right panel shows the cross section weighted with the normalized neutrino flux.

signal it is interesting to compare the cross section in terms of lepton angles. We show the free proton contribution and the vector-axial interference term on carbon separately in these figures in order to show where the differences in both cross sections mainly come from. The free proton contribution tends to be roughly similar in magnitude to the vector-axial interference term in carbon for the anti-neutrino interactions such that the cross sections in terms of scattering angles are similar in both cases. This behavior is not at all reflected in the data, while excellent agreement is found for the antineutrino case, the neutrino data is far larger than the model predictions apart from the smallest angular bins. This agreement with antineutrino, and severe underprediction of the neutrino data is the main finding in the comparison to the π^0 production data.

Before drawing any conclusions, it is important to consider how large the effect of pion FSI might be for the neutral pion data. The cascade model results of NuWro [36] and GENIE [228, 229] indicate that distributions other that the cross section in terms of pion energies are almost unaffected by pion FSI. In particular, GENIE predicts a practically negligible decrease for the ν induced channel and a slight increase for the $\overline{\nu}$ channel, while NuWro produces a negligible increase of the integrated cross sections post-FSI for both channels. The reason is that the loss in neutral pions from FSI is compensated almost exactly by the feed-in of neutral pions created through charge-exchange of charged pions. The cross section in terms of pion energies changes shape from the combination of these effects while other distributions are barely affected. The feed-in of neutral pions through charge exchange comes mainly at small pion energies, as the neutrino induced charged pion production process couples more strongly to the delta. As such, the shape of the T_π distributions shown in Fig. 6.13 is reasonable, as an increase for small T_π might be expected.

The isospin symmetry of the nucleus means that any FSI process would affect the neutrino and anti-neutrino interactions in a similar way. Given the large difference in the description of the ν and $\overline{\nu}$ data, it would be difficult to find an explanation of the large underprediction of the neutrino induced process only through FSI.

The cross sections as function of Q^2 for both processes are shown in Fig. 6.15. The comparison to the neutrino data is comparable to what was found for θ_μ, a large underprediction of almost a factor two is found at large Q^2 while only at the smallest Q^2 points we comply with the data. The antineutrino process on the other hand is described rather

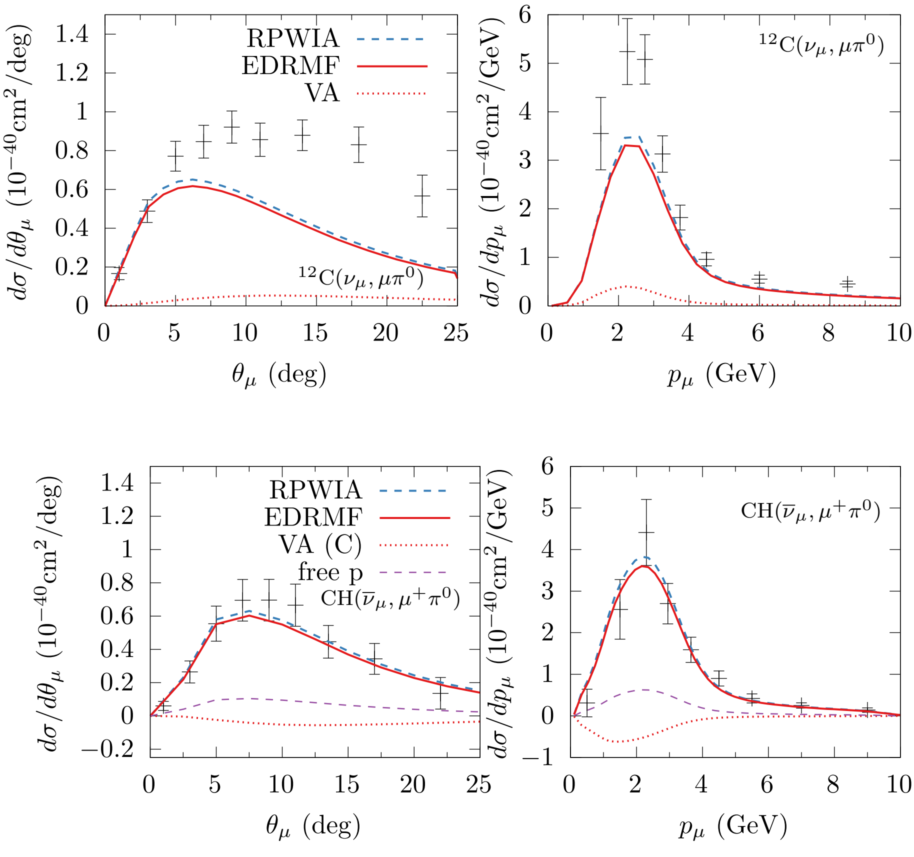

Figure 6.12: Cross sections differential in lepton kinematics for the MINERνA CC1π^0 measurement, top(bottom) panels correspond to (anti-)neutrino reactions, normalized per nucleon.

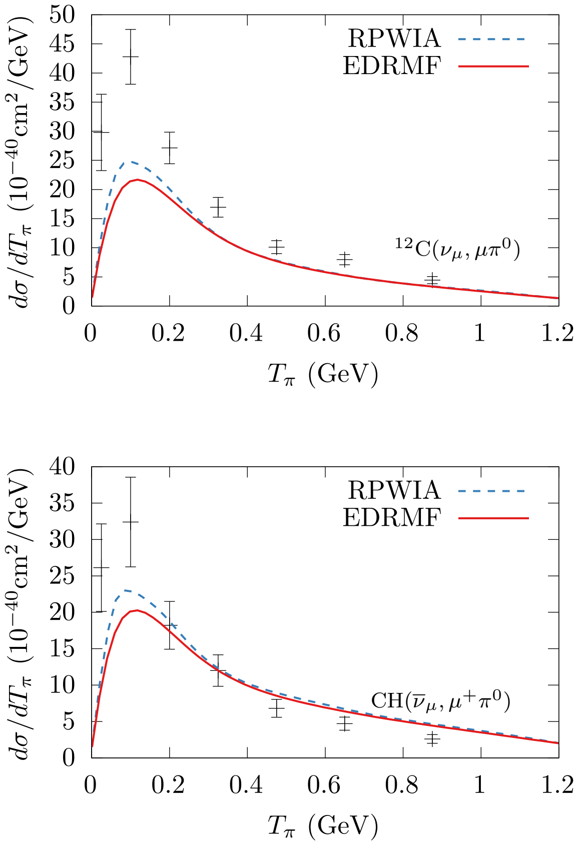

Figure 6.13: Cross sections differential in pion kinetic energy for the MINERνA CC1π^0 measurement, top(bottom) panels correspond to (anti-)neutrino reactions, normalized per nucleon.

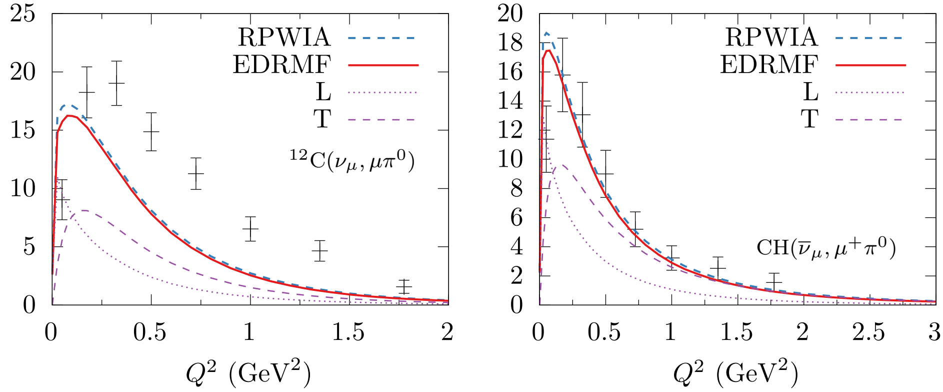

Figure 6.14: Cross section as function of Q^2 for the MINERνA CC1π^0 measurements. (anti-)Neutrino interactions are on the left(right). Note that the calculations correspond to true Q^2.

well, although one again finds somewhat of an overprediction of the low-Q^2 cross section.

Additionally the Q^2 data for the neutrino-induced process was separated in terms of neutrino energy. We show the comparison to this data in Fig. 6.15. The comparison to the small energy region is similar as for the full phase space, as this energy region lies around the peak of the flux-averaged cross section. For the higher energies, one finds that the data is much below the model at small values of Q^2. We see that while the longitudinal contribution is around the same value of the data at $Q^2 \approx 0$ for the low energy region, it is more than twice as large in the high-energy region.

It is important to consider how the hybrid model compares to π^0 production on free neutrons. The total cross section for $W < 1.4$ GeV is of the same magnitude as the reanalyzed ANL and BNL data, and is only slightly larger than the BEBC data. When larger W are allowed, the model tends to underpredict the cross section, indicating a possible lack of strength coming from higher mass resonances. The reconstructed W^{free} distribution is compared to the model in Fig. 6.16. From a direct comparison one finds that the datapoint on the delta peak is just barely of the same magnitude as the calculation, while the large W^{free} data is much larger than the model. Additionally, a large cross section is measured for small W^{free}, while the model does not yield any strength

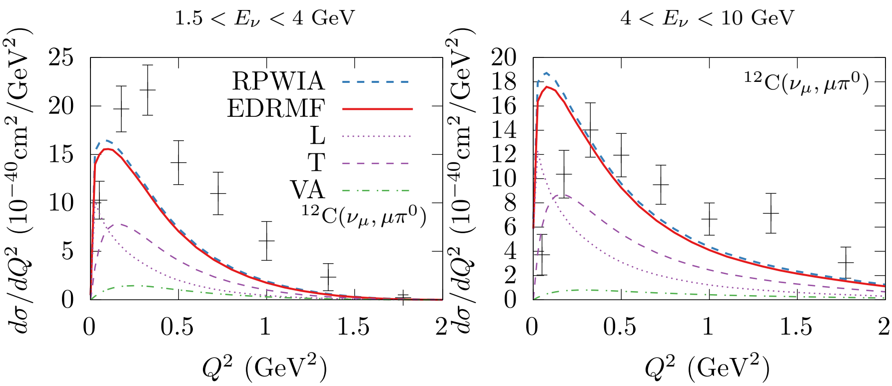

Figure 6.15: Cross section as function of Q^2 for the MINERνA CC1π^0 measurements. (anti-)Neutrino interactions are on the left(right). Note that the calculations correspond to true Q^2.

in this region. The data is presented in terms of reconstructed variables however, while the calculation is done for true values. In Ref. [233] it is reported that, according to MC simulations, the reconstructed values are spread almost symmetrically around the true values with a width of 180 MeV. We therefore also show our result smeared by a Lorentzian of width 180 MeV, the shape comparison is good but we need to multiply by a factor 2 to get a similar magnitude as in the experimental data.

6.3 T2K

The T2K experiment has measured single π^+ production on both carbon and oxygen targets in the T2K near detector. We have compared the RPWIA results to the oxygen data in the previous chapter, and we will provide results for a carbon target in this section. The T2K data makes use of both direct measurements of charged pions, and from an indirect measurement of Michel electrons which come from the decay of the pions. In the results reported in Ref. [236], use is made of direct measurements of the pion for which the pion scattering angle with respect to the neutrino beam is restricted to $\cos\theta_\pi > 0.2$ for the single-differential cross sections. We hence cannot directly compare to these data as we obtain responses integrated over the pion angles. In Ref. [237], where the original analysis of this data is presented, distributions are reported

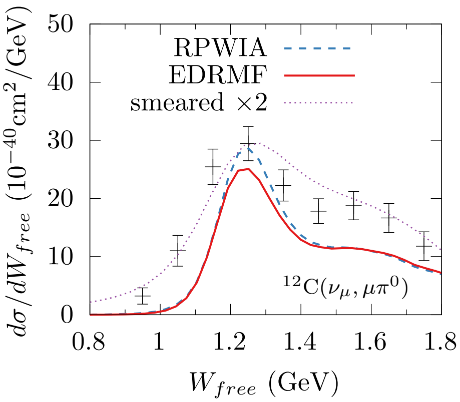

Figure 6.16: Cross section as function of W^{free} for the MINERνA CC1π^0 measurements.

which make use of a combination of both the direct detection and Michel-electron sets, and are free of restrictions on the pion kinematics. We will hence compare our results to these data instead.

We first show the total cross section as function of neutrino energy in Fig. 6.17. One can appreciate that the T2K data is sensitive to lower energies than MINERνA, the flux-weighted cross section peaks around 800 MeV, but the high energy tail is quite significant. Contrary to the MINERνA case, no restriction on the invariant mass is made in this measurement.

In Fig. 6.18 we show the results for the momentum of the muon and the pion. The agreement of the model to the muon data is good, although as in the comparison to the NuWro result and the T2K data on oxygen, one could expect a reduction of the cross section due to pion FSI. The comparison for the pion momentum is also fairly good, but the model result becomes too small in the high p_π tail. One sees that the low p_π data correspond to a single datapoint which covers momenta up to 400 MeV, this is a result from the measurement with Michel electrons for which the exact momentum cannot be determined, this becomes only possible for larger momenta.

T2K have reported a first measurement of the (semi-)inclusive double-differential cross section for π^+ production. We show the comparison in Fig. 6.19. Due to the broad binning one cannot compare the data to a continuous distribution hence we provide model predictions with the same binning. The model seems to be in line with the data in most cases

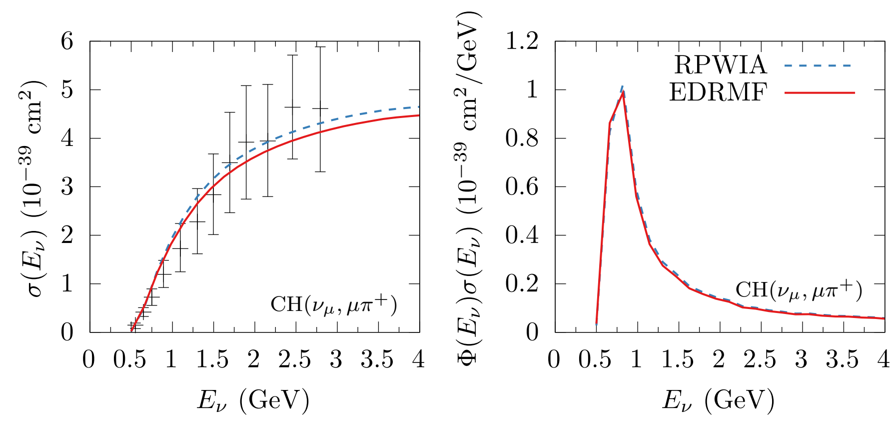

Figure 6.17: Total cross section as function of energy for the T2K νCC1π^+ kinematics, normalized per nucleon. The right panel shows the cross section weighted with the normalized neutrino flux.

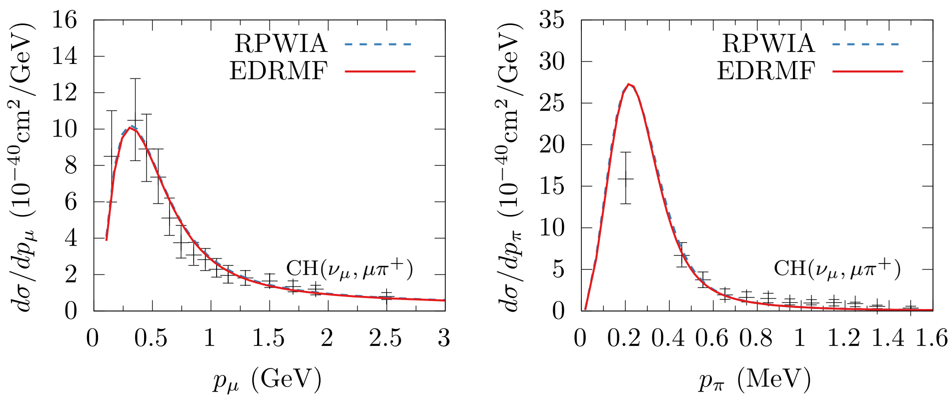

Figure 6.18: Cross section as function of muon (left) and pion momentum (right) compared to the T2K CC1π^+ data. The data and calculations are for $\cos\theta_\mu > 0.2$. Additionally for the cross section in terms of pion momentum $p_\mu > 0.2$ GeV.

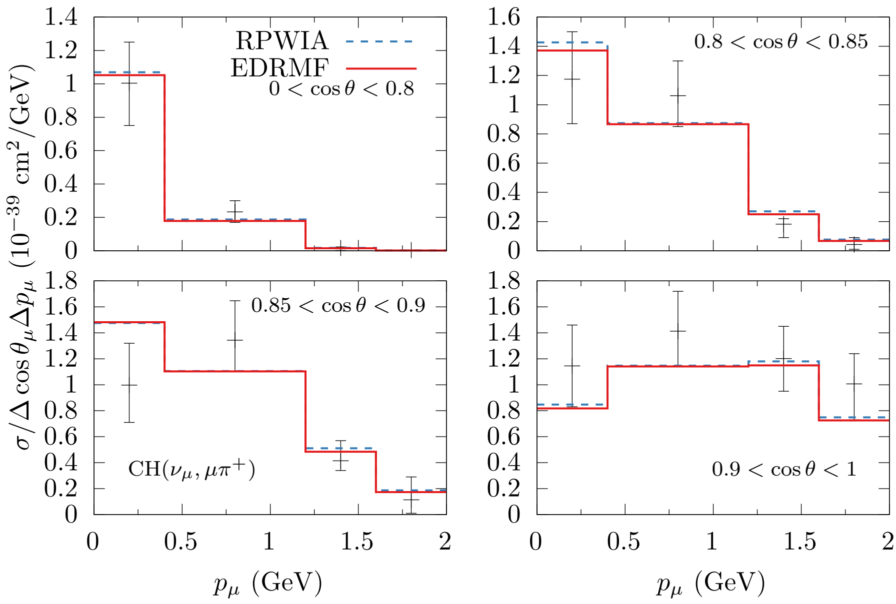

Figure 6.19: Double differential cross section in terms of lepton kinematics compared to the T2K νCC1π^+ data, normalized per nucleon.

although the large error bars allow for significant spread. Even then we find that for some bins the model falls outside of the errorbars. RDWIA and RPWIA results are practically the same, and no clear trend arises in the comparison of the RDWIA and RPWIA in terms of the lepton kinematics.

The cross section as function of Q^2 is shown in Fig. 6.20. Kinematic cuts $\cos\theta_l > 0.2$ and $p_\mu > 200$ MeV are applied to both the data and the model. We find a reasonable description of the data at high Q^2, and a consistently large cross section at small Q^2, although the model still falls within experimental errorbars.

Again Q^2 is a reconstructed variable, requiring knowledge of the incoming energy which in this case has to be estimated. As the data includes the Michel electron sample, this measurement will be at least somewhat model-dependent, because the pion kinematics are not reconstructed in the Michel electron sample, and one has to rely on simulations to reconstruct the energy. We assume that this model dependence is reflected in the size of the error bars.

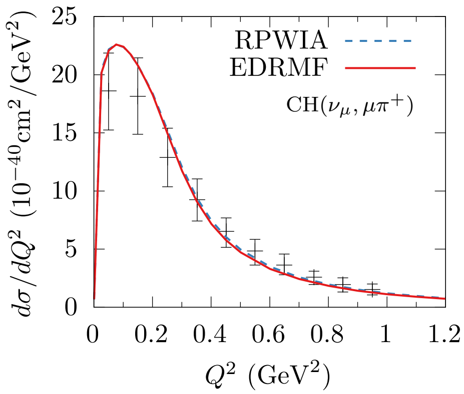

Figure 6.20: Differential cross section in terms of Q^2 compared to the T2K νCC1π^+ data, normalized per nucleon.

Ref. [237] lists additional results, which are not included in the T2K publication of Ref. [236]. We show in Fig. 6.21 the results for the reconstructed W and q. Here the reasonable description found for the previous cross sections disappears, we see that the model gives a value in the delta region which is about twice as large as the data, while the higher W and q regions are underestimated. Clearly, as we obtain good results for the other variables, the total strength should be reproduced well, but it lies in the wrong kinematic region. We might entertain the possibility that this is due to an inherent smearing due to the reconstruction procedure, while we are showing true values. To illustrate this possibility we smear the cross section in terms of W with a Lorentzian, we use the same width of 180 MeV as in the discussion of the MINERνA data. With this smearing we indeed find that the height and width of the delta peak as found in the data are reproduced, and the high W cross section is slightly underestimated. This would be in line with what one obtains in the scattering off free nucleons. However, due to our symmetric smearing we introduce quite some strength in the low W region, while the data starts from the πN threshold.

6.4 Conclusions

We have compared the model predictions in RPWIA and EDRMF to a comprehensive dataset of neutrino-induced single pion production, in all cases the pion was treated in the RPWIA. Based on the success of

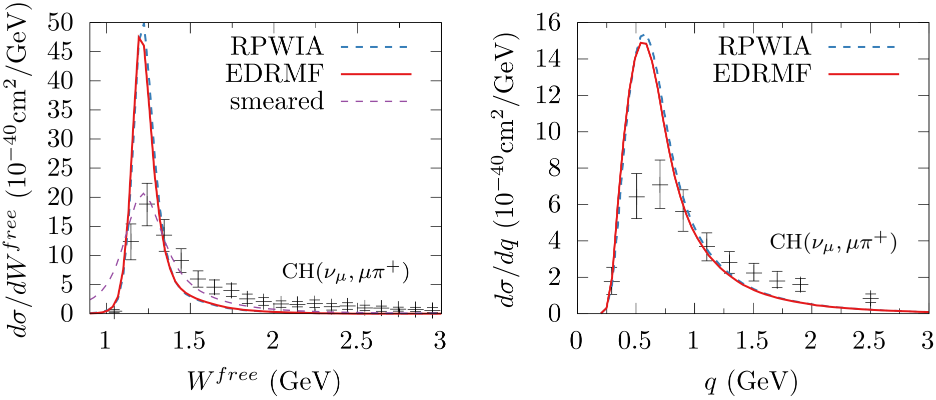

Figure 6.21: Cross section as function of W_{free} (left) and q (right) compared to the T2K CC1π^+ data. The data and calculations are for $\cos\theta_\mu > 0.2$ and $p_\mu > 0.2$ GeV.

the RDWIA in describing inclusive electron and neutrino scattering for single-nucleon knockout, we may assume that the EDRMF treatment should be well suited for a description of the undetected outgoing nucleon, even if it undergoes final-state interactions. The EDRMF treatment in particular provides a consistent treatment of the nuclear degrees of freedom, it includes Pauli blocking, and the necessary treatment of FSI. One can assert that the RPA-like corrections that are applied in Ref. [235, 238] in the context of a local Fermi gas description of the nucleus are mostly included already at the mean-field level in the RDWIA [167].

We find by comparison of the EDRMF to the RPWIA results that the EDRMF yields a modest reduction of the cross section, which is smaller than in the case of single-nucleon knockout. This is at least in part because the energy and momentum transferred to the nuclear system are shared between the pion and nucleon in this case. Although it would be instructive to also treat the outgoing pion as a distorted wave, one might expect that, given that a large part of inelastic pion FSI should be retained to describe the neutrino interaction, the overall effect would be of the same magnitude. As such we might, albeit cautiously, ascribe data-model discrepancies to the electroweak SPP operator instead of to nuclear physics uncertainties.

We may draw a number of conclusions from the comparison to the experimental data. Firstly, the overall magnitude of the cross section and the distribution of lepton observables of the π^+ production channels are well described for both the T2K and MINERνA data, although for T2K, in anticipation of a slight reduction of the cross section obtained in cascade models due to pion FSI, the cross section should preferably be larger. Both these datasets, in MINERνA due to the cut on invariant mass, and in T2K due to the lower incoming energy are dominated mostly by the delta resonance,however in T2K one does get some more contributions from higher invariant mass as there is no explicit kinematic cut imposed.

Overprediction of the low-Q^2 region is clearly present in the comparison to π^+ production data of MINERνA, and to a lesser extent with the T2K data. Given the assumptions on the EDRMF stated above, we may assert that a Pauli-blocking correction or what is referred to as an 'RPA-like' effect in analogy to the one-nucleon knockout case, is likely not the source of this discrepancy. The effect of consistent nuclear wavefunctions and Pauli-blocking is overall found to be smaller as it is spread-out over a larger kinematic region, and doesn't necessarily reside in the region of small Q^2. It is therefore reasonable to look for a different explanation of this discrepancy. In the comparison to the higher-energy BEBC data on hydrogen and deuteron we find an overprediction of similar shape and magnitude as found in the comparison to nuclear target data reported by MINERνA as shown in Fig. 3.29.

The description of anti-neutrino induced neutral pion production is in line with the data, and according to the model the neutrino-induced data should be similar in magnitude. The neutrino data however is severely underpredicted. It is in principle difficult to find a mechanism which would increase the neutrino cross section, while leaving the agreement with anti-neutrino data intact. It should be noted however that the agreement in magnitude is at least partly accidental as both datasets include different kinematic cuts and the anti-neutrino interaction gets contributions from the free protons in the target. If a cancellation of the free proton contribution with the VA interference is retained one could in principle increase the strength of higher mass resonances to explain the neutrino data, while leaving the agreement with the anti-neutrino cross section data intact.

Chapter 7

Summary and Conclusions

There is large theoretical and experimental interest in the physics of neutrinos and neutrino oscillations in particular. In order to study the parameters which describe these oscillations, large collaborations are conducting experiments all over the globe. A major obstacle in the analysis of these experiments is that neutrinos only interact weakly, such that they are effectively 'invisible' to traditional particle detectors. To overcome this problem, some of the largest experiments have placed detectors and metric tons of target material in neutrino beams created at particle accelerators. The goal of such an experiment is to measure the particles that are produced in interactions with the target and thereby infer the properties of the incoming neutrino. These targets consist mostly of atomic nuclei, and hence to accurately interpret the data a precise knowledge of the neutrino-nucleus scattering cross section is necessary. In addition, the accumulation of increasingly precise neutrino scattering data can give a unique view on the axial structure of hadrons.

The production of pions is a significant contribution to either the signal or the background in many neutrino experiments. Electroweak pion production in the region of hadronic invariant mass W up to around 2 GeV is characterized by the excitation of baryon resonances. Due to the non-perturbative nature of QCD, the description of these interactions based on quarks and gluons is intractable. The most effective models of strong and electroweak interactions in this kinematic region are formulated in terms of effective hadronic degrees of freedom. As such models are not fully based on fundamental principles, their success is at least partly based on the availability of a large amount of experimental data obtained in hadron-hadron scattering and electromagnetic interactions with hadrons. For neutrino-induced interactions, due to the weak interactions and experimental complexity, data is scarce and of poor quality compared to the strong and electromagnetic sectors. While the knowledge of the resonance structure and electromagnetic couplings obtained in e.g. electron scattering experiments are important in determining the neutrino-induced pion production process, the axial couplings are left practically unknown.

In this work, we describe and update the model for electroweak SPP of nucleons presented in Ref. [31]. The model includes 4 resonances in the s- and u-channels ($P_{33}(1232)$, $P_{11}(1440)$, $S_{11}(1520)$, and $D_{13}(1535)$) in addition to the lowest order background diagrams consistent with ChPT. The resonance properties and their coupling to the πN final state are quite well established and taken as the central values reported in Review of Particle Physics. The proton form factors are determined from experimental data on the helicity amplitudes measured in electromagnetic interactions. The determination of the isovector form factors requires neutron target data which is more sparse, and we rely on different models which are compared to the MAID07 results. As the lowest order ChPT background does not give a natural description of the degrees of freedom beyond tree-level at high invariant mass, we transition smoothly from the low-energy ChPT model to a high-energy model for the background based on Regge theory. In the Regge model we take into account Regge trajectories, which can be interpreted as the exchange of a whole family of meson states in the t-channel, which are described by the same parameters as those used in the low-energy description. The axial couplings for the $P_{11}(1440)$, $S_{11}(1520)$, and $D_{13}(1535)$ are determined by assuming PCAC and pion-pole dominance for the pseudoscalar coupling. This determines all axial couplings of the spin 1/2 resonances, but leaves 2 possible couplings undetermined for the D_{13}. In this work we set them to zero. The Q^2 dependence of the axial couplings is taken as in Ref. [26], close to a dipole with cut-off mass 1.05 GeV. For the $P_{33}(1232)$ we use the fit of Ref. [30] which was performed with practically the same low-energy model.

The model for pion production is implemented in the nucleus using the relativistic distorted wave impulse approximation (RDWIA). The initial nucleus is described in the relativistic mean field (RMF) approach. The ground state nucleus then consists of single-particle orbitals with fixed energy and angular momentum. In the IA, the interaction with the nucleus is described by the incoherent sum of one-body interactions with the single particle states. We use the same operator used to describe the interaction on free nucleons in the nuclear medium. The effect of modifications of the delta width according to the model of

Oset et al. [210] was also studied. The final-state nucleon wavefunction is described with the phenomenological energy-dependent RMF (ED-RMF) potential introduced in Refs. [131, 148]. At small nucleon energies this real potential tends to the RMF potential used to describe the initial state, and its strength is reduced for larger energies as required. The matrix elements obtained in this way satisfy the principles of orthogonality and consistency of initial- and final-state wavefunctions, and was shown to give good results for inclusive electron and neutrino scattering [131]. The current model may be used to study the effect of distorted pion waves, with a negligible increase in computational complexity in the factorized approach. The pion state is treated as a plane wave throughout this work however.

The results for pion production of nucleons are extensively benchmarked against the MAID07 and ANL-Osaka Dynamic Coupled Channels (DCC) models for electroproduction [34, 66]. We find that despite the model's relative simplicity it compares more than adequately for electroproduction observables. We extract also the isovector current from the MAID07 and ANL-Osaka analyses. It is interesting to note that while there exist quite large differences between the cross sections obtained with the MAID07 and DCC models at large Q^2 for electromagnetic pion production channels, the agreement between both models tends to be much better for the isovector current. The same is true in the comparison of our results with MAID07 and DCC. In particular for cross sections averaged over the experimental neutrino flux we find the agreement between our approach and the DCC model to be excellent.

We also compute pion-nucleon elastic and total cross sections and compare them to experimental data. This provides a further consistency check of the different components of the model, in particular for the interference between resonances and background due to the axial current. In the comparison to the total cross section, we find that s-channel resonance contributions alone yield a good description of the shape and magnitude of the cross section, especially in the delta region. When the background contributions are included there is a large cancellation between the ChPT background and u-channel resonance contributions which still results in a quite good description of the cross section, but where the delta peak tends to be shifted slightly. The Regge background includes only the ρ meson exchange in the axial current, which gives a good reproduction of the size of the charge-exchange cross section at high-W, but underpredicts the other interaction channels.

Finally we compare the model with data for neutrino-induced pion production off nucleons. We find a reasonable description of the total cross section for π^+ production off the proton and for neutral pion production when $W < 1.4$. In contrast, the data for π^+ production off the neutron (also for $W < 1.4$GeV) is severely underpredicted. Because of the good agreement of the vector current cross section at these kinematics with the ANL-Osaka model and the fact that the vector-axial interference contribution is negligible, this discrepancy is likely caused by the description of the axial current. It seems not possible however to explain the full discrepancy by the coupling to the higher mass resonances as the cut on W eliminates most of their contribution. We compare differential cross sections as function of Q^2 to the high energy BEBC data. Apart for π^+ on the neutron which is underpredicted, the model tends to overshoot the data at low Q^2 while giving better results at large Q^2, agreement worsens notably for higher invariant mass. This contrasts with the result for the ANL data, to which the delta coupling was fit, and which is hence described well. The difference in the description of both datasets might point to some problems with the determination of the axial delta coupling to ANL data alone. The shape-only comparison to W-distributions measured in ANL and BNL also proves interesting. The $p\pi^+$ channel agrees in shape and magnitude, while for the other interactions a more significant smearing tends to be present in the data. It is unclear whether this is due to experimental error on the quite scattered datapoints, or if this is an inherent smearing. If one assumes only minimal smearing in the data, and a proper characterization of the delta peak in the hybrid model, the data-model comparison could point to a significant underestimation of the large W region in the hybrid model, although the shape is well described.

We compare results for scattering off nuclei and compare to experimental data. Firstly results in the RPWIA (i.e. without distortion of the final nucleon) are compared to the T2K dataset for oxygen. The effect of medium modification of the delta is studied and the effect of FSI is estimated through comparison with the NuWro event generator [42]. The general comparison of the RPWIA model to the T2K data is favorable, the model reproduces the shape and strength of the data well, meanwhile leaving room for FSI at low pion and lepton momenta. We find that the contributions from the high energy tail of the T2K flux are significant, and using low-energy ChPT leads to a sizable overestimation of the cross section, while the high-energy Regge approach provides a better result.

We compare the EDRMF and RPWIA results to pion production data on carbon obtained by the MINERνA and T2K experiments. We find by comparison of the EDRMF to the RPWIA results that the EDRMF yields a modest reduction of the cross section, which is smaller than in the case of single-nucleon knockout. Moreover no significant shape-differences between the models are found for the current datasets. The charged pion production channel is mostly well described both in neutrino and anti-neutrino interactions for both experiments. Overprediction of the low-Q^2 region is clearly present in the comparison to π^+ data of MINERνA, and to a lesser extent with the T2K data in both the RPWIA and EDRMF. As Pauli-blocking, and the most important nuclear structure effects are present in the EDRMF approach, it is reasonable to assume that this disagreement finds its origin in the couplings on the nucleon level. The disagreement is similar to the one found in the comparison to the BEBC data obtained on protons and deuterium. The description of antineutrino-induced neutral pion production is in line with the data, and according to the model the neutrino-induced data should be similar in magnitude when the relevant kinematic cuts and differences in the fluxes are taken into account. The neutrino data however is severely underpredicted. It is difficult to find a mechanism which would increase the neutrino cross section, while leaving the agreement with anti-neutrino data intact. It should be noted however that the agreement in magnitude is at least partly accidental as both datasets apply different kinematic cuts and the anti-neutrino interaction gets contributions from the free protons the target.

Chapter 8

Samenvatting

Het onderzoek naar neutrino's is een snel groeiende tak in de experimentele fysica, met een groot potentieel voor fundamentele ontdekkingen in de nabije toekomst. Voor de ontdekking van neutrino-oscillaties werd aan T. Kajita en A. B. McDdonald in 2015 de Nobelprijs in de fysica uitgereikt. Het verder karakteriseren van de neutrino mengingshoeken, het ontrafelen van de neutrino massa hiërarchie, mogelijke confirmatie van het bestaan van steriele neutrino's, en metingen van de CP-schendende fase zijn voorbeelden van de doelen van het hedendaagse onderzoek naar neutrino's.

Neutrino experimenten aan versnellers Neutrino's worden gecreëerd in zwakke interacties en verschillende bronnen zorgen voor neutrino's die op aarde waargenomen kunnen worden. Zo zijn er buitenaardse neutrino's die onder meer gevormd worden in de kernreacties in het centrum van de zon, in de botsing van hoogenergetische kosmische straling met de atmosfeer, en in supernova explosies. Anderzijds zijn er neutrino's uit aardse bronnen zoals kernreactoren, het betaverval van kernen, en in deeltjesversnellers. Intense stralen van neutrino's uit deeltjesversnellers bieden een grote opportuniteit voor onderzoek naar oscillaties. Zulke stralen zijn intens genoeg om voldoende interacties in een detector mogelijk te maken en zijn relatief goed gekarakteriseerd, een detector kan zich dan op de ideale positie plaatsen om neutrino oscillaties te meten.

De setup van een neutrino experiment gebaseerd op een versneller lijkt, wanneer het niet triviale technische aspect buiten beschouwing blijft, bedrieglijk eenvoudig. Hoogenergetische protonen uit de versneller worden gericht naar een eerste target, en in interacties met het target worden een grote hoeveelheid geladen mesonen gevormd. Deze geladen mesonen worden gefocust in een intense straal, en een deel van deze mesonen zal zwak vervallen met een intense straal van neutrino's tot gevolg. Deze neutrino's reizen over een bepaalde afstand tot bij een detector waar dan geteld wordt hoeveel neutrino's binnenkomen. Als we dus weten hoeveel neutrino's van een bepaalde smaak origineel gecreëerd werden, en hoeveel er na het reizen over een bepaalde afstand overblijven, kunnen we de neutrino oscillatie karakteriseren.

Dit naïef plaatje wordt echter sterk gecompliceerd omwille van twee redenen. Ten eerste interageren neutrino's enkel via de zwakke wisselwerking, dit maakt directe observatie van neutrino's met traditionele detectoren onmogelijk. In de plaats daarvan detecteert men de deeltjes die ontstaan door de interactie van het neutrino met het detectormateriaal. Gezien de zwakke interactie inderdaad zwak is, is het echter heel onwaarschijnlijk dat een neutrino een interactie zal ondergaan met een deeltje in de detector. Dit zorgt ervoor dat een neutrino detector moet bestaan uit een enorme massa waarmee interactie mogelijk is, en in de praktijk bestaan deze dan ook voornamelijk uit atoomkernen. Dit betekent dat om het aantal neutrino's dat in een detector binnenkomt te karakteriseren we de werkzame doorsnede voor het produceren van deeltjes in de neutrino-kern interactie moeten kennen.

Dit is een niet triviaal probleem dat verder gecompliceerd wordt door het feit dat de stralen uit versnellers niet mono-energetisch zijn, maar bestaan uit een breed continuüm van energieën. Dit contrasteert met de klassieke elektron-atoomkern verstrooiingsexperimenten waaruit een groot deel van onze huidige kennis van atoomkernen en het beschrijven van interacties met kernen de voorbije decennia is opgebouwd. In zo'n experiment is de inkomende elektronenergie nauwkeurig gekend, door meting van het verstrooide elektron kan dan bepaald worden wat de energie and momentum die getransfereerd worden naar de kern is. De kennis van wat het kernsysteem binnenkomt, maakt het mogelijk om bij het meten van hadronen gevormd in de reactie, de ontbrekende energie en momentum te bepalen. Dit zorgt ervoor dat men kan focussen op bepaalde kinematische opstellingen zodat men metingen kan doen van specifieke interacties met kernen. Door de significante spreiding van inkomende energie in een neutrino experiment wordt dit echter onmogelijk, en moeten in principe alle mogelijke neutrino-kern interacties die kunnen bijdragen tot het waargenomen signaal in de detector beschreven worden.

De combinatie van de brede waaier aan inkomende energieën en de complexiteit van de neutrino-kern interactie betekent dus dat wat op eerste zicht lijkt op een simpel telexperiment, een invers verstrooiingsprobleem blijkt te zijn waarbij de interactiewaarschijnlijkheid moeilijk te bepalen is. De metingen van neutrino-oscillatie parameters kunnen hierdoor enkel op statistische wijze bepaald worden. In de praktijk wordt in de analyse van een experiment gebruik gemaakt van simulaties van het verwachte signaal in de detector op basis van de neutrinoflux voor oscillatie, de respons van de detector, de werkzame doorsnede, en de ansatz voor de oscillatieparameters. Door het vergelijken van de simulaties met de data kan op die manier de waarschijnlijkheid voor elke waarde van de geoscilleerde flux bepaald worden. Met nieuwere generaties aan experimenten worden statistische fluctuaties kleiner, detectoren beter, en de kennis van de inkomende flux preciezer. Intussen komen we bij het punt waar de kennis van de werkzame doorsnede de dominante bron van onzekerheid in dit soort metingen zal worden.

Neutrino-geïnduceerde pion productie Pionproductie is een belangrijke reactie voor huidige en toekomstige experimenten. Het pion, als het lichtste meson, is het meest voorkomende reactieproduct in inelastische interacties met het nucleon in de regio van hadronische invariante massa $W \approx 1.1-1.4$ GeV die bijdraagt in het energiegebied van typische experimenten aan versnellers. In lage-energie experimenten zoals T2K en MiniBooNE, waarbij de hadronische finale toestand niet, of amper, gemeten wordt vormt de productie van het pion een bijdrage in het experimenteel signaal die niet rechtstreeks ontrafeld kan worden, en dus alsook gekend moet zijn. In experimenten waar de hadronische finale toestand wel preciezer gemeten wordt zijn pionen een vaak voorkomend reactieproduct die al dan niet tot het experimentele signaal behoren. In elk geval is de kennis van de werkzame doorsnede voor pion productie een belangrijke onzekerheid. Naast het belang voor neutrino-oscillaties, bieden metingen van neutrino-geïnduceerde pion productie bovendien ook een unieke kijk in de axiale structuur van het nucleon.

Onze beschrijving van pionproductie op kernen start met de beschrijving van de interactie op een vrij nucleon. Enkelvoudige pion productie in lepton-nucleon interacties bij intermediaire energieën wordt voornamelijk gedomineerd door het aanslaan van resonanties die vervolgens vervallen tot een pion-nucleon paar. Door het niet-perturbatieve karakter van de kwantumchromodynamica bij laag vier-momentum transfer en lage hadronische invariante massa is een precieze beschrijving van dit proces met quark en gluon vrijheidsgraden praktisch onmogelijk. Daarom neemt men zijn toevlucht tot het beschrijven van het proces op het niveau van het proton en neutron, de zogenaamde kwantumhadrodynamica.

Bij lage invariante massa gebruiken we een model waarbij de laagste-orde diagrammen van een effectieve Lagrangiaan in rekening worden gebracht. De relevante diagrammen zijn een combinatie van zogenaamde 'achtergrond'-contributies die volgen uit een pion-nucleon Lagrangiaan, en resonante contributies die de vorm hebben van de uitwisseling van een onstabiel hadron met bepaalde massa en kwantumgetallen. De parameters van de achtergrond zijn bepaald door laagste orde ChPT bij $Q^2 = 0$. Voor de extensie naar hogere Q^2 worden de vormfactoren van het nucleon toegevoegd, gekend uit elastische electron- en neutrino-nucleon verstrooiing. Om de conservatie van de vectorstroom te behouden wordt de F_1 nucleon vormfactor dan ook in de vectorstroom door pion-uitwisseling gegeven. Onder deze aannames zijn is de achtergrond praktisch vrij van onbekende parameters.

We voegen bij de achtergrond 4 resonanties, de delta ($P_{33}(1232)$), $P_{11}(1440)$, $S_{11}(1520)$, en $D_{13}(1535)$. De excitatie van een nucleonresonantie in de tree-level benadering bestaat uit 3 delen: de elektrozwakke excitatie van de aangeslagen toestand, de propagator, en de hadronische koppeling aan de pion-nucleon finale toestand. Voor de hadronische koppeling maken we gebruik van de massa, totale breedte, en partiële breedte voor het verval naar pion-nucleon zoals gemeten in hadronische interacties en opgelijst in Review of Partice Physics. De propagator leidt tot een Breit-Wigner vorm met een W-afhankelijke breedte die afgeleid wordt uit de hadronische vertex. Om onfysische sterkte van resonanties ver van hun pool te onderdrukken wordt gebruik gemaakt van een product van een Gaussische en dipool vormfactor. Voor de excitatie van resonanties moeten we terugvallen op een meer fenomenologische beschrijving. Voor interacties met een nucleon kan de excitatie van een resonantie op vrij algemene manier beschreven worden met een beperkt aantal fenomenologische vormfactoren. We nemen aan dat deze vormfactoren enkel afhankelijk zijn van Q^2. De elektrozwakke respons van een hadron bij de koppeling met een ijkboson krijgt contributies van een vector- en axiale stroom. De vectorstroom in zwakke interacties kan gerelateerd worden aan de vectorstroom in elektromagnetische interacties. Voor de geladen-stroom interactie hebben we de isovector vormfactoren nodig, die voor alle resonanties behalve de delta enkel bepaald kan worden door elektromagnetische pion productie op zowel protonen als neutronen. We maken gebruik van recente experimentele data voor heliciteitsamplitudes verkregen door de elektromagnetische excitatie van resonanties op het proton om de Q^2 afhankelijkheid van de proton vormfactoren te motiveren en te bepalen. In plaats van de neutron vormfactor rechtstreeks te proberen bepalen, vergelijken we heliciteitsamplitudes en vormfactoren verkregen uit verschillende modellen met de resultaten uit de MAID07 analyse.

Voor de axiale vormfactoren kunnen we niet terugvallen op een extensieve dataset. Met uitzondering van de delta worden de axiale koppelingen bij $Q^2 = 0$ bepaald door gebruik te maken van het partieel behoud van de axiale stroom, hetgeen impliceert dat de koppeling gerelateerd is aan de hadronische koppeling. De Q^2 afhankelijkheid van de pseudoscalaire vormfactor wordt gerelateerd aan andere vormfactoren onder de assumptie van dominantie van de pion-pool voor de pseudoscalaire koppeling. Voor de vormfactoren waarvan de koppeling kan bepaald worden uit partieel behoud van axiale stroom parametrizeren we de Q^2 afhankelijkheid als een product van een dipool met cut-off $M_A = 1.05$ GeV en een monopool met cut-off $\sqrt{3}M_A$. Voor de vormfactoren waarvan de koppeling niet op deze manier bepaald kan worden, wordt aangenomen dat hun contributie verwaarloosbaar is bij gebrek aan een betere beschrijving. Dit betekent in het bijzonder dat voor de D_{13} twee axiale termen niet geïncludeerd zijn, die potentieel een significante bijdrage tot de werkzame doorsnede kunnen leveren. Voor de axiale koppelingen van de delta en hun Q^2 afhankelijkheid wordt gebruik gemaakt van een fit aan data voor pion productie in neutrino-deuterium interacties in de context van het model van Adler. De axiale koppeling die zodoende verkregen wordt is consistent met wat men verkrijgt uit het partieel behoud van axiale stroom.

Gezien interferentie tussen de achtergrond en de resonanties mogelijk is is het belangrijk om de relatieve fase tussen de resonante en achtergrond amplitudes te bepalen. In het simpele model tot hiertoe besproken is de achtergrond reeël, en de complexe fase van de resonanties wordt volledig bepaald door hun breedte. Voor invariante massa's onder de twee-pion productie barrière zijn de totale fase in multipoolamplitudes voor elektrozwakke pion productie gelinkt aan deze in de equivalente amplitudes voor pion-nucleon verstrooiing door het theorema van Watson. We maken gebruik van de parametrisatie van complexe fases die met de delta contributie vermenigvuldigd dienen te worden om, gegeven dit model, aan Watson's theorema te voldoen in de dominante multipoolamplitudes in het deltagebied.

Bij hoge invariante massa's is de beschrijving van de achtergrondamplitude in termen van laagste orde diagrammen onnatuurlijk. Bij invariante massa's voorbij het resontiegebied anderzijds wordt de pionproductie amplitude gedomineerd door een diffractieve voorwaartse piek die beschreven kan worden door de uitwisseling van Regge trajectories. Een Regge trajectory kan geïnterpreteerd worden als het uitwisselen van een hele familie van mesonen in het t-kanaal met dezelfde kwantumgetallen en oplopende spin en massa. We gebruiken een Regge model waarvan de parameters gebaseerd zijn op die van de lage-energie koppelingen voor mesonuitwisseling in het t-kanaal, om op deze manier slechts een minimum aan additionele parameters in te voeren. Deze hoge-energie beschrijving wordt geëxtrapoleerd naar lagere invariante massa en gaat via een soepele transitie over in de lage-energie beschrijving. Op deze manier creëeren we een achtergrondamplitude die over het hele energiegebied bruikbaar is.

Resultaten voor pion productie op het nucleon Om de validiteit van het model voor pion productie op het nucleon te toetsen bekijken we eerst de resultaten voor elektromagnetische interacties. Om te focussen op observabelen die het meest relevant zijn voor neutrino-experimenten vergelijken we de geïntegreerde werkzame doorsnedes als functie van Q^2 en W. We vergelijken ons model met de MAID07 fit en het dynamisch gekoppelde kanalen model van de ANL-Osaka groep. Gezien de simpliciteit van het model, dat weinig vrije parameters bevat in vergelijking met de meer geavanceerde modellen zijn de resultaten verrassend goed. We isoleren we uit de MAID07 en ANL-Osaka modellen de isovector amplitude die rechtstreeks bijdraagt in neutrino-geïnduceerde geladen-stroom interacties. We vinden dat de drie modellen gelijkaardige resultaten geven voor de isovector contributie. In het bijzonder nemen we waar dat voor werkzame doorsnedes die uitgemiddeld zijn over een brede experimentele neutrinoflux de overeenkomst tussen de vector-vector contributie in ons model en het state-of-the-art ANL-Osaka model meer dan voldoende is voor het beschrijven van neutrino data.

Gezien de axiale koppeling in het model geconstrueerd is aan de hand van de pion-nucleon koppelingen, kan de axiale stroom in het model gebruikt worden om werkzame doorsnedes voor pion-nucleon verstrooiing te berekenen. We vergelijken de resultaten van het model met werkzame doorsnedes voor elastische en totale pion-nucleon verstrooiing, dit biedt opnieuw een consistentiecheck voor de axiale stroom, in het bijzonder voor de interferentie tussen achtergrond en resonante contributies. We vinden dat, in het bijzonder voor elastische $\pi^- p$ verstrooiing, er grote cancellaties tussen de achtergrond en de gekruiste resonante diagrammen optreden die resulteren in een correcte magnitude voor de werkzame doorsnede.

We vergelijken de resultaten van het model met gemeten werkzame doorsnedes voor neutrino-geïnduceerde pion productie op protonen en deuterium. Het blijkt niet mogelijk om alle interactiekanalen gelijktijdig te beschrijven. Terwijl de vergelijking met data voor de productie van π^+ op het proton en π^0 op het neutron adequaat is, wordt de data voor π^+ productie op het neutron sterk onderschat. Het wordt onder meer ook duidelijk dat zelfs in het deltagebied, de beschrijving van de data voor π^+ productie op het proton niet consistent blijkt tussen experimenten op hoge en lage energie. Doordat het model quasi identieke resultaten geeft voor de vector-vector stroom als het ANL-Osaka model, en de bijdrage van de vector-axiale stroom verwaarloosbaar is bij hoge energie, lijkt de conclusie dat de discrepanties tussen het model en de data moeten gezocht worden in de beschrijving van de axiale vormfactoren. De grote onzekerheden op de huidige data laten echter niet toe om te bepalen waar de discrepanties exact moeten gezocht worden.

Pion productie op kernen We implementeren het model voor pion productie op het nucleon in de atoomkern door gebruik te maken van het onafhankelijk-deeltjes model. De grondtoestand van de kern wordt beschreven door een set van orbitalen gekarakteriseerd door een bindingsenergie en angulair momentum. Deze toestanden worden verkregen in een relativistisch gemiddeld veld, dat een zelfconsistente oplossing is van een niet-lineair sigma-omega model in de Hartree benadering. De interactie met de kern wordt dan beschreven als de incoherente som van de interacties met de verschillende nucleonen in de een-deeltjesorbitalen. De golffunctie van het nucleon dat uit de kern wordt gestoten door de interactie wordt beschreven met een relativistische vervormde golf. Gezien dit nucleon in neutrino experimenten niet gedetecteerd wordt, moet de totale flux behouden worden. Dit kan gedaan worden door gebruik te maken van een effectieve reeële potentiaal voor het uitgaand nucleon. We gebruiken de empirische energie afhankelijke relativistisch gemiddeld veld potentiaal (ED-RMF). Deze potentiaal is geconstrueerd om praktisch identiek te zijn aan de gemiddeld veld potentiaal wanneer de energie van het uitgaand nucleon laag is, terwijl bij hogere energieën de diepte van de potentiaal afneemt zoals vereist. Dit zorgt ervoor dat bij uitgaande energieën die vergelijkbaar zijn met het momentum van een gebonden nucleon, beide nucleon golffuncties consistent verkregen worden uit dezelfde potentiaal. Hiermee worden spurieuze niet-orthogonale contributies aan het matrixelement vermeden, zo is onder meer aan het Pauli-exclusie principe voldaan en blijft de vectorstroom behouden. Vergelijking met data voor elektron-kern verstrooiing toont dat deze methode leidt tot een goede beschrijving van de werkzame doorsnede over een breed energiegebied wanneer het uitgaande nucleon niet gedetecteerd wordt. Dit is in het bijzonder het geval voor de kinematische regio gedomineerd door 1-nucleon uitstoot.

Resultaten voor pion productie op kernen We vergelijken de werkzame doorsnedes voor enkelvoudige pion productie met experimentele data voor neutrino interacties op koolstof. De interpretatie van de vergelijking met data wordt ietwat bemoeilijkt door niet-triviale kinematische restricties in de data, en het feit dat de precieze opmaak van de hadronische finale toestand niet volledig gekarakteriseerd kan worden. We vergelijken enerzijds met data van het MINERνA experiment, dewelke zowel geladen als neutrale pion productie door neutrino's en antineutrino's beslaat, en anderzijds met de recente data van T2K voor neutrino-geïnduceerde geladen pion productie. We vergelijken alsook resultaten in de relativistische vervormde-golf benadering met de resultaten in de relativistische vlakke-golf benadering. Dit leert ons dat de verschillen in werkzame doorsnede omwille van de uitgaande nucleon potentiaal, hoewel ze tot 10% kunnen zijn, een stuk kleiner zijn dan in het geval van 1-nucleon uitstoot. In het bijzonder zien we geen grote verschillen in de vorm van de werkzame doorsnedes als functie van de meeste kinematische variabelen.

De vergelijking met data voor geladen pion productie, voor zowel neutrino's als antineutrino's lijkt consistent. De beschrijving van de π^+ productie data van T2K en MINERνA is alsook gelijkaardig van kwaliteit. Hier merken we wel op dat een reductie van de werkzame doorsnede vanwege pion finale-toestandsinteracties verwacht wordt. We vinden dat de MINERνA π^+ data, die slechts invariante massa in het deltagebied toelaat, overschat wordt en plaats laat voor zo'n reductie. Anderzijds laat de werkzame doorsnede voor T2K en π^- productie in MINERνA, dewelke beide hogere invariante massa's toelaten, geen ruimte voor dergelijke reductie.

De beschrijving van neutrale pion productie door neutrino's en antineutrino's in MINERνA anderzijds is niet consistent. Met het in rekening brengen van de kinematische restricties in de data voorspelt het model dat de magnitude van de werkzame doorsnede voor de neutrino interactie gelijkaardig is aan die voor de antineutrino interactie. Het model beschrijft de data voor antineutrino's over het algemeen goed, terwijl de neutrino data significant onderschat wordt.

Onze bevinding voor geladen pion productie is consistent met de idee dat de werkzame doorsnede bij invariante massa voorbij het deltagebied onderschat wordt. De origine van de discrepanties in de beschrijving voor neutrale pion productie is moeilijker aan iets toe te schrijven, maar zou dezelfde oorzaak kunnen hebben. In de werkzame doorsnede voor het antineutrino proces is er namelijk een cancellatie tussen de contributie van de interactie op een vrij proton, en de vector-axiale interferentieterm. Zolang deze beide contributies gelijkaardig blijven is het in principe mogelijk om de werkzame doorsnede voor het neutrino proces te vergoten zonder de overeenkomst met de antineutrino data te verliezen.

Appendices

Appendix A

Notation and conventions

This appendix summarizes the notation and conventions used throughout this work and provides some background for selected concepts. We follow the normalization conventions for spinors of Ref. [48].

We use natural units throughout this work i.e. the reduced planck constant, and the speed of light are

$$\hbar = 1, \ c = 1, \tag{A.1}$$

and we do not explicitly write these constants unless neccesary. The fine structure constant in natural units reads

$$\alpha = \frac{e^2}{4\pi} = \frac{1}{137.04}, \tag{A.2}$$

with e the fundamental charge.

A.1 Four-vectors Lorentz transformations and Tensors

Four vectors are four-component vectors which describe properties of an event which is observed at a particular point in space-time. Lorentz transformations are linear transformations which relate the components of a four-vector observed in an inertial frame to the components observed in a different inertial frame. The four-position x describes the position and time of an event in a particular inertial frame is denoted

$$x = (x_0, x_1, x_2, x_3) = (x_0, \mathbf{x}) = (t, \mathbf{x}) \tag{A.3}$$

where the zeroth component is the time-like coordinate and the other components form a vector in 3-dimensional space. We write four vectors in italics, or with an explicit index in superscript when this is more clear. To distinguish them from ordinary three-component vectors we write the latter in bold. A general linear transformation can be written in tensor form

$$x^{\nu\prime} = \Lambda^{\nu}{}_{\mu} x^{\mu}, \tag{A.4}$$

where summation over repeated indices should be understood.

The Lorentz transformations are now those that keep the norm of the four-vector invariant, where the norm is defined as

$$x^2 = x \cdot x = g_{\mu\nu} x^{\mu} x^{\nu}, \tag{A.5}$$

with $g_{\mu\nu}$ the metric tensor. The metric tensor hence defines what lineair transformations constitute Lorentz transformations, it is defined

$$g_{\mu\nu} = \begin{pmatrix} 1 & 0 & 0 & 0 \\ 0 & -1 & 0 & 0 \\ 0 & 0 & -1 & 0 \\ 0 & 0 & 0 & -1 \end{pmatrix}. \tag{A.6}$$

This means that the invariant under Lorentz transformations is $t^2 - |\mathbf{x}|^2$, this follows from the speed of light being the same in all inertial frames.

We define the Levi-Civita symbol $\epsilon_{\alpha\beta\gamma\delta}$, a totally anti-symmetric tensor with

$$\epsilon_{0123} = 1, \tag{A.7}$$

where if the indices $(\alpha\beta\gamma\delta)$ are an even permutation of $(0, 1, 2, 3)$ the sign is positive while for uneven permutations the sign is negative, the tensor is zero if any indices are repeated. Here introduced for 4-dimension the definition remains the same in n-dimensions.

Four vectors with an upper index are contravariant, it is convenient to introduce the covariant four-vector, denoted with a lower index as

$$x_{\mu} = g_{\mu\nu} x^{\nu}, \tag{A.8}$$

such that the scalar product can be written

$$x \cdot x = x_{\mu} x^{\mu}. \tag{A.9}$$

Covariant four vectors transform under Lorentz transformations as

$$x'_{\nu} = \Lambda_{\nu}{}^{\mu} x_{\mu}, \tag{A.10}$$

where

$$\Lambda_\mu^{\ \nu} = g_{\mu\alpha}\Lambda^\alpha_{\ \beta}g^{\nu\beta} = (\Lambda^{-1})^\mu_\nu \tag{A.11}$$

is the inverse transformation.

Lorentz transformations, when expressed in matrix form have determinant 1 or -1 the former are referred to as proper tranformations which are comprised of boosts ($B^\mu_{\ \nu}$) and rotations ($R^\mu_{\ \nu}$) and the latter are the improper transformations time reversal T^μ_ν and parity inversion ($P^\mu_{\ \nu}$). Any proper transformation can be written as a rotation and a subsequent boost. A boost corresponds to a transformation to an inertial frame that is moving with velocity $\beta = (\beta_x, \beta_y, \beta_z)$ relative to the current frame. A boost can be written in matrix notation as

$$[B(\beta)]^\nu_{\ \mu}\, x^\mu = \begin{pmatrix} \gamma & -\gamma\beta_x & -\gamma\beta_y & -\gamma\beta_z \\ -\gamma\beta_x & 1+\alpha\beta_x^2 & \alpha\beta_x\beta_y & \alpha\beta_x\beta_z \\ -\gamma\beta_y & \alpha\beta_y\beta_x & 1+\alpha\beta_y^2 & \alpha\beta_y\beta_x \\ -\gamma\beta_z & \alpha\beta_x\beta_z & \alpha\beta_y\beta_z & 1+\alpha\beta_z^2 \end{pmatrix} \begin{pmatrix} x_0 \\ x_1 \\ x_3 \\ x_4 \end{pmatrix} \tag{A.12}$$

with the Lorentz factor $\gamma = (1-\beta^2)^{-1/2}$ and $\alpha = \gamma^2/(\gamma+1) = (\gamma-1)/\beta^2$. A general rotation does not affect the time like-components, hence for all rotations $R^0_{\ 0} = 1$ and $R^0_{\ i} = R^i_{\ 0} = 0$ for all $i \neq 0$. For the space-like components the rotation matrix is the same as a classical rotation, for a given rotation axis represented by the unit vector $\hat{\mathbf{n}}$, and an angle θ the elements of the rotation matrix which rotates along this axis with given angle are

$$R_{ij} = \cos\theta\delta_{ij} + \sin\theta\epsilon_{ijk}\hat{\mathbf{n}}_k + (1-\cos\theta)\hat{\mathbf{n}}_i\hat{\mathbf{n}}_j. \tag{A.13}$$

Finally, the improper Lorentz transformations parity inversion and time reversal are their own inverses, parity flips the sign of all spatial components while time reversal flips the sign of the time component.

Apart from the position in space-time of an event, other quantities transform as four-vectors under Lorentz transformations when observed from a different inertial system. The four-momentum of a particle is

$$P^\mu = (E, \mathbf{p})\,, \tag{A.14}$$

for which the conserved quantity is it's invariant mass

$$P \cdot P = E^2 - \mathbf{p}^2 = m^2. \tag{A.15}$$

As energy and momentum are separately conserved in interactions, the four momentum is also a conserved quantity.

For use in the next section we mention the four-spin. The intrinsic angular momentum, i.e. the spin of a particle, is always measured with respect to some spatial direction. If a particle is polarized along some specific direction in a specific frame, due to the change of spatial coordinates, the direction of the polarization will change under Lorentz transformations. The four-spin is a four-vector which gives the direction along which its spin is polarized in the particles rest frame and for which the time-like component is zero.

A.2 The free Dirac equation

The Dirac equation for free particles can be introduced in quite general terms

$$\hat{E}\psi = (\alpha \cdot \hat{\mathbf{p}} + \alpha_0 m)\,\psi, \tag{A.16}$$

where $\hat{E}$ and $\hat{\mathbf{p}}$ are energy and momentum operators. $\alpha = (\alpha_1, \alpha_2, \alpha_3)$ is a tree-component vector. The quantities α_i (including α_0) should satisfy

$$\alpha_i^2 = 1,\ \alpha_i\alpha_j + \alpha_j\alpha_i = 0\ (j \neq i). \tag{A.17}$$

With the anticommutation of the α_i, upon squaring both sides of A.16 the cross terms dissapear and one obtains the Klein-Gordan equation

$$\hat{E}^2\psi = \hat{\mathbf{p}}^2\psi + m^2\psi, \tag{A.18}$$

such that solutions of the Dirac equation satisfy Einstein's energy-momentum relation. Furthermore, if the Hamiltonian A.16 is to yield real eigenvalues this means that the α should be Hermitian $\alpha_i = \alpha_i^\dagger$. We use the Dirac-Pauli representation, in which the α are traceless Hermitian 4×4 matrices with eigenvalues ± 1. It is customary to write the Dirac equation in a form which is suggestive of the covariance under Lorentz transformations. If the energy and momentum operators are cast into a four vector $\hat{P}_\mu = (\hat{E}, -\hat{\mathbf{p}})$ one can multiply Eq. (A.16) by α_0 to obtain

$$\left(\gamma^\mu \hat{P}_\mu - m\right)\psi = 0, \tag{A.19}$$

where $\gamma^\mu = (\alpha_0, \alpha_0\alpha_1, \alpha_0\alpha_2, \alpha_0\alpha_3)$ is a conventient shorthand notation for the different matrices, such that $\gamma^\mu \hat{P}_\mu$ can effectively be treated as a product of four-vectors. From the anti-commutation relations of the α_i one then has that the gamma matrices should satisfy the anti-commutation relation

$$\{\gamma^\mu, \gamma^\nu\} = 2g^{\mu\nu}\mathbf{1}_4 \tag{A.20}$$

with $\gamma^{\mu\nu}$ the metric tensor introduced earlier. And that $(\gamma^0)^\dagger = \gamma^0$ is Hermitian while for $k \neq 0$, $(\gamma^k)^\dagger = -\gamma^k$ they are anti-Hermitian .

The components of γ^μ in the Dirac-Pauli representation are the four-by-four matrices

$$\gamma^0 = \begin{pmatrix} \sigma_0 & 0 \\ 0 & -\sigma_0 \end{pmatrix}, \ \gamma^i = \begin{pmatrix} 0 & \sigma_i \\ -\sigma_i & 0 \end{pmatrix} \ (i \neq 0). \tag{A.21}$$

Here the σ_i in the spatial components are the two-by-two Pauli matrices

$$\sigma_1 = \begin{pmatrix} 0 & 1 \\ 1 & 0 \end{pmatrix}, \ \sigma_2 = \begin{pmatrix} 0 & -i \\ i & 0 \end{pmatrix}, \ \sigma_3 = \begin{pmatrix} 1 & 0 \\ 0 & -1 \end{pmatrix}, \tag{A.22}$$

and

$$\sigma_0 = \mathbf{1}_2 = \begin{pmatrix} 1 & 0 \\ 0 & 1 \end{pmatrix}. \tag{A.23}$$

Solutions ψ of Eq. are four-component Dirac wavefunctions on which the γ^μ can act. One can define linear combinations of products of gamma matrices to span the space of four-by-four matrices which can act on the Dirac wavefunctions. Of particular significance is

$$\gamma^5 = \gamma_5 = i\gamma^0\gamma^1\gamma^2\gamma^3\gamma^4 = \begin{pmatrix} 0 & \sigma_0 \\ \sigma_0 & 0 \end{pmatrix}. \tag{A.24}$$

which is Hermitian and anticommutes $\left[\gamma^\mu, \gamma^5\right] = 0$ with the four gamma matrices.

Another combination is defined by the commutator of the gamma matrices

$$\sigma^{\mu\nu} = \frac{i}{2}\left[\gamma^\mu, \gamma^\nu\right]. \tag{A.25}$$

As mentioned, the gamma matrices γ^μ may be effectively treated as a four-vector. The covariant form is $\gamma_\mu = g_{\mu\nu}\gamma^\nu$, and products with a four-vector $x = (x_0, x_1, x_2, x_3)$ are $x \cdot \gamma = x_\mu \gamma^\mu = x_0\gamma_0 - x_1\gamma^1 - x_2\gamma^2 - x_3\gamma^3$. Due to the common occurence of such products the Feyman slash notation is introduced where for a four vector x

$$\not{x} = x_\mu \gamma^\mu. \tag{A.26}$$

Free particle (plane-wave) solutions to the Dirac equation can easily be found. Working in coordinate space the operator $\hat{P}_\mu = (\hat{E}, -\hat{\mathbf{p}}) = i\partial_\mu = i(\frac{\partial}{\partial t}, \frac{\partial}{\partial x}, \frac{\partial}{\partial z}, \frac{\partial}{\partial z})$. For a plane-wave ansatz $\psi(t, \mathbf{x}) = u\,(E, \mathbf{p})\, e^{i(\mathbf{p}\cdot\mathbf{x} - Et)}$ we have upon substitution in eq. A.2 that

$$(\not{p} - m)\, u\,(E, \mathbf{p}) = 0. \tag{A.27}$$

We refer to $u(E, \mathbf{p})$ as the (free) Dirac spinor. There are four independent solutions to this equation. If we write the Dirac spinor, dropping energy and momentum dependence, as $u^T = (\phi, \chi)$, where ϕ and χ have two components each, one observes that the Dirac equation decomposes into two coupled equations

$$\phi = \frac{\sigma \cdot \mathbf{p}}{E - m} \chi \tag{A.28}$$

$$\chi = \frac{\sigma \cdot \mathbf{p}}{E + m} \phi. \tag{A.29}$$

Eliminating either ϕ or χ from these equations yields two solutions

$$u_+ = \begin{pmatrix} \phi \\ \frac{\sigma \cdot \mathbf{p}}{E+m} \phi \end{pmatrix}, \quad u_- = \begin{pmatrix} \frac{\sigma \cdot \mathbf{p}}{E-m} \chi \\ \chi \end{pmatrix}. \tag{A.30}$$

These are positive and negative energy solutions to the Dirac equation. This is most easily seen if the particle is at rest, in which case the Dirac equation (A.2) becomes

$$E \gamma^0 u = m u, \tag{A.31}$$

such that $E = \pm m$ for the $u_\pm$. Instead of dealing with the negative energy states it is customary to introduce antiparticle spinors $v(E, \mathbf{p})$ by looking for solutions of the Dirac equation where $\psi(t, \mathbf{x}) = v(E, \mathbf{p}) e^{-i(\mathbf{p} \cdot \mathbf{x} - Et)}$, i.e. in which the sign in the exponent is reversed. One then finds that the antiparticle spinors satisfy

$$\left(\not{p} + m \right) v(E, \mathbf{p}) = 0, \tag{A.32}$$

and that hence the positive-energy antiparticle solutions are

$$v_+ = \begin{pmatrix} \frac{\sigma \cdot \mathbf{p}}{E+m} \phi \\ \phi \end{pmatrix}. \tag{A.33}$$

These can of course be written as combinations of negative energy solutions of the original Dirac equation, however the interpretation is more natural as anti-particles with positive energies.

The choice of ϕ is arbitrary, and allows for two independent solutions which correspond to the spin degrees of freedom of the Dirac spinor. One can choose two orthogonal two-component vectors, the two simplest choices are

$$\phi_+ = N \begin{pmatrix} 1 \\ 0 \end{pmatrix}, \quad \phi_- = N \begin{pmatrix} 0 \\ 1 \end{pmatrix} \tag{A.34}$$

where N determines the overall normalization of the wavefunctions. With this choice the two spinors corresponding to ϕ_+ and ϕ_- are spin-up and down solutions where the spin quantization axis is along the z-axis in the particle's rest frame.

The operator acting on spinors which corresponds to a boost with velocity β along the direction of the unit vector $\hat{\mathbf{n}}$

$$\hat{B}(\hat{\mathbf{n}}, \beta) = \cosh\frac{\xi}{2} + \hat{n}_i\gamma^0\gamma^i \sinh\frac{\xi}{2}, \tag{A.35}$$

where summation over the three spacelike gamma matrices is understood and the rapidity ξ is defined by $\cosh\xi = \left(1-\beta^2\right)^{-1/2}$. A rotation wih an angle θ around the direction of a unit vector $\hat{\mathbf{n}}$ is given by the operator

$$\hat{R}(\hat{\mathbf{n}}, \theta) = \cos\frac{\theta}{2} - i\hat{n}_i\gamma^5\gamma^0\gamma^i \sin\theta 2. \tag{A.36}$$

Parity inversion is given by

$$\hat{P} = \gamma^0. \tag{A.37}$$

In many cases the spin is unobserved and summed over such that the specific spin-axis is irrelevant. Following Ref. [48] we will label the two spinor spin states by their four-spin $\pm s^\mu = \pm\Lambda^\mu{}_\nu s_0^\nu$, where $s_0 = (0, \boldsymbol{s}_0)$ and $\boldsymbol{s}_0$ is the direction of polarization in the particles rest-frame.

We follow the normalization convention that

$$u^\dagger(p, s)u(p, s') = E/M\delta_{ss'}, \tag{A.38}$$

and

$$v^\dagger(p, s)v(p, s') = -E/M\delta_{ss'}, \tag{A.39}$$

such that $N = \sqrt{\frac{E+M}{2M}}$. For may applications it is convenient to introduce adjoint spinors defined as

$$\overline{u} = u^\dagger\gamma^0,\ \overline{v} = v^\dagger\gamma^0. \tag{A.40}$$

The inner product of an adjoint spinor with a spinor can be shown to be a Lorentz invariant scalar and in particular we have

$$\overline{u}(p, s)u(p, s') = -\overline{v}(p, s)v(p, s') = \delta_{ss'}, \tag{A.41}$$

and a completeness relation

$$\sum_s \left(u(p, s)\overline{u}(p, s) - v(p, s)\overline{v}(p, s)\right) = \mathbf{1}_4. \tag{A.42}$$

One can introduce a projection operator for spin

$$\Sigma(s^\mu) = \frac{1 + \gamma^5 \not{s}}{2}, \tag{A.43}$$

and for positive and negative energy components

$$\Lambda(p^\mu)_\pm = \frac{\pm \not{p} + m}{2m}. \tag{A.44}$$

The action of the spin projection operator on an arbitrary spinor is to project out the component with spin along the axis defined by s. The energy projection operators, for a given momentum $\mathbf{p}$, project out the positive and negative energy spinors. From the normalization and completeness the spinors one then sees that

$$u(p,s)\overline{u}(p,s) = \Lambda_+(p)\Sigma(s) = \frac{\not{p} + m}{2m}\frac{1 + \gamma^5 \not{s}}{2}, \tag{A.45}$$

$$v(p,s)\overline{v}(p,s) = -\Lambda_-(p)\Sigma(s) = -\frac{m - \not{p}}{2m}\frac{1 + \gamma^5 \not{s}}{2}, \tag{A.46}$$

and upon summation over positive and negative spin

$$\sum_{\pm s} u(p,s)\overline{u}(p,s) = \Lambda_+(p) = \frac{\not{p} + m}{2m}, \tag{A.47}$$

$$\sum_{\pm s} v(p,s)\overline{v}(p,s) = -\Lambda_-(p) = -\frac{m - \not{p}}{2m}. \tag{A.48}$$

Appendix B

The Relativistic Mean Field

In this appendix an overview of the relativistic mean field formalism is presented. We first deal with a general overview of the Dirac equation with central potentials, and then provide a more in dept look at mean field theory and at how bound and scattering states obtained with scalar and vector potentials.

B.1 The Dirac equation

The Dirac equation describes particle states with spin 1/2 in terms of Dirac spinors. We will deal with the stationary Dirac equation with central finite-range nuclear scalar ($S(r)$) and vector potentials ($V(r)$), a long-range coulomb potential may also be contained in $V(r)$. The stationary Dirac equation in this case is of the form:

$$[\hat{\alpha} \cdot \hat{\mathbf{p}} + \beta \left(m_N + S\left(r\right)\right) - \left(E - V\left(r\right)\right)] \psi = 0, \tag{B.1}$$

where

$$V(r) = V_{strong}(r) + V_C(r),\ V_C(r \to \infty) \sim \frac{Z\alpha}{r}, \tag{B.2}$$

contains a short range potential due to the strong interaction and the long-range coulomb potential. Because of the spherical symmetry of the potentials we write the angular dependence of the Dirac equation in terms of the spin-spherical harmonics $\phi_{\kappa}^{m}\left(\Omega_r\right)$. A solution with well defined parity and angular momentum then is of the general form

$$\Psi_{\kappa}^{m} = \begin{pmatrix} g_{\kappa}(r)\phi_{\kappa}^{m}\left(\Omega_r\right) \\ if_{\kappa}(r)\phi_{-\kappa}^{m}\left(\Omega_r\right) \end{pmatrix}, \tag{B.3}$$

with the spin spherical harmonics given as

$$\phi_\kappa^m(\Omega_r) = \sum_{m_l s} \langle l\, m_l\, 1/2\, s |\, j\, m_j\, \rangle\, Y_l^{m_l}(\Omega_r)\, \chi^s. \tag{B.4}$$

The relativistic quantum number κ is related to the orbital angular momentum l, and total angular momentum j by

$$l = \left\{ \begin{matrix} \kappa & \text{if} & \kappa > 0 \\ -\kappa - 1 & \text{if} & \kappa < 0 \end{matrix} \right\}, \tag{B.5}$$

with $j = |\kappa| - 1/2$. The upper and lower component radial wavefunctions $g(r)$ and $f(r)$ are solutions of the well-known coupled radial Dirac equation which in this case reads

$$\begin{aligned} \frac{\mathrm{d}g}{\mathrm{d}r} &= -\frac{\kappa}{r} g + [E + m_N + S - V]\, f \\ \frac{\mathrm{d}f}{\mathrm{d}r} &= +\frac{\kappa}{r} f - [E - m_N - S - V]\, g, \end{aligned} \tag{B.6}$$

where we dropped the explicit r dependence of the potentials. To interpret the effect of the scalar and vector potentials in terms of a non-relativistic theory, it is instructive to rewrite these coupled equations in a second-order form that resembles the Shrodinger equation. Indeed, equation (B.1) can be rewritten in terms of the upper component to yield

$$\left[-\frac{\hbar^2 \nabla^2}{2M_N} + V_c + V_{so}\left(\boldsymbol{\sigma} \cdot \boldsymbol{L} - i\boldsymbol{r} \cdot \boldsymbol{p}\right) \right] u(\boldsymbol{k}, s) = \frac{k^2}{2M_N} u(\boldsymbol{k}, s), \tag{B.7}$$

where then the central and spin-orbit potentials are given in terms of the original scalar and vector potentials as

$$\begin{aligned} V_c &= S + \frac{E}{M_N} V + \frac{S^2 - V^2}{2M_N}, \\ V_{so} &= \frac{1}{2M_N\,(E + M + S - V)} \frac{1}{r} \frac{\mathrm{d}}{\mathrm{d}r} [V - S]\,. \end{aligned} \tag{B.8}$$

From this one sees that a non-energy dependent vector potential naturally leads to an energy dependent central potential in a Shrodinger picture. Large vector and scalar potentials lead to a spin orbit coupling with a typical surface-peaked form, where the depth of the potential is determined by the difference between the scalar and vector potentials.

B.2 Relativistic mean field Lagrangian in the Hartree approximation

The relativistic Lagrangian used in our calculations is an extension of the linear $\sigma - \omega$ model originally introduced by Walecka, which contains scalar σ and vector ω mesons. This model is extended by including the ρ-meson, the maxwell field A^μ, the pion, and non-linear terms for the σ [239]. This leads to a lagrangian of the form:

$$
\begin{aligned}
\mathcal{L} = &\overline{\Psi}\left(i\gamma_\mu\partial^\mu - M\right)\Psi && \text{(B.9)}\\
&+\frac{1}{2}\left(\partial_\mu\sigma\partial^\mu - m_\sigma^2\sigma^2\right) - U(\sigma) && \text{(B.10)}\\
&-\frac{1}{4}\Omega_{\mu\nu}\Omega^{\mu\nu} + \frac{1}{2}m_\omega^2\omega_\mu\omega^\mu && \text{(B.11)}\\
&-\frac{1}{4}\mathbf{R}_{\mu\nu}\mathbf{R}^{\mu\nu} + \frac{1}{2}m_\rho^2\rho_\mu\rho^\mu && \text{(B.12)}\\
&-\frac{1}{4}F_{\mu\nu}F^{\mu\nu} && \text{(B.13)}\\
&-g_s\overline{\Psi}\sigma\Psi - g_\omega\overline{\Psi}\gamma_\mu\omega^\mu\Psi - g_\rho\overline{\Psi}\gamma_\mu\tau\rho^\mu\Psi - g_e\frac{1+\tau_3}{2}\overline{\Psi}\gamma_\mu A^\mu\Psi, && \text{(B.14)}
\end{aligned}
$$

where we have dropped the pion terms and the coupling of the Maxwell field to the charged meson as they do not enter the equations of motion in the Hartree approximation [239]. The term $U(\sigma) = \frac{1}{3}g_2\sigma^3 + \frac{1}{4}g_3\sigma^4$ is the non-linear term for the scalar meson. With these extensions the model has 6 free parameters, the meson coupling constants $g_\sigma, g_2, g_3, g_\omega, g_\rho$, and the mass of the σ meson. The tensor fields are

$$
\begin{aligned}
\Omega^{\mu\nu} &= \partial^\mu\omega^\mu - \partial^\nu\omega^\nu, && \text{(B.15)}\\
\mathbf{R}^{\mu\nu} &= \partial^\mu\rho^\mu - \partial^\nu\rho^\nu - g_\rho(\rho^\mu \times \rho^\nu), && \text{(B.16)}\\
F^{\mu\nu} &= \partial^\mu A^\mu - \partial^\nu A^\nu. && \text{(B.17)}
\end{aligned}
$$

With these definitions the mean field approach can be implemented, where the meson fields are replaced by classical fields. This approach was originally applied to infinite nuclear matter, then the meson fields only have a time-like component and are constant, and the system can be solved exactly [181, 240]. For finite nuclei the fields will neccesarily have a spatial dependence and exact solutions are not possible. The self-consistent Hartree equations for the fields can be written down directly from the Lagrangian with certain approximations as we will do here. These equations were also derived with a Greens function approach in [241] which makes the adopted approximations more clear.

When we assume spherical symmetry and look for static solutions, the vector fields are r dependent and again only enter with their time-like components. Since the isovector current is conververd (i.e. protons stay protons and neutrons neutrons) only the third component of the isospin operator τ is non-zero. Furthermore if the nucleus is a parity eigenstate the pion fields (which we have not included in the lagrangian for clarity) do not enter. The scalar and vector potentials that enter the radial Dirac equation (B.6) are then given in terms of the fields as

$$S(r) = g_\sigma \sigma(r) \tag{B.18}$$

$$V(r) = g_\omega \omega^0(r) + g_\rho \tau_3 \rho_3^0(r) + e\frac{1+\tau_3}{2}A^0(r). \tag{B.19}$$

Under the previous approximations and by conservation of the baryon current the tensor fields of eq. (B.15) simplify such that the Lagrange equations for the mesons all reduce to Klein-Gordon-like equations with static source terms

$$\left(\nabla^2 - m_\sigma^2\right)\sigma(r) = g_\sigma \rho_s(r) + g_2\sigma^2(r) + g_3\sigma^3(r), \tag{B.20}$$

$$\left(\nabla^2 - m_\omega^2\right)\omega^0(r) = g_\omega \rho_B(r), \tag{B.21}$$

$$\left(\nabla^2 - m_\rho^2\right)\rho_3^0(r) = g_\rho \rho_I(r), \tag{B.22}$$

$$\nabla^2\sigma(r) = -e\rho_e(r), \tag{B.23}$$

which are the scalar, baryon, isovector, and charged nuclear densities. These are defined in in the Hartree aproach as their expectation values in the single particle basis:

$$\rho_s(r) = \sum_i \overline{\Psi}_i(r)\Psi_i(r), \tag{B.24}$$

$$\rho_B(r) = \sum_i \Psi_i^\dagger(r)\Psi_i(r), \tag{B.25}$$

$$\rho_I(r) = \sum_i \Psi_i^\dagger(r)\tau_3\Psi_i(r), \tag{B.26}$$

$$\rho_e(r) = \sum_i \Psi_i^\dagger(r)\frac{1+\tau_3}{2}\Psi_i(r). \tag{B.27}$$

These equations together with the radial Dirac equation are then solved self-consistently until convergence is reached.

B.3 Bound states

A bound state in a central potential has fixed angular momentum quantum numbers κ and m_j, and negative kinetic energy. It is thus of the form of eq. (B.3) and is normalized as

$$\int r\mathrm{d}r \int \mathrm{d}\Omega\ \Psi_\kappa^{m_j\dagger}\Psi_\kappa^{m_j} = \int r\mathrm{d}r\ g_\kappa^2(r) + f_\kappa^2(r) = 1, \tag{B.28}$$

where the integral over the solid angles is trivial as the spin-spherical harmonics are normalized to one.

It is possible to find a bound state using a shooting point method. The radial Dirac equation is integrated outward from a small radius, and inward from a large radius. These solutions are then matched at a 'shooting point' in between and their distance is used to define the energy error, and the next guess for the bound state energy. This method is repeated until the solutions converge and a stable bound state solution is found.

B.4 Scattering states

A scattering state in a central potential with a fixed energy and spin can be obtained in a partial wave expansion

$$\Psi^s(r) = 4\pi\sqrt{\frac{E+M}{2M}} \sum_{\kappa,m_j,m_l} e^{i\delta_\kappa} i^l \left\langle l\ m_l\ 1/2\ s \right| j\ m_j\ \rangle\, Y^*_{l,m_l}(\Omega_k)\, \Psi_\kappa^{m_j}(\boldsymbol{r}), \tag{B.29}$$

where $\Psi_\kappa^{m_j}(\boldsymbol{r})$ is the solution to the radial Dirac equation for fixed κ and m_j defined in eq. (B.3). Note that the normalization has a relative factor E/M compared to Refs. [126, 242], consistent with the normalization of the free spinors in Appendix A. The boundary conditions for solving Eqs. (B.6) for fixed κ are found from the asymptotic behaviour at $r \to 0$ and $r \to \inf$. The wavefunctions are normalized such that in the absence of a potential they would be plane waves. This requires that the scattering solutions are matched at large r to the expected behaviour in order to fix the normalization. In absence of the Coulomb potential both the scalar and vector potential are of finite range and tend to zero faster than $1/r$ such that the solution for large r is a phase-shifted Dirac plane wave. This means that for large enough r the upper and lower components behave as

$$\Psi_\kappa^m \to \begin{pmatrix} j_l(kr+\delta'_\kappa)\phi_\kappa^m(\Omega_r) \\ isgn(\kappa) j_{\bar{l}}(kr+\delta'_\kappa)\phi_{-\kappa}^m(\Omega_r) \end{pmatrix} \tag{B.30}$$

with j_l the spherical bessel functions, and $\bar{l} = l - sgn(\kappa)$ as determined from Eq. (B.5). For charged particles however we have to take into account the long-range coulomb potential. In this case the asymptotic behaviour can be described by phase shifted Dirac-Coulomb wavefunctions [243]. The asymptotic behavior in terms of sine and cosine functions then is

$$\Psi_\kappa^m \to \begin{pmatrix} \frac{1}{kr}\cos\left(\left(kr + \delta_\kappa + \delta_\kappa^C\right)\phi_\kappa^m\left(\Omega_r\right)\right) \\ \frac{1}{kr}\sin\left(kr + \delta_\kappa + \delta_\kappa^C\right)\phi_{-\kappa}^m\left(\Omega_r\right) \end{pmatrix}, \tag{B.31}$$

with the Coulomb phaseshift:

$$\delta_\kappa^C = y\log\left(2kr\right) - arg\left[\Gamma\left(\gamma + iy\right)\right] - \pi\gamma/2 + \phi. \tag{B.32}$$

Here we have $y = E/k\eta$, with $\eta = Z/\alpha$ the relativistic Sommerfeld parameter, and $\gamma = +\sqrt{\kappa^2 - \eta^2}$. The phase ϕ is given by

$$e^{2i\phi} = \frac{\kappa - iyM/E}{\gamma + iy}. \tag{B.33}$$

However it tends to be more convenient to directly match solutions at large r to the Dirac-Coulomb wavefunctions instead of to their asymptotic behaviour.

Appendix C

Multipole decomposition of the electroweak SPP amplitude

The results of the ANL-Osaka DCC model and the MAID07 isobar model presented in this work are obtained from the multipole amplitudes that are made available online [106, 107]. The description of the electroweak vector current in terms of electromagnetic multipoles follows the standard conventions which have been discussed in detail in e.g. Refs [244, 245], we repeat the neccesary expressions to reproduce the results for the electromagnetic and charge-changing vector current presented in this work for completeness.

The cross section for electromagnetic SPP by virtual photons is written as

$$\frac{d\sigma}{d\Omega_\pi^*} = \sigma_T + \epsilon\sigma_L + \sqrt{\epsilon\,(1+\epsilon)}\sigma_{LT}\cos\phi^* \tag{C.1}$$

$$+ \epsilon\sigma_{TT}\cos 2\phi^* + h\sqrt{\epsilon\,(1+\epsilon)}\sigma_{LT'}\sin\phi^*. \tag{C.2}$$

The cross section is defined in the πN center of mass system, where the exchanged virtual photon defines the z-axis and the azimuthal angle ϕ_π^* is defined with respect to the lepton scattering plane. Following the results of Section 2.3, and using vector current conservation, the different terms in this expression can be identified in terms of the elements of the hadron tensor as

$$\sigma_T = \sigma_0 \frac{H^{11} + H^{22}}{2}, \tag{C.3}$$

$$\sigma_L = \sigma_0 \frac{Q^2}{q^{*2}} H^{00}, \tag{C.4}$$

$$\sigma_{LT} = \sigma_0 \sqrt{\frac{Q^2}{q^{*2}}} \mathrm{Re}(H^{10}), \tag{C.5}$$

$$\sigma_{TT} = \sigma_0 \frac{H^{11} - H^{22}}{2}, \tag{C.6}$$

$$\sigma_{LT'} = \sigma_0 \sqrt{\frac{Q^2}{q^{*2}}} \mathrm{Im}(H^{10}), \tag{C.7}$$

where the coordinate system is such that the pion lies in the lepton scattering plane i.e. defined by the unit vectors

$$\mathbf{k}_3 = \frac{\mathbf{q}}{|\mathbf{q}|}, \ \mathbf{k}_2 = \frac{\mathbf{q}^* \times \mathbf{k}_\pi^*}{|\mathbf{q}^* \times \mathbf{k}_\pi^*|}, \ \mathbf{k}_3 = \mathbf{k}_2 \times \mathbf{k}_3. \tag{C.8}$$

The normalization is determined by $\sigma_0 = \frac{|k_\pi^*|}{k_\gamma^*}$, with $k_\gamma^* = \frac{W^2 - M_N^2}{2W}$ the equivalent photon energy in the CMS. One can compare this to the normalization in Eqs. (3.148-3.152) which applies for the hadron tensor determined by the currents in Chapter 3, and note that in particular the electromagnetic coupling $\sqrt{\alpha}$ is absorbed in the definition of the hadron current in this case.

The hadron tensor is given in terms of the hadron current as

$$H^{\mu\nu}(W, Q^2, \cos\theta^*) = \overline{\sum} \left(J^\mu(W, Q^2, \cos\theta^*, s_i, s_f) \right)^* J^\nu \left(W, Q^2, \cos\theta^* s_i, s_f \right), \tag{C.9}$$

with the appropriate summing and averaging over initial and final nucleon spin implied. One may decompose the hadron current in terms of a complete set of matrices and associated amplitudes, e.g. in terms of Dirac spinors

$$J^\mu(W, Q^2, \cos\theta^*, s_i, s_f) = \overline{u}_f(s_f, k_f) \sum_{n=1}^{n=6} (A_n \mathcal{M}_n^\mu) \, u_i(s_i, k_i), \tag{C.10}$$

where, when taking into account vector current conservation to eliminate 2 degrees of freedom, one needs 6 independent amplitudes to describe the current. Completely equivalently one can write the matrix element $\epsilon_\mu J^\mu$ in terms of Pauli spinors that are eigenstates of the spin along the

$\mathbf{k}_3$ direction, thus making the kinematic dependence of the Dirac spinors explicit

$$\epsilon_\mu J^\mu(W,Q^2,\cos\theta^*) = \chi_f \epsilon_\mu \mathcal{F}^\mu(W,Q^2,\cos\theta^*)\chi_i \tag{C.11}$$

the CGLN amplitudes F_i are then defined as

$$-\epsilon_\mu \mathcal{F}^\mu(W,Q^2,\cos\theta^*) = i\sigma\cdot\epsilon_\perp F_1 + \sigma\cdot\hat{\mathbf{k}}_\pi \sigma\cdot\left(\hat{\mathbf{k}}_\gamma \times \epsilon_\perp\right) F_2 + i\sigma\cdot\hat{\mathbf{k}}_\gamma \hat{\mathbf{k}}_\pi\cdot\epsilon_\perp F_3 \tag{C.12}$$

$$+ i\sigma\cdot\hat{\mathbf{k}}_\pi\hat{\mathbf{k}}_\pi\cdot\epsilon_\perp F_4 + i\sigma\cdot\hat{\mathbf{k}}_\gamma\hat{\mathbf{k}}_\gamma\cdot\epsilon F_5 + i\sigma\cdot\hat{\mathbf{k}}_\pi\hat{\mathbf{k}}_\gamma\cdot\epsilon F_6 - i\sigma\cdot\hat{\mathbf{k}}_\pi\epsilon_0 F_7 - i\sigma\cdot\hat{\mathbf{k}}_\gamma\epsilon_0 F_8 \tag{C.13}$$

where $\epsilon^\mu = (\epsilon_0, \epsilon)$ and the component perpendicular to the direction of the virtual photon is $\epsilon_\perp = \epsilon - \left(\epsilon\cdot\hat{\mathbf{k}}_\gamma\right)\hat{\mathbf{k}}_\gamma$. One can identify the components of the hadron current in the reference system defined by Eq. (C.8) as

$$J^1(s_i,s_f) = \chi_f\left[i\sigma_1\left(F_1 - \cos\theta^* F_2 + \sin^2\theta^* F_4\right)\right. \tag{C.14}$$

$$\left. + i\sigma_3 \sin\theta^*\left(F_2 + F_3 + \cos\theta^* F_4\right)\right]\chi_i, \tag{C.15}$$

$$J^2(s_i,s_f) = \chi_f\left[i\sigma_2\left(F_1 - \cos\theta^* F_2\right) - \sigma_0\sin\theta^* F_2\right]\chi_i, \tag{C.16}$$

$$J^0(s_i,s_f) = \chi_f\left[i\sigma_3\left(\cos\theta^* F_7 + F_8\right) + \sigma_1\sin\theta^* F_7\right]\chi_i. \tag{C.17}$$

$$\tag{C.18}$$

One may square the currents and perform the sums and averaging over the spin to write the relevant hadron tensor elements in terms of the amplitudes as

$$\frac{1}{2}\sum_{s_i,s_f}\frac{H^{11}+H^{22}}{2} = |F_1|^2 + |F_2|^2 + \frac{1}{2}\sin^2\theta^*\left(|F_3|^2 + |F_4|^2\right)$$

$$-\mathrm{Re}\left[F_1^* F_2 - \sin^2\theta^*\left(F_1^*F_4 + F_2^*F_3 + \cos\theta^* F_3^* F_4\right)\right], \tag{C.19}$$

$$\frac{1}{2}\sum_{s_i,s_f} H^{00} = |F_7|^2 + |F_8|^2 + 2\cos\theta^*\mathrm{Re}\left[F_8^*F_7\right] \tag{C.20}$$

$$\frac{1}{2}\sum_{s_i,s_f}\frac{H^{11}-H^{22}}{2} = \frac{1}{2}\sin^2\theta^*\left(|F_3|^2 + |F_4|^2\right)$$

$$+\mathrm{Re}\left[F_1^*F_4 + F_2^*F_3 + \cos\theta^* F_3^*F_4\right], \tag{C.21}$$

$$\frac{1}{2}\sum_{s_i,s_f} H^{03} = -\sin\theta^* \left(F_2^* + F_3^* + \cos\theta^* F_4^*\right) F_8$$
$$- \sin\theta^* \left(F_1^* + F_4^* + \cos\theta^* F_3^*\right) F_7. \quad \text{(C.22)}$$

Finally, by projecting out the dependence on $\cos\theta^*$ [245], the relevant CGLN amplitudes F_i are obtained in terms of a series of electromagnetic multipoles $E_{l\pm}(Q^2, W)$, $M_{l\pm}(Q^2, W)$, and $S_{l\pm}(Q^2, W)$ as

$$F_1 = \sum_l \left(P'_{l+1} E_{l+} + P'_{l-1} E_{l-} + l P'_{l+1} M_{l+} + (l+1) P'_{l-1} M_{l-}\right), \quad \text{(C.23)}$$
$$F_2 = \sum_l \left((l+1) P'_l M_{l+} + l P'_l M_{l-}\right), \quad \text{(C.24)}$$
$$F_3 = \sum_l \left(P''_{l+1} E_{l+} + P''_{l-1} E_{l-} - P''_{l+1} M_{l+} + P''_{l-1} M_{l-}\right), \quad \text{(C.25)}$$
$$F_4 = \sum_l \left(-P''_l E_{l+} - P''_l E_{l-} + P''_l M_{l+} - P''_l M_{l-}\right), \quad \text{(C.26)}$$
$$F_7 = \sum_l \left(-(l+1) P'_l S_{l+} + l P'_l S_{l-}\right), \quad \text{(C.27)}$$
$$F_8 = \sum_l \left((l+1) P'_{l+1} S_{l+} - l P'_{l-1} S_{l-}\right). \quad \text{(C.28)}$$

Here P_l denotes the Legendre polynomial of degree l with argument $\cos\theta^*$, and single and double primes denote their first and second derivative respectively. Finally we note that with this the angle integrated longitudinal and transverse cross sections can be conveniently expressed in terms of the electromagnetic multipoles using

$$\int d\Omega_\pi^* \frac{1}{2}\sum_{s_i,s_f} \frac{H^{11} + H^{22}}{2}$$
$$= 2\pi \sum_l (l+1)^2 \left((l+2)\left(|E_{l+}|^2 + |M_{(l+1)-}|^2\right) + l\left(|M_{l+}|^2 + |E_{(l+1)-}|^2\right)\right), \quad \text{(C.29)}$$

for the transverse cross section and

$$\int d\Omega_\pi^* \frac{1}{2}\sum_{s_i,s_f} H^{00} = 4\pi\,(l+1)^3 \left(|S_{l+}|^2 + |S_{(l+1)-}|^2\right) \quad \text{(C.30)}$$

for the longitudinal.

C.0.1 Charge-changing vector current

To obtain the charge-changing vector current which enters in the weak process from the electromagnetic multipoles we divide out the electromagnetic coupling. Additionally, comparing the normalization σ_0 in the previous section with the one in Eqs. (3.148-3.152) we redefine the amplitudes as

$$\tilde{A}_{l\pm} = \sqrt{\frac{W}{M_N 4\pi\alpha}} A_{l\pm}, \tag{C.31}$$

such that the currents computed with these amplitudes are normalized in the same way as those in Chapter 3. From the isospin relations in section 3.1, one finds following relations between the charge changing neutrino induced isovector current ($J_{CC+,V}$) and electromagnetic J_{EM} currents

$$\langle\pi^+ p|J_{CC+,V}|p\rangle = \sqrt{2}\langle\pi^0 n|J_{EM}|n\rangle + \langle\pi^- p|J_{EM}|n\rangle \tag{C.32}$$

$$\langle\pi^+ n|J_{CC+,V}|n\rangle = \sqrt{2}\langle\pi^0 p|J_{EM}|p\rangle - \langle\pi^- p|J_{EM}|n\rangle, \tag{C.33}$$

and in terms of these two one may write the final physical weak amplitude as

$$\langle\pi^0 p|J_{CC+,V}|n\rangle = -\frac{1}{\sqrt{2}}\left(\langle\pi^+ p|J_{CC+,V}|p\rangle - \langle\pi^+ p|J_{CC+}|p\rangle\right). \tag{C.34}$$

We apply these relations to the multipole amplitudes of the electromagnetic pion production channels to obtain the isovector current needed in the charged-current interactions, the calculation of the hadron current then proceeds as before.

It is important to note that in some cases a different sign convention is used in the isospin decomposition of the amplitudes, and that in general any of the physical amplitudes could be multiplied by an arbitrary phase without affecting the cross sections. In MAID07 for example the electromagnetic amplitude involving a positive pion is defined with a relative minus sign with respect to our convention. As the relations in Eqs. (C.32-C.34) do not involve the π^+ channel, this does not have to be taken into account.

Appendix D

Publications

The publications listed in chronological order below were published, or submitted for publication, during the course of studies. The manuscripts of which results were included in this work are marked with an asterisk, and the contributions of A. Nikolakopoulos to these works is explicitly mentioned.

Journal articles

- *Nuclear medium effects in neutrino- and antineutrino-nucleus scattering*
  N. Jachowicz, A. Nikolakopoulos
  Eur. Phys. J. Spec. Top. (2021)

- *Neutrino energy reconstruction from semi-inclusive samples*
  R. González-Jiménez, M. B. Barbaro, J. A. Caballero, T. W. Donnelly, N. Jachowicz, G. D. Megias, K. Niewczas, A. Nikolakopoulos, J. W. Van Orden, J. M. Udías
  arXiv:2104.01701

- *Angular distributions in Monte Carlo event generation of weak single-pion production*
  K. Niewczas, A. Nikolakopoulos, J. T. Sobczyk, N. Jachowicz, R. González-Jiménez
  Phys. Rev. D 103 (2021) 5, 053003

- *Modeling quasielastic interactions of monoenergetic kaon decay-at-rest neutrinos'*

A. Nikolakopoulos, V. Pandey, J. Spitz, N. Jachowicz
Phys. Rev. C 103 (2021) 6, 064603

- *Lepton kinematics in low energy neutrino-Argon interactions*
  N. Van Dessel, N. Jachowicz, A. Nikolakopoulos
  Phys. Rev. C 101 (2020) no. 4, 045502

- *Constraints in modeling the quasielastic response in inclusive lepton-nucleus scattering*
  R. González-Jiménez, M. B. Barbaro, J. A. Caballero, T. W Donnelly, N. Jachowicz, G. D. Megias, K. Niewczas, A. Nikolakopoulos, J. M. Udías
  Phys. Rev. C 101 (2020) 1, 015503

- *Low energy neutrino scattering in experiments and astrophysics*
  N. Jachowicz, N. Van Dessel, A. Nikolakopoulos
  J. Phys. G: Nucl. Part. Phys. 46 084003 (2019)

∗ *Nuclear effects in electron- and neutrino-nucleus scattering within a relativistic quantum mechanical framework*
R. González-Jiménez, A. Nikolakopoulos, N. Jachowicz, J.M. Udías
Phys. Rev. C 100 (2019) no. 4, 045501

A. Nikolakopoulos: helped to develop parts of the codes, performed part of the numerical calculations, wrote parts of the manuscript, and helped revise the manuscript to its final form.

- *Forbidden transitions in neutral and charged current interactions between low-energy neutrinos and Argon*
  N. Van Dessel, N. Jachowicz, A. Nikolakopoulos
  Phys. Rev. C 100 (2019) no. 5, 055503

∗ *Electron versus muon neutrino induced cross sections in charged current quasi-elastic processes*
A. Nikolakopoulos, N. Jachowicz, N. Van Dessel, K. Niewczas, R. González-Jiménez, J.M. Udías, V. Pandey
Phys. Rev. Lett. 123 (2019) no. 5, 052501

A. Nikolakopoulos: performed the calculations, made the figures, and wrote the first draft of the manuscript. A.N. helped develop the Pauli-blocking approach.

- *Mean field approach to reconstructed neutrino energy distributions in accelerator-based experiments*
  A. Nikolakopoulos, M. Martini, M. Ericson, N. Van Dessel, R. González-Jiménez, N. Jachowicz
  Phys. Rev. C98 (2018) no.5, 054603

∗ *Modeling neutrino-induced charged pion production on water at T2K kinematics*
  A. Nikolakopoulos, R. González-Jiménez, K. Niewczas, J. Sobczyk, N. Jachowicz
  Phys. Rev. D97 (2018) no.9, 093008

A. Nikolakopoulos helped develop parts of the code, performed the calculations, made the figures, and wrote the first draft of the manuscript.

Bibliography

[1] S. M. Bilenky and S. T. Petcov, "Massive neutrinos and neutrino oscillations," *Rev. Mod. Phys.* **59**, 671 (1987).

[2] F. T. Avignone, S. R. Elliott, and J. Engel, "Double beta decay, majorana neutrinos, and neutrino mass," *Rev. Mod. Phys.* **80**, 481 (2008).

[3] M. Gonzalez-Garcia and M. Maltoni, "Phenomenology with massive neutrinos," *Physics Reports* **460**, 1 (2008).

[4] K. Zuber, *Neutrino physics* (Institute of Physics Publishing, Bristol BS1 6BE, UK, 2004).

[5] L. Alvarez-Ruso, M. Sajjad Athar, M. Barbaro, D. Cherdack, M. Christy, P. Coloma, T. Donnelly, S. Dytman, A. de Gouvêa, R. Hill, P. Huber, N. Jachowicz, T. Katori, A. Kronfeld, K. Mahn, M. Martini, J. Morfín, J. Nieves, G. Perdue, R. Petti, D. Richards, F. Sánchez, T. Sato, J. Sobczyk, and G. Zeller, "Nustec1 1neutrino scattering theory experiment collaboration http://nustec.fnal.gov. white paper: Status and challenges of neutrino–nucleus scattering," *Progress in Particle and Nuclear Physics* **100**, 1 (2018).

[6] T. Katori and M. Martini, "Neutrino–nucleus cross sections for oscillation experiments," *J. Phys.* **G45**, 013001 (2018), arXiv:1611.07770 [hep-ph] .

[7] `https://www-boone.fnal.gov/`.

[8] `http://www.t2k-experiment.org/`.

[9] L. Aliaga *et al.* (NuSTEC), in *NuSTEC Workshop on Neutrino-Nucleus Pion Production in the Resonance Region* (2020) arXiv:2011.07166 [hep-ph] .

[10] O. Lalakulich and U. Mosel, "Pion production in the miniboone experiment," *Phys. Rev. C* **87**, 014602 (2013).

[11] T. Leitner and U. Mosel, "Neutrino-nucleus scattering reexamined: Quasielastic scattering and pion production entanglement and implications for neutrino energy reconstruction," *Phys. Rev. C* **81**, 064614 (2010).

[12] M. Martini, M. Ericson, G. Chanfray, and J. Marteau, "Unified approach for nucleon knock-out and coherent and incoherent pion production in neutrino interactions with nuclei," *Phys. Rev. C* **80**, 065501 (2009).

[13] D. Rein and L. M. Sehgal, "Neutrino-excitations of baryon resonances and single pion production," *Annals of Physics* **133**, 97 (1981).

[14] E. Hernández, J. Nieves, and M. Valverde, "Weak pion production off the nucleon," *Phys. Rev. D* **76**, 033005 (2007).

[15] J. Y. Yu, E. A. Paschos, and I. Schienbein, "Comparison of the adler-nussinov-paschos model with the data for neutrino induced single pion production from the miniboone and MINERνA experiments," *Phys. Rev. D* **91**, 054038 (2015).

[16] M. V. Ivanov, G. D. Megias, R. González-Jiménez, O. Moreno, M. B. Barbaro, J. A. Caballero, and T. W. Donnelly, "Charged-current inclusive neutrino cross sections in the superscaling model including quasielastic, pion production and meson-exchange contributions," *Journal of Physics G* **43**, 045101 (2016).

[17] O. Buss, T. Leitner, U. Mosel, and L. Alvarez-Ruso, "Influence of the nuclear medium on inclusive electron and neutrino scattering off nuclei," *Phys. Rev. C* **76**, 035502 (2007).

[18] C. Praet, O. Lalakulich, N. Jachowicz, and J. Ryckebusch, "Δ-mediated pion production in nuclei," *Phys. Rev. C* **79**, 044603 (2009).

[19] S. Ahmad, M. S. Athar, and S. K. Singh, "Neutrino induced charged current $1\pi^+$ production at intermediate energies," *Phys. Rev. D* **74**, 073008 (2006).

[20] M. Rafi Alam, M. Sajjad Athar, S. Chauhan, and S. K. Singh, "Weak charged and neutral current induced one pion production

off the nucleon," *International Journal of Modern Physics E* **25**, 1650010 (2016).

[21] X. Zhang and B. D. Serot, "Coherent neutrinoproduction of photons and pions in a chiral effective field theory for nuclei," *Phys. Rev. C* **86**, 035504 (2012).

[22] S. X. Nakamura, H. Kamano, and T. Sato, "Dynamical coupled-channels model for neutrino-induced meson productions in resonance region," *Phys. Rev. D* **92**, 074024 (2015).

[23] E. Hernández, J. Nieves, and M. J. V. Vacas, "Single π production in neutrino-nucleus scattering," *Phys. Rev. D* **87**, 113009 (2013).

[24] S. X. Nakamura, H. Kamano, and T. Sato, "Dynamical coupled-channels model for neutrino-induced meson productions in resonance region," *Phys. Rev. D* **92**, 074024 (2015).

[25] M. Kabirnezhad, "Single pion production in neutrino-nucleon Interactions," *Phys. Rev. D* **97**, 013002 (2018), arXiv:1711.02403 [hep-ph] .

[26] O. Lalakulich, E. A. Paschos, and G. Piranishvili, "Resonance production by neutrinos: The second resonance region," *Phys. Rev. D* **74**, 014009 (2006).

[27] M. Kabirnezhad, "Single pion production in electron-nucleon interactions," *Phys. Rev. D* **102**, 053009 (2020), arXiv:2006.13765 [hep-ph] .

[28] O. Lalakulich, T. Leitner, O. Buss, and U. Mosel, "One pion production in neutrino reactions: Including nonresonant background," *Phys. Rev. D* **82**, 093001 (2010).

[29] E. Hernández and J. Nieves, "Neutrino-induced one-pion production revisited: The $\nu_\mu n \to \mu^- n\pi^+$ channel," *Phys. Rev. D* **95**, 053007 (2017).

[30] L. Alvarez-Ruso, E. Hernández, J. Nieves, and M. J. Vicente Vacas, "Watson's theorem and the $n\Delta(1232)$ axial transition," *Phys. Rev. D* **93**, 014016 (2016).

[31] R. González-Jiménez, N. Jachowicz, K. Niewczas, J. Nys, V. Pandey, T. Van Cuyck, and N. Van Dessel, "Electroweak single-pion production off the nucleon: From threshold to high invariant masses," *Phys. Rev. D* **95**, 113007 (2017).

[32] E. Hernández, J. Nieves, M. Valverde, and M. J. Vicente Vacas, "n-$\Delta(1232)$ axial form factors from weak pion production," *Phys. Rev. D* **81**, 085046 (2010).

[33] E. Hernández, J. Nieves, and M. J. V. Vacas, "Single π production in neutrino-nucleus scattering," *Phys. Rev. D* **87**, 113009 (2013).

[34] H. Kamano, S. X. Nakamura, T.-S. H. Lee, and T. Sato, "Isospin decomposition of $\gamma n \to N^*$ transitions within a dynamical coupled-channels model," *Phys. Rev. C* **94**, 015201 (2016).

[35] N. Rocco, S. X. Nakamura, T. S. H. Lee, and A. Lovato, "Electroweak Pion-Production on Nuclei within the Extended Factorization Scheme," *Phys. Rev. C* **100**, 045503 (2019), arXiv:1907.01093 [nucl-th] .

[36] R. González-Jiménez, K. Niewczas, and N. Jachowicz, "Pion production within the hybrid relativistic plane wave impulse approximation model at MiniBooNE and MINERvA kinematics," *Phys. Rev. D* **97**, 013004 (2018).

[37] A. Nikolakopoulos, R. González-Jiménez, K. Niewczas, J. Sobczyk, and N. Jachowicz, "Modeling neutrino-induced charged pion production on water at T2K kinematics," *Phys. Rev. D* **97**, 093008 (2018).

[38] T. Leitner, O. Buss, L. Alvarez-Ruso, and U. Mosel, "Electron- and neutrino-nucleus scattering from the quasielastic to the resonance region," *Phys. Rev. C* **79**, 034601 (2009).

[39] T. J. Leitner, *Neutrino-Nucleus Interactions In A Coupled-Channel Hadronic Transport Model*, Ph.D. thesis, Justus-Liebig-Universität Giessen (2009).

[40] N. Rocco, C. Barbieri, O. Benhar, A. De Pace, and A. Lovato, "Neutrino-Nucleus Cross Section within the Extended Factorization Scheme," *Phys. Rev. C* **99**, 025502 (2019), arXiv:1810.07647 [nucl-th] .

[41] L. Salcedo, E. Oset, M. Vicente-Vacas, and C. Garcia-Recio, "Computer simulation of inclusive pion nuclear reactions," *Nucl. Phys. A* **484**, 557 (1988).

[42] T. Golan, C. Juszczak, and J. T. Sobczyk, "Effects of final-state interactions in neutrino-nucleus interactions," *Phys. Rev. C* **86**, 015505 (2012).

[43] C. Andreopoulos *et al.*, "The GENIE Neutrino Monte Carlo Generator," *Nucl. Instrum. Meth.* **A614**, 87 (2010), arXiv:0905.2517 [hep-ph] .

[44] Y. Hayato, "A neutrino interaction simulation program library neut," *Acta Phys. Pol. B* **40**, 2477 (2009).

[45] S. Dytman, Y. Hayato, R. Raboanary, J. T. Sobczyk, J. Tena Vidal, and N. Vololoniaina, "Comparison of validation methods of simulations for final state interactions in hadron production experiments," *Phys. Rev. D* **104**, 053006 (2021), arXiv:2103.07535 [hep-ph] .

[46] O. Lalakulich, K. Gallmeister, and U. Mosel, "Neutrino- and antineutrino-induced reactions with nuclei between 1 and 50 gev," *Phys. Rev. C* **86**, 014607 (2012).

[47] O. Buss, T. Gaitanos, K. Gallmeister, H. van Hees, M. Kaskulov, O. Lalakulich, A. Larionov, T. Leitner, J. Weil, and U. Mosel, "Transport-theoretical description of nuclear reactions," *Physics Reports* **512**, 1 (2012), transport-theoretical Description of Nuclear Reactions.

[48] J. D. Bjorken and S. D. Drell, *Relativistic Quantum Mechanics* (McGraw-Hill, New York, 1964).

[49] S. Boffi, C. Giusti, and F. Pacati, "Nuclear response in electromagnetic interactions with complex nuclei," *Physics Reports* **226**, 1 (1993).

[50] J. D. Walecka, *Electron Scattering for Nuclear and Nucleon Structure* (Cambridge University Press, Cambridge, 2001).

[51] I. G. Aznauryan and V. D. Burkert, "Electroexcitation of nucleon resonances," *Prog. Part. Nucl. Phys.* **67**, 1 (2012), arXiv:1109.1720 [hep-ph] .

[52] M. Tanabashi *et al.* (Particle Data Group), "Review of particle physics," *Phys. Rev. D* **98**, 030001 (2018).

[53] S. L. Adler, "Application of current-algebra techniques to soft-pion production by the weak neutral current: V, A case," *Phys. Rev. D* **12**, 2644 (1975).

[54] E. A. Paschos and D. Schalla, "Coherent pion production by neutrinos," *Phys. Rev. D* **80**, 033005 (2009).

[55] E. A. Paschos and D. Schalla, "Neutrino production of hadrons at low energy and in the small Q^2 region," *Phys. Rev. D* **84**, 013004 (2011).

[56] A. Kartavtsev, E. A. Paschos, and G. J. Gounaris, "Coherent pion production by neutrino scattering off nuclei," *Phys. Rev. D* **74**, 054007 (2006).

[57] H. Kamano, S. X. Nakamura, T.-S. H. Lee, and T. Sato, "Neutrino-induced forward meson-production reactions in nucleon resonance region," *Phys. Rev. D* **86**, 097503 (2012).

[58] D. Rein and L. M. Sehgal, "Neutrino-excitation of baryon resonances and single pion production," *Annals of Physics* **133**, 79 (1981).

[59] H. Kamano, S. X. Nakamura, T.-S. H. Lee, and T. Sato, "Nucleon resonances within a dynamical coupled-channels model of πn and γn reactions," *Phys. Rev. C* **88**, 035209 (2013).

[60] C. Praet, *Modeling quasi-free neutrino-nucleus reactions for accelerator-based experiments*, Ph.D. thesis, Ghent University (2009).

[61] R. M. Davidson and R. Workman, "Effect of form factors in fits to photoproduction data," *Phys. Rev. C* **63**, 058201 (2001).

[62] R. M. Davidson and R. Workman, "Form factors and photoproduction amplitudes," *Phys. Rev. C* **63**, 025210 (2001).

[63] C. Fernández-Ramírez, E. Moya de Guerra, and J. M. Udías, "Effective Lagrangian Approach to pion photoproduction from the nucleon," *Annals of Physics* **321**, 1408 (2006).

[64] H. Garcilazo and E. de Guerra, "A model for pion electro- and photo-production from threshold up to 1 gev," *Nucl. Phys. A* **562**, 521 (1993).

[65] T. Feuster and U. Mosel, "Electromagnetic couplings of nucleon resonances," *Nucl. Phys. A* **612**, 375 (1997), arXiv:nucl-th/9604026 .

[66] D. Drechsel, S. S. Kamalov, and L. Tiator, "Unitary Isobar Model - MAID2007," *Eur. Phys. J. A* **34**, 69 (2007), arXiv:0710.0306 [nucl-th] .

[67] T. Vrancx, L. De Cruz, J. Ryckebusch, and P. Vancraeyveld, "Consistent interactions for high-spin fermion fields," *Phys. Rev. C* **84**, 045201 (2011).

[68] J. J. Kelly, "Simple parametrization of nucleon form factors," *Phys. Rev. C* **70**, 068202 (2004).

[69] "Nucleon resonance photo-/electrocouplings determined from analyses of experimental data on exclusive meson electroproduction off protons," `https://userweb.jlab.org/~mokeev/resonance_electrocouplings/`.

[70] R. C. E. Devenish, T. S. Eisenschitz, and J. G. Korner, "Electromagnetic $N - N^*$ transition form factors," *Phys. Rev. D* **14**, 3063 (1976).

[71] E. Hernández, J. Nieves, S. K. Singh, M. Valverde, and M. J. Vicente Vacas, "ν induced threshold production of two pions and $N^*(1440)$ electroweak form factors," *Phys. Rev. D* **77**, 053009 (2008).

[72] G. M. Radecky *et al.*, "Study of single-pion production by weak charged currents in low-energy νd interactions," *Phys. Rev. D* **25**, 1161 (1982).

[73] T. Kitagaki *et al.*, "Charged-current exclusive pion production in neutrino-deuterium interactions," *Phys. Rev. D* **34**, 2554 (1986).

[74] K. M. Graczyk, D. Kiełczewska, P. Przewłocki, and J. T. Sobczyk, "C_5^A axial form factor from bubble chamber experiments," *Phys. Rev. D* **80**, 093001 (2009).

[75] C. Wilkinson, P. Rodrigues, S. Cartwright, L. Thompson, and K. McFarland, "Reanalysis of bubble chamber measurements of muon-neutrino induced single pion production," *Phys. Rev. D* **90**, 112017 (2014).

[76] S. X. Nakamura, H. Kamano, and T. Sato, "Impact of final state interactions on neutrino-nucleon pion production cross sections extracted from neutrino-deuteron reaction data," *Phys. Rev. D* **99**, 031301 (2019).

[77] J. E. Sobczyk, E. Hernández, S. X. Nakamura, J. Nieves, and T. Sato, "Angular distributions in electroweak pion production off nucleons: Odd parity hadron terms, strong relative phases, and model dependence," *Phys. Rev. D* **98**, 073001 (2018).

[78] K. M. Watson, "The effect of final state interactions on reaction cross sections," *Phys. Rev.* **88**, 1163 (1952).

[79] V. Mathieu, G. Fox, and A. P. Szczepaniak, "Neutral pion photoproduction in a regge model," *Phys. Rev. D* **92**, 074013 (2015).

[80] Joint Physics Analysis Center (JPAC), "High energy model for π^0 photoproduction," `http://cgl.soic.indiana.edu/jpac/Pi0Phot.php`.

[81] I. G. Aznauryan, "Multipole amplitudes of pion photoproduction on nucleons up to 2GeV using dispersion relations and the unitary isobar model," *Phys. Rev. C* **67**, 015209 (2003).

[82] I. G. Aznauryan *et al.* (CLAS Collaboration), "Electroexcitation of nucleon resonances from CLAS data on single pion electroproduction," *Phys. Rev. C* **80**, 055203 (2009).

[83] L. De Cruz, J. Ryckebusch, T. Vrancx, and P. Vancraeyveld, "Bayesian analysis of kaon photoproduction with the regge-plus-resonance model," *Phys. Rev. C* **86**, 015212 (2012).

[84] T. Corthals, J. Ryckebusch, and T. Van Cauteren, "Forward-angle $K^+\Lambda$ photoproduction in a regge-plus-resonance approach," *Phys. Rev. C* **73**, 045207 (2006).

[85] P. D. B. Collins, "An Introduction to Regge Theory and High Energy Physics," (Cambridge University Press, Cambridge, United Kingdom, 2009).

[86] A. D. Martin and T. D. Spearman, "Elementary particle theory," (North-Holland publishing company, Amsterdam, The Netherlands, 1970).

[87] S. Donnachie, G. Dosc, P. Landshoff, and O. Nachtmann, " Pomeron physics and QCD," (Cambridge University Press, Cambridge, United Kingdom, 2002).

[88] Vladimir Gribov, "Strong Interactions of Hadrons at High Energies," in *Gribov Lectures on Theoretical Physics* (Cambridge University Press, Cambridge, United Kingdom, 2001).

[89] J. Nys, *Analyticity constraints for hadron amplitudes*, Ph.D. thesis, Ghent University (2018).

[90] G. F. Chew, "s-matrix theory of strong interactions without elementary particles," *Rev. Mod. Phys.* **34**, 394 (1962).

[91] T. Regge, "Introduction to complex orbital momenta," *Il Nuovo Cimento* **14**, 951 (1959).

[92] M. Froissart, "Asymptotic behavior and subtractions in the mandelstam representation," *Phys. Rev.* **123**, 1053 (1961).

[93] S. Mandelstam, "An extension of the regge formula," *Annals of Physics* **19**, 254 (1962).

[94] M. Guidal, J.-M. Laget, and M. Vanderhaeghen, "Pion and kaon photoproduction at high energies: forward and intermediate angles," *Nucl. Phys. A* **627**, 645 (1997).

[95] M. Vanderhaeghen, M. Guidal, and J.-M. Laget, "Regge description of charged pseudoscalar meson electroproduction above the resonance region," *Phys. Rev. C* **57**, 1454 (1998).

[96] M. M. Kaskulov and U. Mosel, "Deep exclusive charged π electroproduction above the resonance region," *Phys. Rev. C* **81**, 045202 (2010).

[97] M. M. Kaskulov, "Neutral pion electroproduction in $p(e, e'\pi^0)p$ above $\sqrt{s} > 2$ gev," *arXiv:1105.1993v1 [nucl-th]* (2011).

[98] T. Vrancx and J. Ryckebusch, "Charged-pion electroproduction above the resonance region," *Phys. Rev. C* **89**, 025203 (2014).

[99] R. González-Jiménez, N. Jachowicz, K. Niewczas, J. Nys, V. Pandey, T. Van Cuyck, and N. Van Dessel, "Electroweak single-pion production off the nucleon: From threshold to high invariant masses," *Phys. Rev. D* **95**, 113007 (2017).

[100] H. Damien, *Neutral current Single Pion Production at High Energies*, Master's thesis, Ghent University (2020).

[101] T. Sato, D. Uno, and T.-S. H. Lee, "Dynamical model of weak pion production reactions," *Phys. Rev. C* **67**, 065201 (2003).

[102] F. Huang, A. Sibirtsev, S. Krewald, C. Hanhart, J. Haidenbauer, and U.-G. Meissner, "Pion-nucleon charge-exchange amplitudes above 2-GeV," *Eur. Phys. J. A* **40**, 77 (2009), arXiv:0810.2680 [hep-ph] .

[103] A. V. Barnes, D. J. Mellema, A. V. Tollestrup, R. L. Walker, O. I. Dahl, R. A. Johnson, R. W. Kenney, and M. Pripstein, "Pion charge-exchange scattering at high energies," *Phys. Rev. Lett.* **37**, 76 (1976).

[104] V. Mathieu, I. V. Danilkin, C. Fernández-Ramírez, M. R. Pennington, D. Schott, A. P. Szczepaniak, and G. Fox, "Toward complete pion nucleon amplitudes," *Phys. Rev. D* **92**, 074004 (2015).

[105] P. Lichard, "Some implications of meson dominance in weak interactions," *Phys. Rev. D* **55**, 5385 (1997).

[106] "MAID07 homepage," `https://maid.kph.uni-mainz.de/maid2007/maid2007.html`.

[107] "ANL-Osaka Partial Wave Amplitudes," `https://www.phy.anl.gov/theory/research/anl-osaka-pwa/`.

[108] R. L. Workman, R. A. Arndt, W. J. Briscoe, M. W. Paris, and I. I. Strakovsky, "Parameterization dependence of t-matrix poles and eigenphases from a fit to πn elastic scattering data," *Phys. Rev. C* **86**, 035202 (2012).

[109] "SAID πN analysis," `https://gwdac.phys.gwu.edu/analysis/pin_analysis.html`.

[110] D. Allasia, C. Angelini, G. van Apeldoorn, A. Baldini, S. Barlag, L. Bertanza, F. Bobisut, P. Capiluppi, P. van Dam, M. Faccini-Turluer, A. Frodesen, G. Giacomelli, H. Huzita, B. Jongejans, G. Mandrioli, A. Marzari-Chiesa, R. Pazzi, L. Ramello, A. Romero, A. Rossi, A. Sconza, P. Serra-Lugaresi, A. Tenner, and D. Vignaud, "Investigation of exclusive channels in $\nu/\overline{\nu}$-deuteron charged current interactions," *Nuclear Physics B* **343**, 285 (1990).

[111] P. Rodrigues, C. Wilkinson, and K. McFarland, "Constraining the GENIE model of neutrino-induced single pion production using reanalyzed bubble chamber data," *arXiv:1601.01888v2 [hep-ex]* (2016).

[112] P. Stowell *et al.* (MINERvA Collaboration), "Tuning the GENIA pion production model with MINERvA data," *Phys. Rev. D* **100**, 072005 (2019).

[113] R. González-Jiménez, T. Van Cuyck, N. Van Dessel, V. Pandey, and N. Jachowicz, "Neutrino-induced 1-pion production," *Proc.*

10th Int. Workshop on Neutrino-Nucleus Interactions in Few-GeV Region (NuInt15), *JPS Conf. Proc.* **12**, 010047 (2016).

[114] K. Niewczas, A. Nikolakopoulos, J. T. Sobczyk, N. Jachowicz, and R. González-Jiménez, "Angular distributions in Monte Carlo event generation of weak single-pion production," *Phys. Rev. D* **103**, 053003 (2021), arXiv:2011.05269 [hep-ph] .

[115] J.-J. Wu, T. Sato, and T.-S. H. Lee, "Incoherent pion production in neutrino-deuteron interactions," *Phys. Rev. C* **91**, 035203 (2015).

[116] O. Lalakulich, N. Jachowicz, C. Praet, and J. Ryckebusch, "Quark-hadron duality in lepton scattering off nuclei," *Phys. Rev. C* **79**, 015206 (2009).

[117] J. M. in (NuSTEC), in *NuSTEC Workshop on Neutrino-Nucleus Pion Production in the Resonance Region* (2020) arXiv:2011.07166 [hep-ph] .

[118] T. S. in (NuSTEC), in *NuSTEC Workshop on Neutrino-Nucleus Pion Production in the Resonance Region* (2020) arXiv:2011.07166 [hep-ph] .

[119] R. González-Jiménez, "Theory of neutrino pion production: kinematics and cross section," *PoS* **NuFACT2018**, 086 (2019), arXiv:1905.00535 [nucl-th] .

[120] O. Benhar, V. R. Pandharipande, and S. C. Pieper, "Electron-scattering studies of correlations in nuclei," *Rev. Mod. Phys.* **65**, 817 (1993).

[121] O. Benhar, N. Farina, H. Nakamura, M. Sakuda, and R. Seki, "Electron- and neutrino-nucleus scattering in the impulse approximation regime," *Phys. Rev. D* **72**, 053005 (2005).

[122] A. M. Ankowski, O. Benhar, and M. Sakuda, "Improving the accuracy of neutrino energy reconstruction in charged-current quasielastic scattering off nuclear targets," *Phys. Rev. D* **91**, 033005 (2015).

[123] N. Rocco, A. Lovato, and O. Benhar, "Unified description of electron-nucleus scattering within the spectral function formalism," *Phys. Rev. Lett.* **116**, 192501 (2016).

[124] O. Benhar, A. Fabrocini, S. Fantoni, and I. Sick, "Spectral function of finite nuclei and scattering of gev electrons," *Nuclear Physics A* **579**, 493 (1994).

[125] R. González-Jiménez, M. B. Barbaro, J. A. Caballero, T. W. Donnelly, N. Jachowicz, G. D. Megias, K. Niewczas, A. Nikolakopoulos, J. W. Van Orden, and J. M. Udías, "Neutrino energy reconstruction from semi-inclusive samples," (2021), arXiv:2104.01701 [nucl-th] .

[126] M. C. Martínez, P. Lava, N. Jachowicz, J. Ryckebusch, K. Vantournhout, and J. M. Udías, "Relativistic models for quasielastic neutrino scattering," *Phys. Rev. C* **73**, 024607 (2006).

[127] M. Vanderhaeghen, *Pion production off nucleons and nuclei in electromagnetic nuclear reactions*, Ph.D. thesis, Ghent University.

[128] M. Ivanov, R. González-Jiménez, J. Caballero, M. Barbaro, T. Donnelly, and J. Udías, "Off-shell effects in the relativistic mean field model and their role in cc (anti)neutrino scattering at miniboone kinematics," *Physics Letters B* **727**, 265 (2013).

[129] J. A. Caballero, T. W. Donnelly, E. M. de Guerra, and J. M. Udías, "Analysis of factorization in $(e, e'p)$ reactions: A survey of the relativistic plane wave impulse approximation," *Nucl. Phys. A* **632**, 323 (1998).

[130] S. Gardner and J. Piekarewicz, "Relativistically generated asymmetry in the missing-momentum distribution from the (e,e'p) reaction," *Phys. Rev. C* **50**, 2822 (1994).

[131] R. González-Jiménez, A. Nikolakopoulos, N. Jachowicz, and J. M. Udías, "Nuclear effects in electron-nucleus and neutrino-nucleus scattering within a relativistic quantum mechanical framework," *Phys. Rev. C* **100**, 045501 (2019).

[132] E. D. Cooper, S. Hama, and B. C. Clark, "Global dirac optical potential from helium to lead," *Phys. Rev. C* **80**, 034605 (2009).

[133] E. D. Cooper, S. Hama, B. C. Clark, and R. L. Mercer, "Global dirac phenomenology for proton-nucleus elastic scattering," *Phys. Rev. C* **47**, 297 (1993).

[134] M. V. Ivanov, J. R. Vignote, R. Álvarez-Rodríguez, A. Meucci, C. Giusti, and J. M. Udías, "Global relativistic folding optical

potential and the relativistic green's function model," *Phys. Rev. C* **94**, 014608 (2016).

[135] W. H. Dickhoff, R. J. Charity, and M. H. Mahzoon, "Novel applications of the dispersive optical model," *Journal of Physics G: Nuclear and Particle Physics* **44**, 033001 (2017).

[136] C. Mahaux and R. Sartor, "Dispersion relation approach to the mean field and spectral functions of nucleons in 40ca," *Nuclear Physics A* **528**, 253 (1991).

[137] C. Mahaux and R. Sartor, "Calculation of the shell-model potential from the optical-model potential," *Phys. Rev. Lett.* **57**, 3015 (1986).

[138] W. H. Dickhoff, D. Van Neck, S. J. Waldecker, R. J. Charity, and L. G. Sobotka, "Nonlocal extension of the dispersive optical model to describe data below the fermi energy," *Phys. Rev. C* **82**, 054306 (2010).

[139] J. M. Udías, P. Sarriguren, E. Moya de Guerra, E. Garrido, and J. A. Caballero, "Spectroscopic factors in ^{40}Ca and ^{208}Pb from (e,e'p): Fully relativistic analysis," *Phys. Rev. C* **48**, 2731 (1993).

[140] J. M. Udías, P. Sarriguren, E. Moya de Guerra, E. Garrido, and J. A. Caballero, "Relativistic versus nonrelativistic optical potentials in a(e,e'p)b reactions," *Phys. Rev. C* **51**, 3246 (1995).

[141] J. M. Udías, J. A. Caballero, E. M. de Guerra, J. R. Vignote, and A. Escuderos, "Relativistic mean field approximation to the analysis of $^{16}\mathrm{O}(e,e^{'}p)^{15}\mathrm{N}$ data at $|Q^2|$ $0.4(\mathrm{GeV}/c)^2$," *Phys. Rev. C* **64**, 024614 (2001).

[142] J. M. Udías, P. Sarriguren, E. Moya de Guerra, E. Garrido, and J. A. Caballero, "Spectroscopic factors in ^{40}Ca and ^{208}Pb from (e,e'p): Fully relativistic analysis," *Phys. Rev. C* **48**, 2731 (1993).

[143] Y. Horikawa, F. Lenz, and N. C. Mukhopadhyay, "Final-state interaction in inclusive electromagnetic nuclear processes," *Phys. Rev. C* **22**, 1680 (1980).

[144] A. Meucci, F. Capuzzi, C. Giusti, and F. D. Pacati, "Inclusive electron scattering in a relativistic green's function approach," *Phys. Rev. C* **67**, 054601 (2003).

[145] A. Meucci, C. Giusti, and F. D. Pacati, "Relativistic green's function approach to parity-violating quasielastic electron scattering," *Nuclear Physics A* **756**, 359 (2005).

[146] A. Meucci, J. A. Caballero, C. Giusti, F. D. Pacati, and J. M. Udías, "Relativistic descriptions of inclusive quasielastic electron scattering: Application to scaling and superscaling ideas," *Phys. Rev. C* **80**, 024605 (2009).

[147] A. Meucci and C. Giusti, "Relativistic descriptions of final-state interactions in charged-current quasielastic antineutrino-nucleus scattering at miniboone kinematics," *Phys. Rev. D* **85**, 093002 (2012).

[148] R. González-Jiménez, M. Barbaro, J. Caballero, T. Donnelly, N. Jachowicz, G. Megias, K. Niewczas, A. Nikolakopoulos, and J. Udías, "Constraints in modeling the quasielastic response in inclusive lepton-nucleus scattering," *Phys. Rev. C* **101**, 015503 (2020), arXiv:1909.07497 [nucl-th] .

[149] K. S. Kim and L. E. Wright, "Constraints on medium modifications of nucleon form factors from quasielastic electron scattering," *Phys. Rev. C* **68**, 027601 (2003).

[150] K. S. Kim and L. E. Wright, "y scaling in quasielastic electron scattering from nuclei," *Phys. Rev. C* **76**, 044613 (2007).

[151] R. González-Jiménez, G. D. Megias, M. B. Barbaro, J. A. Caballero, and T. W. Donnelly, "Extensions of superscaling from relativistic mean field theory: The susav2 model," *Phys. Rev. C* **90**, 035501 (2014).

[152] M. B. Barbaro, J. A. Caballero, A. De Pace, T. W. Donnelly, R. González-Jiménez, and G. D. Megias, "Mean-field and two-body nuclear effects in inclusive electron scattering on argon, carbon, and titanium: The superscaling approach," *Phys. Rev. C* **99**, 042501 (2019).

[153] G. D. Megias, M. V. Ivanov, R. González-Jiménez, M. B. Barbaro, J. A. Caballero, T. W. Donnelly, and J. M. Udías, "Nuclear effects in neutrino and antineutrino charged-current quasielastic scattering at MINERνA kinematics," *Phys. Rev. D* **89**, 093002 (2014).

[154] A. Nikolakopoulos, N. Jachowicz, N. Van Dessel, K. Niewczas, R. González-Jiménez, J. M. Udías, and V. Pandey, "Electron versus muon neutrino induced cross sections in charged current quasielastic processes," *Phys. Rev. Lett.* **123**, 052501 (2019).

[155] S. Boffi, F. Cannata, F. Capuzzi, C. Giusti, and F. Pacati, "Orthogonality and the perey factor in knockout reactions induced by electromagnetic probes," *Nuclear Physics A* **379**, 509 (1982).

[156] C. C. d. Atti, M. M. Giannini, and G. Salmè, "Antisymmetry and orthogonality effects in single-particle models of (γ, p) reactions," *Il Nuovo Cimento A (1965-1970)* **76**, 225 (1983).

[157] J. Johansson, H. Sherif, and F. Ghoddoussi, "Orthogonality effects in relativistic models of nucleon knockout reactions," *Nuclear Physics A* **665**, 403 (2000).

[158] A. D. Pace, M. Nardi, W. Alberico, T. Donnelly, and A. Molinari, "The 2p-2h electromagnetic response in the quasielastic peak and beyond," *Nuclear Physics A* **726**, 303 (2003).

[159] G. Megias, T. Donnelly, O. Moreno, C. Williamson, J. Caballero, R. González-Jiménez, A. De Pace, M. Barbaro, W. Alberico, M. Nardi, and J. Amaro, "Meson-exchange currents and quasielastic predictions for charged-current neutrino-^{12}C scattering in the superscaling approach," *Phys. Rev. D* **91**, 073004 (2015).

[160] A. A. Aguilar-Arevalo *et al.* (MiniBooNE Collaboration), "Significant excess of electronlike events in the miniboone short-baseline neutrino experiment," *Phys. Rev. Lett.* **121**, 221801 (2018).

[161] K. Abe, R. Akutsu, A. Ali, J. Amey, C. Andreopoulos, and L. Anthony (T2K Collaboration), "Search for *cp* violation in neutrino and antineutrino oscillations by the t2k experiment with 2.2×10^{21} protons on target," *Phys. Rev. Lett.* **121**, 171802 (2018).

[162] `http://www.dunescience.org`.

[163] `http://hyperk.org/`.

[164] `http://www.microboone.fnal.gov/`.

[165] `https://minerva.fnal.gov/`.

[166] A. M. Ankowski, "Effect of the charged-lepton's mass on the quasielastic neutrino cross sections," *Phys. Rev. C* **96**, 035501 (2017).

[167] M. Martini, N. Jachowicz, M. Ericson, V. Pandey, T. Van Cuyck, and N. Van Dessel, "Electron-neutrino scattering off nuclei from two different theoretical perspectives," *Phys. Rev. C* **94**, 015501 (2016).

[168] J. Nieves and J. E. Sobczyk, "In medium dispersion relation effects in nuclear inclusive reactions at intermediate and low energies," *Annals Phys.* **383**, 455 (2017), arXiv:1701.03628 [nucl-th] .

[169] M. Day and K. S. McFarland, "Differences in Quasi-Elastic Cross-Sections of Muon and Electron Neutrinos," *Phys. Rev.* **D86**, 053003 (2012), arXiv:1206.6745 [hep-ph] .

[170] G. D. Megias, M. B. Barbaro, J. A. Caballero, J. E. Amaro, T. W. Donnelly, I. Ruiz Simo, and J. W. Van Orden, "Neutrino-Oxygen CC0π scattering in the SuSAv2-MEC model," *Journal of Physics G* **46**, 015104 (2019).

[171] J. Ryckebusch, M. Waroquier, K. Heyde, J. Moreau, and D. Ryckbosch, "An rpa model for the description of one-nucleon emission processes and application to 16o(γ, n) reactions," *Nuclear Physics A* **476**, 237 (1988).

[172] J. Ryckebusch, K. Heyde, D. V. Neck, and M. Waroquier, "Aspects of the final-state interaction and long-range correlations in quasi-elastic (e, eṕ) and (e, eń) reactions," *Nuclear Physics A* **503**, 694 (1989).

[173] N. Jachowicz, K. Heyde, J. Ryckebusch, and S. Rombouts, "Continuum random phase approximation approach to charged-current neutrino-nucleus scattering," *Phys. Rev. C* **65**, 025501 (2002).

[174] N. Jachowicz, S. Rombouts, K. Heyde, and J. Ryckebusch, "Cross sections for neutral-current neutrino-nucleus interactions: Applications for ^{12}C and ^{16}O," *Phys. Rev. C* **59**, 3246 (1999).

[175] V. Pandey, N. Jachowicz, T. Van Cuyck, J. Ryckebusch, and M. Martini, "Low-energy excitations and quasielastic contribution to electron-nucleus and neutrino-nucleus scattering in the continuum random-phase approximation," *Phys. Rev. C* **92**, 024606 (2015).

[176] S. Jeschonnek and T. W. Donnelly, "Relativistic effects in the electromagnetic current at gev energies," *Phys. Rev. C* **57**, 2438 (1998).

[177] V. Pandey, N. Jachowicz, J. Ryckebusch, T. Van Cuyck, and W. Cosyn, "Quasielastic contribution to antineutrino-nucleus scattering," *Phys. Rev.* **C89**, 024601 (2014), arXiv:1310.6885 [nucl-th] .

[178] V. Pandey, N. Jachowicz, M. Martini, R. González-Jiménez, J. Ryckebusch, T. Van Cuyck, and N. Van Dessel, "Impact of low-energy nuclear excitations on neutrino-nucleus scattering at miniboone and t2k kinematics," *Phys. Rev. C* **94**, 054609 (2016).

[179] N. Van Dessel, N. Jachowicz, R. González-Jiménez, V. Pandey, and T. Van Cuyck, "*A*-dependence of quasielastic charged-current neutrino-nucleus cross sections," *Phys. Rev.* **C97**, 044616 (2018), arXiv:1704.07817 [nucl-th] .

[180] T. Van Cuyck, N. Jachowicz, R. González-Jiménez, M. Martini, V. Pandey, J. Ryckebusch, and N. Van Dessel, "Influence of short-range correlations in neutrino-nucleus scattering," *Phys. Rev. C* **94**, 024611 (2016).

[181] J. Walecka, "A theory of highly condensed matter," *Annals of Physics* **83**, 491 (1974).

[182] P. Ring, "Relativistic mean field theory in finite nuclei," *Progress in Particle and Nuclear Physics* **37**, 193 (1996).

[183] C. Maieron, M. C. Martínez, J. A. Caballero, and J. M. Udías, "Nuclear model effects in charged-current neutrino-nucleus quasielastic scattering," *Phys. Rev. C* **68**, 048501 (2003).

[184] A. Meucci, J. A. Caballero, C. Giusti, F. D. Pacati, and J. M. Udías, "Relativistic descriptions of inclusive quasielastic electron scattering: Application to scaling and superscaling ideas," *Phys. Rev. C* **80**, 024605 (2009).

[185] R. González-Jiménez, G. D. Megias, M. B. Barbaro, J. A. Caballero, and T. W. Donnelly, "Extensions of superscaling from relativistic mean field theory: The susav2 model," *Phys. Rev. C* **90**, 035501 (2014).

[186] R. González-Jiménez, A. Nikolakopoulos, N. Jachowicz, and J. M. Udías, "Nuclear effects in electron- and neutrino-nucleus scattering within a relativistic quantum mechanical framework," (2019), arXiv:1904.10696 [nucl-th] .

[187] J. E. Amaro, M. B. Barbaro, J. A. Caballero, T. W. Donnelly, A. Molinari, and I. Sick, "Using electron scattering superscaling to predict charge-changing neutrino cross sections in nuclei," *Phys. Rev. C* **71**, 015501 (2005).

[188] Y. Umino and J. M. Udías, "Exchange current corrections to neutrino-nucleus scattering. i. nuclear matter," *Phys. Rev. C* **52**, 3399 (1995).

[189] N. Jachowicz, N. V. Dessel, and A. Nikolakopoulos, "Low-energy neutrino scattering in experiment and astrophysics," *Journal of Physics G: Nuclear and Particle Physics* (2019).

[190] S. Boffi, F. Cannata, F. Capuzzi, C. Giusti, and F. D. Pacati, "Orthogonality and the Perey factor in knockout reactions induced by electromagnetic probes," *Nucl. Phys.* **A379**, 509 (1982).

[191] C. Ciofi degli Atti, M. M. Giannini, and G. Salme, "Antisymmetry and Orthogonality Effects in Single Particle Models of (γ, p) Reactions," *Nuovo Cim.* **A76**, 225 (1983).

[192] J. I. Johansson, H. S. Sherif, and F. Ghoddoussi, "Orthogonality effects in relativistic models of nucleon knockout reactions," *Nucl. Phys.* **A665**, 403 (2000), arXiv:nucl-th/9911010 [nucl-th] .

[193] A. Nikolakopoulos, N. Jachowicz, R. González-Jiménez, J. M. Udías, K. Niewczas, and V. Pandey, "Non-trivial differences between charged current ν_e and ν_μ induced interactions with nuclei," *PoS* **NuFact2019**, 048 (2020).

[194] A. A. Aguilar-Arevalo, C. E. Anderson, A. O. Bazarko, S. J. Brice, B. C. Brown, *et al.* (MiniBooNE Collaboration), "Measurement of neutrino-induced charged-current charged pion production cross sections on mineral oil at $E_\nu \sim 1$ GeV," *Phys. Rev. D* **83**, 052007 (2011).

[195] A. A. Aguilar-Arevalo, C. E. Anderson, A. O. Bazarko, S. J. Brice, B. C. Brown, L. Bugel, J. Cao, *et al.* (MiniBooNE Collaboration), "Measurement of ν_μ-induced charged-current neutral pion production cross sections on mineral oil at $E_\nu \in 0.5\breve{}2.0$ GeV," *Phys. Rev. D* **83**, 052009 (2011).

[196] K. Abe, N. Abgrall, H. Aihara, T. Akiri, J. B. Albert, C. Andreopoulos, S. Aoki, A. Ariga, T. Ariga, S. Assylbekov, D. Autiero, *et al.* (T2K Collaboration), "Measurement of the inclusive ν_μ

charged current cross section on carbon in the near detector of the T2K experiment," *Phys. Rev. D* **87**, 092003 (2013).

[197] K. Abe, C. Andreopoulos, M. Antonova, S. Aoki, A. Ariga, S. Assylbekov, D. Autiero, S. Ban, M. Barbi, G. J. Barker, *et al.* (T2K Collaboration), "First measurement of the muon neutrino charged current single pion production cross section on water with the T2K near detector," *Phys. Rev. D* **95**, 012010 (2017).

[198] B. Eberly, L. Aliaga, O. Altinok, M. G. Barrios Sazo, L. Bellantoni, M. Betancourt, *et al.* (MINERvA Collaboration), "Charged pion production in ν_μ interactions on hydrocarbon at $<E_\nu> = 4.0$ GeV," *Phys. Rev. D* **92**, 092008 (2015).

[199] O. Altinok, T. Le, L. Aliaga, L. Bellantoni, A. Bercellie, M. Betancourt, *et al.*, "Measurement of ν_μ charged-current single π^0 production on hydrocarbon in the few-GeV region using MINERvA," *Phys. Rev. D* **96**, 072003 (2017).

[200] `https://www-nova.fnal.gov/`.

[201] E. Hernández, J. Nieves, and M. Valverde, "Weak pion production off the nucleon," *Phys. Rev. D* **76**, 033005 (2007).

[202] S. Scherer and M. R. Schindler, *A primer for Chiral perturbation theory* (Springer, 2012).

[203] O. Lalakulich, E. A. Paschos, and G. Piranishvili, "Resonance production by neutrinos: The second resonance region," *Phys. Rev. D* **74**, 014009 (2006).

[204] R. M. Davidson and R. Workman, "Form factors and photoproduction amplitudes," *Phys. Rev. C* **63**, 025210 (2001).

[205] T. Vrancx, L. De Cruz, J. Ryckebusch, and P. Vancraeyveld, "Consistent interactions for high-spin fermion fields," *Phys. Rev. C* **84**, 045201 (2011).

[206] M. Guidal, J.-M. Laget, and M. Vanderhaeghen, "Pion and kaon photoproduction at high energies: forward and intermediate angles," *Nuclear Physics A* **627**, 645 (1997).

[207] M. M. Kaskulov and U. Mosel, "Deep exclusive charged π electroproduction above the resonance region," *Phys. Rev. C* **81**, 045202 (2010).

[208] Y. Hayato, "A neutrino interaction simulation program library NEUT," *Acta Phys. Polon.* **B40**, 2477 (2009).

[209] T. Golan, C. Juszczak, and J. T. Sobczyk, "Effects of final-state interactions in neutrino-nucleus interactions," *Phys. Rev. C* **86**, 015505 (2012).

[210] E. Oset and L. L. Salcedo, "Δ Self-energy in Nuclear Matter," *Nucl. Phys.* **A468**, 631 (1987).

[211] "Nuwro user guide," `https://nuwro.github.io/user-guide/`.

[212] S. L. Adler, "Application of current-algebra techniques to soft-pion production by the weak neutral current: v, a case," *Phys. Rev. D* **12**, 2644 (1975).

[213] J. A. Nowak and J. T. Sobczyk, "Hadron production in Wroclaw neutrino event generator," *Acta Phys. Polon.* **B37**, 2371 (2006), arXiv:hep-ph/0608108 [hep-ph] .

[214] A. Bodek and U. Yang, "Modeling deep inelastic cross sections in the few gev region," *Nuclear Physics B - Proceedings Supplements* **112**, 70 (2002).

[215] T. Sjöstrand, P. Edén, C. Friberg, L. Lönnblad, G. Miu, S. Mrenna, and E. Norrbin, "High-energy-physics event generation with pythia 6.1," *Computer Physics Communications* **135**, 238 (2001).

[216] J. T. Sobczyk, J. A. Nowak, and K. M. Graczyk, "Wrong – wrocław neutrino generator of events for single pion production," *Nuclear Physics B - Proceedings Supplements* **139**, 266 (2005), proceedings of the Third International Workshop on Neutrino-Nucleus Interactions in the Few-GeV Region.

[217] C. Wilkinson, P. Rodrigues, S. Cartwright, L. Thompson, and K. McFarland, "Reanalysis of bubble chamber measurements of muon-neutrino induced single pion production," *Phys. Rev. D* **90**, 112017 (2014).

[218] U. Mosel and K. Gallmeister, "Muon-neutrino-induced charged-current pion production on nuclei," *Phys. Rev. C* **96**, 015503 (2017).

[219] T. Leitner, O. Buss, L. Alvarez-Ruso, and U. Mosel, "Electron- and neutrino-nucleus scattering from the quasielastic to the resonance region," *Phys. Rev. C* **79**, 034601 (2009).

[220] K. Abe, J. Adam, H. Aihara, T. Akiri, C. Andreopoulos, S. Aoki, A. Ariga, S. Assylbekov, D. Autiero, *et al.*, "Measurements of neutrino oscillation in appearance and disappearance channels by the t2k experiment with 6.6×10^{20} protons on target," *Phys. Rev. D* **91**, 072010 (2015).

[221] A. A. Aguilar-Arevalo, C. E. Anderson, A. O. Bazarko, S. J. Brice, B. C. Brown, L. Bugel, *et al.* (MiniBooNE Collaboration), "Neutrino flux prediction at miniboone," *Phys. Rev. D* **79**, 072002 (2009).

[222] L. Aliaga, M. Kordosky, T. Golan, O. Altinok, L. Bellantoni, A. Bercellie, and M. Betancourt (MINERνA Collaboration), "Neutrino flux predictions for the numi beam," *Phys. Rev. D* **94**, 092005 (2016).

[223] P. Adamson *et al.*, "The numi neutrino beam," *Nuclear Instruments and Methods in Physics Research Section A: Accelerators, Spectrometers, Detectors and Associated Equipment* **806**, 279 (2016).

[224] B. Eberly *et al.* (MINERvA Collaboration), "Charged pion production in ν_μ interactions on hydrocarbon at $<E_\nu> = 4.0$ GeV," *Phys. Rev. D* **92**, 092008 (2015).

[225] T. Le *et al.*, "Single neutral pion production by charged-current $\overline{\nu}_\mu$ interactions on hydrocarbon at $\langle E_\nu \rangle = 3.6$ GeV," *Phys. Lett. B* **749**, 130 (2015).

[226] C. L. McGivern *et al.* (MINERvA Collaboration), "Cross sections for ν_μ and $\overline{\nu}_\mu$ induced pion production on hydrocarbon in the few-GeV region using MINERvA," *Phys. Rev. D* **94**, 052005 (2016).

[227] J. Wolcott *et al.*, "Evidence for neutral-current diffractive neutral pion production from hydrogen in neutrino interactions on hydrocarbon," *arXiv:1604.01728 [hep-ex]* (2016).

[228] O. Altinok *et al.*, "Measurement of ν_μ charged-current single π^0 production on hydrocarbon in the few-GeV region using MINERvA," .

[229] C. L. McGivern *et al.* (MINERvA Collaboration), "Cross sections for ν_μ and $\overline{\nu}_\mu$ induced pion production on hydrocarbon in the few-GeV region using MINERvA," *Phys. Rev. D* **94**, 052005 (2016).

[230] T. Le *et al.*, "Measurement of $\overline{\nu}_\mu$ charged-current single π^- production on hydrocarbon in the few-GeV region using MINERvA," .

[231] N. Jachowicz and A. Nikolakopoulos, "Nuclear medium effects in neutrino and antineutrino scattering," *Eur. Phys. J. Spec. Top.* (2021), 10.1140/epjs/s11734-021-00286-8.

[232] MINERva Collaboration, "Updated charged pion production resuls," `https://minerva.fnal.gov/wp-content/uploads/2017/03/Updated_1pi_data.pdf`.

[233] O. Altinok, *Measurement of Muon Neutrino Charged Current Single π^0 Production on Hydrocarbon using MINERvA*, Ph.D. thesis, Tufts U. (2017).

[234] M. A. Acero *et al.* (The NOvA Collabortation), "Measurement of the Double-Differential Muon-neutrino Charged-Current Inclusive Cross Section in the NOvA Near Detector," (2021), arXiv:2109.12220 [hep-ex] .

[235] J. Nieves, I. R. Simo, and M. J. V. Vacas, "Inclusive charged-current neutrino-nucleus reactions," *Phys. Rev. C* **83**, 045501 (2011).

[236] K. Abe *et al.* (The T2K Collaboration), "Measurement of the muon neutrino charged-current single π^+ production on hydrocarbon using the T2K off-axis near detector ND280," *Phys. Rev. D* **101**, 012007 (2020).

[237] R. Castillo Fernández, "Measurement of the Muon Neutrino Charged Current interactions and the muon neutrino single pion cross section on CH using the T2K near detector," (2015).

[238] M. Martini, M. Ericson, G. Chanfray, and J. Marteau, *Phys. Rev. C* **81**, 045502 (2010).

[239] M. Sharma, M. Nagarajan, and P. Ring, "Rho meson coupling in the relativistic mean field theory and description of exotic nuclei," *Physics Letters B* **312**, 377 (1993).

[240] B. D. Serot and J. D. Walecka, "Recent progress in quantum hadrodynamics," *Int. J. Mod. Phys.* **E6**, 515 (1997), arXiv:nucl-th/9701058 [nucl-th] .

[241] C. Horowitz and B. D. Serot, "Self-consistent hartree description of finite nuclei in a relativistic quantum field theory," *Nuclear Physics A* **368**, 503 (1981).

[242] J. M. Udías, *Análisis Relativista del proceso* $(e, e'p)$ *en Núcleos Complejos*, Ph.D. thesis, Instituto de Estructura de la Materia, C.S.I.C., Madrid (1993).

[243] W. Greiner, *Relativistic Quantum Mechanics: Wave Equations* (Springer-Verlag, 2000).

[244] H. Kamano, T. S. H. Lee, S. X. Nakamura, and T. Sato, "The ANL-Osaka Partial-Wave Amplitudes of πN and γN Reactions," (2019), arXiv:1909.11935 [nucl-th] .

[245] F. Berends, A. Donnachie, and D. Weaver, "Photoproduction and electroproduction of pions (i) dispersion relation theory," *Nuclear Physics B* **4**, 1 (1967).